

ROLE OF MICROSTRUCTURAL FACTORS ON THE CORROSION BEHAVIOR
OF Mg-9Al-1Zn ALLOYS UNDER DIFFERENT PROCESSING CONDITIONS

A Dissertation

by

YENNY PAOLA CUBIDES GONZALEZ

Submitted to the Office of Graduate and Professional Studies of
Texas A&M University
in partial fulfillment of the requirements for the degree of

DOCTOR OF PHILOSOPHY

Chair of Committee,	Homero Castaneda-Lopez
Committee Members,	Ibrahim Karaman
	Raymundo Case
	Sarbajit Banerjee
Head of Department,	Ibrahim Karaman

May 2020

Major Subject: Materials Science and Engineering

Copyright 2020 Yenny Paola Cubides Gonzalez

ABSTRACT

Magnesium and its alloys exhibit low density and high specific strength making them excellent candidates for a variety of applications in automotive, aerospace, biomedical and electronics fields. Despite these potential applications of magnesium alloys, there are still some major challenges that need to be overcome. Magnesium alloys exhibit poor formability, relatively low strength compared to conventional steel and aluminum alloys and poor corrosion resistance. Processing routes involving severe plastic deformation (SPD) and/or heat treatment methods have been extensively developed to produce magnesium alloys that exhibit superior mechanical properties than traditional cast structures. These processing methods can lead to compositional, microstructural and crystallographic changes that can have a drastic impact on the corrosion behavior of magnesium alloys. Thus, this study aims to provide more details that correlates microstructure evolution during processing with corrosion performance of Mg-9Al-1Zn (AZ91) alloys with emphasis in the role of grain size, grain structure, and morphology and distribution of cathodic secondary phases.

The results revealed that AZ91 alloy exhibit good mechanical properties combined with high corrosion resistance after microstructure modification through equal channel angular pressing (ECAP). Enhanced corrosion resistance of the fine-grain AZ91 alloy is related to presence of a more protective oxide layer, formation of a more adherent and compact layer of corrosion products, and development of more uniform corrosion with shallow corrosion pits. The micro-galvanic corrosion mechanism of a

peak-aged AZ91 alloy was also investigated. It was found that corrosion simultaneously initiates in the interior of α -Mg grains and in the local α -Mg phase within the $\alpha + \beta$ lamellar precipitate. In addition, it was also found that the β -Mg₁₇Al₁₂ phase/ α -Mg matrix interface acts as a barrier against corrosion propagation. Finally, the corrosion susceptibility of recrystallized and un-recrystallized grains in ECAPed AZ91 alloys was studied. From this study, it was revealed that corrosion preferentially initiates and propagates in the recrystallized grains owing to the higher microchemistry difference between the β -Mg₁₇Al₁₂ precipitates and the adjacent α -Mg matrix that induces a strong microgalvanic coupling between these phases. It was also concluded that the superior corrosion resistance and strength of the ECAPed alloys as increasing the strain level was attributed to the combination of smaller grain size, higher volume fraction of refined grains and higher volume fraction of uniformly distributed fine β -Mg₁₇Al₁₂ precipitates.

DEDICATION

To my beloved parents who taught me that dreams become true with constant effort and persistence and to my lovely boyfriend for his endless support, understanding and encouragement during this journey

ACKNOWLEDGEMENTS

I would like to thank my committee chair, Dr. Homero Castaneda for his academic, technical and financial support throughout the process of writing this dissertation. I would like to extend my gratitude to my committee members, Dr. Ibrahim Karaman, Dr. Raymundo Case, and Dr. Sarbajit Banerjee for their guidance, insightful comments, and constructive criticism during my research studies.

Thanks also go to friends, colleagues, and faculty and staff in the Department of Materials Science and Engineering at Texas A&M University for their valuable help and support during my doctoral program. I would especially like to thank my colleagues and friends, Dr. Ramatou Ly, Hanna Hlushko, Abhinav Srivastava, Lin Chen, and Dr. Ivan Karayan for their great contributions during conducting my research, but more importantly, for their personal support and for making my time at Texas A&M University more enjoyable. Thanks to my brilliant undergraduates; Lucas Nash and Bianca Avila for their tremendous help in getting this project done. My sincere gratitude to the staff, Jules Henry, Murat Kaynak, and Michael Elverud for their willingness in helping me solving technical, administrative and personal issues.

Last but not least, this dissertation would not have been possible without the support of my family and friends. Thanks to my parents for their incalculable support during this journey and for always being there for me. Most of all, I am deeply thankful to my boyfriend for his patience and unconditional support and love and for not letting me give up in the most stressful, sad, and intimidating moments during all these years.

CONTRIBUTORS AND FUNDING SOURCES

Contributors

This work was supervised by a dissertation committee consisting of Professor Homero Castaneda and Professors Ibrahim Karaman and Raymundo Case of the Department of Materials Science and Engineering and Professor Sarbajit Banerjee of the Department of Chemistry.

The as-cast AZ91 alloy used for this study was provided by US Magnesium LCC, Salt Lake City, UT. The processing of the as-cast AZ91 alloy through heat treatment and equal channel angular pressing was conducted with the assistance of Robert Barber and Michael Elverud from the Department of Materials Science and Engineering.

In Chapter III, the materials characterization by scanning electron microscopy before and after corrosion testing was conducted in part by Dr. Ahmad Ivan Karayan from the Department of Materials Science and Engineering. The tensile tests of the AZ91 alloys was performed by Matthew Vaughan from the Department of Materials Science and Engineering. Dr. Ahmad Ivan Karayan and Matthew Vaughan also contributed in the discussion of the data. The research conducted in Chapter III was supervised by Dr. Homero Castaneda and Dr. Ibrahim Karaman from the Department of Materials Science and Engineering.

In Chapter IV, the transmission electron microscopy data was performed by Dexin Zhao from the Department of Material Science and Engineering. The data from

the electrochemical microcell technique was conducted by Lucas Nash from the Department of Engineering Technology and Industrial Distribution. Dr. Ahmad Ivan Karayan from the Department of Materials Science and Engineering provided assistance during the data acquisition obtained from scanning Kelvin probe microscopy and electrochemical microcell technique, he also contributed in the data analysis. The research conducted in Chapter IV was supervised by Dr. Homero Castaneda and Dr. Kelvin Xie from the Department of Materials Science and Engineering.

In Chapter V, Dexin Zhao from the Department of Materials Science and engineering performed and analyzed the data obtained by transmission electron microscopy and electron backscatter diffraction. Digvijay Yadav from the Department of Materials Science and Engineering prepared the sample for transmission electron microscopy analysis using dual-focused ion beam. The data from the electrochemical microcell technique was conducted by Lucas Nash from the Department of Engineering Technology and Industrial Distribution. The research conducted in Chapter V was supervised by Dr. Homero Castaneda, Dr. Kelvin Xie, and Dr. Ibrahim Karaman from the Department of Materials Science and Engineering.

All other work conducted for the dissertation was completed by the student independently.

Funding Sources

Graduate study was supported by research and teaching assistantships from the Department of Materials Science and Engineering at Texas A&M University.

NOMENCLATURE

R_a	Arithmetical Mean Height
E_b	Breakdown Potential
β_c	Cathodic Tafel Slope
R_{ct}	Charge Transfer Resistance
CPE	Constant Phase Element
i_{corr}	Corrosion Current Density
E_{corr}	Corrosion Potential
P_H	Corrosion Rate Calculated from Hydrogen Evolution
P_i	Corrosion Rate Calculated from Potentiodynamic Polarization
P_w	Corrosion Rate Calculated from Weight Loss
DDRX	Discontinuous Dynamic Recrystallization
CPE_{dl}	Double Layer Capacitance
DRV	Dynamic Recovery
DRX	Dynamic Recrystallization
EDM	Electrical Discharge Machining
EIS	Electrochemical Impedance Spectroscopy
R_s	Electrolyte Resistance
EBSD	Electron Backscatter Diffraction
EDS	Energy Dispersive X-Ray Spectroscopy
ECAP	Equal Channel Angular Pressing

ED	Extrusion Direction
FD	Flow Direction
FIB	Focused Ion Beam
d	Grain Size
HCP	Hexagonal Close-Packed
HAGBs	High Angle Grain Boundaries
HE	Hydrogen Evolution
HER	Hydrogen Evolution Reaction
$ Z _{0.01\text{Hz}}$	Impedance Magnitude at 0.01 Hz
L	Inductance
R_L	Inductance Resistance
IPF	Inverse Pole Figure
LD	Longitudinal Direction
LAGBs	Low Angle Grain Boundaries
R_z	Maximum Height Profile
NDE	Negative Difference Effect
N	Number of passes
OCP	Open Circuit Potential
OM	Optical Microscopy
CPE_{ox}	Oxide Capacitance
R_{ox}	Oxide Resistance
PSN	Particle-Stimulated Nucleation

R _p	Polarization Resistance
PF	Pole Figure
PDP	Potentiodynamic Polarization
SCE	Saturated Calomel Electrode
SEM	Scanning Electron Microscopy
SKPFM	Scanning Kelvin Probe Force Microscopy
STEM	Scanning Transmission Microscopy
SPD	Severe Plastic Deformation
SFE	Stacking Fault Energy
SIDP	Strain-Induced Dynamic Precipitation
TEM	Transmission Electron Microscopy
UTS	Ultimate Tensile Strength
UFG	Ultrafine-Grained
VPD	Volta Potential Difference
XRD	X-Ray Diffraction
YS	Yield Strength

TABLE OF CONTENTS

	Page
ABSTRACT	ii
DEDICATION	iv
ACKNOWLEDGEMENTS	v
CONTRIBUTORS AND FUNDING SOURCES.....	vi
NOMENCLATURE.....	viii
TABLE OF CONTENTS	xi
LIST OF FIGURES.....	xiv
LIST OF TABLES	xxii
CHAPTER I INTRODUCTION AND LITERATURE REVIEW	1
1.1 Motivation	1
1.2 Problem Statement	5
1.3 Objectives.....	6
1.4 Potential Impact.....	8
1.5 Research Background.....	9
1.5.1 Opportunities and Challenges of Mg Alloys	9
1.5.2 Severe Plastic Deformation for Grain Refinement of Mg Alloys	12
1.5.3 Fundamentals of Corrosion in Magnesium	24
1.5.4 Effect of Microstructural Features on the Corrosion Behavior of Mg and its Alloys	32
CHAPTER II EXPERIMENTAL METHODS	42
2.1 Material and Processing Methods	42
2.2 Microstructure Characterization.....	45
2.3 Mechanical Testing	47
2.4 Localized Potential Distribution.....	47
2.5 Electrochemical and Corrosion Measurements.....	48
2.5.1 Potentiodynamic Polarization (PDP).....	48
2.5.2 Electrochemical Impedance Spectroscopy (EIS)	50

	Page
2.5.3 Hydrogen Evolution and Weight Loss Measurements	50
2.5.4 Immersion Testing.....	51
2.5.5 Electrochemical Microcell Technique.....	53
CHAPTER III ENHANCED MECHANICAL PROPERTIES AND CORROSION RESISTANCE OF AN ULTRAFINE-GRAINED Mg-9Al-1Zn ALLOY	55
3.1 Microstructural Characterization of AZ91 Alloys	56
3.2 Mechanical Properties	64
3.2.1 Hardness	64
3.2.2 Tensile Behavior.....	67
3.3 Electrochemical and Corrosion Measurements.....	70
3.3.1 Open Circuit Potential (OCP).....	70
3.3.2 Potentiodynamic Polarization (PDP).....	72
3.3.3 Electrochemical Impedance Spectroscopy (EIS)	76
3.3.4 Hydrogen Evolution	87
3.3.5 Weight Loss Measurements	97
3.4 Corrosion Mechanism of Fine-Grained AZ91 Alloys	110
3.5 Summary and Conclusions.....	113
CHAPTER IV MICROGALVANIC CORROSION MECHANISM OF A PEAK- AGED Mg-9Al-1Zn ALLOY.....	116
4.1. Microstructural Characterization of Peak-Aged AZ91 Alloy	117
4.2 Localized Potential Distribution in the Peak-Aged AZ91 Alloy	119
4.3 Corrosion Initiation in the Peak-Aged AZ91 Alloy Immersed in Chloride- Containing Media.....	123
4.3.1 Immersion Testing in 3.5 wt.% NaCl Solution	123
4.3.2 In-Situ Corrosion Monitoring in 3.5 wt.% NaCl Solution	136
4.4 Micro-Electrochemical Behavior of α -Mg Matrix and Lamellar $\alpha + \beta$ Precipitates in Chloride-Containing Media.....	139
4.4 Corrosion Mechanism of Peak-Aged AZ91 Alloy in Chloride-Containing Media.....	142
4.4.1 Corrosion Initiation	142
4.4.2 Corrosion Propagation.....	145
4.4 Corrosion Initiation in the As-Cast AZ91 Alloy Immersed in Chloride- Containing Media.....	146
4.5 Summary and Conclusions.....	150
CHAPTER V EFFECT OF DYNAMIC RECRYSTALLIZATION AND STRAIN- INDUCED DYNAMIC PRECIPITATION ON THE CORROSION BEHAVIOR OF PARTIALLY RECRYSTALLIZED Mg-9Al-1Zn ALLOYS	154

	Page
5.1 Microstructural Characterization.....	155
5.1.1 Initial Microstructure Prior to ECAP	155
5.1.2 Microstructure Evolution During ECAP Processing.....	157
5.2. Electrochemical and Corrosion Measurements.....	167
5.2.1 Corrosion Initiation in ECAPed Alloys with Bimodal Grain Structure.....	167
5.2.2 Localized Volta Potential Distribution in the Recrystallized and Non- Recrystallized Regions	175
5.2.3 Localized Electrochemical Behavior of Recrystallized and Non- Recrystallized Regions	177
5.2.4 Corrosion Propagation in ECAPed Alloys with Bimodal Grain Structure ...	180
5.2.5 Influence of Dynamic Recrystallization and Refined Precipitates on the Corrosion Rate.....	186
5.2.6 Influence of Dynamic Recrystallization and Dynamic Precipitation on the Passive Behavior	188
5.3 Summary and Conclusions.....	199
CHAPTER VI CONCLUSIONS AND FUTURE DIRECTIONS	201
REFERENCES	205

LIST OF FIGURES

	Page
Figure 1. Schematic representation of the ECAP process. X is the transverse plane perpendicular to the flow direction, Y is the flow plane parallel to the side face at the exit, and Z is the longitudinal plane parallel to the top face at the exit. Adapted from [10].	15
Figure 2. Basic routes in ECAP process. Adapted from [10].	17
Figure 3. Model proposed by Figueiredo et al. [9] for grain refinement in magnesium alloys using ECAP. Second and third columns correspond to grain structures after one and multiple passes, respectively. Reprinted by permission from Springer Nature: Journal of Materials Science, Grain refinement and mechanical behavior of a magnesium alloy processed by ECAP, vol. 45(17), 4827-4836, Roberto B. Figueiredo, Terence G. Langdon, Copyright (2010) [9].	22
Figure 4. Schematic illustration of a) evolution of LAGB into HAGB during CDRX b) necklace structure during DDRX. Adapted from [42].	24
Figure 5. Potential-pH diagram of Mg-H ₂ O system at 25°C. Adapted from [47].	26
Figure 6. Schematic representation showing the incomplete coverage of the oxide/hydroxide film formed on conventional α -Mg. Adapted from [2].	27
Figure 7. Schematic representation of the negative difference effect. Adapted from [49].	30
Figure 8. Schematic illustration showing the dual role of the β -Mg ₁₇ Al ₁₂ precipitates on the corrosion behavior of Mg-Al alloys. Adapted from [65].	37
Figure 9. Vickers hardness evolution of (a) homogenized AZ91 alloy and (b) ECAPed AZ91 alloy with aging time.	44
Figure 10. Schematic representation of the heat treatment and ECAP processing used in this study.	45
Figure 11. Schematic illustration of the microcell setup for electrochemical testing at local site.	54
Figure 12. SEM micrographs of (a-c) as-cast alloy, (d) homogenized alloy, and (e-f) peak-aged alloy.	57

Figure 13. SEM micrographs of ECAPed alloy showing (a) significant grain refinement of the original homogenized alloy after ECAP processing, (b) bimodal grain structure of elongated coarse grains and equiaxed fine grains, (c) β -Mg ₁₇ Al ₁₂ precipitates formed in the DRXed region and (d) lath-shaped continuous β -Mg ₁₇ Al ₁₂ precipitates formed in the unDRXed regions.....	58
Figure 14. SEM micrographs of ECAP-aged alloy showing (a) and (b) bimodal grain structure of elongated coarse grains and equiaxed fine grains, (c) β -Mg ₁₇ Al ₁₂ precipitates formed in the DRXed region and (d) lath-shaped continuous β -Mg ₁₇ Al ₁₂ precipitates formed in the unDRXed regions.....	62
Figure 15. XRD patterns of as-cast and processed AZ91 alloys.....	64
Figure 16. Vickers hardness of as-cast and processed AZ91 alloys.	66
Figure 17. (a) Tensile stress-strain curves and (b) tensile properties of the as-cast and processed AZ91 alloys.....	67
Figure 18. Evolution of open circuit potential (OCP) during 1 hour of as-cast and processed AZ91 alloys immersed in 3.5 wt.% NaCl solution.	72
Figure 19. Potentiodynamic polarization (PDP) curves of as-cast and processed AZ91 alloys immersed in 3.5 wt.% NaCl solution.....	74
Figure 20. Evolution of EIS spectra for the (a) homogenized alloy, (b) peak-aged alloy, (c) ECAPed alloy and (d) ECAP-aged alloy immersed for 7 days in 3.5 wt.% NaCl solution.....	78
Figure 21. Equivalent electrical circuit to fit the EIS response of the heat-treated alloys and ECAPed alloys.	81
Figure 22. Equivalent circuit elements derived from fitting of EIS spectra for heat-treated and ECAPed specimens; (a) charge transfer resistance (R_{ct}), (b) double layer capacitance (CPE_{dl}), and (c) reciprocal polarization resistance ($1/R_p$).....	82
Figure 23. (a) Volume of hydrogen evolution (b) corrosion rate calculated from hydrogen evolution measurements and (c) pH evolution of the AZ91 samples immersed in 3.5 wt.% NaCl solution for 7 days.....	88

Figure 24. Corrosion morphologies of the heat-treated alloys after hydrogen evolution test for 7 days in 3.5 wt.% NaCl solution: homogenized alloy with (a) and without (c) corrosion products, peak-aged alloy with (d) and without (f) corrosion products. EDS analysis of the corrosion products in (b) homogenized alloy and (e) peak-aged alloy.	90
Figure 25. Corrosion morphologies of the ECAP processed AZ91 Mg alloys after hydrogen evolution test for 7 days in 3.5 wt.% NaCl solution: ECAPed alloy with (a) and without (c) corrosion products, ECAP-aged alloy with (d) and without (f) corrosion products. EDS analysis of the corrosion products in (b) ECAP alloy and (e) ECAP-aged alloy.	92
Figure 26. XRD patterns of the corrosion products formed on the AZ91 alloys after hydrogen evolution test for 7 days in 3.5 wt.% NaCl solution.	93
Figure 27. (a) Weight loss measurements of the AZ91 alloys after immersion for 1, 3, 5, and 7 days in 3.5 wt.% NaCl solution, (b) corrosion rate (P_w) calculated from the weight loss measurements, (c) comparison between P_H and P_w after immersion for 7 days in 3.5 wt.% NaCl solution.	99
Figure 28. Surface appearance of the AZ91 alloys after immersion for 1, 3, 5, and 7 days in 3.5 wt.% NaCl solution.	100
Figure 29. SEM micrographs of (a) homogenized alloy, (b) peak-aged alloy, (c, e) ECAPed alloy and (d, f) ECAP-aged alloy after immersion for one day in 3.5 wt.% NaCl solution.	102
Figure 30. Topography images and roughness profiles of (a) homogenized alloy, (b) peak-aged alloy, (c) ECAPed alloy, and (d) ECAP-aged alloy after one day of immersion in 3.5 wt.% NaCl solution.	108
Figure 31. Roughness parameters (a) R_a and (b) R_z of the different AZ91 alloys after immersion for 1, 3, 5, and 7 days in 3.5 wt.% NaCl solution.	110
Figure 32. Schematic illustration of the micro-galvanic corrosion mechanism of fine-grained AZ91 alloys processed by ECAP.	113
Figure 33. Optical (a) and SEM (b-d) micrographs of the peak-aged alloy and the corresponding line profiles through (c) an α -Mg grain containing lamellar precipitates at the grain boundaries and through (d) an Al_8Mn_5 particle.	119

- Figure 34. Topography (left) and Volta potential (right) maps and profiles of the peak-aged AZ91 alloy in selected areas: (a) lamellar $\alpha + \beta$ precipitate, (b) eutectic β -phase, (c) the interior of the lamellar precipitate and (d) Al_8Mn_5 intermetallic particle. 121
- Figure 35. (a) SEM micrograph of an Al_8Mn_5 intermetallic particle and the corresponding (b-d) X-ray elemental maps of Mg, Al, and Mn. (e) SEM micrograph of a lamellar $\alpha + \beta$ precipitate and the corresponding (f-h) X-ray elemental maps of Mg, Al, and Mn. 123
- Figure 36. Optical micrographs of the peak-aged AZ91 alloy before and after immersion in 3.5 wt.% NaCl for 6 h showing: (a, b) corrosion initiation at the interior of an α -Mg grain far away from the lamellar precipitate, (c, d) corrosion initiation and propagation inside the α -Mg matrix that is delayed at the lamellar $\alpha + \beta$ phase/ α -Mg matrix boundary, (e, f) corrosion initiation inside the lamellar precipitate, and (g, h) extensive corrosion inside the lamellar precipitate that spreads along the precipitate but is also delayed at the lamellar $\alpha + \beta$ phase/ α -Mg matrix boundary. 124
- Figure 37. Cathode-to-anode area ratio between (a) the β - $\text{Mg}_{17}\text{Al}_{12}$ phase and the local α -Mg phase within the lamellar precipitate and (b) the lamellar precipitate and the α -Mg matrix measured using the ImageJ software. 127
- Figure 38. SEM micrographs of the peak-aged AZ91 alloy after immersion in 3.5 wt.% NaCl for 6 h showing: (a-c) corrosion initiation inside the α -Mg matrix, (d-e) X-ray elemental mapping of Al and Mg showing aluminum enrichment in the corroded area shown in c; (f-g) micro-galvanic coupling between Al_8Mn_5 intermetallic particles and the surrounding α -Mg matrix and (h) corrosion propagation in α -Mg grains that is delayed at the lamellar $\alpha + \beta$ phase/ α -Mg matrix boundary. 129
- Figure 39. SEM micrographs of the peak-aged AZ91 alloy after immersion in 3.5 wt.% NaCl for 6 h showing: (a-c) corrosion initiation inside the lamellar precipitate due to micro-galvanic coupling between the β -phase and the local α -Mg phase and (d-e) X-ray elemental mapping of Mg and Al showing aluminum enrichment in the corroded area. 131
- Figure 40. STEM micrographs showing: (a, b) the lamellar $\alpha + \beta$ phase/ α -Mg matrix boundary and (g, h) the interior of the lamellar precipitate. EDX maps of the yellow box regions in a and g indicating the elemental distribution of (c, i) Mg, (d, j) Al and (e, k) Zn. (f, l) Point elemental analysis at the marked regions in a and g showing the lower Al and Zn content in the local α -Mg phase compared to that of the adjacent α -Mg matrix. 133

- Figure 41. Topography and roughness profiles of the peak-aged AZ91 alloy after immersion in 3.5 wt.% NaCl for 6 h showing: (a-c) corrosion initiation and propagation inside the α -Mg matrix and (d-f) corrosion initiation and propagation along the lamellar precipitate. 135
- Figure 42. In situ corrosion observations of the peak-aged AZ91 alloy during 30 h in 3.5 wt.% NaCl solution showing: (a-c) micro-galvanic corrosion between the Al_8Mn_5 intermetallic particle and the adjacent α -Mg matrix; (d-f) corrosion initiation in a lamellar $\alpha + \beta$ precipitate that is underneath a hydrogen bubble that evolves after it reaches a relatively large size; (g) formation of hydrogen bubbles mainly at the lamellar precipitates indicating that they can act as effective cathodes; and (h-i) corrosion propagation inside an α -Mg grain that stops at the lamellar precipitate, indicating that the lamellar precipitate acts as a barrier against corrosion propagation. 137
- Figure 43. (a) Schematic glass capillary with a silicone gasket and the SEM micrographs of the (b) top view and (c) side view of the silicone sealed capillary. 140
- Figure 44. Electrochemical microcell studies showing: morphology of the peak-aged alloy (a) before and (b) after the testing; (c) potentiodynamic polarization measurements of the α -Mg matrix and the lamellar $\alpha + \beta$ precipitate in 3.5 wt.% NaCl solution; closer view of the corroded morphology after the test (d, e) inside the α -Mg matrix and (f, g) inside the lamellar $\alpha + \beta$ precipitate. 142
- Figure 45. Schematic representation of the mechanism of (a) corrosion initiation and (b) corrosion propagation of peak-aged AZ91 alloy immersed in a NaCl environment. 144
- Figure 46. Evolution of the corrosion morphology of the peak-aged AZ91 alloy at different immersion times for up to 7 days in 3.5 wt.% NaCl solution. 146
- Figure 47. Corrosion initiation in the as-cast AZ91 alloy occurring (a, b) in the α -Mg matrix, (c, d) inside the eutectic phase, and (e, f) inside the lamellar precipitates. 147
- Figure 48. (a-d) SEM micrographs of the as-cast AZ91 alloy after immersion in 3.5 wt.% NaCl for 6 h showing corrosion initiation and propagation inside the eutectic and lamellar precipitates due to micro-galvanic coupling between the β -phases (eutectic and lamellar) and the eutectic α -Mg phase. (e) Volta potential map and profile of the partially divorced eutectic phase. 149

- Figure 49. (a) SEM micrograph of the as-cast AZ91 alloy showing the eutectic and lamellar phases and the corresponding X-ray maps of (b) Mg and (c) Al. 150
- Figure 50. SEM micrographs of the microstructure of (a) as-cast alloy, (b) homogenized alloy and (c and d) alloy after pre-heating at 310 °C for 30 min before ECAP processing..... 156
- Figure 51. Optical micrographs of the ECAPed specimens with various number of ECAP passes (a) N = 1 (b) N = 2, (c) N = 3 and (d) N = 4. 158
- Figure 52. SEM micrographs of the ECAPed alloy after the first pass (N = 1) showing (a, b) bimodal grain structure with bulging of the initial grain boundaries and presence of large amount of β -Mg₁₇Al₁₂ precipitates in both the un-DRXed and DRXed regions and (c, d) DRX occurring in neighboring regions of an undissolved eutectic β -phase demonstrating the occurrence of PSN mechanism..... 160
- Figure 53. SEM micrographs of the ECAPed specimens with various number of ECAP passes showing (a-d) the bimodal grain structure, (e-h) a DRXed region and (i-l) an un-DRXed region after N = 1, N = 2, N = 3, and N = 4, respectively. The values in (e-h) indicate the average grain size of the DRXed grains. 164
- Figure 54. (a) XRD patterns of the ECAPed specimens with various number of ECAP passes. (b) Enlarged patterns for the three major peaks of the Mg matrix showing splitting and shifting of the peaks as increasing the number of ECAP passes..... 166
- Figure 55. Optical micrographs of the ECAP alloys with (a, b) N = 1 and (c, d) N = 4 before and after immersion for 1 h in 3.5 wt.% NaCl solution. High magnification SEM micrographs of the (c) ECAP alloy with N = 1 and (d) ECAP with N = 4 after immersion for 1 h in 3.5 wt.% NaCl solution showing corrosion initiation in the DRXed regions. 169
- Figure 56. STEM micrographs of the ECAPed alloy with N = 4 showing (a) lath-shaped β -Mg₁₇Al₁₂ precipitates formed in the un-DRXed regions and (b) spherical β -Mg₁₇Al₁₂ precipitates formed in the DRXed regions with their corresponding EDS maps of (b, f) Mg, (c, g) Al and (d, h) Zn, respectively. (i) Average aluminum content of the β -Mg₁₇Al₁₂ phase and α -Mg matrix in the DRXed and un-DRXed regions. 171

- Figure 57. EBSD IPF maps (out-of-plane crystal orientation) of ECAPed alloy with $N = 4$: (a) large region mapping with both DRXed grains and un-DRXed grains with their corresponding (0002) pole figures and (b) zoom-in map from the black rectangle in (a) showing detailed grains information of the DRXed region along with the corresponding (0002) pole figure. 174
- Figure 58. SKPFM measurements of the ECAPed alloy with $N = 4$ showing (a, d) topography, (b, e) Volta potential difference map, and (c, f) the corresponding line profile along the white arrow of a lath-shaped β - $Mg_{17}Al_{12}$ precipitate in the un-DRXed grains and a spherical β - $Mg_{17}Al_{12}$ precipitate in the DRXed grains, respectively. 176
- Figure 59. Optical micrographs of the ECAPed alloy with fourth passes (a) before and (b) after the local potentiodynamic polarization test in 3.5 wt.% NaCl using the electrochemical microcell technique. (c) local potentiodynamic polarization curves of the DRXed and un-DRXed regions in the ECAPed alloy with fourth passes. SEM micrographs of the (d) un-DRXed region and (f) the DRXed region after the local electrochemical test and after removal of corrosion products. 178
- Figure 60. SEM micrographs of the ECAP alloys with (a, b, c) $N = 1$ and (d, e, f) $N = 4$ after immersion for 24 h in 3.5 wt.% NaCl solution. 181
- Figure 61. Topography and roughness profiles of the ECAPed alloys with (a) $N = 1$ and (b) $N = 4$ after immersion in 3.5 wt.% NaCl for 24 h. 184
- Figure 62. Maximum penetration depth of the ECAPed alloys after 24 h of immersion in 3.5 wt.% NaCl solution against size of the β - $Mg_{17}Al_{12}$ precipitates formed at the grain boundaries of the DRXed grains. 185
- Figure 63. (a) Corrosion rate obtained from weight loss measurements of the ECAPed alloys immersed in 3.5 wt.% NaCl solution for seven days. (b) Vickers hardness against corrosion rate for the different ECAPed samples showing the simultaneous improvement in hardness and corrosion resistance as increasing the number of ECAP passes. 187
- Figure 64. (a) Open circuit potential (OCP), (b) potentiodynamic polarization and EIS measurements showing the (c) Nyquist representation and the (d) the Bode plot of ECAPed alloys with various number of passes immersed in 0.05 M NaCl solution. 190

Figure 65. Variation of $E_b - E_{corr}$ of the ECAPed alloys with different number of ECAP passes against (a) reciprocal square root of grain size and (b) volume fraction of β -Mg ₁₇ Al ₁₂ precipitates at the DRXed grain boundaries.....	195
---	-----

LIST OF TABLES

	Page
Table 1. Predominant deformation modes in magnesium alloys. Adapted from [33]	13
Table 2. Grain structure of Mg alloys after ECAP processing.....	20
Table 3. Processing conditions for the AZ91 specimens investigated in this study	44
Table 4. Microstructural parameters of as-cast and processed AZ91 alloys.....	63
Table 5. Electrochemical parameters obtained from potentiodynamic polarization curves of as-cast and processed AZ91 alloys immersed in 3.5 wt.% NaCl solution	76
Table 6. Microstructural parameters of AZ91 alloys after different ECAP passes.....	165
Table 7. Electrochemical parameters obtained from OCP and polarization measurements of ECAPed AZ91 alloys after different ECAP passes immersed in 0.05 M NaCl solution.....	190
Table 8. Electrical parameters obtained from fitting the EIS data of the ECAPed alloys immersed in 0.05 M NaCl solution	198

CHAPTER I

INTRODUCTION AND LITERATURE REVIEW

1.1 Motivation

Magnesium alloys are emerging as technological materials due to their low density ($\sim 1.7 \text{ g/cm}^3$) and high specific strength with a variety of new potential applications, including those in transportation, biomedicine, and electronics, wherein light weight and biocompatibility are critical design factors [1]. They are the lightest metals next to beryllium alloys, making them attractive for next generation structural materials. In the automotive industry, replacement of aluminum or steel components by light weight magnesium components can significantly enhance energy efficiency resulting in fuel savings and lower CO₂ emissions [2]. It has been reported that 10% reduction in weight for a conventional passenger car results in 20-30% less fuel consumption [2]. AZ91 alloy is a Mg-Al binary alloy that contains 9 wt.% Al, 0.5-1 wt.% Zn, and about 0.2 wt.% Mn. Addition of Al increase the strength, castability, and corrosion resistance of magnesium, similarly, the addition of zinc improves the strength of the alloy by reducing the solid solubility of aluminum in magnesium that increases the amount of precipitates formed during aging resulting in higher strength. Finally, addition of Mn also improves the corrosion resistance of the alloy by reducing the amount of iron impurities through the formation of Al-Mn-Fe intermetallic compounds [3]. Mg-9Al-1Zn (AZ91) alloy has been one of the most used and promising magnesium alloys in the automotive sector due to its damping capacity, excellent castability, and high production

rate [4]. However, AZ91 alloy exhibits undesirable properties such as relatively low strength compared to commonly used carbon steel and aluminum alloys, limited formability particularly at room temperature, and poor corrosion resistance in chloride and acidic environments that drastically limits its application in exterior components [2, 4, 5]. Even worse, AZ91 alloy is susceptible to different types of corrosion such as general dissolution, (macro and micro) galvanic corrosion, localized corrosion, and stress corrosion cracking [6].

Regarding mechanical performance, grain refinement represents an effective method of improving strength and ductility of magnesium alloys [7]. Equal channel angular pressing (ECAP) is a severe plastic deformation (SPD) technique commonly used to produce ultrafine-grained or even nanostructured magnesium alloys with enhanced mechanical properties [1, 8-11]. For precipitate hardening alloys, such as AZ91 alloy, precipitation hardening represents another effective method to improve the strength of the material [7]. The standard heat treatment method following ASTM B661 [12] to strengthen AZ91 alloy considers solution annealing at 413 °C for 24 h, quenching in water at room temperature, and further aging at 168 °C for 16 h to achieve peak-aged condition. Furthermore, post-aging after severe plastic deformation had been also reported to further improve the strength of fine-grained AZ91 alloys [3, 7, 13].

The microstructure that results following different processing conditions can have a large impact on the local or general corrosion behavior of AZ91 alloy when exposed to aggressive environments. Typically, the effect of alloy composition and microstructure derived from a particular processing method on mechanical behavior or

corrosion resistance is investigated separately. However, it is commonly observed that improvement of mechanical properties such as strength or creep resistance is achieved at the expense of corrosion performance [2], therefore is vital to simultaneously investigate both the mechanical properties and corrosion resistance of magnesium alloys in severe environments. Limited publications have been reported considering both, mechanical properties and corrosion resistance after microstructural and compositional changes achieved by different processing methods. Orlov et al. [14] reported simultaneous improvement of strength and corrosion resistance of ZK60 Mg alloy after processing by an integrated process of extrusion and ECAP. They reported that corrosion resistance in chloride environments was improved due to grain refinement and more homogeneous distribution of Zn and Zr alloying elements. In contrast, Hamu et al. [15] found higher hardness values but lower corrosion resistance in an ECAPed AZ31 alloy that was mainly attributed to higher dislocation density and twinning that accelerated corrosion. Miao et al. [16] investigated the effect of pre-solution heat treatment before extrusion on mechanical properties and corrosion resistance of Mg-Zn-Gd alloys immersed in simulated body solutions. They found improvement in corrosion resistance when pre-homogenization before extrusion was performed due to more uniform distribution of secondary particles that induced less localized corrosion attack. However, they found a decrease in yield and tensile strength with solution heat treatment before extrusion due to grain coarsening and basal texture randomization. Deng et al. [17, 18] also found inverse correlation between corrosion resistance and yield strength for Mg–Al–Ca alloys after extrusion process. They report that yield strength decreased as increasing Ca/Al ratio in

the extruded materials, whereas UTS, elongation, and corrosion resistance exhibited an inverse trend. Improvement of corrosion resistance was attributed to grain refinement and homogeneous distribution of secondary phases along grain boundaries which provided a slightly barrier effect for corrosion propagation.

In addition to simultaneous investigation of mechanical properties and corrosion resistance of Mg alloys, fundamental understanding of the effect of microstructural factors such as morphology and distribution of secondary phases, grain size, dislocation density, and crystallographic texture; tailored by different fabrication and processing methods, on the corrosion mechanism of Mg alloys is of highly interest to provide more insights for better materials design. Currently, there are several conflicting findings with regards to how these microstructural features influence the corrosion initiation and propagation of Mg alloys. For instance, Birbilis et al. [19] investigated the influence of grain size on corrosion of ECAPed pure magnesium, they found that corrosion current density decreased as increasing the number of ECAP passes (decreasing grain size). They attributed this behavior to a gradual decrease in the anodic reaction rate as increasing ECAP passes as a result of higher number density of high angle grain boundaries in the refined grains that promoted formation of a more coherent, uniform, and protective oxide film. In contrast, Song et al. [20] observed a completely opposite trend, in which corrosion resistance of ECAPed pure magnesium in NaCl environment was deteriorated as increasing the number of ECAP passes. They observed deeper pits, higher mass loss, larger corrosion current density values and lower charge transfer resistance as decreasing grain size. They correlated the detrimental effect of grain size

on corrosion of pure magnesium with development of strain-induced crystalline defects such as subgrain boundaries and dislocations as well as higher stored energy at the deformed grain boundaries that served as highly energetic activation sites for corrosion. In addition, they found that these crystalline defects induced formation of an unstable oxide film that could not provide corrosion protection in chloride environments. Similar conflicting findings have been reported in the corrosion behavior of magnesium alloys influenced by other metallurgical factors such as morphology/distribution of cathodic and anodic precipitates, dislocation density, and twinning. These lead to a great interest in further exploring and understanding the corrosion initiation and propagation of magnesium alloys.

1.2 Problem Statement

According to the United States Department of Energy (DOE) in a meeting held at Oak Ridge National Laboratory in April 2016 entitled “Current Status and Future Directions in Magnesium Corrosion Research” [21], the three major limitations for using magnesium alloys particularly in automotive applications to effectively improve fuel savings and reduce greenhouse gas emissions include: 1) cost of primary Mg alloy, 2) low formability, and 3) poor corrosion resistance of Mg alloys in automotive environments. The DOE meeting also discussed gaps in fundamental understanding of Mg corrosion particularly related to micro-galvanic coupling between magnesium matrix and secondary phases or impurities [21]. Numerous studies have been performed to improve formability of magnesium alloys as well as yield strength and creep resistance mainly through alloying and processing. Processing routes involving SPD and/or heat

treatment methods have been extensively developed over the last three decades to produce magnesium alloys that exhibit better mechanical properties than conventional cast structures. These processing methods lead to small compositional changes as well as microstructural and crystallographic changes such as grain refinement, texture development, changes in dislocation density, redistribution of solute atoms in the microstructure, or precipitation of secondary phases. All these compositional, microstructural, and crystallographic changes can have a dramatic impact on corrosion behavior of magnesium alloys. However, there are still limited studies addressing the role of these factors on Mg corrosion and several conflicting findings have been reported. Therefore, there is a need to further investigate the influence of these factors on the corrosion performance of magnesium alloys. Thus, this study aims to provide more details that correlates microstructure evolution during processing with corrosion performance of AZ91 alloys with emphasis in the role of grain size, grain structure, and morphology and distribution of cathodic secondary phases. In addition, a more comprehensive study of corrosion initiation and propagation mechanisms of AZ91 alloys processed by different routes will be included to better elucidate predominant microstructural factors controlling corrosion as well as intensity of micro-galvanic effects in the microstructure after processing.

1.3 Objectives

This work aims at the characterization of the microstructure, mechanical properties and corrosion behavior of AZ91 alloys in chloride environments after four different processing methods including solution heat treatment, aging, equal channel

angular pressing (ECAP), and post-aging after ECAP processing. A primary focus will be given on correlating microstructural features such as grain size, grain distribution, and morphology and distribution of secondary phases with corrosion behavior. The corrosion testing includes weight loss measurements, hydrogen evolution testing, and electrochemical characterization using DC basis techniques as well as electrochemical impedance spectroscopy (EIS). Furthermore, chemical and morphological characterization of corroded alloys after exposure will be performed to determine mechanisms of corrosion degradation of AZ91 alloys.

Furthermore, a special attention will be taken in characterizing the micro-galvanic corrosion mechanism in a peak-aged AZ91 alloy. The mechanism of micro-galvanic corrosion initiation of peak-aged AZ91 alloy exposed to NaCl electrolyte will be characterized using microstructural analysis and corrosion and electrochemical methods such as ex-situ and in-situ immersion test, electrochemical microcell technique, and scanning Kelvin probe force microscopy (SKPFM). Morphological and analytical characterization will be also performed to support the proposed mechanism of corrosion degradation of peak-aged AZ91 alloy. The high-resolution surface characterization was critical to identify the dominant role of the β -Mg₁₇Al₁₂ phase either as an effective cathode or as an anodic barrier against corrosion.

Finally, this study will investigate the corrosion susceptibility of recrystallized and non-recrystallized regions in a partially recrystallized AZ91 magnesium alloy processed by equal channel angular pressing (ECAP) in chloride-containing media. High-resolution methods such as scanning Kelvin probe force (SKPFM), transmission

electron microscopy (TEM), and electron backscatter diffraction (EBSD) will be included to elucidate differences in Volta potential, microchemistry, and crystallographic orientation, respectively, between recrystallized and non-recrystallized regions that allows to identify the predominant factors leading to preferential dissolution at specific sites. Furthermore, the microcell electrochemical technique will be used to investigate the electrochemically activity of these recrystallized and non-recrystallized regions. The combined effect of dynamic recrystallization and strain-induced dynamic precipitation on the electrochemical behaviour of ECAPed alloys at different levels of deformation strain will be also analysed. ECAPed alloys after different number of ECAP passes (from $N = 1 - 4$) will be used, in which variations on the grain size of recrystallized grains, volume fraction of recrystallized grains, volume fraction of $\beta\text{-Mg}_{17}\text{Al}_{12}$ phase and size of $\beta\text{-Mg}_{17}\text{Al}_{12}$ precipitates will be correlated with the electrochemical response. Corrosion rate calculations the ECAPed alloys at different strain levels will be obtained by gravimetric technique. In addition, electrochemical measurements such as open circuit potential (OCP), potentiodynamic polarization (PDP) and electrochemical impedance spectroscopy (EIS) will be also included to evaluate the effect of these factors on the corrosion kinetics; a diluted NaCl solution will be used to better identify changes in passivation regions and breakdown potentials with increasing the strain level.

1.4 Potential Impact

A good combination of mechanical properties and corrosion performance is desired when using magnesium alloys in automotive, aerospace, biomedical and electronic applications. Therefore, it is essential to investigate both mechanical

properties and corrosion resistance of processed magnesium alloys to determine optimum combinations of materials properties. This study provides insights of particular processing routes that lead to simultaneous improvement of strength, ductility, and corrosion resistance. These processing methods can be further explored for real applications. In addition, this study offers details correlating microstructure, mechanical, and corrosion performance that allow to identify desire and non-desire microstructural characteristics to improve the overall performance of AZ91 alloys. In that sense, this work can serve as a guide for future research studies when producing AZ91 alloys under different processing conditions.

Furthermore, this study will contribute towards more fundamental understanding of the corrosion behavior of magnesium alloys, in particular of the severity of micro-galvanic coupling between secondary phases and magnesium matrix and the role of microstructural features on mechanisms of corrosion initiation and propagation. These findings will provide some answers in how to design magnesium alloys with superior corrosion resistance.

1.5 Research Background

1.5.1 Opportunities and Challenges of Mg Alloys

Magnesium is one of the lightest structural metals with a significantly low density ($1,7 \text{ g/cm}^3$) compared to aluminum ($2,7 \text{ g/cm}^3$), titanium ($4,5 \text{ g/cm}^3$), and iron ($7,9 \text{ g/cm}^3$). Therefore, magnesium-based alloys are highly attractive in automotive applications, in which weight reduction results in improving fuel efficiency and decreasing CO₂ emissions into the atmosphere [2]. Currently, several automotive

companies such as Volkswagen, Audi, Mercedes Benz, Ford, and Kia Motors have already substituted steel and aluminum components with Mg alloys [22]. Magnesium alloys are commonly used in gearboxes, steering wheels, seat frames, door inner components, steering columns, and driver's airbag housings [22]. The United States Automotive Materials Partnership (USAMP) predicted that by 2020, approximately 350 lbs. of magnesium will replace 500 lbs. of steel/cast iron and 130 lbs. of aluminum resulting in an overall weight reduction of 15% and a reduction in fuel consumption of 9 to 10 percent [23]. Similarly to the automotive sector, magnesium alloys have been also implemented in the aerospace industry for reducing weight in several aircraft components such as helicopter transmission casings, fuselage structures, interior components, gearboxes, flight control systems, and aero engine frames [22]. Magnesium has been also found very attractive in biomedical applications as orthopedic implants, it has similar density as the one for natural bone (1.8 to 2.1 g/cm³) as well as comparable mechanical properties such as fracture toughness, Young's modulus, and compressive yield strength [22]. Furthermore, magnesium has excellent biocompatibility, is non-toxic and is biodegradable in body fluids eliminating further surgical procedures to remove the implant. Finally, magnesium alloys are also promising for electronic applications, they have excellent heat transfer and dissipation and shielding effect for electromagnetic and radio frequency interference. In addition, magnesium alloys have similar density as currently used polymers but with better mechanical performance [22]. Magnesium alloys are currently used in casings for cameras, laptops, cell phones, and portable media devices.

Despite all these potential applications of magnesium alloys, there are still some major challenges that need to be overcome. Magnesium alloys have usually poor ductility and formability owing to their hexagonal close packed crystal structure that limits plastic deformation by slip dislocation [24]. They also have relatively low strength compared to conventional steel and aluminum alloys. In addition, poor corrosion resistance represents one of the major limitations of magnesium alloys that restricts their practical application in exterior environments. Several approaches have been proposed to improve the mechanical properties and corrosion resistance of magnesium alloys. Improvement of mechanical properties is usually achieved by alloying and processing. Some alloying elements commonly used in magnesium alloys to enhance mechanical properties (and sometimes corrosion resistance) include Al, Mn, Zr, rare earths, and Y, in which mechanical strength is improved through precipitation hardening and grain refinement assisted by solute atoms in the microstructure [14, 25]. Additionally, severe plastic deformation (SPD) is widely recognized as one of the most effective methods to enhance mechanical properties of Mg alloys that results from significant grain refinement. SPD has been extensively used to develop ultrafine-grained (UFG) materials (materials with submicron grain size) or even nanostructure materials with simultaneous improvement of both strength and ductility [1, 7, 11, 14]. Regarding corrosion resistance, there are several approaches to improve corrosion performance of Mg alloys including alloying, surface treatments, coating systems, mechanical processing, and texture modifications [25, 26]. Moreover, deeper fundamental understanding of magnesium corrosion will allow to improve materials selection and design.

1.5.2 Severe Plastic Deformation for Grain Refinement of Mg Alloys

One of the main limitations of Mg alloys still relies on their poor formability, particularly at room temperature, due to their hexagonal close-packed (HCP) crystalline structure that exhibits an insufficient number of independent deformation systems at low temperatures (<200°C) [27]. The deformation of Mg alloys at low temperature is primarily limited to dislocation slip in the basal (0001) \langle 11 $\bar{2}$ 0 \rangle slip system and deformation twinning in (10 $\bar{1}$ 2) \langle 10 $\bar{1}$ 1 \rangle . Activation of non-basal slip systems (i.e., prismatic and pyramidal) usually requires higher temperatures owing to their high critical resolved shear stress (CRSS) values at low temperatures [28]. Table 1 summarizes the most predominant deformation modes in Mg alloys with their corresponding number of independent slip systems. From this table, it is seen that basal slip only provides two independent slip systems, which are not sufficient to satisfy von Mises criterion that requires 5 independent slip systems for a material to sustain a general homogeneous strain [29]. Consequently, ductility of magnesium alloys at room temperature is limited when basal slip is the only deformation mode active under these conditions. Although tension twinning can also be active at low temperatures, it does not contribute significantly to the total deformation of the material. Thus, for improving ductility in magnesium alloys, it is crucial to activate non-slip systems such as the pyramidal \langle c+a \rangle , which is the only slip system that can provide c-axes deformation and five independent slip systems.

An effective method to improve formability as well as strength of magnesium alloys is through grain refinement using severe plastic deformation (SPD) methods. The

fundamentals of severe plastic deformation (SPD) techniques were firstly introduced by Percy Williams Bridgman back in the 1930s at Harvard University and since then SPD processing has become one of the most effective methods to develop ultrafine-grained or nano-structured materials with superior mechanical properties as compared to those achieved by traditional thermomechanical processing methods [30]. SPD has been defined as a group of metal processing techniques, in which a considerably large strain is imposed in a bulk material without noticeable change in the overall dimensions of the material leading to a significant grain refinement that typically results in manufacturing of UFG materials ($d < 500$ nm; d : grain size) or even nanocrystalline structures ($d < 100$ nm) [31, 32]. Besides significant grain refinement, UFG materials also exhibit a relatively uniform and equiaxed microstructure with most of the grains boundaries exhibiting high misorientations angles [31]. Some of the most common and well-developed SPD techniques include equal channel angular pressing (ECAP), high pressure torsion (HPT), multi-directional forging, and accumulative roll-bonding (ARB).

Table 1. Predominant deformation modes in magnesium alloys. Adapted from [33]

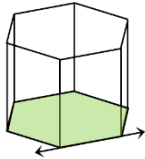
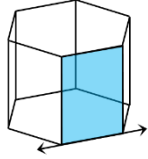
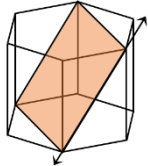
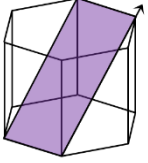
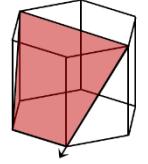
Deformation mode	Slip plane and direction	# of independent slip systems
Basal slip $\langle a \rangle$ 	$(0001)\langle 11\bar{2}0 \rangle$	2

Table 1. Continued

Deformation mode	Slip plane and direction	# of independent slip systems
Prismatic slip $\langle a \rangle$ 	$(10\bar{1}0)(11\bar{2}0)$	2
Pyramidal slip $\langle c+a \rangle$ 	$(11\bar{2}2)(11\bar{2}3)$	5
Tension Twinning 	$10\bar{1}2(10\bar{1}1)$	-
Compression Twinning 	$(10\bar{1}1)(10\bar{1}2)$	-

1.5.2.1 Principles of ECAP Processing

ECAP was developed by Segal and co-workers in the 1970s, the principles of this SPD processing method are shown in Figure 1. During ECAP, a machined billet is pressed through a die containing an angular channel (typically with a 90° angle) using a

plunger and an applied pressure P , as the material passes through the intersection of the channel, it experiences simple shear deformation that induces a shear strain in the material leading to significant grain refinement without a notorious change in its cross-sectional area [10, 34]. Since there is no substantial change in cross-sectional area, the billet can be pressed repeatedly to produce a more refine and uniform microstructure. This special feature of ECAP makes it different from other conventional thermo-mechanical methods such as rolling, extrusion, and drawing, in which there is a remarkable change in cross-sectional area after each pass [10]. The orthogonal planes X, Y, and Z shown in Figure 1 corresponds to transverse plane, flow plane, and longitudinal plane, respectively.

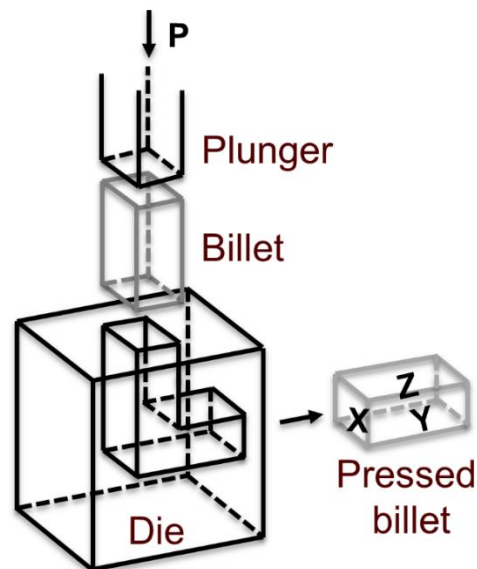


Figure 1. Schematic representation of the ECAP process. X is the transverse plane perpendicular to the flow direction, Y is the flow plane parallel to the side face at the exit, and Z is the longitudinal plane parallel to the top face at the exit. Adapted from [10].

The shear strain imposed on the sample after each ECAP pass depend on the die angle, ϕ , between the two parts of the channel and the angle of curvature, ψ , related to the outer arc of curvature where the two channels intersect, and it can be determined from the following expression:

$$\gamma = 2\cot\left(\frac{\phi}{2} + \frac{\psi}{2}\right) + \psi\cos\left(\frac{\phi}{2} + \frac{\psi}{2}\right) \quad (1)$$

When $\psi = 0$,

$$\gamma = 2\cot\left(\frac{\phi}{2} + \frac{\psi}{2}\right) \quad (2)$$

According to equation (2), the optimum die angle for maximizing the shear strain is $\phi=90^\circ$.

1.5.2.2 ECAP Routes

For ECAP processing involving multiple passes, there are four major processing routes, namely routes A, B_A, B_C, and C, that introduce different slip systems and can dramatically influence the resulting microstructure after ECAP. In route A the billet is pressed without changing orientation between passes, in route B_A the billet is rotated by 90° in alternating directions after each pass, in B_C the billet is rotated by 90° in the same direction after each pass, and in route C in the billet is rotated by 180° after each pass [10]. A schematic illustration of these ECAP processing routes is shown in Figure 2. It has been reported that route B_C produces the most uniform and equiaxed microstructure among all different processing routes due to rapid evolution of subgrains into high angle grain boundaries [10].

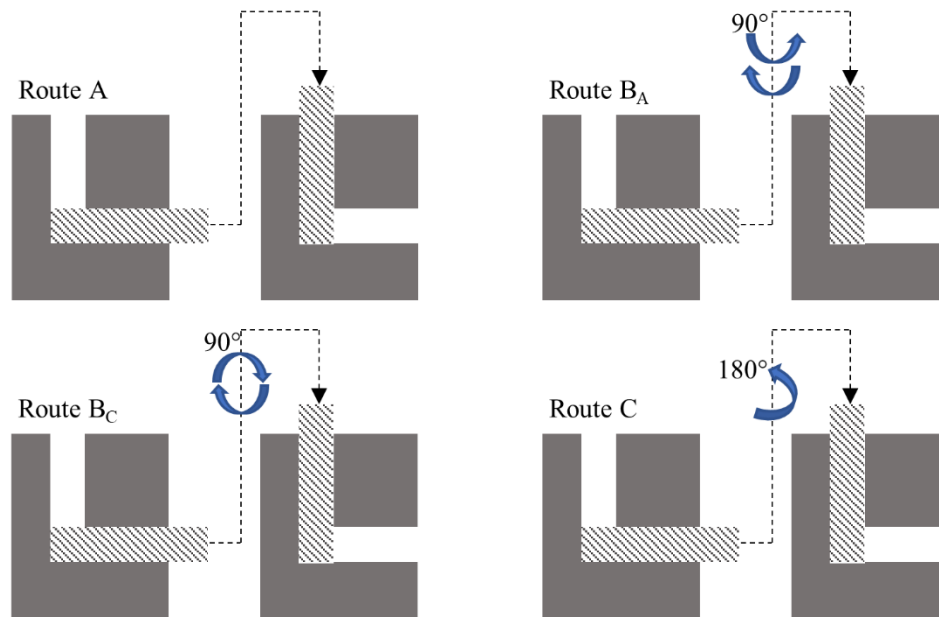


Figure 2. Basic routes in ECAP process. Adapted from [10].

1.5.2.3 Critical Factors in ECAP Processing

There are several factors that can influence the microstructure during ECAP processing. These factors can be classified into three major categories [10]: 1) factors related to design, such as channel angle and outer arc of curvature where the two parts of the channel intersect, 2) factors associated with ECAP processing conditions such as pressing speed, pressing temperature, presence of back pressure, processing route, and number of passes, and 3) factors related to microstructural conditions of the unprocessed material such as initial crystallographic texture and presence of secondary phases. Typically, research studies are mainly focus on investigating the influence of factors related to ECAP processing conditions (category 2) and initial microstructure (category 3) because they are somewhat easier to manipulate as compared with design factors.

Among the ECAP processing conditions, the pressing temperature is a crucial factor that influence the microstructure of the pressed sample. It has been reported that increasing the pressing temperature usually leads to increase in the grain size. In addition, increasing in pressing temperature can also lead to higher fraction of low angle grain boundaries due to faster recovery rates at high temperature inducing annihilation of dislocations and therefore less adsorption of dislocations in subgrain boundaries [10]. Therefore, a more significant grain refinement and a high fraction of high-angle boundaries will be promoted as decreasing pressing temperature, however, special attention should be taken to prevent cracking of the billet when pressing at relatively low temperatures [10]. Cracking during processing can be prevented by imposing back-pressure on the ECAP system.

1.5.2.4 ECAP in Mg Alloys

ECAP tool is an effective method to refine the microstructure of magnesium alloys and to enhance their ductility [9]. Typically, grain refinement of magnesium alloys by ECAP processing occurs by dynamic recrystallization (DRX) of new fine grains that are formed along the original grain boundaries or twin boundaries of the initial coarse-grained microstructure following a necklace-like pattern. These newly recrystallized grains further spread towards the interior of the original grains, such that the original grains are gradually consumed as increasing the number of ECAP passes [9]. The preferential dynamic recrystallization at the original grain boundaries and twin boundaries might be associated with presence of higher stresses at these sites due to slip incompatibilities between adjacent grains. These higher stresses induce activation of

harder slip systems and promote the formation of dislocation arrays resulting in dynamic recrystallization at these regions. Figueiredo et al. [9] reported that activation of non-basal slip systems correlated to the extent of dynamic recrystallization, is favored by increasing pressing temperature or decreasing the grain size of the un-pressed starting material. Based on the initial grain size of the material, Figueiredo et al. [9] proposed a model to describe the microstructural evolution of Mg and magnesium alloys processed by ECAP. They reported a similar table as the one reported in Table 2 to investigate the effect of initial grain size on the microstructure of magnesium alloys after ECAP processing for 1 pass and multiple passes that allowed them to verify their model. From this table they found that a homogeneous grain structure was achieved after the first ECAP pass only when the initial grain size of the un-pressed material was relatively small. Conversely, they observed a bimodal or heterogeneous grain structure after the first pass when the initial grain size was large ($> \sim 40 \mu\text{m}$). Under these circumstances, the grain structure can become homogeneous after multiple passes except when the initial size is considerably large (e.g., AZ91 alloy with an initial grain size of $223 \mu\text{m}$). For the particular case of AZ91 alloy, all the processing conditions reported in Table 2 led to a bimodal microstructure after the first pass that evolved into a homogeneous microstructure after multiple passes, typically between 4 to 8 passes.

Table 2. Grain structure of Mg alloys after ECAP processing

Alloy	Processing conditions	Initial grain size (μm)	Final grain size (μm)	Structure after one pass	Structure after multiple passes	Reference
AZ31	Route B _C , 200°C 4 passes	48.1	1.4	Homogeneous	Homogeneous	Su et al. [34]
AZ31	Route B _C , 320- 200°C 4 passes	48.3	2.5	Heterogeneous	Homogeneous	Kim et al. [35]
AZ31	Route B _C , 400°C 4 passes	223	5.8	Heterogeneous	Heterogeneous	Khang et al. [36]
Extruded AZ61	Route B _C , 200°C 4 passes	16	0.62	Homogeneous	Homogeneous	Miyahara et al. [37]
AZ91	Route B _C , 350°C- 290°C, 3mm/min, 6 passes	758	4.5	Heterogeneous (bimodal)	Homogeneous	Khani et al. [11]
As-cast AZ91	Route B _C , 320°C, 4 mm/min, 6 passes	300	6	Heterogeneous (bimodal)	Homogeneous	Chung et al. [38]
As-cast AZ91	Route B _C , 225°C, 6 passes	250	4	Heterogeneous	Homogeneous	Jufu et al. [39]
Hot-rolled AZ91	Route B _C , 4 passes at 225°C + 2 passes at 180°C	15	2	Heterogeneous	Homogeneous	Chen et al. [40]
AZ91	Route C, 270°C, 8 passes	40	1.2	Heterogeneous	Homogeneous	Mathis et al. [41]

Figure 3 shows the model proposed by Figueiredo et al. [9]. In this model, they introduced the concept of critical grain size (d_c), which is the size of the initial microstructure that will promote a homogeneous grain refinement throughout the original grains during processing. It is believed that d_c depends on the specific alloy as well as on the processing conditions, particularly on the pressing temperature. According to this model, it is seen that whenever the initial grain size is higher than d_c (Figure 3a, d, and g), the grain structure after the first pass will be heterogeneous exhibiting a bimodal or multimodal grain distribution (Figure 3b, e, and h), in which the fraction of coarse and fine grains will depend upon the initial grain size. Figure 3a-c shows that for original grain sizes that are significantly higher than d_c (Figure 3a), a bimodal or multimodal microstructure will persist even after multiple passes. It is worth to notice, that the initial grain sizes in Figure 3a and d are identical, however different processing conditions, such as the pressing temperature will lead to different values of d_c and therefore to different grain structures and grain sizes of the newly recrystallized grains. In this case, the grain structure in Figure 2d represents the situation in which the material was processed at higher pressing temperature or lower pressing speed, such that the grain sizes of the recrystallized grains showed in Figure 3e and f are bigger than the ones in Figures 3b and c for an equivalent number of passes. This higher grain size of the newly formed grains will facilitate the formation of a more homogeneous grain structure since they occupied a larger volume fraction in the material. For similar processing conditions but different initial grain sizes as the scenarios in Figures 3d and g, it is seen that an initial grain structure with smaller grain size (Figure 3g) will lead to a more

recrystallized structure as compared to the one with larger initial grain size. Finally, when the initial grain size is smaller than d_c (Figure 3j), a homogenous microstructure of very fine grains can be achieved after the first pass.

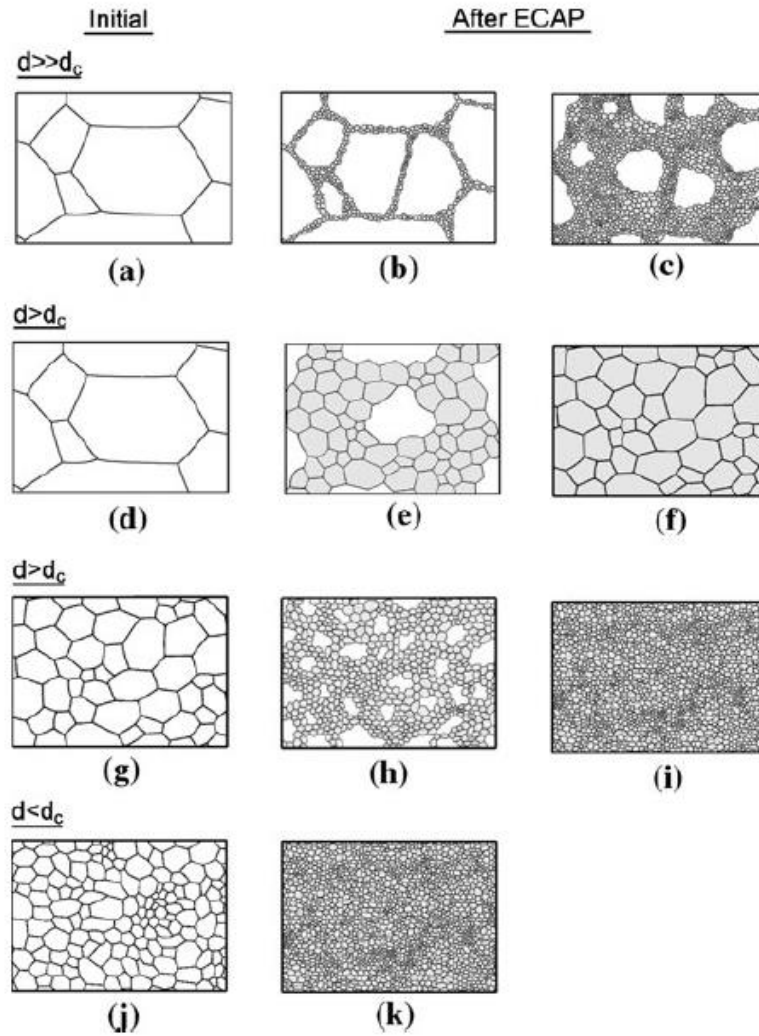


Figure 3. Model proposed by Figueiredo et al. [9] for grain refinement in magnesium alloys using ECAP. Second and third columns correspond to grain structures after one and multiple passes, respectively. Reprinted by permission from Springer Nature: Journal of Materials Science, Grain refinement and mechanical behavior of a magnesium alloy processed by ECAP, vol. 45(17), 4827-4836, Roberto B. Figueiredo, Terence G. Langdon, Copyright (2010) [9].

As mentioned above, grain refinement of magnesium alloys occurs by DRX processes, which can exhibit different mechanisms depending on the deformation conditions and particular alloy. DRX is a recrystallization process in which the nucleation and growth of new strain-free grains occurs during a deformation process at elevated temperatures [42]. For Mg alloys, there are three major DRX mechanisms that have been observed: continuous DRX, discontinuous DRX, and twinning DRX. Continuous dynamic recrystallization (CDRX) is a recovery process that involves formation of arrays of low angle grain boundaries (subgrain structures) during deformation that can gradually evolve into high angle grain boundaries at larger deformations [28, 42, 43]. It has been reported that the transformation low angle grain boundaries (LAGBs) into high angle grain boundaries (HAGB) can happen by homogeneous increase of misorientation (HIM) of LAGBs at high temperatures, lattice rotation near grain boundaries (LRGB), or by formation of microshear bands (MSBs) (Figure 4a) [42]. During CDRX, recrystallization occurs uniformly throughout the entire microstructure without clear distinction of nucleation and growth of the recrystallized grains [42]. In contrast, discontinuous dynamic recrystallization (DDRX) occurs by nucleation and subsequent growth of new grains through a local migration mechanism of HAGBs called bulging. Nucleation during DDRX usually occurs by strain induced bulging of original HAGBs that results in a necklace structure of fine and equiaxed recrystallized grains (Figure 4b) [42]. DDRX is commonly observed in materials with low to medium stacking fault energy (SFE). Finally, twinning dynamic recrystallization (TDRX) is particularly unique in magnesium and its alloys that usually occurs by three

nucleation processes 1) mutual intersection of primary twins, 2) secondary twinning within a coarse twin lamella, and 3) transformation of coarse twin lamella by deformation-induced LAGBs into HAGBs upon further deformation [28].

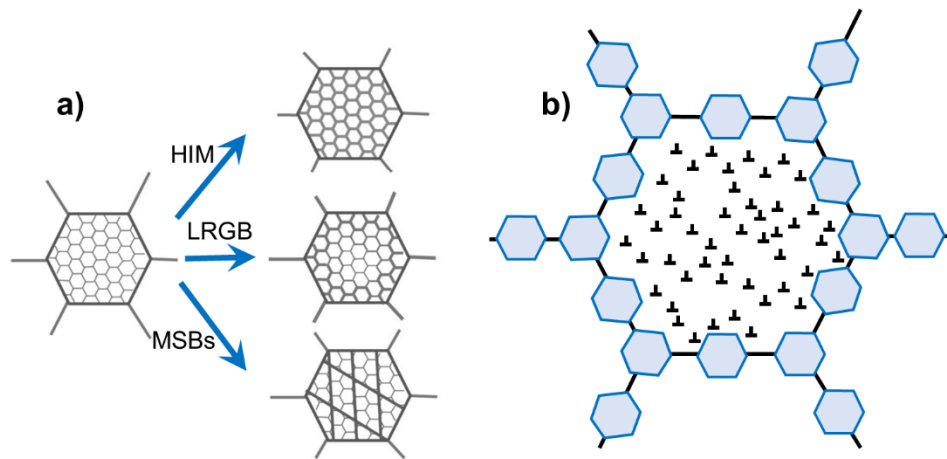


Figure 4. Schematic illustration of a) evolution of LAGB into HAGB during CDRX b) necklace structure during DDRX. Adapted from [42].

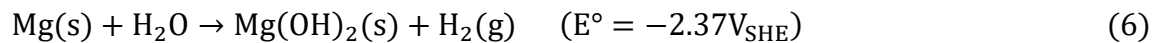
1.5.3 Fundamentals of Corrosion in Magnesium

1.5.3.1 Corrosion Mechanism of Mg

Magnesium is considered as one of the most reactive metals used in engineering applications. From the potential-pH diagram in Figure 5, it is seen that the immunity region of magnesium is quite small with an electrode potential of about -2.4 V against the standard hydrogen electrode (SHE), which is significantly more negative than the open circuit potentials of magnesium when immersed in chloride-containing media (-1.16 to -1.36 V vs. SHE) [2]. In acidic and neutral environments, magnesium will

corrode with the production of soluble ions, whereas in alkaline pH environments (>11.5), it will tend to form a magnesium hydroxide on its surface that can play a role as a partially protective oxide film [44]. As also seen from Figure 5, corrosion of magnesium takes place in the presence of hydrogen evolution reaction, which is indeed the predominant cathodic reaction regardless of the aeration conditions of the system [45].

In aqueous environments, magnesium corrodes through an electrochemical process, which occurs by charge transfer at the electrode surface that involves anodic dissolution of magnesium to produce Mg^{2+} ions (reaction 3) accompanied by water reduction (hydrogen evolution reaction) that produces OH^- ions and evolution of H_2 bubbles (reaction 4). The Mg^{2+} and OH^- ions produced from the anodic and cathodic reactions can further undergo a chemical reaction to produce $Mg(OH)_2$ (reaction 5). These electrochemical and chemical reactions will result in the overall corrosion reaction of Mg reacting with water to produce $Mg(OH)_2$ and H_2 gas (reaction 6). It is worth mentioning that this corrosion mechanism can result in pH gradients on the magnesium surface, in which local alkalization will occur at the cathodic sites whereas a more neutral pH will be observed at the anodic sites. It has been reported that the local increase in pH in the cathodic sites can lead to local passivation at these regions [44, 46].



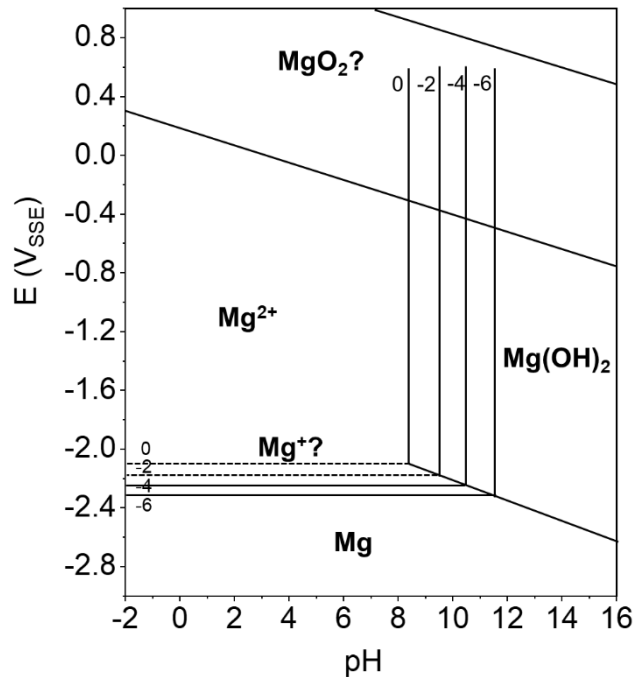


Figure 5. Potential-pH diagram of Mg-H₂O system at 25°C. Adapted from [47].

The poor corrosion resistance of Mg and its alloys can be mainly attributed to 1) their highly electronegative potential that make them very reactive in corrosive media even in the absence of oxygen, 2) micro-galvanic coupling between constituent phases, in which presence of cathodic secondary phases will induce preferential corrosion of the α -Mg phase, and 3) the poor protective properties of the oxide film that is formed during Mg corrosion in chloride-containing media [2]. It has been shown that the oxide film formed on Mg during corrosion in aqueous solutions consists of a bilayer structure with a thin inner MgO layer adjacent to the Mg metal and an outer porous Mg(OH)₂ layer in direct contact with the electrolyte [44]. The inner MgO layer is formed due to interaction of the Mg substrate with air, whereas the Mg(OH)₂ layer is formed due to further hydration of the MgO layer. During immersion in aqueous solutions, the Mg(OH)₂ outer

layer continuous to grow through a dissolution-precipitation formation mechanism [48]. The partially protective properties of this film can be associated with the Pilling-Bedworth ratio of the MgO to the Mg substrate (i.e., ratio between the elementary unit cell of MgO and the elementary unit cell of the Mg metal) which is 0.81, indicating that the film is unable to completely cover the underlying metal and volume mismatch between the MgO and the Mg metal can cause tensile stresses in the MgO layer that can lead to cracking of the oxide film (Figure 6). Thus, the MgO layer cannot provide an effective barrier for further diffusion of corrosive species [2]. Furthermore, MgO is relatively soluble in water which implies that is not stable in neutral and acidic aqueous solutions, such that immersion in these environments will cause its dissolution, exposing the metal to the aqueous solution [2].

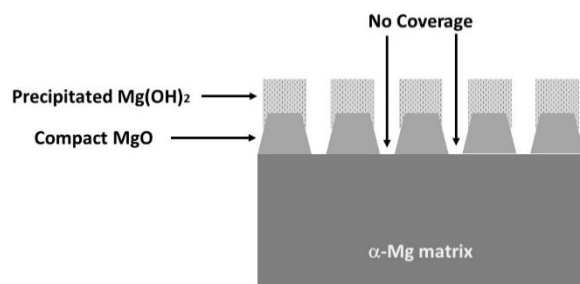


Figure 6. Schematic representation showing the incomplete coverage of the oxide/hydroxide film formed on conventional α -Mg. Adapted from [2].

1.5.3.2 Negative Difference Effect on Anodically Polarized Mg Surfaces

Magnesium exhibits a very anomalous behavior called the negative difference effect (NDE), in which the rate of hydrogen evolution (HE) increases with increasing

anodic polarization. This phenomenon is completely opposite to the conventional behavior of anodically polarized metal surfaces where increasing the magnitude of anodic polarization results on an increase of the metal dissolution rate but with a decrease of the cathodic reaction rate. The term *Negative Difference Effect* results from its definition as the difference between the hydrogen evolution rate at OCP and the corresponding one under certain anodic polarization is negative [2]. Based on electrochemical principles, the NDE contradicts the well-known Butler-Volmer equation (equation 7) that describes the activation-controlled kinetics of corrosion processes [2]:

$$i_{\text{HER}} = i_{0,\text{H}} \left[\exp \left(\frac{-(E - E_{\text{rev,H}})}{|b_c|} \right) - \exp \left(\frac{(E - E_{\text{rev,H}})}{b_a} \right) \right] \quad (7)$$

where i_{HER} is the hydrogen evolution current density, $i_{0,\text{H}}$ is the exchange current density associated with the HE, E is the applied potential, $E_{\text{rev,H}}$ is the reversible potential for the HE reaction and b_a and b_c are the anodic and cathodic Tafel slopes, respectively. From this equation, it is seen that the rate of HE should exponentially decrease with increasing anodic polarization. Figure 7 shows a schematic representation comparing the normal behavior of materials under anodic polarization that follows Tafel behavior with the anodic polarization behavior observed in magnesium. In Figure 7, the blue lines named $\text{H}_{2,\text{normal}}$ and $\text{Mg}_{\text{normal}}$ corresponds to the normal cathodic and anodic curves, respectively that follows Tafel kinetics. In this case, it is seen that applying a more positive potential (E_{applied}) than the corrosion potential (E_{corr}) will result in an increase in the anodic current density ($i_{\text{Mg,normal}}$) and a decrease in the cathodic current density ($i_{\text{H}_{2,\text{normal}}}$) compared with the corrosion current density (i_{corr}). For magnesium,

however, the hydrogen evolution reaction (HER) is described by the red curve $H_{2,actual}$ in Figure 7, in which a positive applied potential will lead to an increase in the current density of the HER ($i_{H_2,actual}$) with respect to i_{corr} . Furthermore, the red curve Mg_{actual} in Figure 7 represents the experimental anodic current density for magnesium, which is higher than the predicted from the anodic polarization curve ($i_{Mg,actual}$). It has been reported that the higher anodic dissolution of magnesium compared to the one expected from anodic polarization is associated with the inability of the potentiostat to account for all electrons generated from the anodic reaction since some of these electrons will be consumed by the HER on the electrode surface [2]. Thus, for a specific anodic applied potential in a magnesium electrode, the rate of hydrogen evolution will be described by $i_{H_2,actual}$ whereas the anodic dissolution rate of magnesium will be associated with $i_{Mg,actual}$. These current density quantities are significantly higher than the corresponding values considering Tafel behavior (i.e., $i_{H_2,normal}$ and $i_{Mg,normal}$, respectively). Several approaches have been proposed to describe the NDE phenomenon. The most recognized theories correspond to 1) Univalent Mg (Mg^+) theory, 2) catalytic activity of the corrosion film and surface enrichment of impurities, and 3) increased exchange current density [2].

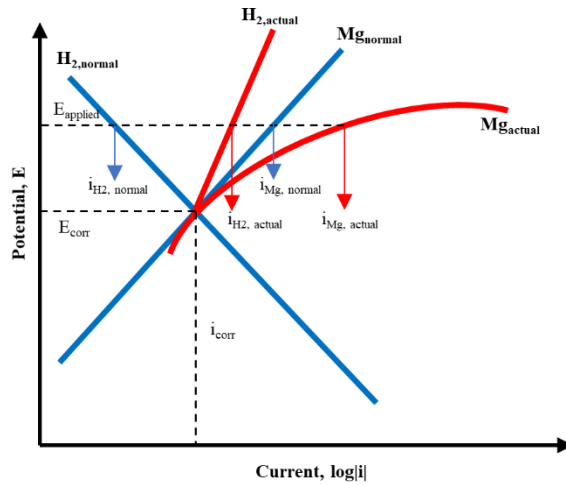
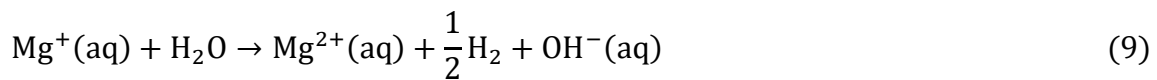


Figure 7. Schematic representation of the negative difference effect. Adapted from [49].

The univalent Mg theory is the most widely discussed theory to describe NDE, it is based on the assumption that Mg^+ ion is an intermediate specie involved during the anodic dissolution of magnesium, according to this theory, the magnesium dissolution occurs in two steps as described by equations (8) and (9) that involves 1) an electrochemical reaction of Mg to produce Mg^+ and 2) a chemical reaction between Mg^+ and water to form Mg^{2+} and H_2 gas. Based on this mechanism, it is noticed that as the Mg dissolution increases, a higher amount of Mg^+ ions will be produced that will subsequently lead to a higher HE rate.



The NDE phenomenon has also been described by the catalytic activity of the corrosion film, in which it has been proposed that Mg corrosion products exhibit catalytic properties that can accelerate the rate of HE on the corroded areas of a Mg

sample exposed to a corrosive medium [2]. The catalytic properties of Mg corrosion films to enhance the kinetics of the HER have been attributed to the enrichment in alloying elements or noble impurities at the corroded surface, especially Fe-rich impurities, which are located beneath the film as a result of preferential Mg dissolution [50]. These Fe-rich phases can accelerate the Mg dissolution as well as increase the amount of evolved hydrogen [44]. Several experimental observations have shown that during corrosion of Mg in NaCl solutions, dark areas are formed due to magnesium dissolution and subsequent formation of corrosion products, in which these areas can promote a higher activity of HER compared to the rate of HE at the uncorroded areas [51-53]. In addition, it has been also found that the rate of HE in Mg substrates artificially covered with $\text{Mg}(\text{OH})_2$ is significantly faster than in pristine substrates, indicating that Mg corrosion products can catalyze the HER and therefore they are preferential sites for cathodic reactions during Mg dissolution [50]. Based on these findings, it has been proposed that as increasing anodic polarization, there is a higher coverage of corrosion products that will lead to a higher ability of the corroded material to support the HER.

Another mechanism to explain the NDE phenomenon is related to the increase in the exchange current density of the HER on the Mg surface during anodic polarization [44]. According to the Butler-Volmer equation shown in equation 7, the rate of HE increases with anodic polarization when there is a rapid increase in the exchange current density for the HER such that it overcomes the decrease of the exponential Tafel term [44]. It is proposed that during Mg dissolution of anodically polarized Mg samples, the

catalytic activity of the surface is enhanced that can result in an increase of the exchange current density for HER as increasing the applied current density [2]. Conversely to the previous mechanism to explain the NDE phenomenon, which is related to enhanced catalytic activity of the corrosion film associated with surface enrichment of noble impurities, in this mechanism, the anomalous increase in HER with anodic polarization is associated with the net anodic sites (i.e., sites for Mg dissolution) [2].

1.5.4 Effect of Microstructural Features on the Corrosion Behavior of Mg and its Alloys

1.5.4.1 Grain Size

Grain size is a metallurgical factor that can significantly influence the corrosion performance of Mg and its alloys [44]. Grain boundaries are more chemically reactive than the bulk due to their higher electron activity and diffusion [54]. Therefore, a high density of grain boundaries can promote electron transfer between the metal surface and the electrolyte resulting in more sites for corrosion and consequently in less corrosion resistance as decreasing grain size. However, the higher reactivity of grain boundaries can also provide more sites for nucleation of an oxide film. Hence grain refinement can lead to faster formation of an oxide layer and better mechanical adhesion to the underlying metal substrate that will result in higher corrosion resistance [54]. Currently, there are contradictory conclusions with regards to the relationship between grain size and corrosion, and a fundamental understanding into how the grain size will influence the corrosion resistance of Mg is still lacking [54]. These contradictory results on the general relationship between grain size and corrosion can be related to the difficulty to isolate the effect of grain size from other metallurgical factors that are also changing

during the processing method used for achieving grain refinement (e.g., thermomechanical processing or SPD). These metallurgical factors that are also changing during processing, in addition to grain size, and that can also play a role in the corrosion resistance of Mg include presence of residual stresses, development of crystallographic texture, segregation of alloying elements at the grain boundaries, dislocation density, and precipitation of secondary phases [54]. An experimental approach to reduce the influence of other microstructural factors in the effect of grain size on the electrochemical behavior of Mg is to investigate the effect of grain size on pure Mg samples in which chemistry effects such as segregation of alloying elements and contributions from secondary phases can be avoided. Several authors have reported that grain refinement (decrease in grain size) improves the corrosion resistance of magnesium in neutral and alkaline chloride-containing solutions [14, 55-58]

Birbilis et al. [19] investigated the influence of grain size on the corrosion resistance of ECAPed pure magnesium in 0.1 M NaCl solution, they found that corrosion current density obtained from potentiodynamic polarization decreased with the number of ECAP passes, which means that it decreased as the grain size decreased. By deeper examination on the potentiodynamic polarization behavior, they also found that grain refinement by increasing the number of ECAP passes led to a significant decrease in the anodic kinetics, a slightly increased in the cathodic kinetics during the first pass that subsequently decreased with further passes, and an ennoblement in E_{corr} . Based on these findings, they suggested that the simultaneous decrease in anodic and cathodic kinetics as decreasing grain size by ECAP processing can be related to the formation of a

more coherent, uniform, and protective oxide film on the surface of the magnesium samples during the electrochemical measurements. They proposed that the better protection properties of the oxide film as decreasing the grain size can be associated with a large volume fraction of grain boundaries that can relieve stresses induced at the Mg surface due to geometrical mismatching between the substrate and the oxide film that could otherwise cause cracks in the film. In addition, they also proposed that a better coherency of the oxide film was achieved as increasing the number of ECAP passes due to the formation of a more homogeneous grain structure with grain boundaries having high misorientation angles. Similar observations related to the formation of a more stable oxide film with decreasing grain size were also proposed by other authors [14, 24, 59]. Orlov et al. [14] explained that fine-grained microstructures can relieve the stresses mentioned above by increase in porosity through grain boundary diffusion of vacancies that can reduce the susceptibility of cracking in the oxide film. However, there is not substantial evidence to support this statement. Kim et al. [24] proposed instead that the enhance in passivity of the oxide film when decreasing the grain size can be attributed to the formation of a mixed layer of MgO and Mg phase between the MgO layer and the metal substrate that served as a buffer layer to decrease the sharp stress gradient developed between them. Song et al. [56] also proposed that improvement in the corrosion resistance of fine-grained AZ31 Mg alloys was achieved through increase in the density of grain boundaries that can effectively dissolve intermetallic precipitates reducing the susceptibility for micro-galvanic corrosion between these precipitates and the α -Mg matrix. However, they also reported that after significant grain refinement in

which most of the intermetallic particles have been dissolved, further grain refinement can only result in increase of crystallographic defects (i.e., dislocations, twins, and grain boundaries) that can lead to higher corrosion rates upon further refinement [56].

In contrast, Song et al. [20] observed an opposite behavior in a similar study, in which they found a detrimental corrosion resistance of a pure Mg sample immersed in a NaCl solution as increasing the number of ECAP passes. Through in-situ corrosion test, weight loss measurements, and electrochemical measurements, they found deeper pits, higher weight loss rates, higher corrosion current density (i_{corr}) values, and lower charge transfer resistance (R_{ct}) values as increasing the number of ECAP passes. They also found nobler corrosion potential (E_{corr}) values as increasing the number of ECAP passes that could indicate less electrochemical activity of the Mg surface, however i_{corr} values still increased regardless of the E_{corr} trend, suggesting that even though the ECAPed specimens were less electrochemically active in terms of thermodynamics, the kinetics of corrosion of these specimens was faster. The lower corrosion resistance of pure Mg with increasing the number of passes was attributed to strain-induced crystalline defects such as dislocations and energetic grain boundaries of deformed grains or subgrains boundaries, which are non-equilibrium grain boundaries that can store significantly high internal energy. These crystalline defects let to higher corrosion activation of the ECAPed pure Mg samples. It was also suggested that the more noble E_{corr} values in the ECAPed specimens was also related to these crystalline defects that provide more nucleation sites for the formation and growth of an oxide film. However, the authors proposed that even though the ECAPed specimens promoted the formation of a thicker

oxide film, the high corrosion reactivity of the Mg substrate induced a more severe breakdown of the oxide film resulting in an overall decrease of the corrosion resistance with ECAP processing. Hamu et al. [15] also found that corrosion resistance of an AZ31 Mg alloy was deteriorated as decreasing grain size through ECAP processing. They proposed that the higher anodic dissolution in the fine-grained AZ31 Mg alloy compared to that of the coarse material was associated with high dislocation density and twins formed during deformation that acted as more electrochemically active sites for corrosion.

1.5.4.2 Cathodic Precipitates

In Mg-Al alloys, aluminum is typically present as part of the solid solution but also precipitated as a β -Mg₁₇Al₁₂ phase. The β -Mg₁₇Al₁₂ phase exhibits a corrosion potential of approximately 300 mV more positive than the corrosion potential of the α -Mg phase, indicating that it can act as an effective cathode inducing a strong galvanic activity at β -Mg₁₇Al₁₂ phase/ α -Mg phase interface [60-62]. The effect of the β -Mg₁₇Al₁₂ phase on the corrosion behavior of Mg-Al alloys has also been under debate and contradictory results have been reported. Song et al. [63] suggested that β -Mg₁₇Al₁₂ phase has a dual role on the corrosion behavior of AZ91 Mg alloy; they suggested that when its volume fraction is small, the β -Mg₁₇Al₁₂ phase mainly acts as an effective galvanic cathode accelerating the corrosion process of the α -Mg matrix. In this case, the preferential dissolution of the α -Mg phase adjacent to the β -phase can induce undercutting surrounding the precipitate that will consequently result in falling out of the β -phase from the Mg alloy. In contrast, for a high-volume fraction, the β -Mg₁₇Al₁₂ phase

can act as an electrochemical barrier to hinder corrosion propagation in the alloy. They also reported that micro-galvanic coupling between the β - $\text{Mg}_{17}\text{Al}_{12}$ phase and the α -Mg matrix is mainly controlled by the cathode-to-anode area ratio and the potential difference between the phases, whereas the effectiveness of the barrier protection depends mainly on the volume fraction and distribution of the β - $\text{Mg}_{17}\text{Al}_{12}$ phase and is favored when the β - $\text{Mg}_{17}\text{Al}_{12}$ phase exhibits a continuous network along grain boundaries [63, 64]. Kim et al. [24] found that micro-galvanic corrosion between β - $\text{Mg}_{17}\text{Al}_{12}$ phase particles and α -Mg phase was reduced due to refinement of β -phase to nanoscale size during high-ratio differential speed rolling, in which a high-volume fraction of nanosized precipitates were uniformly distributed along grain boundaries of α -Mg ultrafine grains. They suggested these particles can also provide a barrier against corrosion propagation due to their considerably small interspacing between the precipitates. A schematic illustration of this dual role of the β - $\text{Mg}_{17}\text{Al}_{12}$ phase on the corrosion behavior of Mg-Al alloys is shown in Figure 8.

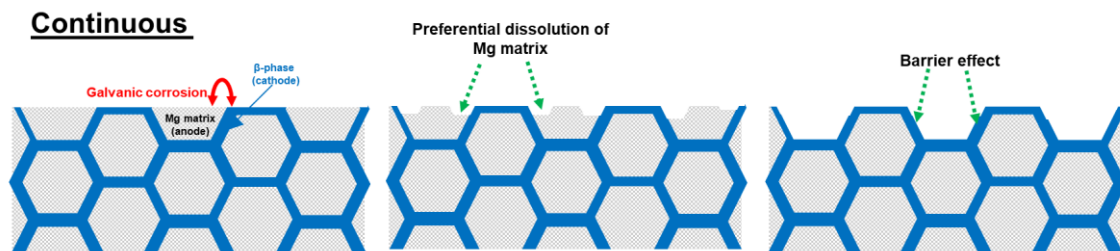


Figure 8. Schematic illustration showing the dual role of the β - $\text{Mg}_{17}\text{Al}_{12}$ precipitates on the corrosion behavior of Mg-Al alloys. Adapted from [65].

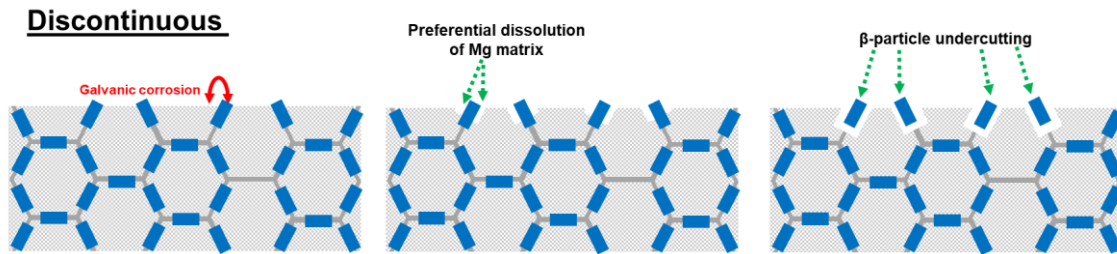


Figure 8. Continued

1.5.4.3 Other Microstructural Features

In addition to metallurgical factors such as grain size and amount and distribution of secondary phases, there are other structural factors such as dislocation density, twinning, and crystallographic texture that can play a significant role in the corrosion behavior of Mg alloys. For instance, there is a good agreement in the literature that a high density of dislocations increases the rate of anodic dissolution in Mg alloys [24, 66, 67]. Dislocations distort the crystallographic lattice of the metal and therefore atoms located at these distorted regions will be more susceptible to anodic dissolution [66]. Similarly, twins are also more energetic sites than the matrix, and hence, they are preferential sites for corrosion [66]. Aung et al. [68] found intragranular corrosion in an AZ31 Mg alloy that was accelerated by the existence of twins, they suggested that areas with high accumulation of twins exhibited more active electrochemical potential that can lead to preferential anodic dissolution in the vicinity of twins (or dislocations). Annealing of Mg alloys after deformation processes is usually recommended to decrease the density of dislocations (or twins) in the matrix that can subsequently lead to enhance of the corrosion resistance. However, under certain annealing conditions, the positive

effect of reducing dislocation density or twinning through recovery can be overcome by the negative effect of increasing the size of grains by grain growth [24, 68].

Residual stresses have been also found to be detrimental to corrosion resistance of Mg alloys. Hoog et al. [69] investigated the corrosion behavior of pure Mg as function of grain size and processing route immersed in 0.1 M NaCl solution. They found that when using surface mechanical attrition treatment (SMAT), the corrosion rate was higher compared to other grain refinement methods, a behavior that was mainly associated with the higher residual stresses by using SMAT processing.

According to crystallographic texture, it has been consistently reported that Mg grains with basal orientation exhibit higher corrosion resistance as compared to Mg grains with non-basal crystal planes [14, 70-72]. Orlov et al. [14] reported that pits are more likely to nucleate in basal planes but they have a higher rate of propagation in prismatic planes. The closely packed basal plane exhibits a higher corrosion resistance compared to more loosely packed planes because of its higher atomic density (basal (0001) plane = 1.13×10^{19} atoms/m², prismatic (11 $\bar{2}$ 0) plane = 6.94×10^{18} atoms/m² and prismatic (01 $\bar{1}$ 0) plane = 5.99×10^{18} atoms/m²) [26]. The higher atomic density of the closely packed basal plane is associated with a higher coordination number, a higher binding energy, and a lower surface energy as compared to the loosely packed non-basal planes that results in an overall higher activation energy for removal of atoms from the metal lattice [54, 72]. Consequently, the basal plane exhibits the lowest corrosion rate among all other planes in Mg alloys [26]. Song et al. [72] investigated the effect of crystal orientation on corrosion of pure Mg, they found that grains with basal orientation

exhibited higher corrosion resistance with respect to grains with non-basal orientation. These findings were evidenced by more positive E_{corr} , lower anodic current density, higher impedance, and thinner but more compact oxide film in the grains with basal planes on the surface. However, they also found that in alkaline and less aggressive environments, in which passivation of the Mg substrate is promoted, the effect of grain orientation become less evident [72]. In other studies, Song et al. [73, 74] investigated the effect of crystallographic orientation on the corrosion behavior of a rolled AZ31 Mg alloy exposed to chloride-containing solutions, in which the rolling surface mainly consisted of grains with basal orientation whereas the cross-section surface is composed of grains with $(10\bar{1}0)$ and $(11\bar{2}0)$ prismatic orientation. They observed that the rolling surface consisting of mainly basal planes exhibited higher corrosion resistance in a chloride-containing environment than the cross-section surface composed of prismatic planes. They attributed these differences to the different surface energy levels of the crystallographic planes, in which the closely-packed basal plane exhibited the lowest surface energy that results in higher electrochemical stability and corrosion resistance than the less packed non-basal planes. They also found that the rolling surface exhibited OCP values more positive than those of the cross-section surface suggesting that micro-galvanic coupling between grains with different orientations can occur leading to preferential dissolution of grains with non-basal orientation [73]. Interestingly, they observed that subsequent heat treatment of the rolled AZ31 Mg alloy did not modify the grain orientation, however it decreased the corrosion resistance of both the rolling and cross section surfaces due to the nucleation and growth of Al_8Mn_5 intermetallic particles

during annealing that induced severe micro-galvanic corrosion [74]. Hagihara et al. [70] investigated the effect of crystallographic orientation on the corrosion behavior of pure Mg single crystals immersed in Hanks' balanced salt solution, they found consistently from different corrosion and electrochemical methods that corrosion rate increased in the following order $(0001) < (11\bar{2}0) < (10\bar{1}0) < (11\bar{2}3) < (10\bar{1}2)$. In addition, they also found that crystal orientation only affected the anodic kinetics and planes with the highest packing density of atoms exhibited the highest charge transfer resistance and the highest ability to form protective oxide films. Pawar et al. [71] also found that corrosion in non-basal grains of AZ31 Mg alloys was significantly higher as compared with the corrosion propagation in the α -Mg grains of basal orientation, in which the former showed a very localized filiform-like corrosion whereas the latter exhibited a more uniform corrosion propagation with the presence of canyon-like features perpendicular to the basal plane and along the prismatic planes.

CHAPTER II

EXPERIMENTAL METHODS

This chapter provides a detailed description of the different processing methods and experimental techniques used in this study.

2.1 Material and Processing Methods

Commercial AZ91 alloy ingots were supplied by US Magnesium LCC, Salt Lake City, UT, in the as-cast condition with a chemical composition of 9.2 wt.% Al, 0.67 wt.% Zn, 0.25 wt.% Mn, and balance Mg. Following ASTM B661–12 [12], the as-cast ingots were solution heat treated in a protective argon atmosphere at 413 °C for 24 h followed by water quenching at room temperature. Then, the homogenized specimens were further aged to the peak-aged condition at 168 °C for 16 h. Figure 9(a) shows the Vickers hardness evolution of the homogenized alloy with aging time at 168 °C, in which the peak-aged condition was achieved after 16 h of aging in accordance with the ASTM B661. A peak hardness value of 82 HV was obtained. For ECAP processing, billets were machined from the as-cast ingot to obtain dimensions of 2.5 cm x 2.5 cm x 17.8 cm and then solution heat treated at 413 °C for 24 h followed by water quenching at room temperature to homogenize the dendritic microstructure and dissolve the majority of β -Mg₁₇Al₁₂ precipitates, thereby reducing potential sites for cracking as well as improving the workability during processing [75]. The ECAP processing was conducted in an ECAP tool with a 90° die angle (i.e., angle between the two intersecting channels was 90°) and sharp corners (i.e. the outer arc of curvature was zero). Before ECAP

processing, the die was preheated to 310° C and then, the homogenized billets were placed and heated for 30 min to ensure uniform temperature throughout the specimens. The billets were ECAP for four passes using route B_c (i.e., billets were rotated clockwise by 90° along the longitudinal axis after each ECAP pass) under a back-pressure of 2000 psi and using a pressing speed of 5 mm/min. A multi-temperature step down approach was used during ECAP processing to prevent cracking and reduce grain growth [11, 33]. Thus, the first, second, third, and fourth passes were conducted at 310° C, 300°C, 275°C, and 250°C, respectively. After each ECAP pass, the billets were rapidly water quenched to prevent grain growth or any other microstructural changes that could happen due to slow cooling [33]. ECAPed specimens were subsequently aged for up to 72 h at 100 °C, 130 °C, 168 °C, and 180 °C. Figure 9(b) shows the age-hardening response after ECAP processing through Vickers hardness measurements as function of aging time and aging temperature. According to these measurements, the maximum peak hardness value after ECAP processing was attained after 48 h of aging at 100 °C with a hardness value of ~94.8 HV. This post-aged condition after ECAP processing was denoted as ECAP-aged alloy as shown in Figure 9(b). More details above the hardening behavior after ECAP processing will be discussed in chapter III.

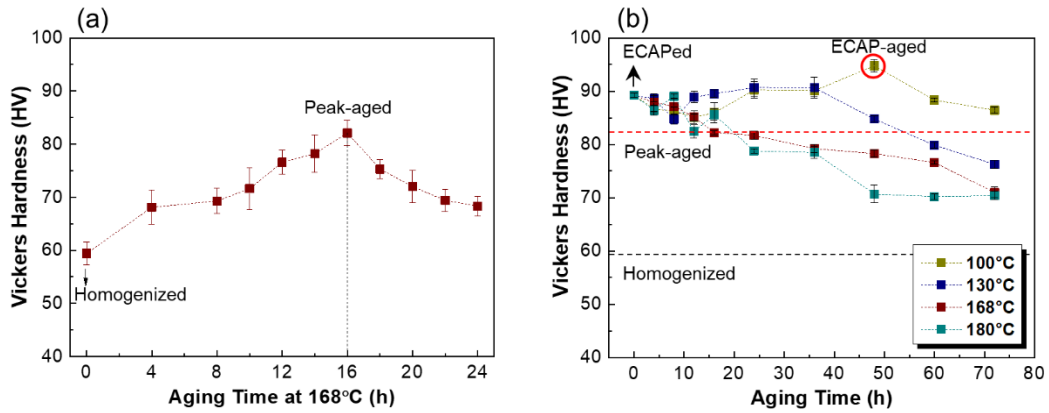


Figure 9. Vickers hardness evolution of (a) homogenized AZ91 alloy and (b) ECAPed AZ91 alloy with aging time.

Table 3 summarizes the processing conditions of the AZ91 specimens. A schematic illustration of the heat treatment and ECAP processing used in this study is shown in Figure 10. The orthogonal directions after ECAP shown in Figure 10 corresponds to the extrusion direction (ED), the longitudinal direction (LD; normal to the extrusion direction) and the flow direction (FD; orthogonal to both ED and LD).

Table 3. Processing conditions for the AZ91 specimens investigated in this study

Processing condition	Homogenization	Peak-aging	ECAP	Post-aging after ECAP
Homogenized	413°C for 24 h + water quenching			
Peak-aged	413°C for 24 h + water quenching	168°C for 16h		
ECAPed	413°C for 24 h + water quenching		Route B _c , 4 passes, back pressure of 2000 psi, 5 mm/min. Pass 1: 310°C Pass 2: 300°C Pass 3: 275°C Pass 4: 250°C	

Table 3. Continued

Processing condition	Homogenization	Peak-aging	ECAP	Post-aging after ECAP
ECAP-aged	413°C for 24 h + water quenching		Route B _c , 4 passes, back pressure of 2000 psi, 5 mm/min. Pass 1: 310°C Pass 2: 300°C Pass 3: 275°C Pass 4: 250°C	100°C for 48 h

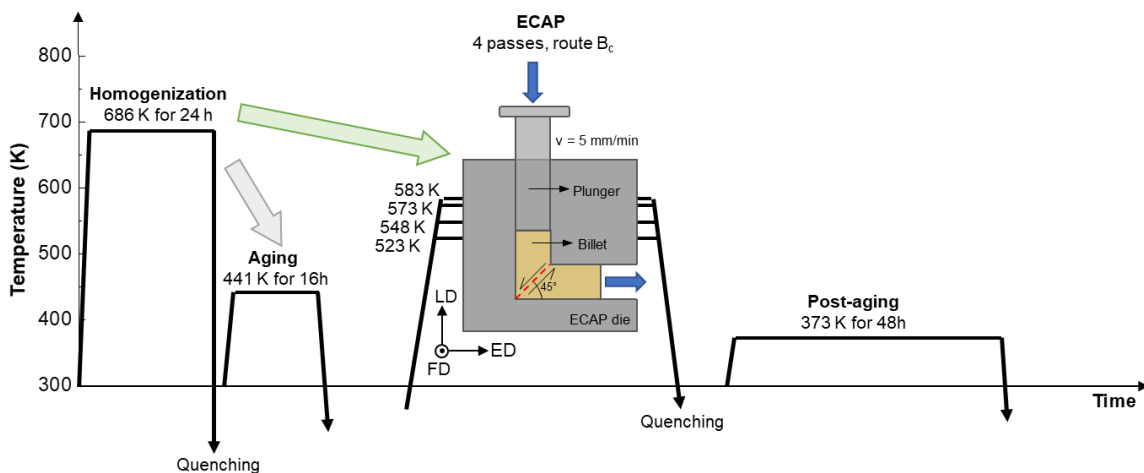


Figure 10. Schematic representation of the heat treatment and ECAP processing used in this study.

2.2 Microstructure Characterization

For the microstructural characterization, samples were wet ground with SiC grinding paper from P240 to P1200, followed by polishing with diamond pastes of 9, 3, and 1 μm , and finally polished with a colloidal silica suspension of 0.05 μm . Then, the samples were thoroughly rinsed with deionized water and cleaned ultrasonically in pure ethanol. Polished samples were subsequently etched in an acetic-glycol solution

consisting of 1 mL HNO₃, 20 mL acetic acid, 60 mL ethylene glycol, and 19 mL water for 5-20 s. Microstructure analysis of the AZ91 alloys were conducted by optical microscopy (OM, Nikon ECLIPSE MA100) and scanning electron microscopy (SEM; JEOL JMC-6000Plus) equipped with energy dispersive X-ray spectroscopy (EDS, JED-2300). Morphology micrographs of the ECAPed alloys were taken from the LD – ED plane, which is also known as flow plane. Image analysis for calculating average grain size, volume fraction of recrystallized grains, and volume fraction and size of β -Mg₁₇Al₁₂ precipitates were performed using ImageJ software. The constituent phases in the AZ91 specimens were identified by X-ray diffraction (XRD) using a Bruker powder diffractometer with a Cu-K α source ($\lambda = 1.54 \text{ \AA} = 0.154 \text{ nm}$) operated at 40 kV and 25 mA current. The specimens were scanned continuously from 30° to 80° with a step size of 0.03° per second.

Transmission electron microscopy (TEM) was also used to compare the morphology and elemental composition difference of the AZ91 alloys. Cross-sectional transmission electron microscopy (TEM) samples were prepared using a FEI HELIOS NANOLAB 460F1 dual-focused ion beam (FIB). The chemical information of the AZ91 alloys was identified using scanning transmission microscopy (STEM) energy dispersive spectroscopy (EDS) mapping on FEI Tecnai G2 F20 Super-Twin FE-TEM operated at 200 kV. Electron backscatter diffraction (EBSD, Tescan FERA-3 scanning electron microscope (SEM) with an accelerating voltage of 20 kV) was also performed in the ECAPed alloy, in which, both the recrystallized and non-recrystallized regions of the ECAPed alloy were investigated to compare their crystallographic orientation.

2.3 Mechanical Testing

Vickers hardness was measured to investigate the age-hardening response after homogenization treatment and ECAP as well as to compare the hardness values of the different specimens under study. The hardness measurements were obtained by applying a load of 100 g for a holding time of 10 s. The reported hardness values correspond to the average of at least 15 measurements taken at different locations over the entire sample surface.

Tensile tests were carried out in a MTS machine at room temperature with a strain rate of $5 \times 10^{-4} \text{ s}^{-1}$. Flat dog-bone tensile specimens with dimensions of 8 mm gage length, 3 mm width and 1.5 mm thickness were cut from the as-cast and processed materials using wire electrical discharge machining (EDM). For the ECAPed specimens, tensile samples were cut from the homogeneously deformed regions of the plane perpendicular to the flow direction (FD) also denoted as flow plane. At least three replicates were conducted for each condition.

2.4 Localized Potential Distribution

Volta potential differences between the α -Mg matrix and the β - $\text{Mg}_{17}\text{Al}_{12}$ precipitates in the AZ91 alloys were investigated using scanning Kelvin probe force microscopy (SKPFM, Bruker Dimension Icon AFM). Prior to the SKPFM measurements, the AZ91 alloys were mechanically polished as mentioned above, and then, they were thoroughly rinsed with deionized water and ultrasonically cleaned in pure ethanol. Simultaneous acquisition of surface topography and Volta potential difference was conducted using a SCM-PIT probe working in a tapping/lift mode

sequence with an interleave lift height of 100 μm . All scans were conducted in ambient air at 25 $^{\circ}\text{C}$ and ~40% relative humidity using a scanning frequency of 0.5 Hz, a pixel resolution of 512 x 512, and a zero bias voltage. Results were analyzed by using NanoScope Analysis 1.5 software, in which topography maps were flattened using 1st order flattening and the Volta potential maps were plane fitted against the α -Mg matrix to calculate the relative nobility of the β -Mg₁₇Al₁₂ precipitates against the surrounding α -Mg matrix.

2.5 Electrochemical and Corrosion Measurements

The electrochemical response and corrosion behavior of processed AZ91 alloys were investigated by electrochemical measurements, hydrogen collection, weight loss measurements, and immersion testing. All electrochemical and corrosion measurements of the ECAPed specimens were performed on the flow plane. Samples of 1.25 cm in diameter and 2 mm in thickness were used for the electrochemical and corrosion testing. Prior to each test, samples were mechanically ground with SiC abrasive paper up to 1200 grit and then polished with diamond and silica colloidal suspensions of up to 0.05 μm particle size. After polishing, samples were degreased with ethanol in an ultrasonic bath for 5 min and dried with compressed air.

2.5.1 Potentiodynamic Polarization (PDP)

Potentiodynamic polarization (PDP) measurements were performed on the as-cast and processed materials in a 3.5 wt.% NaCl solution at room temperature to investigate and compare the corrosion kinetics of the different materials. Measurements were conducted using a Gamry, Interface 1000TM Potentiostat/Galvanostat/ZRA and a

flat cell with an exposed area of 1 cm^2 in a conventional three-electrode cell configuration with 300 mL of electrolyte. A saturated calomel electrode (SCE) and a platinum mesh were used as the reference electrode and counter electrode, respectively. Prior to PDP tests, open circuit potential (OCP) was measured for about 1 hour to achieve steady state conditions. Polarization tests were conducted from -500 mV vs. OCP to 500 mV vs. OCP or until a current density of 1 mA cm^{-2} was achieved using a scan rate of 0.1667 mV s^{-1} . Measurements were performed at least three times to ensure reproducibility. Corrosion current density (i_{corr}) was determined by extrapolating the cathodic Tafel slope to the corrosion potential (E_{corr}) [76]. The instantaneous corrosion rate P_i (mmpy) was calculated from i_{corr} (mA cm^{-2}) using the following expression [77]:

$$P_i = 22.85i_{\text{corr}} \quad (10)$$

PDP measurements were also performed on ECAPed alloys with different number of ECAP passes ($N = 1 - 4$) immersed in a 0.05 M NaCl solution at room temperature to investigate the protective properties of the oxide film formed on the ECAP alloys and their resistance to localized breakdown by chloride species. Similar three-electrode configuration as described above was used in this study. PDP tests were performed from -250 mV vs. OCP to 500 mV vs. OCP or until a current density of $100 \mu\text{A cm}^{-2}$ was achieved using a scan rate of 1 mV s^{-1} . i_{corr} was also determined by extrapolating the cathodic Tafel slope to E_{corr} . The breakdown potential (E_b) was also obtained from the PDP curves.

2.5.2 Electrochemical Impedance Spectroscopy (EIS)

Electrochemical impedance spectroscopy (EIS) was also performed to investigate the evolution of the electrochemical response for the different processed materials immersed in an aerated 3.5 wt.% NaCl solution at room temperature for 7 days. EIS measurements were also performed in a Gamry Interface 1000 potentiostat using a three-electrode cell configuration with a saturated calomel electrode used as the reference electrode and a graphite rod used as the counter electrode. Prior to EIS measurements, the samples were allowed to reach steady state (~1 hour) after immersion in the electrolyte and OCP was monitored during this time. The EIS tests were conducted at OCP using a sinusoidal potential signal with an AC amplitude of 10 mV over a frequency range from 100 kHz to 10 mHz with 10 points per decade. The EIS data were fitted with equivalent electrical circuits using the EC-lab V10.40 software.

EIS measurements were also carried out in ECAPed alloys after different number of ECAP passes in a 0.05 M NaCl solution. Similar parameters as described above were used here. EIS measurements were conducted at OCP using a sinusoidal potential signal with an AC amplitude of 10 mV over a frequency range from 100 kHz to 10 mHz with 10 points per decade. The EIS data were fitted with equivalent circuits using the EC-lab V10.40 software.

2.5.3 Hydrogen Evolution and Weight Loss Measurements

Hydrogen evolution and weight loss measurements of the processed alloys were also performed during 7 days of immersion in an aerated 3.5 wt.% NaCl solution at room temperature. Polished samples of 15 mm in diameter and 2 mm in thickness were placed

in a sample holder that exposed a surface area of $\sim 1 \text{ cm}^2$. The evolved hydrogen was collected in a burette by a funnel above the specimen [78, 79] and measurements were recorded every 12 h during the total immersion time. The corresponding corrosion rate, P_H (mmpy) was calculated from the hydrogen evolution rate \dot{V}_H ($\text{mL cm}^2 \text{ d}^{-1}$) according to the following expression [77]:

$$P_H = 2.088\dot{V}_H \quad (11)$$

After the immersion test, the samples were chemically cleaned in a pickling solution of 200 g/L of CrO_3 and 10 g/L of AgNO_3 for 1 min at room temperature to remove the corrosion products. Then the samples were rinsed with deionized water and dried by cold air flow. The dried specimens were weighed before and after the immersion test using a digital balance with a precision of 0.1 mg. The corrosion rate, P_W (mmpy) was calculated from the following equation [77]:

$$P_W = \frac{2.1 \Delta m}{At} \quad (12)$$

Where Δm (mg) is the weight loss, A (cm^2) is the exposed surface area of the specimens, and t (day) is the immersion time. The hydrogen evolution and weight loss measurements were replicated three times and the average values were reported.

2.5.4 Immersion Testing

Immersion tests of the polished samples were also performed in an aerated 3.5 wt.% NaCl solution at room temperature during 1, 3, 5, and 7 days of immersion to investigate the morphology evolution of the corroded specimens. The composition of corrosion products was analyzed by X-ray diffraction. Following the immersion period,

exposed samples were chemically cleaned as described above. Morphology and surface roughness of the corroded samples were investigated by optical microscopy, SEM/EDS, and 3D digital microscopy (Keyence VHX-6000).

Immersion testing of the peak-aged AZ91 alloy was performed in an aerated 3.5 wt.% NaCl solution at room temperature for 6 h. Prior to the test, the specimens were ground and polished as described above for the microstructural examination. Following the immersion period, samples were chemically cleaned with the pickling solution to remove corrosion products. The morphology and surface roughness of the corroded samples were investigated by optical microscopy, SEM/EDS, and 3D digital microscopy (Keyence VHX-6000). Furthermore, an in-situ imaging corrosion observation was also conducted, in which a polished peak-aged AZ91 sample immersed in 3.5 wt.% NaCl solution was monitored continuously for approximately 30 h using an AmScope optical microscope. Corrosion initiation was recorded via screencast with Camtasia software.

Finally, immersion testing of the ECAPed alloys after different ECAP passes was performed in a 3.5 wt.% NaCl solution at room temperature for 1 h and 24 h to investigate the corrosion initiation and propagation, respectively. The solution was not renewed during the immersion period and the samples were suspended from a nylon string in 800 ml of solution without agitation. Optical microscope images were taken before and after immersion for 1 h to clearly identify the preferential corrosion initiation sites. After the immersion testing, samples were chemically cleaned for 1 min with the pickling solution. After removal of corrosion products, specimens were rinsed with deionized water and ethanol and dry with compressed air. Morphology of the corroded

specimens after removal of corrosion products were characterized by SEM, in addition, surface topography maps and roughness profiles were obtained from a 3D profilometer (Keyence VHX-6000).

2.5.5 Electrochemical Microcell Technique

The electrochemical microcell technique was used to investigate the local electrochemical behavior of the constituent phases of the peak-aged AZ91 alloy and ECAPed alloys in a 3.5 wt.% NaCl solution. The schematic setup for microelectrochemical investigations based on the microcell technique is shown in Figure 11. The entire setup is mounted on a microscope allowing for positioning of the microcell on the sample. The microcell mainly consists of a glass capillary with an opened mouth diameter of 70 μm at the end. The capillary is filled with 3.5 wt.% NaCl electrolyte. A layer of silicone rubber is applied as the sealant between the front end of the microcell and the surface of interest. The microcell is fixed at the microscope carousel, replacing an objective, and the specimen is mounted on the microscope stage. This setup enables the search of a site of interest using the microscope before switching to the microcell. A saturated calomel electrode (SCE) and platinum wire used as a reference and counter electrode, respectively, were connected to the microcell to allow the electrochemical testing of the investigated sample surface. The electrochemical behavior of different constituent phases or regions were investigated by a potentiodynamic polarization technique. A series of potentiodynamic polarization tests were separately performed on these phases/regions by sweeping the potential in the

anodic direction from -250 mV to +500 mV versus open circuit potential at a scan rate of 1 mV/s. The corroded morphology of the tested sites was further examined using SEM.

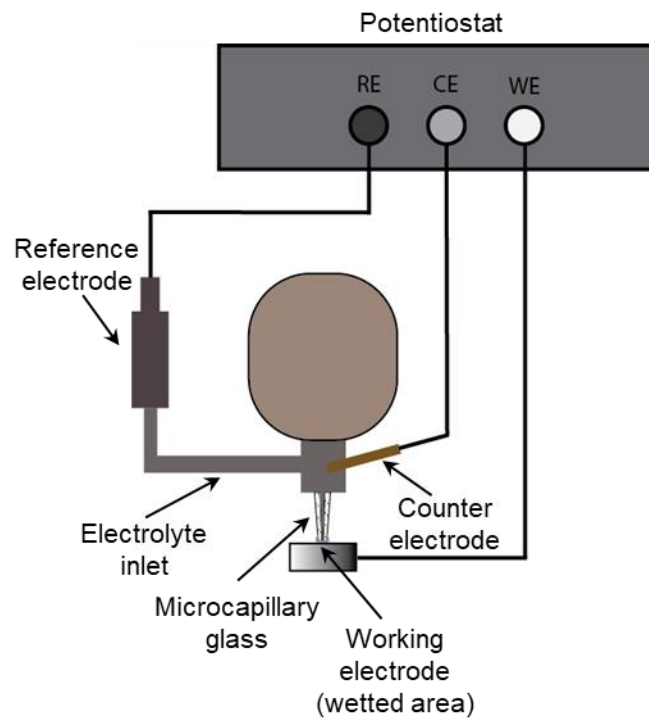


Figure 11. Schematic illustration of the microcell setup for electrochemical testing at local site.

CHAPTER III
ENHANCED MECHANICAL PROPERTIES AND CORROSION RESISTANCE OF
AN ULTRAFINE-GRAINED Mg-9Al-1Zn ALLOY

The current chapter investigates the corrosion behavior of AZ91 alloys in chloride environment after four different processing methods including solution heat treatment, aging, equal channel angular pressing (ECAP), and post-aging after ECAP processing, primary focus will be given on correlating microstructural features such as grain size, grain distribution, and morphology and distribution of secondary phases with corrosion behavior. This work covers microstructural analysis, mechanical testing, and an electrochemical/corrosion characterization of AZ91 alloy under the described conditions. The corrosion testing includes weight loss measurements, hydrogen evolution testing, and electrochemical characterization using potentiodynamic polarization (PDP) and electrochemical impedance spectroscopy (EIS). Furthermore, chemical and morphological characterization of corrosion products after exposure will be performed to determine the mechanisms of corrosion degradation of the AZ91 alloys. According to the results shown below, a simultaneous improvement in strength, ductility and corrosion resistance was achieved after ECAP processing that results from grain refinement of the microstructure and formation of homogeneously distributed fine β -Mg₁₇Al₁₂ precipitates.

3.1 Microstructural Characterization of AZ91 Alloys

Figure 12 shows the microstructure of as-cast and heat-treated AZ91 alloys. As shown from Figure 12(a), the as-cast AZ91 alloy exhibits a typical dendritic structure with coarse grains consisting of α -Mg matrix, a partially divorced eutectic phase, lamellar β -Mg₁₇Al₁₂ precipitates, and Al₈Mn₅ intermetallic particles (Figure 12(b)). The average grain size is about $375 \pm 145 \mu\text{m}$. The enlarged SEM micrograph in Figure 12(c) shows details of the eutectic phase and the lamellar β -Mg₁₇Al₁₂ precipitates. The divorced eutectic phase consists of large β -Mg₁₇Al₁₂ precipitates surrounded by an aluminum-enriched eutectic α -Mg phase [80, 81]. Although the eutectic β -Mg₁₇Al₁₂ phase is expected to form when the aluminum content is about 13%, is usually present in Mg-Al alloys containing as low as 2 wt.% Al due to non-equilibrium solidification during the casting process [80, 81]. Figure 12(c) also shows the presence of islands of eutectic α -Mg phase within the eutectic β -Mg₁₇Al₁₂ phase. The partially divorced eutectic phase is commonly formed in alloys with high aluminum content and during slow solidification [82]. The lamellar precipitates, also shown in Figure 12(c), are formed due to solid state transformation of the eutectic α -Mg phase near the eutectic β -Mg₁₇Al₁₂ phase [62, 83, 84]. Al₈Mn₅ intermetallic particles (Figure 12(b)) were also found in the as-cast material due to addition of Mn to the melt to minimize the detrimental effect of iron impurities on the corrosion resistance of the alloy [3, 85, 86].

Solution annealing of the as-cast AZ91 alloy at 413°C for 24 h caused almost complete dissolution of the eutectic and lamellar precipitates resulting in a supersaturated α -Mg solid solution with an average grain size of $515 \pm 99.5 \mu\text{m}$ (Figure

12(d)). As shown in Figure 12(d), the Al_8Mn_5 intermetallic particles are still found after the heat treatment process due to the low solubility of Mn in the Mg matrix as well as their high thermal stability [43, 87]. Typically, some residual small $\beta\text{-Mg}_{17}\text{Al}_{12}$ phases that were not dissolved during homogenization might still be present.

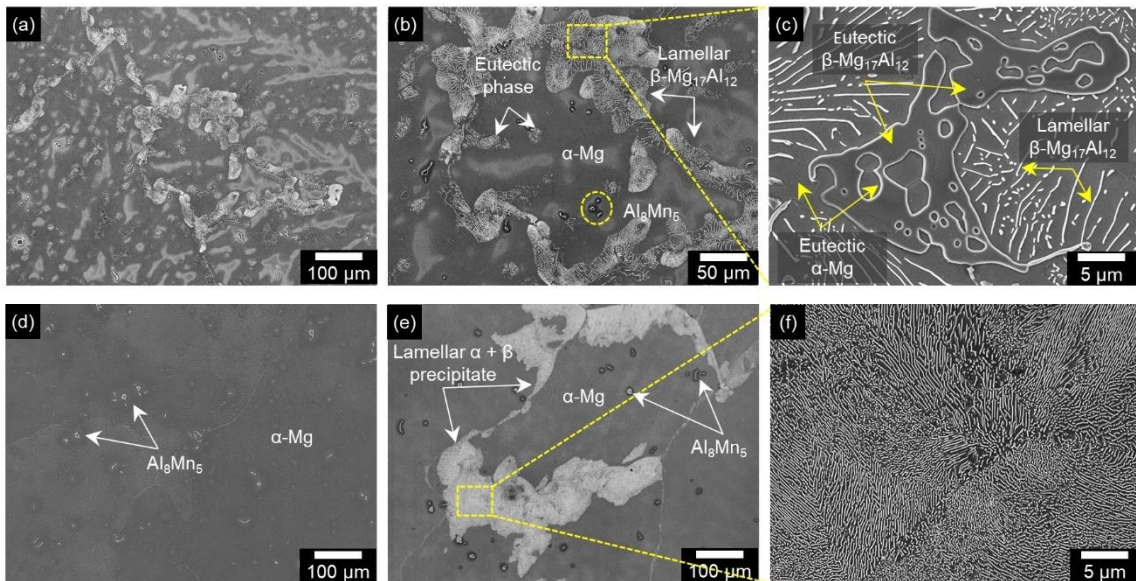


Figure 12. SEM micrographs of (a-c) as-cast alloy, (d) homogenized alloy, and (e-f) peak-aged alloy.

Further aging of the supersaturated solid solution at 168 °C for 16 h (peak-aged condition) results in discontinuous precipitation of a fine lamellar structure consisting of a rod-like $\beta\text{-Mg}_{17}\text{Al}_{12}$ phase and a less saturated $\alpha\text{-Mg}$ phase at the grain boundaries of the original supersaturated solid solution (Figure 12(e)). Figure 12(f) shows the rod-like morphology of the $\beta\text{-Mg}_{17}\text{Al}_{12}$ phase with an evident anisotropy of growth. The average

grain size of the peak-aged alloy is $498 \pm 73 \mu\text{m}$. Al_8Mn_5 intermetallic particles are still present after the aging treatment.

Figure 13 shows SEM micrographs of the AZ91 alloy after ECAP processing. After four ECAP passes, the AZ91 alloy exhibited a bimodal grain structure that consist of original coarse grains, which are elongated in the direction of the shear strain, surrounded by new recrystallized equiaxed fine grains that occupies a large volume fraction (Figure 13(a) and (b)). This bimodal grain structure combined with the presence of equiaxed fine grains surrounding the elongated coarse grains indicates that dynamic recrystallization (DRX) occurred during ECAP processing. The average grain size of the DRXed grains is $1.59 \pm 0.2 \mu\text{m}$.

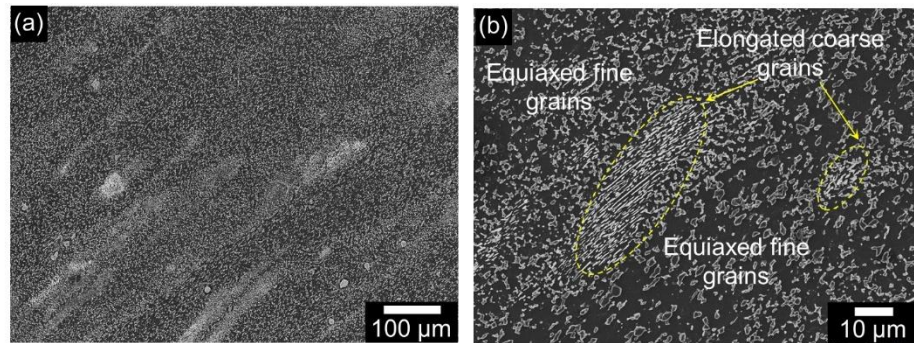


Figure 13. SEM micrographs of ECAPed alloy showing (a) significant grain refinement of the original homogenized alloy after ECAP processing, (b) bimodal grain structure of elongated coarse grains and equiaxed fine grains, (c) $\beta\text{-Mg}_{17}\text{Al}_{12}$ precipitates formed in the DRXed region and (d) lath-shaped continuous $\beta\text{-Mg}_{17}\text{Al}_{12}$ precipitates formed in the unDRXed regions.

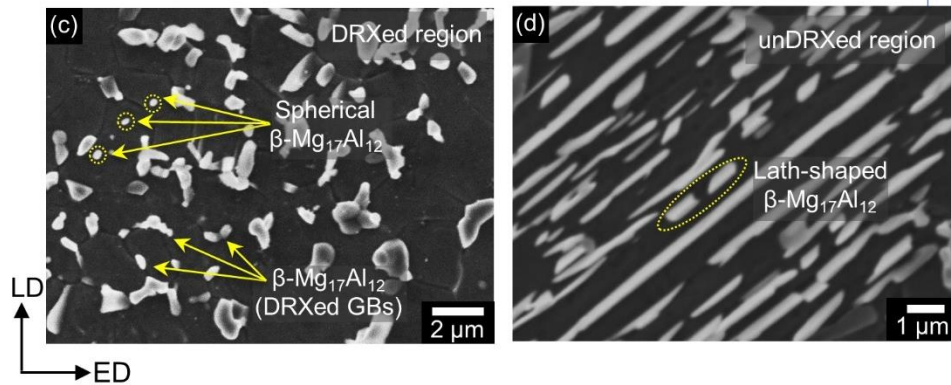


Figure 13. Continued.

Furthermore, a significantly large amount of $\beta\text{-Mg}_{17}\text{Al}_{12}$ precipitates also appeared after ECAP processing; in the DRXed regions (Figure 13(c)), spherical-shaped precipitates are distributed at the newly formed DRXed grain boundaries and within the recrystallized grains, whereas in the unDRXed regions (Figure 13(d)), lath-shaped continuous precipitates elongated in the direction of the shear strain are observed. Xu et al. [3, 88] found similar morphology and distribution of $\beta\text{-Mg}_{17}\text{Al}_{12}$ precipitates after hot compression of a homogenized AZ91 alloy. The presence of this large amount of $\beta\text{-Mg}_{17}\text{Al}_{12}$ precipitates can be associated with precipitation during pre-heating prior to extrusion (pre-formed precipitates), fracturing of undissolved eutectic $\beta\text{-Mg}_{17}\text{Al}_{12}$ precipitates by shearing, and strain-induced dynamic precipitation (SIDP) from the Al supersaturated $\alpha\text{-Mg}$ matrix that occurs during deformation by ECAP [11, 27, 89, 90]. The large deformation strain imposed during ECAP accelerates the kinetics of dynamic precipitation as compared to the precipitation rate during traditional heat treatment. Thus, large amount of precipitates can nucleate at the grain boundaries of the newly formed DRXed grains since they can provide a fast path for diffusion of solute atoms. $\beta\text{-Mg}_{17}\text{Al}_{12}$

Mg₁₇Al₁₂ precipitates can also nucleate at the interior of the grains due to the large density of dislocations and other defects like vacancies that are formed during plastic deformation acting as sites for heterogeneous nucleation of precipitates [7, 11, 91]. Furthermore, the high density of dislocations inside the α -Mg can also promote faster diffusion paths for the solute atoms in the α -Mg matrix accelerating the nucleation and growth of precipitates compared to precipitation during conventional heat treatment [75]. The average size of the precipitates formed at the DRXed grain boundaries is 0.8 ± 0.2 μm whereas the average size of the fine precipitates within the DRXed grains is less than 100 nm. As reported by several authors, coarse precipitates bigger than ~ 1 μm in size can promote DRX by the so-called particle stimulated nucleation (PSN) mechanism, in which high density of dislocations is accumulated around the precipitates during processing, and these deformation zones at the vicinity of the precipitates with large amount of stored energy act as preferential sites for nucleation of new recrystallized grains [11, 42, 92]. It has been also reported that fine precipitates smaller than 1 μm can hinder grain growth by pinning the newly formed DRXed grain boundaries such that they act as barrier for grain boundary migration which retards the grain growth of the DRXed grains and leads to a more refined microstructure [42, 93]. Thus, the remarkable grain refinement after four ECAP passes can be associated not only with dynamic recrystallization of new equiaxed fine grains promoted by the large strain deformation during ECAP, but also with dynamic precipitation, in which precipitates can accelerate the nucleation of DRXed grains by the PSN mechanism or they can retard DRXed grain growth via grain boundary pinning effect [92, 93].

Figure 14 shows SEM micrographs of the AZ91 alloy processed by ECAP for 4 passes followed by aging at 100°C for 48 h. As shown in Figure 14, the microstructure after post-aging is similar to the ECAPed alloy shown in Figure 13 exhibiting a bimodal grain structure including the original coarse grains surrounded by the newly formed DRXed grains, in which spherical shaped precipitates were formed at the DRXed grain boundaries as well as within the DRXed grains (Figure 14(c)) whereas lath-shaped continuous precipitates were formed inside the unDRXed grains (Figure 14(d)). As reported in Table 4, the volume fraction of discrete β -Mg₁₇Al₁₂ precipitates, both, at the grain boundaries of the DRXed grains and in the elongated coarse grains, increased after post-aging treatment. This can be attributed to the high dislocation density accumulated after ECAP processing that served as nucleation sites for further precipitation, accelerating the precipitation kinetics during post-aging [7, 27]. The larger volume fraction of β -Mg₁₇Al₁₂ precipitates formed after post-aging can provide further dispersion and/or precipitation strengthening to the AZ91 alloy [91]. As shown in Figure 13(e) and also reported in Table 4, joining and coarsening of the β -Mg₁₇Al₁₂ precipitates formed at the DRXed grain boundaries occurred after aging. Besides, a large amount of very fine spherical precipitates was formed within the DRXed grains. Similar nano-sized precipitates were also observed by Yuan et al. [7] after ECAP and post aging of an AZ91 alloy. They reported that these fine precipitates can simultaneously enhance both the strength and ductility of the AZ91 alloy due to the development of an homogeneous and equilibrium fine structure [7]. The grain size of the DRXed grains after post-aging treatment was $2.22 \pm 0.3 \mu\text{m}$, indicating that coarsening of the recrystallized grains also

occurred. The coarsening of the DRXed grains can be associated with dislocation recovery as well as growth of the precipitates formed at the DRXed grain boundaries that weakened their pinning effect against grain growth [11].

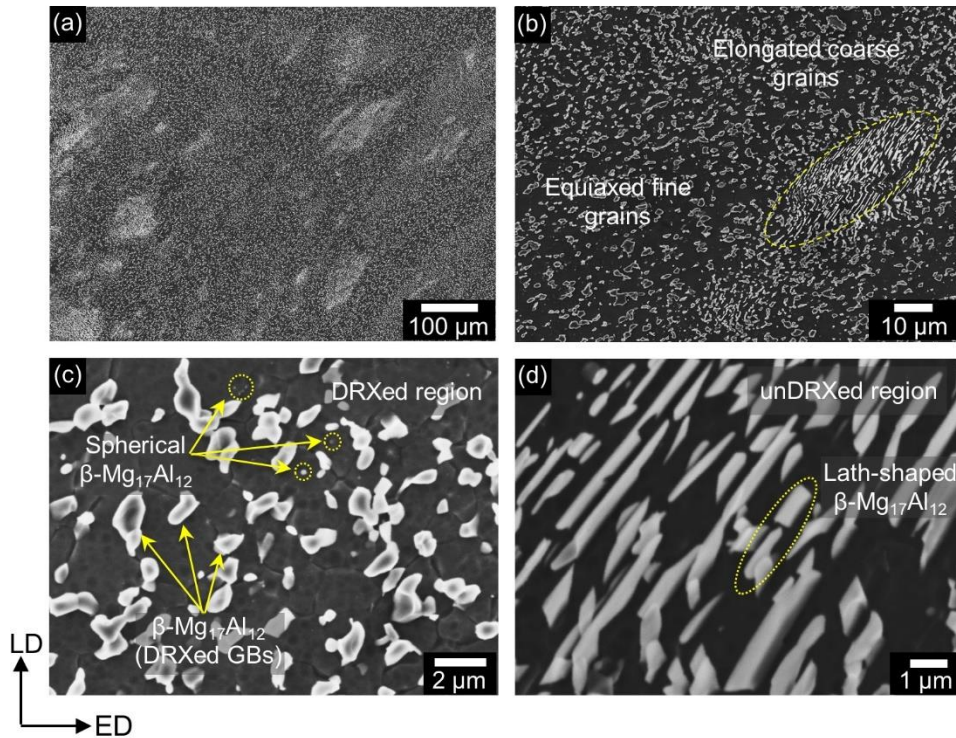


Figure 14. SEM micrographs of ECAP-aged alloy showing (a) and (b) bimodal grain structure of elongated coarse grains and equiaxed fine grains, (c) $\beta\text{-Mg}_{17}\text{Al}_{12}$ precipitates formed in the DRXed region and (d) lath-shaped continuous $\beta\text{-Mg}_{17}\text{Al}_{12}$ precipitates formed in the unDRXed regions.

A summary of microstructural features including grain size, volume fraction of the β -phase in the unDRXed grains and in the DRXed grain boundaries, and size of the β -precipitates at the DRXed grain boundaries are listed in Table 4.

Table 4. Microstructural parameters of as-cast and processed AZ91 alloys

Alloy	Grain size* (μm)	Volume fraction of β -phase in unDRXed regions (%)	Volume fraction of β -phase in DRXed GBs (%)	Size of β -precipitates in DRXed GBs (μm)
As cast	375 ± 145			
Homogenized	515 ± 99			
Peak-aged	498.8 ± 73			
ECAPed	1.59 ± 0.2	30.60	19.20	0.80 ± 0.2
ECAP-aged	2.22 ± 0.3	36.73	26.66	1.18 ± 0.3

* The grain size for the ECAPed alloys corresponds to the size of the DRXed grains.

Figure 15 shows the X-ray diffraction (XRD) patterns of the as-cast and processed AZ91 alloys. The XRD pattern of the as-cast condition indicates that α -Mg and β -Mg₁₇Al₁₂ phases are the main constituents in the alloy. There is no evidence of the Al₈Mn₅ phase due to its low volume fraction. After homogenization treatment, the AZ91 alloy only exhibits the presence of the α -Mg phase, verifying that the majority of the eutectic and lamellar β -Mg₁₇Al₁₂ precipitates presented in the as-cast condition were dissolved in the α -Mg matrix. The XRD diffractograms of the AZ91 alloy after aging and ECAP processing show additional peaks corresponding to the β -Mg₁₇Al₁₂ phase. The intensity of the β -Mg₁₇Al₁₂ phase diffraction peaks in the ECAPed specimens is relatively higher as compared to those in the as-cast and heat-treated alloys as indicated by the vertical dashed lines. The ECAP-aged alloy exhibits the highest peak intensity suggesting that this sample exhibited the highest volume fraction of the β -Mg₁₇Al₁₂

phase, which is consistent with the values reported in Table 4. This confirms that additional precipitation of the β -Mg₁₇Al₁₂ phase occurred during ECAP processing as well as during post-aging treatment.

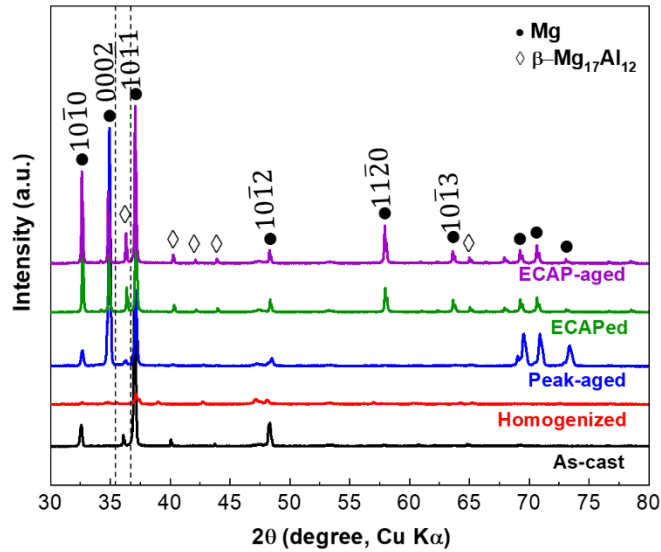


Figure 15. XRD patterns of as-cast and processed AZ91 alloys.

3.2 Mechanical Properties

3.2.1 Hardness

As mentioned above, post-aging after ECAP processing was performed to further increase the strength (and hardness) of the ECAPed alloy. Figure 9(b) shows that the maximum hardness value after ECAP processing is attained after aging at 100°C for 48 h resulting in a peak hardness value of 94.8 HV. However, it is worth to notice that the degree of hardening in the ECAPed alloy exhibits a limited increase as compared to the one obtained in the homogenized alloy, where an increase of 38% is obtained after aging

of the homogenized sample to the peak-aged condition while only 9% of increase is achieved after aging of the ECAPed specimen. Furthermore, it is seen that aging at low temperatures (i.e., 100 °C and 130 °C) increases the hardness up to reaching a peak-aged value and then it decreases with further aging time, due to overaging that results in grain growth and coarsening of the existing precipitates [94]. In contrast, aging at higher temperatures (i.e., 168 °C and 180 °C) does not exhibit a notorious peak-aged value but instead, hardness continuously decreases with aging time even to values significantly below the hardness value for the peak-aged alloy (horizontal dashed red line). It is likely that the peak-aged conditions at these temperatures occurred at very early aging times (< 4 h) that were not recorded in this study. This post-aging behavior after ECAP is relatively different from the conventional aging response of non-deformed alloys and has been associated with a competition of two opposite factors during aging of heavily deformed alloys; precipitation hardening and a softening effect due to dislocation recovery (i.e., decrease of the dislocation density within subgrains or at the grain boundaries) and/or grain growth [94, 95]. It is well known that severely deformed alloys processed by SPD usually exhibit high density of dislocations and non-equilibrium subgrains and grain boundaries, this particular structure allows for extensive recovery during post-aging treatment. According to this, the severe drop in hardness as increasing aging time for the alloys processed at high aging temperatures can be related to extensive recovery that overwhelms the precipitation hardening [94, 95].

Vickers hardness of the as-cast and processed alloys is shown in Figure 16. After homogenization treatment, the Vickers hardness decreased from 70.26 HV in the cast

alloy to 59.41 in the homogenized condition, which is attributed to the almost complete dissolution of the β -Mg₁₇Al₁₂ phase in the α -Mg matrix. Further aging and ECAP processing increase the hardness of the AZ91 alloy. Aging to the peak-aged condition significantly increased the hardness of the alloy reaching a value of 82 HV. ECAP processing increased even more the hardness of the alloy, resulting in a 50% of increase after ECAP (89.19 HV) with respect to the homogenized alloy. Post-aging after ECAP processing led to the highest hardness value among all tested materials with a hardness value of 94.77 HV, which represents an increase of almost 60% as compared to the homogenized condition. This sharp increase in hardness can be associated with the severe strain imposed during ECAP processing that results in a significant increase in dislocation density, remarkable grain refinement, and increase in the volume fraction of the β -Mg₁₇Al₁₂ phase. In addition, the post-aging treatment after ECAP processing also contributed to the increase in hardness due to static precipitation of the β -Mg₁₇Al₁₂ phase that provide further precipitation hardening.

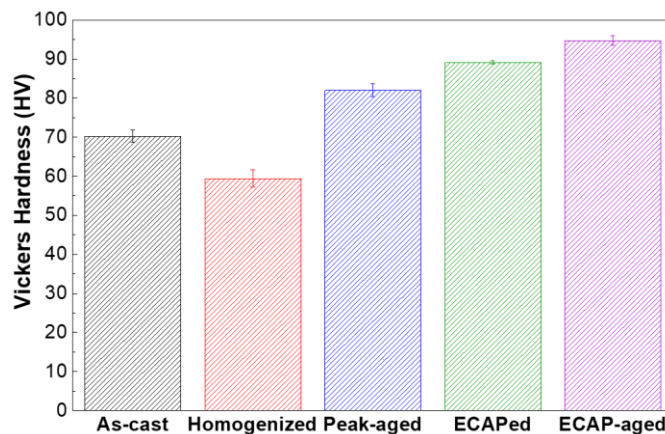


Figure 16. Vickers hardness of as-cast and processed AZ91 alloys.

3.2.2 Tensile Behavior

Tensile tests at room temperature were performed to evaluate the mechanical properties of the as-cast and processed AZ91 alloys. The stress-strain curves as well as the results for the ultimate tensile strength (UTS), yield strength (YS), and elongation to failure are shown in Figure 17. As seen from Figure 17(a), the as-cast condition shows a relatively low ultimate tensile strength and ductility. The homogenization treatment resulted in a slightly increase in UTS and ductility. Further aging after homogenization led to a significant increase in strength accompanied with a decrease in ductility. It is quite evident that ECAP processing resulted in a remarkable improvement of the strength and ductility from the original homogenized condition. Finally, the post-aging treatment after ECAP processing further increased the strength of the alloy but a slightly decreased in ductility was also observed.

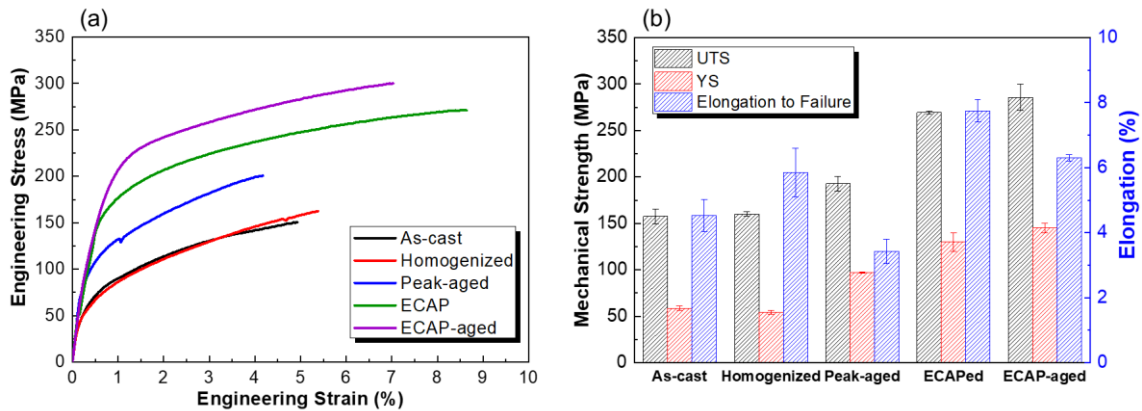


Figure 17. (a) Tensile stress-strain curves and (b) tensile properties of the as-cast and processed AZ91 alloys.

From the tensile properties shown in Figure 17(b), it is seen that the as-cast condition exhibits the lowest UTS value (157.5 ± 8.2 MPa) and a relatively low ductility (4.5 ± 0.5 %). After homogenization, the tensile strength of the alloy is slightly increased to 160.2 ± 2.2 MPa and the ductility is also improved to 5.9 ± 0.8 %. However, the yield strength decreased from 58.7 ± 2.5 MPa (as-cast condition) to 54 ± 2.0 MPa (homogenized condition). Aging of the homogenized alloy increased the UTS and yield strength of the alloy to 192.7 ± 8.0 MPa and 97 ± 1.0 MPa, respectively. However, this improvement in strength was accompanied by a drastic decrease in ductility to 3.4 ± 0.4 %. In contrast, the UTS, YS and ductility were significantly improved after ECAP processing of the homogenized sample. The YS, UTS and elongation to failure of the ECAPed alloy are 130 ± 10 MPa, 269.4 ± 1.8 MPa and 7.8 ± 0.4 %, respectively, which represents an increase of 140%, 68% and 32% with respect to the values obtained for the homogenized sample. These results clearly show that ECAP processing under the investigated conditions was effective in simultaneously improving strength and elongation. Under similar ECAP processing conditions, Khani et al. [11] reported YS, UTS and elongation to failure values of ~ 158 MPa, 270 MPa, and 10%, respectively, which are very similar to the values obtained in this study. As seen from Figure 17(b), the increase in YS and UTS of the homogenized specimen after ECAP processing is significantly higher compared to the increase achieved by the traditional aging treatment (79% increase in YS and 20% increase in UTS). The relatively small precipitation hardening effect obtained after aging treatment has been attributed to several factors such as undesirable orientation for effectively blocking basal slip, slow aging kinetics,

and large size of the β -Mg₁₇Al₁₂ precipitates [95, 96]. In contrast, the significant improvement in the UTS and YS of the AZ91 alloy after ECAP processing can be mainly associated with grain boundary strengthening promoted by the fine DRXed grains as well as precipitation strengthening enhanced by the large volume fraction of well-dispersed fine β -Mg₁₇Al₁₂ precipitates that can restrict dislocation motion during the tensile test [11, 97]. Strain hardening might also play a role in the strengthening of the alloy due to the high dislocation density accumulated during ECAP that can restrict dislocation motion during tensile deformation [94, 98]. It is worth mentioning that besides precipitation strengthening, the relatively fine β -Mg₁₇Al₁₂ precipitates located at the DRXed grain boundaries can retard the grain growth of DRXed grains, providing an additional contribution to grain boundary strengthening [99]. In addition, the fine β -Mg₁₇Al₁₂ precipitates formed within the DRXed grains are more effective in restricting dislocation motion than the large lamellar precipitates formed during aging heat treatment, therefore these fine precipitates can provide a better hardening response than the lamellar ones [90]. The enhancement in ductility after ECAP can be attributed to the refined grain structure and the presence of fine β -Mg₁₇Al₁₂ precipitates uniformly distributed in the entire matrix that reduces stress concentration and therefore induces a more uniform deformation during the tensile test [16, 100]. Wang et al. [100] reported that the excellent ductility of an ultrafine AZ91 alloy was mainly attributed to two factors: 1) the fine grains with a weakened basal texture that were able to activate basal and non-basal slip systems improving the uniform deformation of the material and 2) the existence of coarse grains in the bimodal microstructure that were able to promote

twinning during tensile deformation increasing the number of activated slip systems (i.e., twinning mediated plasticity).

The post-aging treatment of the ECAP sample increased the UTS to 285.8 ± 14.3 MPa, representing an improvement of 78.4% with respect to the homogenized condition. However, the elongation to failure is slightly decreased from $7.8 \% \pm 0.4$ in the ECAPed alloy to $6.3 \pm 0.1\%$ in the ECAP-aged condition. The further increase in UTS and YS after the subsequent aging treatment can be related to static precipitation of the β - $Mg_{17}Al_{12}$ phase during aging that can provide additional dispersion and/or precipitation strengthening. It is worth to notice that the increase in ultimate strength after post-aging indicates that precipitation hardening overcame the aforementioned softening effect caused by dislocation recovery and grain growth. The slightly decrease in ductility after post-aging treatment can be related to coarsening of the β - $Mg_{17}Al_{12}$ precipitates located at the grain boundaries of the DRXed grains (see Table 4). These larger precipitates can exhibit poor interface bonding with the surrounding α -Mg matrix leading to stress concentration during tensile deformation which can promote nucleation and propagation of microcracks [3, 89]. The continuous growth and coalescence of these micro-cracks can lead to premature failure and therefore loss of ductility.

3.3 Electrochemical and Corrosion Measurements

3.3.1 Open Circuit Potential (OCP)

Figure 18 shows the evolution of OCP for the different AZ91 alloys immersed in 3.5 wt.% NaCl solution for 3600 s before the potentiodynamic polarization test. Figure 18 shows a clear difference in the OCP evolution between the coarse-grained alloys (i.e.,

as-cast and heat-treated samples) and the fine-grained alloys (i.e., ECAPed and ECAP-aged samples). For the as-cast and heat-treated specimens, the OCP slightly increases during the first few minutes after immersion and then sharply drops to more negative values reaching a relatively stable trend after approximately 30 minutes. The slightly increase in potential is associated with the formation of an oxide layer on the metal surface whereas the drastic drop in potential is related to a dissolution of the oxide layer that increases the active anodic area [101]. The stability of OCP reached at longer immersion time suggests a steady state condition between the anodic dissolution and the repassivation of the oxide layer [102]. In contrast, the OCP in the fine-grained alloys gradually increases for about 20 minutes and then it remains relatively stable suggesting the formation and growth of a more stable and protective oxide layer than the one in the coarse-grained alloys with no sign of oxide layer dissolution. It is also seen that after reaching stable OCP values, the OCP of the ECAP processed alloys are more positive than that of the as-cast and heat-treated alloys. This behavior suggests that the fine-grained alloys exhibit a more noble behavior compared with the coarse-grained alloys due to the formation of a more protective oxide layer. It is believed that the higher volume fraction of grain boundaries in the fine-grained alloys can provide short diffusion paths for the Al solute atoms to diffuse towards the surface, such that an aluminum-enriched oxide layer can be formed on the alloy surface providing a higher resistance against localized dissolution. Lastly, it is also seen that the homogenized alloy shows the most negative OCP values among all materials, which can be attributed to the very low volume fraction of β -Mg₁₇Al₁₂ phase. It is well known that the β -Mg₁₇Al₁₂

phase is more noble than the α -Mg matrix, which results in shifting of the potential to more positive values [103]. Therefore, the lower volume fraction of β -Mg₁₇Al₁₂ phase in the homogenized alloy causes that the OCP shifts in the more negative direction.

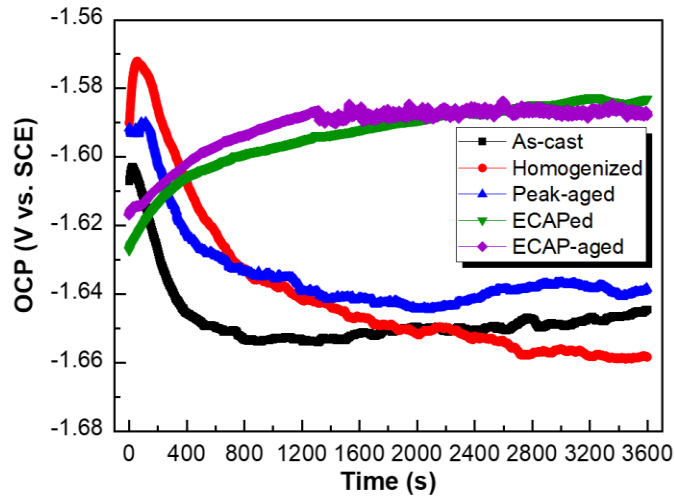


Figure 18. Evolution of open circuit potential (OCP) during 1 hour of as-cast and processed AZ91 alloys immersed in 3.5 wt.% NaCl solution.

3.3.2 Potentiodynamic Polarization (PDP)

Figure 19 shows the potentiodynamic polarization curves of the as-cast and processed AZ91 alloys immersed in 3.5 wt.% NaCl solution. The values of E_{corr} , i_{corr} and cathodic Tafel slope (β_c) were derived from Tafel extrapolation and they are listed in Table 5. Corrosion rate calculated from equation 10 is also included in Table 5. From Figure 19, it is seen that E_{corr} values of the ECAP processed alloys are more positive than the ones of the as-cast and heat-treated alloys. Furthermore, it can be also noticed that the i_{corr} values for the ECAPed materials are lower than those for the as-cast and

heat-treated alloys resulting in lower corrosion rates as reported in Table 5. The polarization curves show significant changes in the anodic polarization response for the different materials, in which the anodic current density of the fine-grained alloys is drastically lower than that of the coarse-grained materials, suggesting a decrease in the anodic reaction kinetics with ECAP processing. Since the anodic reaction kinetics is influenced by the rate of Mg dissolution and presence of a protective oxide layer, this indicates that microstructural changes after ECAP processing slow down the anodic dissolution of the alloy. In contrast, minor changes are observed in their cathodic response, indicating that the different microstructures of as-cast and processed materials had no strong influence on the hydrogen evolution reaction. According to the anodic and cathodic polarization behavior, it is suggested that the more noble E_{corr} and decrease of i_{corr} for the ECAPed alloys are mainly related to the decrease in the anodic reaction rates observed in these processed materials. It has been reported that the ennoblement in E_{corr} and the shift of the anodic kinetics to lower current densities in severely deformed Mg alloys is mainly attributed to two major microstructural changes after processing: 1) grain refinement combined with overall changes in the grain structure such as texture and character of grain boundaries as well as 2) changes in the distribution, volume fraction, and morphology of secondary phases [14].

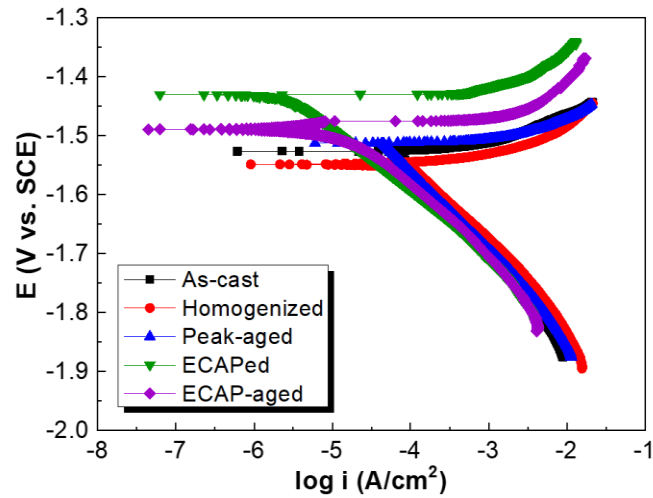


Figure 19. Potentiodynamic polarization (PDP) curves of as-cast and processed AZ91 alloys immersed in 3.5 wt.% NaCl solution.

The effect of heat treatment on E_{corr} and i_{corr} can be seen in the as-cast, homogenized, and peak aged alloys. The solution annealing that dissolves most of the cathodic β -phases in the as-cast alloy leads to a decrease in the E_{corr} from -1,527 (as-cast alloy) to -1,549 (homogenized alloy) mV vs. SCE due to the low volume fraction of β -phases in the homogenized alloy compared to the as-cast alloy. This decrease in E_{corr} is accompanied by an increase in i_{corr} values from 70.63 (as-cast alloy) to 90.63 (homogenized alloy) $\mu\text{A cm}^{-2}$. As a result, the corrosion rate of homogenized alloy was found to be higher (2.140 mmpy) than the one of as-cast alloy (1.614 mmpy). Aging of the homogenized alloy that produces a large volume fraction of cathodic β -phase shifts the E_{corr} in the noble direction from -1,549 (homogenized alloy) to -1,512 (peak-aged alloy) mV vs. SCE. In addition, the i_{corr} and corrosion rate values of peak-aged alloy were found to be a half of the ones of homogenized alloy. These results suggest that the presence of β -phase is beneficial in enhancing the corrosion resistance of AZ91 alloys. It

has been reported that the β -Mg₁₇Al₁₂ phase can accelerate the rate of the cathodic reaction (i.e., hydrogen evolution reaction) and it can also induce a strong micro-galvanic coupling with the α -Mg matrix due to the large difference in Al content between these phases [104]. However, it has been also reported that the β -Mg₁₇Al₁₂ phase promotes the formation of a more protective aluminum-enriched oxide layer and it can act as an electrochemical barrier against corrosion propagation [104, 105]. According to the results shown herein, it is seen that the inhibiting effect of the β -Mg₁₇Al₁₂ phase in decreasing the anodic reaction kinetics and/or retarding the corrosion propagation dominated over the accelerating effect of the cathodic kinetics and micro-galvanic coupling, resulting in lower corrosion current densities for the materials containing β -Mg₁₇Al₁₂ phase.

The effect of ECAP processing that significantly reduces the grain size and increases the volume fraction and distribution of the cathodic β -phase on E_{corr} and i_{corr} can be analyzed when comparing the polarization response of the homogenized and ECAPed alloys. The E_{corr} was found to be significantly nobler in the ECAPed alloy than the one in the homogenized alloy. The E_{corr} values of the ECAPed and homogenized alloys are -1,489 and 1,549 mV vs. SCE, respectively. The i_{corr} values that are proportional to the corrosion rate values dramatically decrease from 93.63 (homogenized alloy) to 2.76 (ECAPed alloy) $\mu\text{A cm}^{-2}$. The corrosion rate values for the homogenized and ECAPed alloys were found to be 2.140 and 0.063 mmpy, respectively. These results clearly indicate that the microstructure achieved after ECAP processing was beneficial in improving the corrosion resistance of the AZ91 alloy when exposed to chloride-

containing media. The post-aging treatment after ECAP was found to be detrimental to the corrosion resistance of the ECAPed alloy as evident by an increase in corrosion rate from 0.063 (ECAPed) to 0.290 (ECAP-aged) mmpy. This trend in the ECAP-aged alloy can be related to microstructural changes introduced after subsequent aging such as grain growth and coarsening of β -Mg₁₇Al₁₂ precipitates.

Table 5. Electrochemical parameters obtained from potentiodynamic polarization curves of as-cast and processed AZ91 alloys immersed in 3.5 wt.% NaCl solution

	E_{corr} (mV vs. SCE)	i_{corr} ($\mu\text{A cm}^{-2}$)	β_c (mV decade ⁻¹)	Corrosion Rate (P_i) (mmpy)
As-cast	-1,527	70.63	-148.2	1.614
Homogenized	-1,549	93.63	-121.2	2.140
Peak-aged	-1,512	43.48	-132.1	0.993
ECAPed	-1,431	2.76	-103.6	0.063
ECAP-aged	-1,489	12.67	-101.3	0.290

3.3.3 Electrochemical Impedance Spectroscopy (EIS)

To further analyze and compare the electrochemical behavior of the heat-treated and ECAPed alloys, electrochemical impedance spectroscopy (EIS) of the processed alloys was performed in 3.5 wt.% NaCl solution for up to 7 days. As seen from the Nyquist and Bode representations in Figure 20, there is a distinct behavior in the impedance signal observed for the heat-treated and ECAPed specimens. The Nyquist representation of the heat-treated alloys (Figure 20(a) and (b)) exhibits three-time

constants during the entire immersion time; two capacitive loops at high and medium frequencies and an inductive loop at the low frequency range. According to previous studies [102, 106], the capacitive loop at high frequencies (1 kHz to 100 Hz) has been associated with charge transfer processes occurring at the alloy/electrolyte interface and the presence of an oxide layer on the alloy surface. The capacitive loop at intermediate frequencies (20 Hz to 5 Hz) has been attributed to a mass transport relaxation process due to formation and dissolution of the partially protective oxide layer. Lastly, the inductive loop at the lowest frequencies (< 1 Hz) has been related to adsorption of intermediate species such as $\text{Mg}(\text{OH})_{\text{ads}}^+$ and Mg_{ads}^+ . The formation of these intermediate species occurs during breakdown of the oxide layer and initiation of localized corrosion processes, where the dissolved Mg ions can combine with other ionic species in the electrolyte forming intermediate species that remained adsorbed on the alloy surface [106]. For the heat-treated alloys, it is seen that the capacitive loops both at high and medium frequencies decrease with increasing immersion time. Similarly, the Bode diagrams show that the impedance magnitude at the lowest frequency ($|Z|_{0.01\text{Hz}}$), a parameter that provides an estimation of the total resistance of the system, gradually decrease with immersion time. This behavior implies that the corrosion process in these alloys proceed under charge transfer control where active anodic dissolution of the Mg alloy is taking place at the alloy/electrolyte interface and the formed corrosion products are not providing an effective protection against corrosive species. It is additionally worth noting that the phase angle describing the time constant at high frequency is

increasing over time, which provides another indication for continuous degradation of the heat-treated alloys as progressing the immersion time.

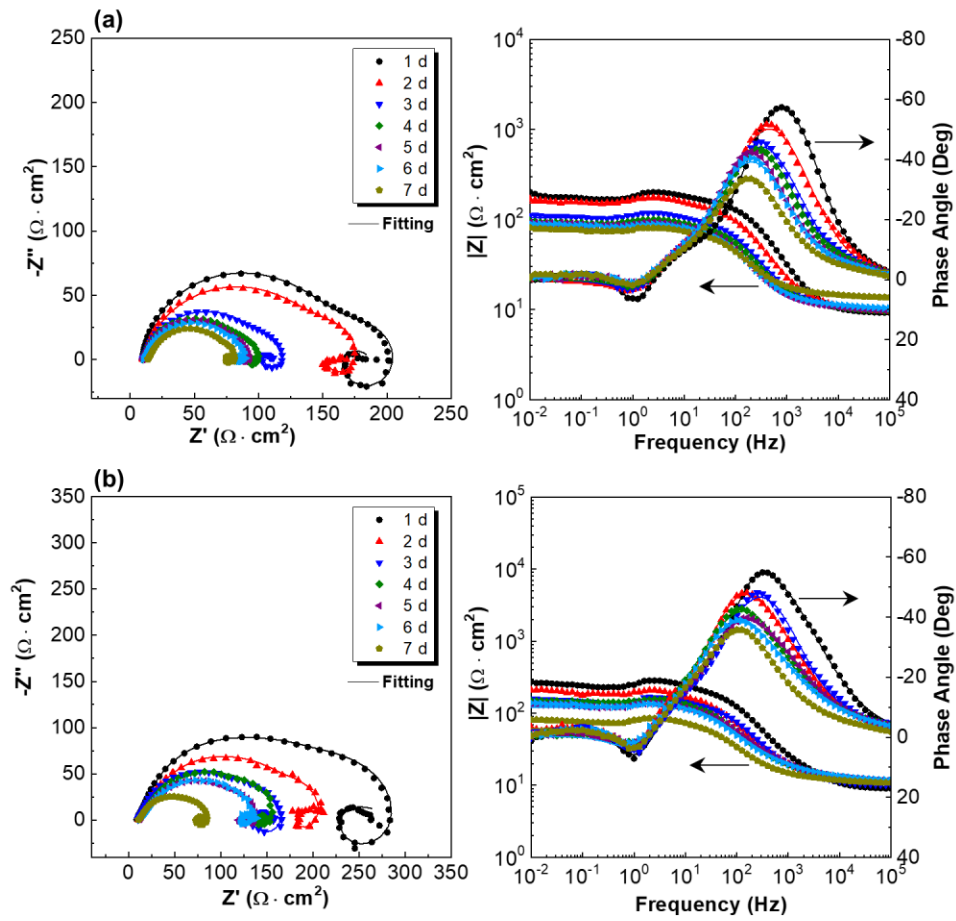


Figure 20. Evolution of EIS spectra for the (a) homogenized alloy, (b) peak-aged alloy, (c) ECAPed alloy and (d) ECAP-aged alloy immersed for 7 days in 3.5 wt.% NaCl solution.

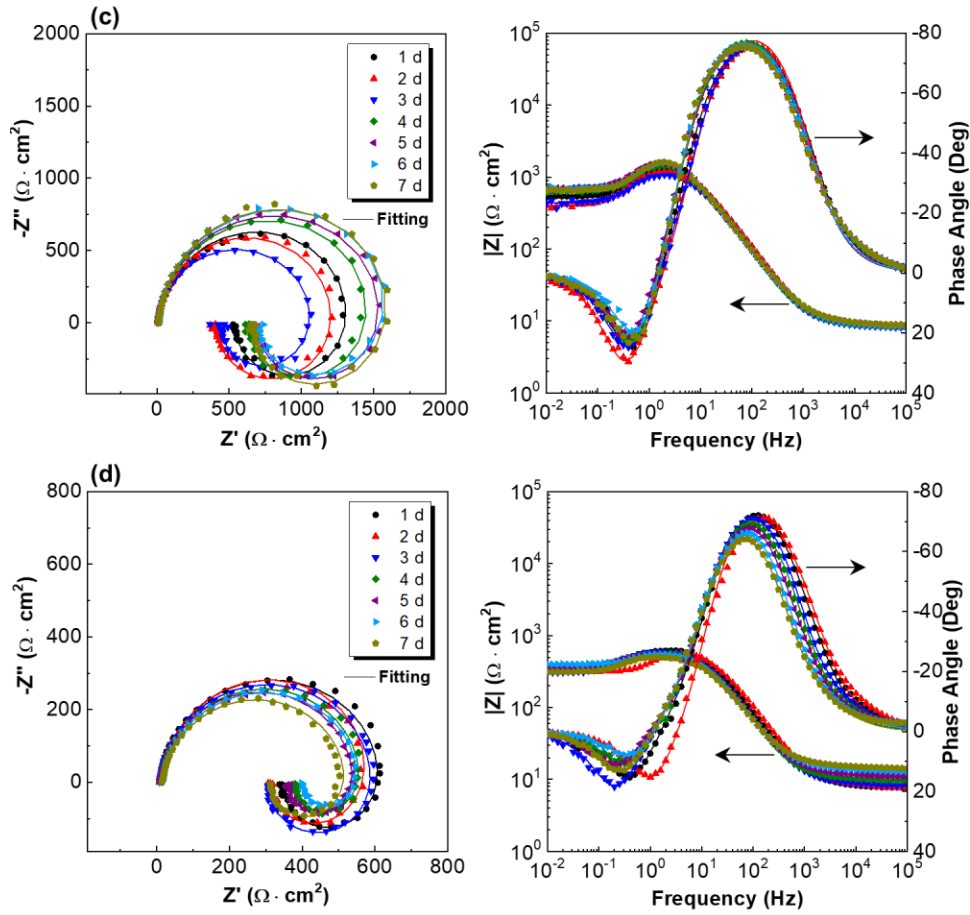


Figure 20. Continued.

Unlike the EIS signal for the heat-treated alloys, Figure 20(c) and (d) shows that the EIS spectra for the ECAPed specimens only exhibit the capacitive loop from high to intermediate frequencies (1 kHz to 10 Hz) and the inductive loop at low frequencies (< 0.5 Hz). The absence of the capacitive loop at intermediate frequencies in the fine-grained alloys indicates that the corrosion products are more stable and they exhibit better adhesion to the alloy surface [107]. Additionally, it is also seen that the ECAPed specimens show larger radius of the capacitive loops as well as higher $|Z|_{0.01\text{Hz}}$ values and lower phase angles than the heat-treated alloys, suggesting that the corrosion

resistance of the fine-grained ECAPed specimens is higher than the one of the coarse-grained heat-treated alloys. As noticed from Figure 20(c), the $|Z|_{0.01\text{Hz}}$ values as well as the capacitive loops in the Nyquist representation of the ECAPed alloy are slightly decreasing during the first three days of immersion as a result of charge transfer processes taking place at active sites. However, upon prolonged exposure, these values gradually increase with immersion time, which can be associated with the formation and growth of stable corrosion products that increases the overall impedance of the system. The EIS signal of the ECAP-aged alloy is similar as that of the ECAPed alloy, exhibiting a slightly decrease in the $|Z|_{0.01\text{Hz}}$ value and radii of the capacitive loop during the first two days of immersion. Nevertheless, it is noticed that the $|Z|_{0.01\text{Hz}}$ values for this specimen do not increase at longer immersion and instead, they remain almost constant until the end of the exposure time. Besides, the phase angle at the high frequency capacitive loop is found to be higher in the ECAP-aged alloy ($\sim -70^\circ$) than the one in ECAPed alloy ($\sim -78^\circ$). These results suggest that the layer of corrosion products formed on the ECAP-aged specimen is less protective than the one formed on the ECAPed alloy.

The equivalent electrical circuit sketched in Figure 21 was used to gain more understanding about the electrochemical response of the processed materials. In this circuit, R_s represents the electrolyte resistance; CPE_{dl} and R_{ct} describe the double layer capacitance and the charge transfer resistance, respectively, of the corrosion process taking place at the electrode/electrolyte interface; CPE_f and R_f represent the capacitance and the resistance, respectively, associated with the relaxation process due to growth and dissolution of corrosion products; and L and R_L denote the inductance and resistance,

respectively, associated with the adsorption of intermediate species on the alloy surface during localized corrosion. This equivalent circuit has been extensively used to fit the EIS spectra of magnesium alloys exposed to corrosive environments [107, 108]. For this equivalent circuit, constant phase elements (CPEs) were used instead of capacitances to account for deviations from ideal capacitive behavior. The impedance of the CPE element, Z_{CPE} , has been defined as follows:

$$Z_{CPE} = \frac{1}{Y_o(j\omega)^n} \quad (13)$$

where Y_o is the admittance of the constant phase element, j is the imaginary number, ω is the frequency, and n is an empirical exponent taking values between 0 and 1.

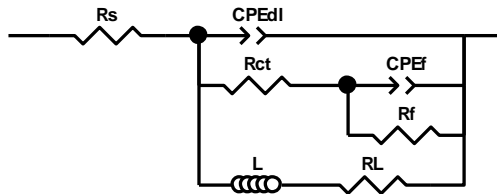


Figure 21. Equivalent electrical circuit to fit the EIS response of the heat-treated alloys and ECAPed alloys.

Figure 22(a) and (b) shows the evolution of charge transfer resistance (R_{ct}) and double layer capacitance (CPE_{dl}) for the different heat-treated and ECAPed alloys derived from the fitting process. In addition, Figure 22(c) also shows the reciprocal of polarization resistance ($1/R_p$) that provide an estimation of the corrosion susceptibility of the different magnesium alloys when exposed to the corrosive environment. The

polarization resistance describes the total corrosion resistance of a particular material and can be calculated based on the equivalent circuits. According to the equivalent circuits used in this study, the reciprocal of the polarization resistance for the heat-treated and ECAPed samples was calculated from equations 14 and 15, respectively, as follows:

$$\frac{1}{R_p} = \frac{1}{R_{ct} + R_f} + \frac{1}{R_L} \quad (14)$$

$$\frac{1}{R_p} = \frac{1}{R_{ct}} + \frac{1}{R_L} \quad (15)$$

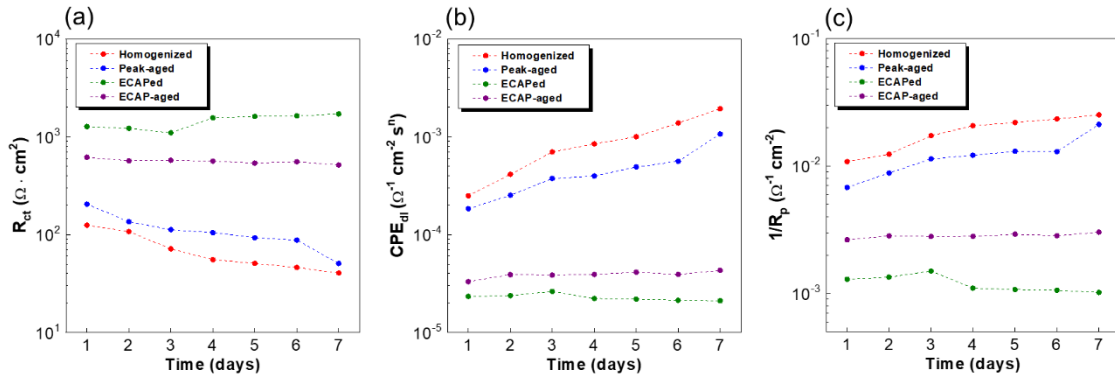


Figure 22. Equivalent circuit elements derived from fitting of EIS spectra for heat-treated and ECAPed specimens; (a) charge transfer resistance (R_{ct}), (b) double layer capacitance (CPE_{dl}), and (c) reciprocal polarization resistance ($1/R_p$).

Figure 22(a) shows the time evolution of the charge transfer resistance (R_{ct}) for the different magnesium alloys exposed to the chloride-containing environment. From Figure 22(a), it is seen that the ECAPed specimen exhibits the highest R_{ct} values among all the different samples, with values above $1 \text{ k}\Omega \cdot \text{cm}^2$ during the entire immersion time,

which are over one order of magnitude higher than the corresponding R_{ct} values for the homogenized sample ($\sim 120 \Omega \cdot \text{cm}^2$). This remarkable improvement in the corrosion resistance of the ECAPed alloy suggests that the microstructural changes induced by ECAP processing characterized by a refined grain structure with the presence of well-distributed $\beta\text{-Mg}_{17}\text{Al}_{12}$ precipitates are beneficial in decreasing the dissolution rate of the magnesium alloy. Furthermore, it is also noticed that the R_{ct} values for the ECAPed specimen slightly decrease during the first three days of immersion owing to development of charge transfer processes occurring at the metal/electrolyte interface, followed by a subsequent increase after 4 days of immersion that persist until the end of the exposure period. This behavior indicates the formation and growth of corrosion products on the magnesium surface that provide extra protection against migration of aggressive species towards the Mg surface, thereby increasing the resistance to charge transfer processes upon prolonged immersion. The ECAP-aged alloy exhibits lower R_{ct} values as compared to the ECAPed specimen ($\sim 600 \Omega \cdot \text{cm}^2$), suggesting that the increase in grain size and coarsening of the $\beta\text{-Mg}_{17}\text{Al}_{12}$ precipitates that result after post-aging treatment of the ECAPed alloy leads to higher corrosion reaction activity of the magnesium alloy. In terms of evolution, the R_{ct} values of the ECAP-aged alloy also exhibit a very small decrease during early immersion time as observed for the ECAPed alloy, however unlike the ECAPed alloy, there is not a notorious increase in R_{ct} over time, indicating that the corrosion products formed on the ECAP-aged alloy during the immersion test are slightly less protective than the ones formed on the ECAPed specimen. This observed progression suggests that the rates of dissolution of corrosion

products and active anodic dissolution of the magnesium alloy is comparable to the rate of formation and growth of corrosion products, leading to a relatively steady state condition where the R_{ct} values remain almost constant at longer immersion times. A different trend in R_{ct} is observed for the heat-treated alloys; it is seen that the R_{ct} values for the heat-treated alloys gradually decrease over time, this is likely related to the formation of loose and porous corrosion products that are unable to provide protection against aggressive species resulting in continuous dissolution of the magnesium alloy. These corrosion products formed on the homogenized sample could either dissolve (or fall) into the electrolyte exposing the bare magnesium alloy to further corrosion attack, or due to its porous nature, aggressive species could penetrate through the micro-pores of the layer of corrosion products reaching the Mg surface and inducing persistent active anodic dissolution of the magnesium alloy for the entire immersion time. The homogenized alloy exhibits the lowest R_{ct} among all different Mg alloys, this behavior is consistent with the potentiodynamic polarization measurements, in which the homogenized alloy shows the most negative corrosion potential and the highest corrosion current density, implying that the β -Mg₁₇Al₁₂ phase increases the corrosion resistance of the AZ91 alloys under study. It is well-known that the β -Mg₁₇Al₁₂ phase can induce micro-galvanic corrosion resulting in preferential dissolution of the α -Mg matrix, however based on the results reported herein, it seems that the rate of micro-galvanic corrosion induced by this secondary phase is lower than the dissolution rate in the homogenized alloy. In addition, it is also known that the β -Mg₁₇Al₁₂ phase can act as

an electrochemical barrier that retards the corrosion propagation in the magnesium matrix.

The double layer capacitance (CPE_{dl}) for the different Mg alloys is presented in Figure 22(b); this parameter is related to the distribution of ionic charges at the Mg surface/electrolyte interface and is proportional to the active area for electrochemical reactions [109]. The evolution of CPE_{dl} is in good agreement with the R_{ct} trend for the different magnesium alloys. As seen from Figure 22(b), the ECAPed specimens, both ECAPed and ECAP-aged alloys, exhibit lower values of double layer capacitances as compared to the heat-treated alloys, which is mainly attributed to the formation of a more compact and protective oxide film at the metal/electrolyte interface that reduces the active area available for charge transfer processes. Additionally, it is also noticed that CPE_{dl} of the ECAPed specimen slightly increases during the first few days of immersion as a result of charge transfer processes, in which pit formation at local active sites increases the active area for further localized attack. However, upon prolonged immersion, the CPE_{dl} values of the ECAPed specimen decrease and then remain almost unchanged until the end of the exposure period, which indicates that the corrosion products formed on this alloy reduces the active area for electrochemical reactions, thereby providing a barrier protection to prevent continuous dissolution at longer immersion times. The ECAP-aged alloy exhibits CPE_{dl} values that are slightly higher than the corresponding values for the ECAPed alloy, this trend indicates that there is a higher active area for charge transfer in the ECAP-aged alloy, likely due to the formation of corrosion products that are less protective (e.g., more porous or less coherent to the

metal surface) than the ECAPed alloy. In addition, CPE_{dl} values for the ECAP-aged alloy are relatively constant instead of decreasing at longer immersion time as in the case for the ECAPed alloy, which can be attributed to a balance between formation and dissolution of corrosion products that lead to an almost constant surface area for electrochemical reactions. Contrary to the trend observed for the ECAP-processed alloys, the CPE_{dl} values for the heat-treated alloys continuously increase as progressing the immersion time, which can be related to severe corrosion that exposed a larger surface area for further corrosion attack and formation of non-protective corrosion products that are unable to decelerate the anodic dissolution process, thereby allowing for continuous degradation of the heat-treated alloys as progressing the exposure time. Furthermore, it is seen that the homogenized sample exhibits the highest CPE_{dl} values, suggesting that this alloy provided the highest surface area for activation of corrosion processes.

Figure 22(c) shows the reciprocal of the polarization resistance ($1/R_p$) as function of immersion time for the different AZ91 alloys. As mentioned above, $1/R_p$ is proportional to the corrosion rate. The evolution of $1/R_p$ is in agreement with the R_{ct} and CPE_{dl} trends observed in Figure 22(a) and (b), in which the ECAPed alloy exhibits the lowest corrosion rate during the entire immersion time followed by the ECAP-aged alloy and the heat-treated alloys.

3.3.4 Hydrogen Evolution

Figure 23 shows the hydrogen evolution of the different AZ91 alloys immersed in 3.5 wt.% NaCl solution for 7 days. As seen from Figure 23(a), the volume of hydrogen evolution of the ECAPed specimens is significantly lower than that of the heat-treated samples. The ECAPed alloy exhibits the lowest hydrogen evolution followed by the ECAP-aged alloy and the heat-treated alloys, in which the homogenized sample shows the highest evolution of hydrogen among all samples. These observations are in agreement with the EIS results presented above. The corrosion rate (P_H) was calculated from the hydrogen evolution results using equation 11. As seen from the P_H results in Figure 23(b), the corrosion rates of the ECAPed specimens are lower than those of the heat-treated alloys throughout the entire test period. In addition, the P_H values of the ECAPed specimens remain almost constant, whereas the ones for the heat-treated alloys increase as increasing the time for immersion. This evolution of P_H for the different alloys is similar to the trend observed for the reciprocal of the polarization resistance ($1/R_p$) calculated from the EIS data (Figure 22(c)). The pH evolution during the hydrogen evolution test was also recorded and the results are shown in Figure 23(c). It is seen that the initial pH was about 6.8 and then it rapidly increases to more alkaline values after the first 12 h of immersion. Upon further immersion, the pH for all the different AZ91 alloys remain almost constant up to the end of the period test. Comparing the different samples, it is noticed that the electrolyte pH values in the ECAPed specimens are lower (~9 for the ECAP alloy and 9.3 for the ECAP-aged alloy) than the

ones in the heat-treated alloys (~10 for the peak-aged alloy and ~10.3 for the homogenized alloy).

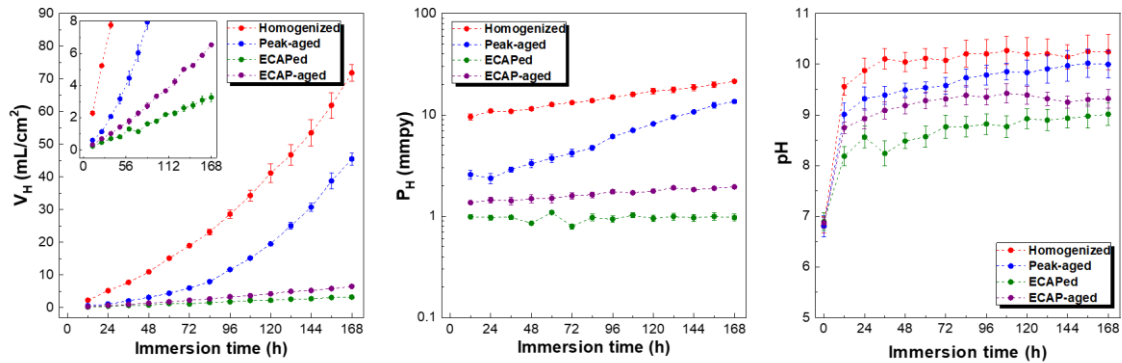


Figure 23. (a) Volume of hydrogen evolution (b) corrosion rate calculated from hydrogen evolution measurements and (c) pH evolution of the AZ91 samples immersed in 3.5 wt.% NaCl solution for 7 days.

SEM micrographs of the heat-treated specimens after hydrogen evolution testing for 7 days in 3.5 wt.% NaCl solution before and after removal of corrosion products are shown in Figure 24. The corrosion products of the homogenized and peak-aged alloys shown in Figures 24(a) and (d), respectively, exhibit a similar morphology characterized by a thick but highly porous and loose structure that covered the entire Mg substrate. From the high magnification micrographs inserted in Figure 24(a) and (d), it is seen that the majority of these corrosion products exhibit a rosette-like morphology that formed clusters resulting in a highly porous structure. The EDS analysis of these flower-like clusters (as marked by red crosses on Figure 24(a) and (d) show that Mg and O elements are the predominant constituent elements in these corrosion products, suggesting the

formation of magnesium oxide/hydroxide. A rosette-like morphology of magnesium hydroxide (brucite) has been widely reported for Mg alloys exposed to chloride-containing media [110, 111]. According to the loosely adherent appearance and porous morphology of these corrosion products, it can be deduced that they are unable to provide an effective protection to the heat-treated alloys, which is in agreement with the electrochemical methods and hydrogen evolution testing where a continuous anodic dissolution and a gradual increase in the corrosion rate is observed as progressing the immersion time. Figure 24(c) and (f) show the corroded morphologies of the heat-treated alloys after removal of the corrosion products. After 7 days of immersion, the homogenized alloy exhibits a highly corroded surface where the corrosion attack was widely spread on almost the entire exposed area (Figure 24(c)). In contrast, the corrosion attack on the peak-aged alloy after 7 days of immersion appears highly localized. As seen in Figure 24(f), the corrosion in the peak-aged alloy is mainly concentrated at the interior of the α -Mg grains with the discontinuous β -Mg₁₇Al₁₂ phase formed at the grain boundaries acting as a barrier for corrosion propagation. It is worth to notice that even though several areas of the peak-aged alloy are not corroded after 7 days of immersion, the depth of the corroded areas is significantly large, even greater than the penetration depth observed in the homogenized alloy. This behavior suggests that the anodic dissolution rate of the α -Mg phase can be accelerated by the β -Mg₁₇Al₁₂ phase through micro-galvanic coupling between these phases that leads to preferential dissolution of the α -Mg phase.

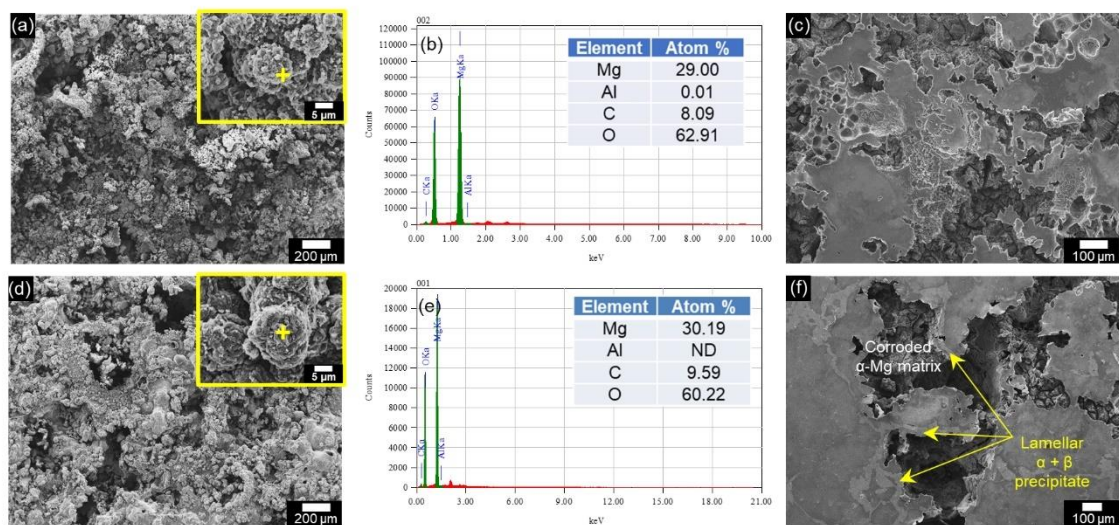


Figure 24. Corrosion morphologies of the heat-treated alloys after hydrogen evolution test for 7 days in 3.5 wt.% NaCl solution: homogenized alloy with (a) and without (c) corrosion products, peak-aged alloy with (d) and without (f) corrosion products. EDS analysis of the corrosion products in (b) homogenized alloy and (e) peak-aged alloy.

Figure 25 discloses SEM micrographs of ECAP alloys after hydrogen evolution test in 3.5 wt.% NaCl for 7 days. The corrosion products shown on Figure 25(a) and (d) for the ECAPed and ECAP-aged specimens covered the entire Mg substrate after 7 days of immersion in the saline solution. Unlike the corrosion products formed on the heat-treated alloys, the corrosion products formed on the ECAPed specimens exhibit a more dense and adherent appearance that can serve as a more protective film resulting in lower corrosion susceptibility as observed from the electrochemical methods and hydrogen evolution test. The high magnification micrographs inserted in Figure 25(a) and (d) show the higher compactness and smooth morphology of the corrosion products formed on the ECAPed specimens as compared to those formed on the heat treated-alloys. Some micro-cracks are also observed showing a dry clay-like pattern, which are

mainly formed from shrinkage of the layer of corrosion products due to dehydration during sample preparation for SEM examination [24]. The EDS analysis of the corrosion products formed on the ECAPed specimens (marked as red crosses on Figure 25(a) and (d)) show the presence of Mg, Al, C, and O as primary elements, suggesting the formation of carbonate and/or hydroxy carbonate compounds in addition to the magnesium hydroxide film. It has been reported that these carbonate-containing corrosion products provide higher protection against aggressive species than brucite by acting as a more effective barrier layer that blocks active sites on the Mg surface [112]. After removal of the corrosion products, it is seen from Figure 24 (c) and (f) that the surface appearance of the ECAP processed alloys exhibit a more uniform corrosion morphology that do not penetrate deeply into the alloy. By comparing the two ECAP specimens, it is noticed that the ECAP-aged alloy exhibits a more severe corrosion damage than the ECAPed alloy with a more localized attack and a slightly higher penetration depth.

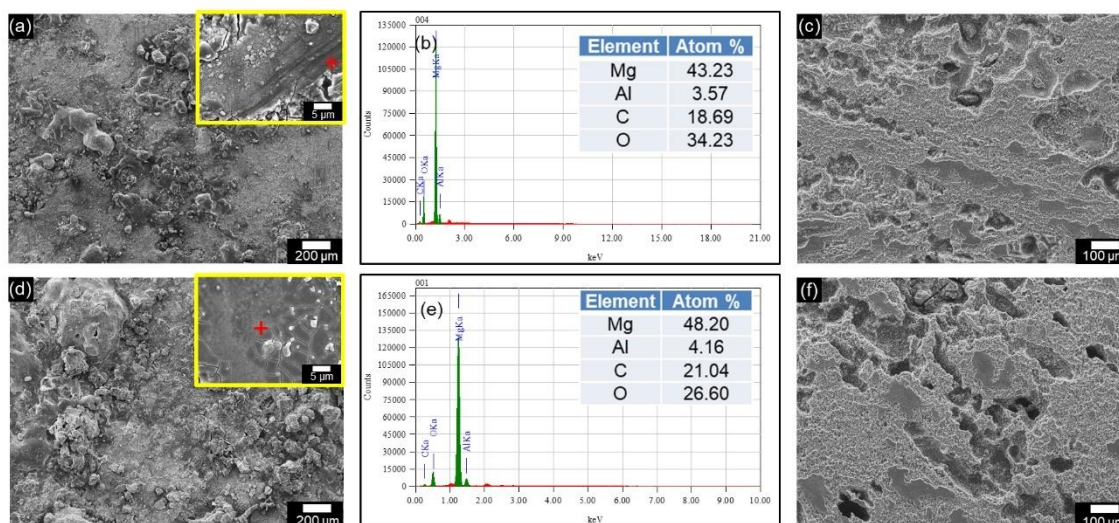


Figure 25. Corrosion morphologies of the ECAP processed AZ91 Mg alloys after hydrogen evolution test for 7 days in 3.5 wt.% NaCl solution: ECAPed alloy with (a) and without (c) corrosion products, ECAP-aged alloy with (d) and without (f) corrosion products. EDS analysis of the corrosion products in (b) ECAP alloy and (e) ECAP-aged alloy.

Figure 26 shows the XRD patterns of the corrosion products collected from the electrolyte solutions used for the different AZ91 alloys after the hydrogen evolution test for 7 days. As seen from the appearance of these corrosion products, it is noticed that the corrosion products formed on the heat-treated alloys are white, whereas the ones formed on the ECAPed specimens are more grayish. In addition, it is also seen that a significantly larger amount of corrosion products was collected from the electrolyte used for the heat-treated samples as compared to the amount collected from the solution used in the ECAPed specimens. These observations confirm the loosely nature of the corrosion products formed on the heat-treated alloys, such that, most of them fall off into the electrolyte exposing the metal substrate to further corrosion attack. The XRD analysis shows that the corrosion products formed on the AZ91 alloys exposed for 7

days to the chloride media are mainly composed of an aluminum magnesium hydroxide carbonate $((\text{Mg}_{0.833}\text{Al}_{0.167})(\text{OH})_2(\text{CO}_3)_{0.083} \cdot 0.75\text{H}_2\text{O})$, hydrotalcite-like compound), a hydrated magnesium carbonate hydroxide $(\text{Mg}_5(\text{CO}_3)_4(\text{OH})_2 \cdot 5\text{H}_2\text{O})$, also known as dypingite), and magnesium hydroxide $(\text{Mg}(\text{OH})_2)$, brucite). The presence of carbonate species on the corrosion products has been widely reported in Mg-Al alloys exposed to chloride containing environments that are formed due to the dissolution of atmospheric CO_2 on the electrolyte solution during the immersion test [101, 113, 114].

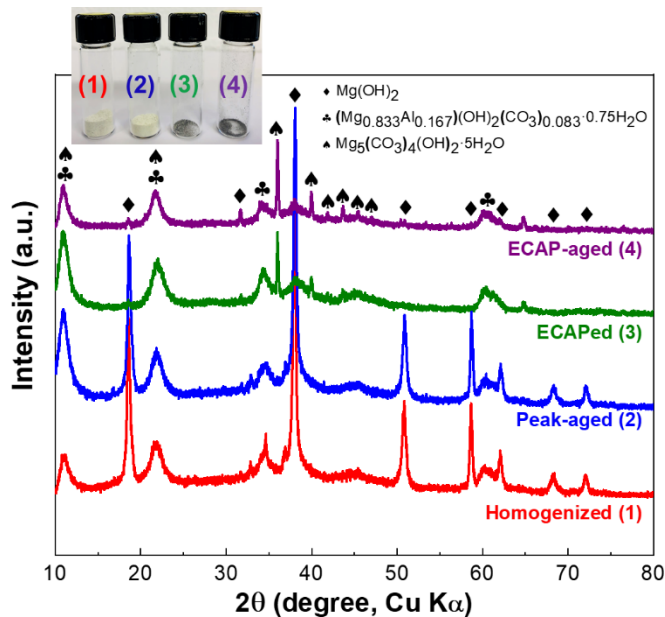


Figure 26. XRD patterns of the corrosion products formed on the AZ91 alloys after hydrogen evolution test for 7 days in 3.5 wt.% NaCl solution.

From the peak intensity of the different components, it is seen that the corrosion products formed on the heat-treated alloys are mainly composed of brucite, whereas the corrosion products formed on the ECAPed specimens consist mainly of the carbonate-

containing species. Liao et al. [114] found that the dark gray surface film formed on a AZ31 Mg alloys exposed to marine and urban environments was mainly composed of aluminum magnesium hydroxide carbonate $((\text{Mg}_{0.833}\text{Al}_{0.167})(\text{OH})_2(\text{CO}_3)_{0.083} \cdot 0.75\text{H}_2\text{O})$, this is in agreement with the color appearance of the corrosion products formed on the ECAPed specimens. It has been reported that magnesium hydroxide surface films do not provide an effective protection against aggressive species due to their high porosity, which allows for a continuous corrosion attack of the Mg substrate as progressing the immersion time [101, 111, 112]. Thus, it can be speculated that formation and growth of a $\text{Mg}(\text{OH})_2$ layer does not play a significant role on slowing down the corrosion rate of Mg alloys immersed in saline solutions. In contrast, the aluminum and/or magnesium carbonates surface films exhibit a more protective ability that reduces the corrosion susceptibility of Mg alloys in chloride-containing media [112, 114]. According to this, it can be suggested that the higher corrosion resistance of the ECAPed specimens can be associated with the presence of a more protective surface film that can slow down the anodic dissolution process by physically blocking the active sites on the metal surface [111]. In addition, it has been also reported that these carbonate-containing corrosion products are non-conductive and therefore, they cannot serve as effective cathodes with results in a lower cathodic reaction kinetics [112]. This indicates that the product layer formed on the ECAPed substrates can simultaneously reduce the rates of anodic and cathodic reactions resulting in a better protection effect as compared to the less protective brucite layer found on the heat-treated alloys.

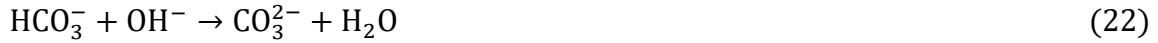
The formation of these corrosion products can occur by the reactions presented below. Upon immersion in chloride-containing solutions, Mg-Al alloys undergo anodic dissolution of magnesium and aluminum to produce Mg^{2+} and Al^{3+} ions, respectively (reaction 16 and 17), which takes place in the presence of hydrogen evolution reaction that produces hydrogen gas and OH^{-} ions (reaction 18):



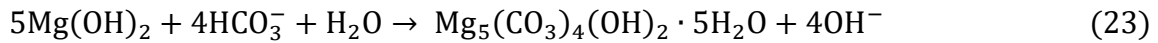
The Mg^{2+} and OH^{-} ions produced from the anodic and cathodic reactions can further undergo a chemical reaction to produce $Mg(OH)_2$ (reaction 19):



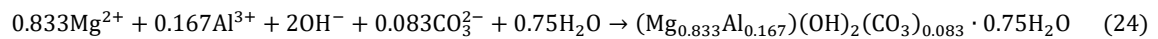
The release of OH^{-} ions into the chloride solution results in a pH increase. The final pH will depend on the corrosion rate and the rate of removal of OH^{-} ions from the metal surface into the bulk of the electrolyte by diffusion or convection. Feliu et al. [111] reported that high corrosion rates result in pH values between 10.5 and 11, whereas lower corrosion rates lead to pH values less than 10.5. According to this and based on the pH results shown in Figure 23(c), it can be speculated that the corrosion rates of the heat-treated alloys is expected to be higher than the ones of the ECAPed specimens, which is in accordance with the electrochemical measurements and the hydrogen evolution test. During the hydrogen evolution test, ambient CO_2 can dissolve in the electrolyte solution forming carbonic acid that subsequently dissociates into HCO_3^{-} and CO_3^{2-} ions in the electrolyte according to equations (20-22) [112]:



Then, magnesium hydroxide can react with HCO_3^- ions to form magnesium hydroxy carbonate according to reaction 23 [112]:



In addition, the formation of $(\text{Mg}_{0.833}\text{Al}_{0.167})(\text{OH})_2(\text{CO}_3)_{0.083} \cdot 0.75\text{H}_2\text{O}$ can be expressed as follows [114]:



As mentioned above, these carbonate-containing surface films are more protective than the magnesium hydroxide layer due to their ability to slow down the chloride-induced corrosion process by blocking active sites and limiting the rate of cathodic reactions. Feliu et al. [111] also reported that these carbonate-containing products are more stable (less soluble) in pH values from 9 to 10 whereas magnesium hydroxide becomes more stable at higher pH values (>10). According to these observations and the pH values reported in Figure 23(c), the lower pH values observed in the ECAPed specimens can lead to the preferential formation of carbonate type compounds, whereas the higher pH values observed for the heat-treated alloys promoted the formation of magnesium hydroxide. These findings are in agreement with the XRD patterns where the corrosion products formed on the ECAPed specimens were mainly composed of carbonate-containing compounds, while the corrosion products formed on

the surface of the heat-treated alloys consist primarily of a layer of magnesium hydroxide.

3.3.5 Weight Loss Measurements

Weight loss measurements were also performed to further confirm the results obtained from the electrochemical measurements and the hydrogen evolution test. The weight loss results of the different AZ91 alloys after 1, 3, 5, and 7 days of immersion in 3.5 wt.% NaCl solution are depicted in Figure 27(a). The results in Figure 27(a) clearly indicate the superior corrosion resistance of the ECAP-processed alloys as compared to the heat-treated alloys. It is seen that the weight loss of the heat-treated samples drastically increases over time, with acceleration of corrosion at long-immersion time (5 and 7 days), whereas a slightly increase in the weight loss values is observed for the ECAPed specimens. Corrosion rate was calculated from the weight loss measurements (P_w) using equation (12) and the results are shown in Figure 27(b). The ECAPed specimen exhibits the lowest corrosion rate among all the different alloys at any immersion time followed by the ECAP-aged alloy and the heat-treated alloys. As seen from the evolution of the corrosion rate, the corrosion rates of the ECAPed specimens remain relatively constant with immersion time, whereas there is a gradual increase in the corrosion rate of the heat-treated alloys as increasing the time of immersion. These trends observed from the weight loss measurements correspond well with the corrosion rate evolution calculated from the hydrogen evolution measurements reported in Figure 23(b). Figure 27(c) shows the corrosion rates, P_H and P_w , for the different AZ91 alloys after immersion for 7 days in 3.5 wt.% solution. As seen from Figure 27(c), the

corrosion rates calculated from hydrogen evolution and weight loss measurements are relatively consistent between each other, with the P_W values being slightly higher than the P_H values. The higher corrosion rates obtained from weight loss measurements can be related to the pickling treatment used to remove corrosion products, it is likely that metallic Mg that was not corroded during the immersion test was removed during the cleaning process. Furthermore, the lower corrosion rates obtained from the hydrogen evolution measurements can be associated with hydrogen that was dissolved into the electrolyte solution and therefore, was not quantified in the reading measurements. After 7 days of immersion in the chloride-containing solution, the corrosion rates of the different alloys can be rank as Homogenized > Peak-aged > ECAP-aged > ECAPed showing values of ~ 25, 14, 2.3, and 1.5 mmpy, respectively. Based on these results, it is seen that the ECAPed alloy exhibits the lowest corrosion rate, which is more than 16 times lower than the homogenized alloy. These results confirmed that the ECAPed specimens are significantly more corrosion resistant than the heat-treated alloys when immersed in chloride-containing media.

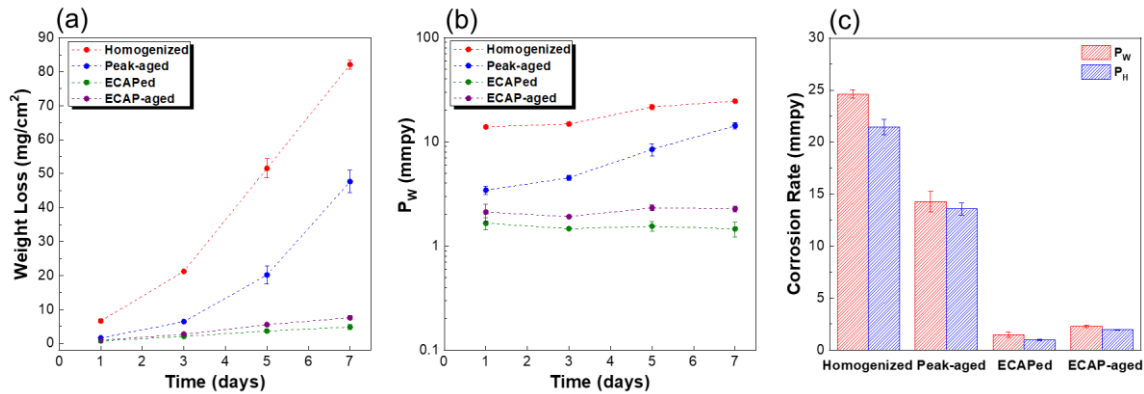


Figure 27. (a) Weight loss measurements of the AZ91 alloys after immersion for 1, 3, 5, and 7 days in 3.5 wt.% NaCl solution, (b) corrosion rate (P_w) calculated from the weight loss measurements, (c) comparison between P_H and P_w after immersion for 7 days in 3.5 wt.% NaCl solution.

The macroscopic surface appearance of the AZ91 alloys immersed for 1, 3, 5, and 7 days in 3.5 wt.% NaCl solution (after removal of the corrosion products) is shown in Figure 28. Severe corrosion is observed in the heat-treated alloys particularly after 5 days of immersion, which is in agreement with the weight loss measurements, where corrosion rate seems to be accelerated after 5 days of immersion. The homogenized alloy exhibits the most severe corrosion attack that spread over the entire surface and result in a significant loss of material after 5 days of immersion. The peak-aged alloy also exhibits a severe attack; however, corrosion seems more localized as compared to the homogenized alloy and even after 7 days of immersion there are still some regions that are uncorroded. Nevertheless, the serious localized corrosion of the peak-aged alloy also led to a significant loss of material, particularly after 5 days of immersion. From Figure 28, it is evident the improvement in the corrosion resistance of the AZ91 alloys after ECAP processing. No substantial loss of material is observed on the ECAP samples as

compared to the heat-treated alloys and the corrosion propagation seems to be more uniform with a shallow penetration depth.

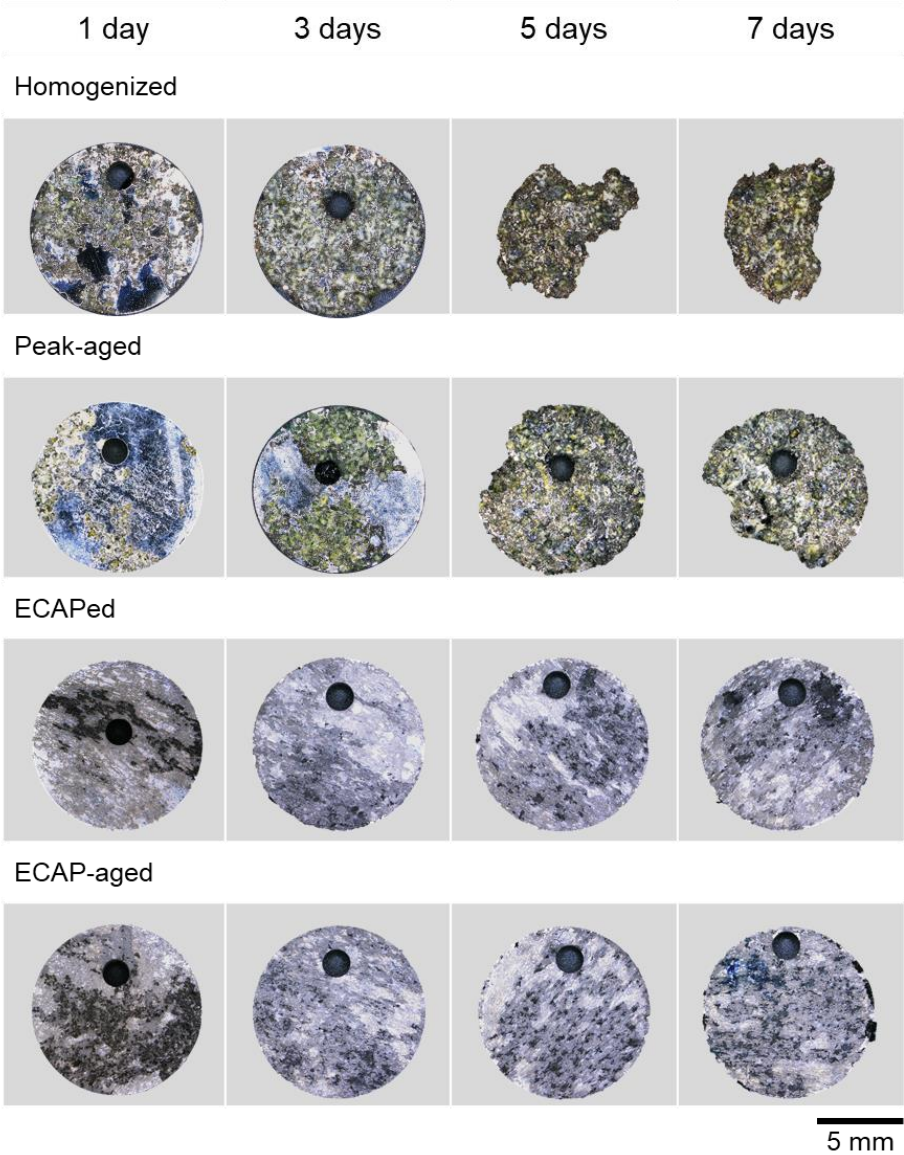


Figure 28. Surface appearance of the AZ91 alloys after immersion for 1, 3, 5, and 7 days in 3.5 wt.% NaCl solution.

To further examine the morphology of the corroded alloys after the immersion test, SEM micrographs of the AZ91 alloys after 1 day of immersion in 3.5 wt.% NaCl solution are shown in Figure 29. Even after only 1 day of immersion, the homogenized alloy exhibits a severe corrosion attack, as shown in Figure 29(a). Large corrosion pits are randomly formed in almost the entire surface. This localized corrosion can be related to the breakdown of the native air-formed oxide film by chloride ions and the initiation of pitting corrosion. As it was mentioned above, the anodic dissolution of Mg takes place in the presence of hydrogen evolution that leads to local increase in pH, this local alkalization slows down the dissolution rate at the active sites, promoting the development of new anodic sites. This mechanism explains the widespread corrosion observed in the homogenized alloy, in which pits will tend to spread laterally with increasing the immersion time, resulting in coalesce of pits and severe uniform corrosion with high dissolution rate. A closer view of the corroded surface also shows the formation of trenches in the α -Mg phase surrounding an Al_8Mn_5 intermetallic particle. This formation of trenches in the vicinity of Al_8Mn_5 intermetallic particles suggests that there is a micro-galvanic coupling between these particles and the adjacent α -Mg matrix that leads to preferential dissolution of the more anodic α -Mg phase [115, 116]. This micro-galvanic coupling can lead to undermining of the Al_8Mn_5 intermetallic particles that eventually will detached from the alloy, resulting in the development of corrosion pits that will spread out over the entire surface and will also contribute to the severe corrosion observed in this alloy [117].

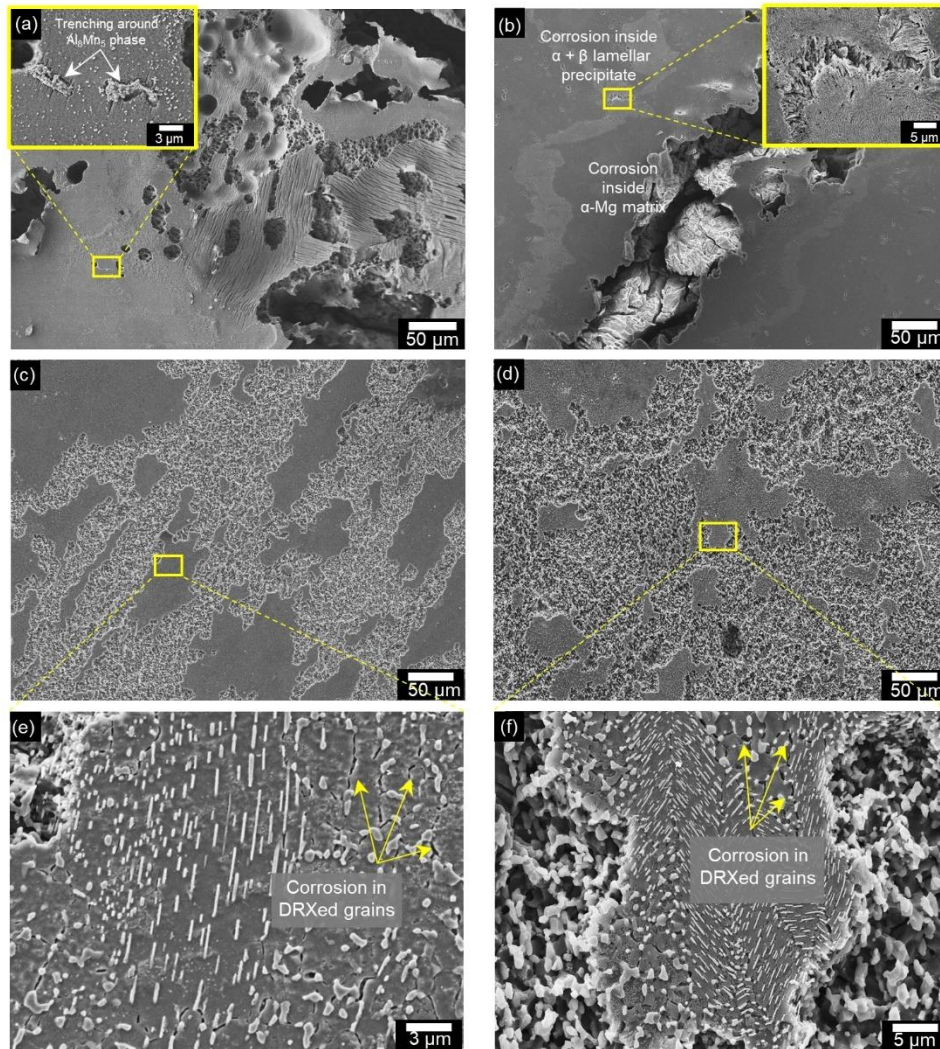


Figure 29. SEM micrographs of (a) homogenized alloy, (b) peak-aged alloy, (c, e) ECAPed alloy and (d, f) ECAP-aged alloy after immersion for one day in 3.5 wt.% NaCl solution.

Figure 29(b) shows the corroded surface of the peak-aged alloy after immersion for 1 day in the 3.5 wt.% NaCl solution. As seen from the SEM micrograph, corrosion is mainly concentrated at the interior of the α -Mg grains with the β -Mg₁₇Al₁₂ phase acting as a kinetic barrier that retards corrosion propagation through α -Mg grains. It is interesting to notice that micro-galvanic corrosion at the interface between the β -

$\text{Mg}_{17}\text{Al}_{12}$ phase and the adjacent α -Mg phase is not observed as previously reported by other studies [5, 118, 119]. This behavior can be attributed to a heterogeneous distribution of aluminum in the α -Mg grains as will be explained in chapter IV where the aluminum content in the grain interior is comparatively less compared to the one in the α -Mg phase at the vicinity of the β - $\text{Mg}_{17}\text{Al}_{12}$ phase. In that sense, the aluminum-depleted α -Mg phase at the interior of the grains is more anodically active than the aluminum-enriched α -Mg phase adjacent to the β - $\text{Mg}_{17}\text{Al}_{12}$ phase, resulting in the preferential dissolution of the primary α -Mg matrix that predominates over the micro-galvanic coupling at the β - $\text{Mg}_{17}\text{Al}_{12}$ phase/ α -Mg phase interface. The relatively higher aluminum content in the α -Mg phase adjacent to the β - $\text{Mg}_{17}\text{Al}_{12}$ phase reduces the driving force for micro-galvanic corrosion and explains why trenching or undermining of the β - $\text{Mg}_{17}\text{Al}_{12}$ phase is not observed. It is suggested that the anodic dissolution at the interior of the α -Mg grains occurs with hydrogen evolution taking place either at the β - $\text{Mg}_{17}\text{Al}_{12}$ phase or in the aluminum-enriched α -Mg phase. It is also likely that micro-galvanic corrosion between Al_8Mn_5 intermetallic particles and their adjacent α -Mg phase occurs, similar as in the homogenized alloy, accelerating the corrosion process of the α -Mg grains. Lunder et al. [120] reported that the superior corrosion resistant of the β - $\text{Mg}_{17}\text{Al}_{12}$ phase and its role as a barrier for corrosion propagation can be attributed to the high stability of this phase (i.e., passive behavior) in a wide pH range (4-14) that combines the passive properties of magnesium in alkaline solutions with the high resistance of aluminum in neutral solutions [120]. In addition, they also reported that the β - $\text{Mg}_{17}\text{Al}_{12}$ phase leads to the formation of a product layer that consists of magnesium and aluminum, which is

more stable than the layer formed on the α -Mg phase [120]. The preferential corrosion at the interior of the α -Mg grains and the barrier effect of the β -Mg₁₇Al₁₂ phase that prevent corrosion propagation from one α -Mg grain into another directly across the β -Mg₁₇Al₁₂ phase, will eventually lead to a corroded morphology characterized by a cellular structure of dissolved α -Mg phase with a network of undissolved β -Mg₁₇Al₁₂ phase as seen in Figure 24(f). The lateral limitation in the corrosion propagation can lead to corrosion progression deep into the α -Mg phase resulting sometimes in higher pit depths as compared to the homogenized alloy. Thus, it can be concluded that the β -Mg₁₇Al₁₂ phase in the peak aged alloy exhibited two opposite effects: 1) reduce the corroding surface area by acting as a barrier for corrosion propagation and 2) induce a more concentrated and severe corrosion on the α -Mg matrix [121]. This explains the more serious localized corrosion with a higher pit penetration depth of the peak-aged alloy as compared to the homogenized alloy. Despite the barrier effect provide by the β -Mg₁₇Al₁₂ phase in the peak-aged alloy, it was surprisingly found that some regions at the interior of the β -Mg₁₇Al₁₂ phase are preferentially corroded with no evidence of corrosion taking place in the α -Mg phase surrounding the precipitate. This anomalous behavior will be explored further in chapter IV.

Figures 29(c-f) show the morphology of the ECAP processed alloys after one day of immersion in 3.5 wt.% NaCl solution. The corroded morphologies of these alloys are relatively similar exhibiting a widespread corrosion with a significantly less penetration depth as compared to the heat-treated alloys. It is interesting to notice that the uncorroded regions of the ECAPed specimens seem to be elongated in the direction of

the shear deformation similar as the elongated unDRXed coarse grains seen in Figure 13(b). By taking a closer examination at these uncorroded areas (Figure 29(e) and (f)), it is seen that corrosion preferentially occurs in the DRXed fine grains whereas the unDRXed coarse grains seems to be less attacked. This preferential corrosion of the fine grains explains the elongated uncorroded patches observed on the surface of the ECAPed specimens taking the shape of the coarse grains that appeared to be more corrosion resistant to the chloride-containing solution. It is also worth noticing, that unlike the peak-aged alloy where corrosion preferentially initiated at the interior of the α -Mg grain, in the ECAPed alloy, corrosion is taking place at the grain boundaries of the DRXed fine grains. This intergranular corrosion suggests micro-galvanic coupling between the β -Mg₁₇Al₁₂ precipitates at the grain boundaries and the adjacent α -Mg matrix leading to preferential dissolution of the α -Mg phase and undermining of the β -Mg₁₇Al₁₂ precipitates that will eventually fall off from the alloy. This means that the β -Mg₁₇Al₁₂ phase acts as an effective galvanic cathode due to the discontinuous distribution of this phase along the grain boundaries that is unable to provide a barrier for corrosion propagation and instead it accelerated the anodic dissolution of the adjacent α -Mg phase [16]. Although the micro-galvanic corrosion in the ECAPed specimens seems to be more predominant than in the peak-aged alloy, it is worth to notice that the β -Mg₁₇Al₁₂ precipitates in the ECAPed alloys are relatively fine and well-distributed along the grain boundaries, this can lead to a significantly lower galvanic activity as compared to alloys with coarse precipitates [24]. In addition, the undermining of these fine β -Mg₁₇Al₁₂ precipitates leads to shallow pits that will spread over the

DRXed grains resulting in a more uniform corrosion morphology with a relatively small penetration depth [16]. Thus, it is suggested that the higher corrosion resistance observed for the ECAPed specimens as compared to the heat-treated alloys can be also attributed to the presence of uniformly distributed fine β -Mg₁₇Al₁₂ precipitates along the grain boundaries of the DRXed grains that can lead to a low intensity of micro-galvanic corrosion and the development of a more uniform and shallow corrosion morphology. According to this, the lower corrosion resistance of the ECAP-aged alloy can be related to the coarsening of β -Mg₁₇Al₁₂ precipitates after the post-aging treatment that can lead to deeper corrosion pits with a higher active exposed area for further corrosion attack. Details about the preferential corrosion of the DRXed grains and the development of intergranular corrosion in the refined equiaxed grains will be further explored in chapter V.

Figure 30 shows high resolution 3D images and roughness profiles of the corroded AZ91 alloys (after removal of corrosion products) immersed for one day in the 3.5 wt.% NaCl solution. It is clearly seen that the average roughness and the maximum pit depth of the ECAPed alloys is significantly small compared to the one for the heat-treated alloys, which demonstrates the lower dissolution rate of the ECAPed alloys in chloride-containing media. As seen from Figure 30(a), the homogenized alloy exhibits a severe corrosion that spreads almost on the entire area, these corroded areas show a relatively uniform roughness only with few areas having a deeper corrosion attack with a maximum pit depth of ~260 μ m. On the contrary, corrosion of the peak-aged alloy is highly localized at the interior of few α -Mg grains and is confined by the β -Mg₁₇Al₁₂

phase (Figure 30(b)). Although the fraction of corroded area in the peak-aged alloy is significantly lower than in the homogenized alloy, deeper pits are observed on the peak-aged alloys having values of $\sim 360 \mu\text{m}$. These results confirm that the $\beta\text{-Mg}_{17}\text{Al}_{12}$ phase acts as an electrochemical barrier that retarded the corrosion propagation through $\alpha\text{-Mg}$ grains, however, it accelerates the corrosion deeper into the $\alpha\text{-Mg}$ grains. The ECAPed processed alloys, particularly the ECAPed alloy exhibits a more uniform corrosion with a mild average roughness of $\sim 11 \mu\text{m}$ and with the deeper pits reaching values less than $80 \mu\text{m}$ (Figure 30(c)). Finally, the ECAP-aged alloy also exhibits a relatively uniform corrosion but with deeper pits as compared to the ECAP alloy with values higher than $130 \mu\text{m}$. This behavior also confirms that the detrimental effect of the post-aging treatment after ECAP processing can be related to the coarsening of the $\beta\text{-Mg}_{17}\text{Al}_{12}$ phase that can lead to deeper pits and therefore, a higher roughness for further corrosion attack.

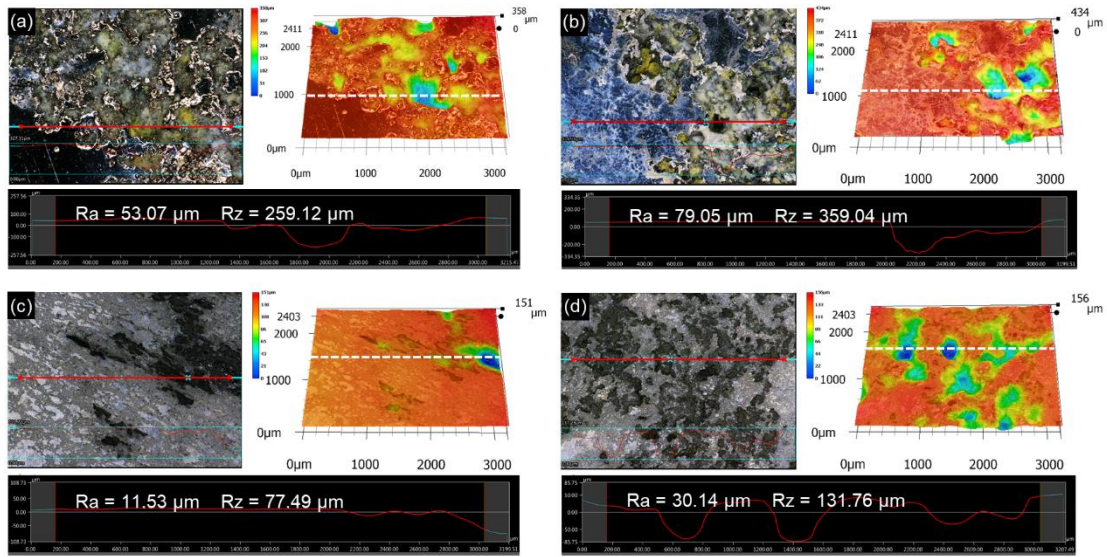


Figure 30. Topography images and roughness profiles of (a) homogenized alloy, (b) peak-aged alloy, (c) ECAPed alloy, and (d) ECAP-aged alloy after one day of immersion in 3.5 wt.% NaCl solution.

Figure 31 summarizes the R_a and R_z values for the different AZ91 alloys exposed for 1, 3, 5, and 7 days of immersion in the 3.5 wt.% NaCl solution. It is seen that the homogenized alloy exhibits the highest average roughness values among all the different alloy with R_a and R_z values that rapidly increase over time due to the continuous dissolution of the alloy. It is worth to notice that even though this alloy shows the more severe corrosion attack, corrosion is spread and it covers almost the entire surface, this can be demonstrated by the error bars on the R_a and R_z plots that are relatively small, these error bars resulted from different horizontal line profiles (parallel to the one shown in Figure 30) taken at random positions along the corroded surface. Thus, the relatively small variability of R_a and R_z confirms that corrosion is relatively uniform but with a high dissolution rate that lead to large roughness values. The peak-aged alloy exhibits R_a

values that are relatively smaller than the R_a values of the homogenized alloy, however, it is clearly noticed that the errors bars on the R_a values of the peak-aged alloy are significantly larger than those obtained for the homogenized alloy. These results demonstrate the serious localized corrosion observed on the peak-aged alloy where corrosion was confined at the interior of the α -Mg matrix and propagate deeper into the grains. Furthermore, it is also seen that the R_z values of the peak-aged alloy were higher than the ones of the homogenized alloy, which indicates that deeper pits were developed on the former alloy. These results confirm that the β -Mg₁₇Al₁₂ phase although, it provides a barrier for corrosion propagation, it can also accelerate the corrosion of the α -Mg matrix. The ECAPed alloy exhibits the lowest R_a and R_z values at any immersion time that increased slowly as progressing the time of immersion, which confirms the lowest dissolution rate of this alloy among all the different tested alloys. In addition, the errors bars for both, the R_a and R_z , are quite small, which also suggest that corrosion was uniformly distributed over the entire surface. The higher R_a and R_z values observed for the ECAP-aged alloy as compared to the ECAPed alloy can be attributed to the coarsening of the β -Mg₁₇Al₁₂ precipitates along the grain boundaries that lead to deeper pits once they are undermined and fall off from the alloy, this results in an increase in roughness that exposed more active area for further corrosion attack.

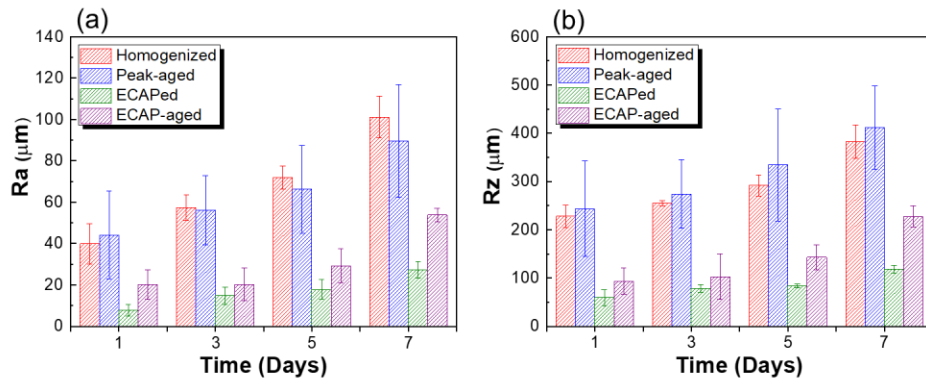


Figure 31. Roughness parameters (a) R_a and (b) R_z of the different AZ91 alloys after immersion for 1, 3, 5, and 7 days in 3.5 wt.% NaCl solution.

3.4 Corrosion Mechanism of Fine-Grained AZ91 Alloys

Secondary phases and grain size are critical metallurgical factors that can significantly influence the corrosion performance of Mg and its alloys [44]. Regarding the influence of grain size on the corrosion behavior of Mg alloys, it has been reported that grain boundaries are more chemically reactive than the bulk matrix due to their higher electron activity and diffusion [54]. Therefore, a high density of grain boundaries can promote electron transfer between the metal surface and the electrolyte resulting in more sites for corrosion and consequently in less corrosion resistance as decreasing grain size. However, the higher reactivity of grain boundaries can also provide more sites for nucleation of an oxide layer. Hence, grain refinement can lead to faster formation of an oxide layer and better mechanical adhesion to the underlying metal substrate that will result in higher corrosion resistance [54]. Secondary phases can also play a significant role on the corrosion performance of Mg alloys; parameters such as volume fraction, size, and distribution can modify the role of secondary phases even if they exhibit

similar chemistry. Song et al. [121] reported that the β -Mg₁₇Al₁₂ phase in Mg-Al alloys has a dual role on the corrosion behavior of Mg-Al alloys; they proposed that high volume fraction of continuously distributed β -Mg₁₇Al₁₂ precipitates along the grain boundaries can improve the corrosion resistance of Mg-Al alloys by acting as a barrier that retards corrosion propagation in the alloy. On the contrary, the presence of a small volume fraction of discontinuous β -Mg₁₇Al₁₂ precipitates can accelerate the corrosion process of the α -Mg matrix by acting as an effective galvanic cathode.

From electrochemical/corrosion measurements and chemical and morphology analysis, it was found that the ECAP processed alloys exhibits a significant higher corrosion resistance as compared to the heat-treated alloys. The significant enhancement in the corrosion performance of the ECAP-processed alloys can be attributed to three major factors: 1) refinement of the microstructure that can promote the formation of a protective oxide film, 2) formation of a more adherent, dense and protective layer of carbonate-containing corrosion products upon immersion, and 3) presence of well-distributed β -Mg₁₇Al₁₂ precipitates along the grain boundaries of the DRXed grains that promote a more uniform corrosion with shallow penetration depth. Figure 32 summarizes the micro-galvanic corrosion mechanism observed in the ECAPed alloy. It is well-known that micro-galvanic corrosion in magnesium alloys is mainly controlled by the potential difference between the phases and the cathode-to-anode area ratio [62, 63]. These factors will dictate the rate of galvanic corrosion of the alloy when exposed to a corrosive environment. According to Figure 32, in stage I, micro-galvanic coupling is established between the β -Mg₁₇Al₁₂ phase precipitated along the DRXed grain

boundaries and the adjacent α -Mg phase. In stage II, the preferential anodic dissolution of the α -Mg matrix surrounding the β -Mg₁₇Al₁₂ precipitates results in intergranular corrosion with trenching around the precipitates followed by particle fall-out from the alloy. This particle detachment leads to corrosion pits, which are active sites for further corrosion attack. More corrosion pits are developed as progressing the immersion time. Owing to the presence of well-distributed fine β -Mg₁₇Al₁₂ precipitates at the grain boundaries of the DRXed grains, the undermining of these precipitates and formation of corrosion pits results in a more uniform corrosion morphology with a shallow penetration depth as shown in the stage III. Micro-galvanic corrosion between the very fine β -Mg₁₇Al₁₂ precipitates at the interior of the DRXed grains and the adjacent α -Mg matrix can also occur leading to intragranular corrosion of the DRXed grains, however, the significantly small cathode-to-anode area ratio of this galvanic couple will lead to a slow galvanic corrosion rate that will not significantly contribute to the corrosion propagation in the DRXed grains. No evidence of micro-galvanic corrosion or anodic dissolution was observed in the unDRXed grains even though there was a large volume fraction of lath-shaped β -Mg₁₇Al₁₂ precipitates that could induced a strong galvanic coupling due to the large cathode-to-anode area ratio. The corrosion mechanism for the preferential dissolution occurring in the DRXed regions will be further explored in chapter V.

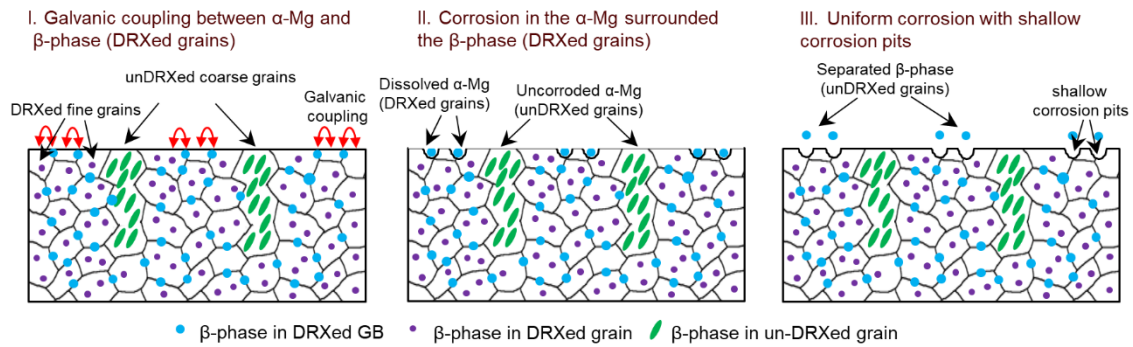


Figure 32. Schematic illustration of the micro-galvanic corrosion mechanism of fine-grained AZ91 alloys processed by ECAP.

The lower corrosion resistance of the ECAP-aged alloy in comparison with the ECAPed alloy can be attributed to the increase in grain size with post-aging treatment that could deteriorate the protective properties of the oxide layer, but also it can be associated with the coarsening of the β - $\text{Mg}_{17}\text{Al}_{12}$ phase that led to deeper pits with greater active areas for further corrosion attack. This coarsening of precipitates could also result in a higher cathode-to-anode area ratio that can lead to higher galvanic corrosion rates. Although, it has been proposed that post-annealing after severe plastic deformation can further improve the corrosion resistance of Mg alloys by decreasing the dislocation density in the α -Mg matrix [24], in this study, the detrimental effect of the increase in grain size and coarsening of β - $\text{Mg}_{17}\text{Al}_{12}$ precipitates predominated over the beneficial effect of reducing the dislocation density.

3.5 Summary and Conclusions

This chapter investigated the microstructure, mechanical properties and corrosion behavior in chloride-containing environments of fine-grained AZ91 alloys processed through ECAP and post-aging treatment. The mechanical and corrosion performance of

these fine-grained AZ91 alloys was compared to the ones of traditional heat-treated alloys. A corrosion mechanism for the fine-grained AZ91 alloys is provided. From these findings, the following conclusions can be drawn:

- The microstructure after ECAP processing exhibited a bimodal grain structure of elongated coarse grains combined with a high-volume fraction of equiaxed fine grains. Lath-shaped continuous β -Mg₁₇Al₁₂ precipitates were found at the interior of the unDRXed grains whereas presence of spherical β -Mg₁₇Al₁₂ precipitates along the grain boundaries and at the grain interior were identified in the DRXed grains. Post-aging treatment after ECAP processing increased the volume fraction of β -Mg₁₇Al₁₂ precipitates, however, grain growth and coarsening of pre-existing β -Mg₁₇Al₁₂ precipitates also occurred.
- The ECAPed alloys exhibited better mechanical properties than the heat-treated alloy. The strengthening of the AZ91 alloy was associated with significant grain refinement after ECAP as well as formation of high-volume fraction of well-dispersed β -Mg₁₇Al₁₂ precipitates that provide grain-boundary and precipitation strengthening. This fine-grain structure promoted a more uniform plastic deformation that resulted in higher ductility. Post-aging treatment provided further increase in strength but a decrease in ductility.
- The corrosion resistance of the AZ91 alloy was significantly enhanced after ECAP processing and it was mainly attributed to three major factors: 1) refinement of the microstructure that can promote the formation of a more protective oxide film, 2) formation of a more protective layer of corrosion products upon immersion, and 3)

presence of well-distributed β -Mg₁₇Al₁₂ phase along the grain boundaries of the DRXed grains that promote a more uniform corrosion with shallow penetration.

- Corrosion in the fine-grained AZ91 alloys initiated at the grain boundaries of the DRXed grains due to micro-galvanic coupling between the β -Mg₁₇Al₁₂ phase and the adjacent α -Mg matrix. This micro-galvanic corrosion resulted in detachment of the β -Mg₁₇Al₁₂ phase from the alloy and development of corrosion pits. The presence of well-dispersed fine β -Mg₁₇Al₁₂ precipitates promoted a more uniform and shallow corrosion morphology.
- The corrosion resistance after post-aging treatment was reduced due to increase in grain size that deteriorated the protective properties of the oxide layer as well as coarsening of the β -Mg₁₇Al₁₂ precipitates along the grain boundaries of the DRXed grains that lead to deeper corrosion pits.

CHAPTER IV
MICROGALVANIC CORROSION MECHANISM OF A PEAK-AGED Mg-9Al-1Zn
ALLOY

The ASTM B661 delineates a standard heat treatment method to increase the strength of Mg-9Al-1Zn (AZ91) alloys that includes solution annealing at 413 °C for 24 h, quenching in water at room temperature, and further aging at 168 °C for 16 h [12]. The processed alloy is commonly known as the peak-aged AZ91 alloy. The microstructure of this alloy mainly consists of primary α -Mg matrix, Al_8Mn_5 intermetallic phase, and a fine lamellar structure of α -Mg + β - $\text{Mg}_{17}\text{Al}_{12}$ phases formed at high angle grain boundaries [84].

It is well known that the β - $\text{Mg}_{17}\text{Al}_{12}$ phase is more cathodic than the α -Mg matrix such that corrosion is expected to preferably occur by micro-galvanic coupling between these two phases [62]. Thus, the corrosion behavior of AZ91 alloy mainly depends on the electrochemical interaction between the α -Mg matrix and the β - $\text{Mg}_{17}\text{Al}_{12}$ phase when exposed to a corrosive environment [62, 119]. Song et al. [62, 63] reported that the β -phase plays a dual role in the corrosion behavior of AZ91 alloys; when the β -phase is continuous along the grain boundaries, this phase behaves as a barrier to hinder corrosion propagation in the alloy. In contrast, when the β -phase is discontinuous along the grain boundaries, it mainly acts as an effective galvanic cathode, accelerating the corrosion process of the α -Mg matrix. Furthermore, they also reported that the micro-galvanic coupling between the β - $\text{Mg}_{17}\text{Al}_{12}$ phase and the α -Mg matrix is mainly controlled by the

cathode-to-anode area ratio and the potential difference between the phases, whereas the effectiveness of the barrier protection provided by the β -Mg₁₇Al₁₂ phase depends mainly on the volume fraction and distribution of the β -Mg₁₇Al₁₂ phase and is favored when the β -Mg₁₇Al₁₂ phase exhibits a continuous network around the α -Mg matrix [63]. Though many corrosion studies have been performed on cast AZ91 alloys, such as those elucidating the dual role mechanism proposed by Song and co-workers [4, 5, 47, 60, 62, 119, 122-125], there is no comprehensive study that addresses the corrosion initiation mechanism of the peak-aged AZ91 alloy.

The aim of this work is to examine the micro-galvanic corrosion mechanism of a peak-aged AZ91 alloy exposed to a NaCl electrolyte at room temperature. This study covers microstructural analysis and a mechanistic electrochemical/corrosion characterization of AZ91 alloy including scanning Kelvin probe force microscopy (SKPFM), immersion test and electrochemical microcell technique. Furthermore, in-situ corrosion analysis and a comprehensive morphological and analytical characterization of the corroded surface after exposure is performed to determine the mechanism of corrosion degradation of peak-aged AZ91 alloy during early immersion in chloride-containing solutions and to identify the dominant role of the β -Mg₁₇Al₁₂ phase either as an effective cathode or as an anodic barrier to corrosion.

4.1. Microstructural Characterization of Peak-Aged AZ91 Alloy

Figure 33 shows optical and SEM micrographs of the peak-aged AZ91 alloy and corresponding EDS line profiles. As seen in Figure 33a, aging of the homogenized alloy at the peak-aged condition results in discontinuous precipitation of a fine lamellar

structure of α -Mg + β -Mg₁₇Al₁₂ phase along the grain boundaries of the original supersaturated α -Mg phase (Figure 33a). The average grain size of the peak-aged condition is $516 \pm 119 \mu\text{m}$. The discontinuous precipitation process during aging involves the cellular growth of alternating layers of the β -phase and a near-equilibrium α -Mg phase (i.e., less Al content than the original supersaturated α -Mg solid solution), resulting in the formation of a lamellar structure that grows behind a migrating grain boundary [3, 84, 126-128]. The inset of Figure 33(b) shows that the lamellar structure exhibits a fine rod-like morphology with a notorious anisotropy of growth [126]. Furthermore, Figure 33(a) and (b) show the presence of undissolved eutectic β -phase due to incomplete homogenization as well as the Al₈Mn₅ intermetallic particles. Aging makes Al solute atoms diffuse towards grain boundaries to form precipitates of β -Mg₁₇Al₁₂ phase, and this process reduced the aluminum content in the α -Mg matrix. Therefore, a nonuniform distribution of Mg and Al is usually expected in the peak-aged alloy as seen from the line profiles shown in Figure 33(c) and (d). The line profile in Figure 33(c) shows that the Al content gradually increases from the center of an α -Mg grain towards the lamellar precipitate located in the grain boundary. The line profile of an Al₈Mn₅ intermetallic particle (Figure 33(d)) also shows gradual changes in Mg, Al, and Mn content from the α -Mg matrix towards the intermetallic particle. Similar concentration gradients have been reported elsewhere [129].

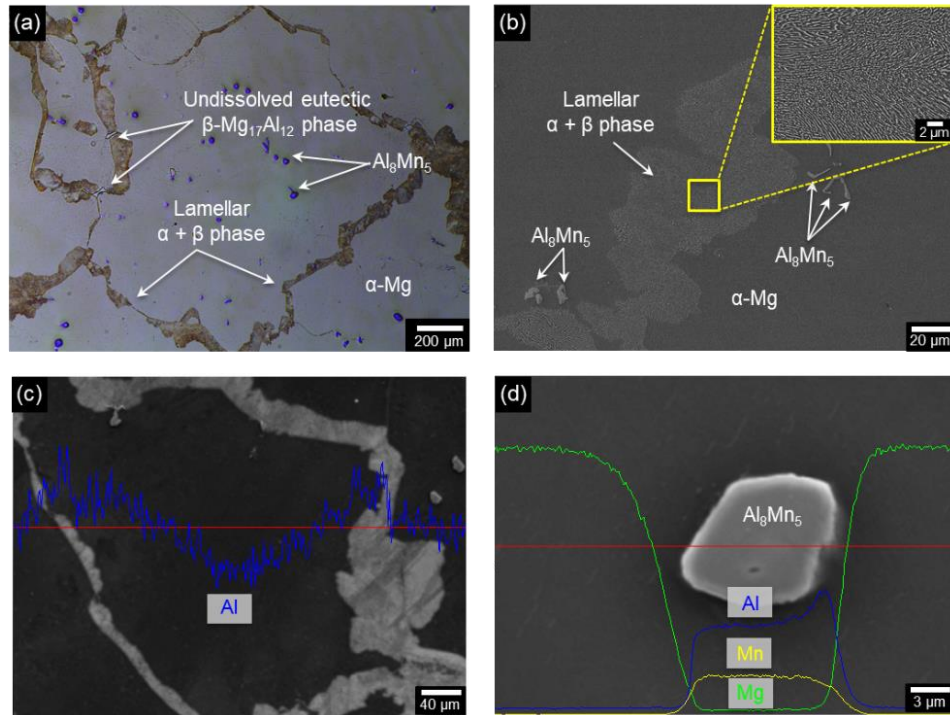


Figure 33. Optical (a) and SEM (b-d) micrographs of the peak-aged alloy and the corresponding line profiles through (c) an α -Mg grain containing lamellar precipitates at the grain boundaries and through (d) an Al_8Mn_5 particle.

4.2 Localized Potential Distribution in the Peak-Aged AZ91 Alloy

The local nobility of secondary phases in the peak-aged AZ91 alloy was evaluated by using scanning Kelvin probe force microscopy (SKPFM). SKPFM measurements provide information regarding electrochemical reactivity at the metal surface, allowing the prediction of local anodic and cathodic sites in a particular material undergoing corrosion processes [61, 130]. Figure 34 shows the surface topography and Volta potential maps and profiles of different phases in the peak-aged AZ91 alloy. In this study, higher and lower potential values correspond to net cathodic (light areas) and net anodic sites (dark areas), respectively. Topography maps and line profiles are

included to facilitate the identification of different constituents in the alloy. From these topography maps and line profiles, it can be seen that all secondary phases including the lamellar $\alpha + \beta$ phase (Figure 34(a) and (c)), the eutectic β -phase (Figure 34(b)), and the Al_3Mn_5 intermetallic particle (Figure 34(d)) protrude from the polished surface (light areas) due to their high hardness, which decreases the polishing rate compared to the adjacent α -Mg matrix. From the Volta potential scanning on the lamellar precipitate and the surrounding α -Mg matrix (Figure 34(a)), it is observed that this lamellar precipitate exhibits a higher Volta potential difference (VPD) with respect to the matrix, suggesting a lower electrochemical activity of the $\alpha + \beta$ phase and, hence, a net cathodic behavior. The VPD is approximately ~ 88.6 mV. The VPD between the undissolved eutectic β -phase and the α -Mg matrix (~ 82.7 mV) is similar to that observed between the lamellar phase and the α -Mg matrix. These relatively high potential differences between the β -phases and the α -Mg matrix (Figure 34(a) and (b)) can serve as a driving force for micro-galvanic corrosion with the α -Mg matrix exhibiting the highest electrochemical activity to promote charge transfer during corrosion reactions [130, 131]. Therefore, it is expected that in a corrosive environment, a galvanic couple between these β -phases (net cathodes) and the adjacent α -Mg matrix (net anode) will be established, leading to the onset of corrosion at the interface boundaries and further preferential dissolution of the surrounding matrix. Closer observation of the Volta potential distribution inside the lamellar precipitate is shown in Figure 34(c), where a small potential difference between the β -phase and the local α -Mg phase inside the lamellar structure can be identified. The

β -phase is slightly more cathodic (~ 30 mV) than the local α -Mg phase, suggesting the possibility of micro-galvanic corrosion within the precipitate.

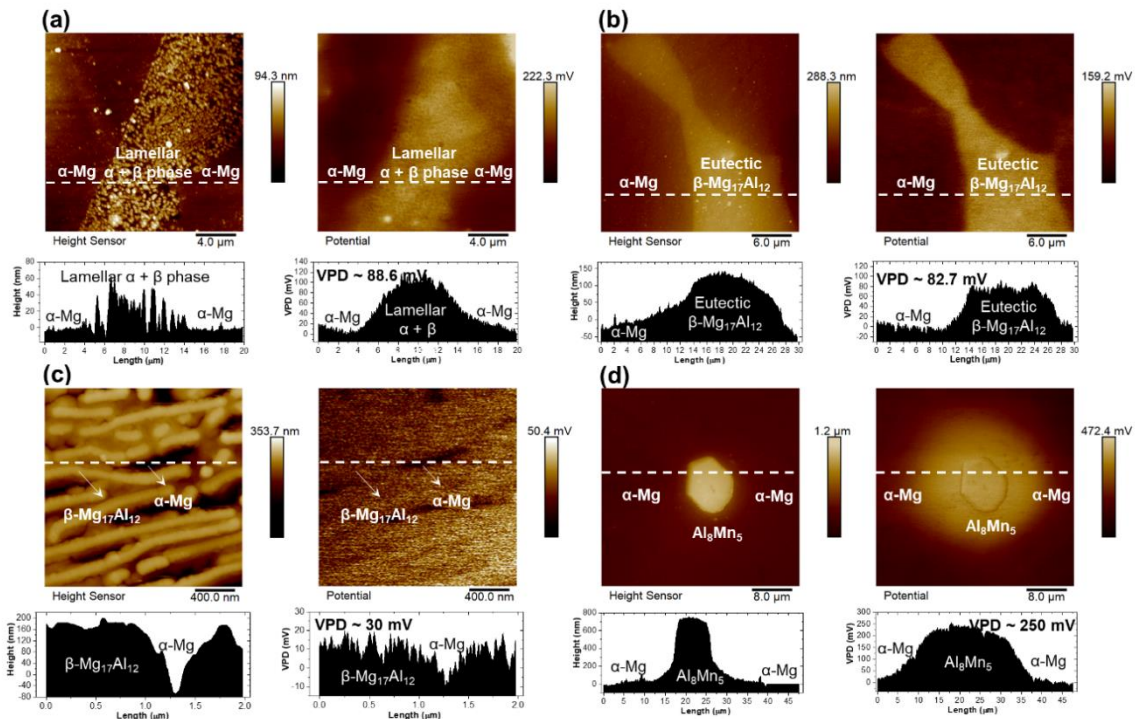


Figure 34. Topography (left) and Volta potential (right) maps and profiles of the peak-aged AZ91 alloy in selected areas: (a) lamellar $\alpha + \beta$ precipitate, (b) eutectic β -phase, (c) the interior of the lamellar precipitate and (d) Al_8Mn_5 intermetallic particle.

From the Volta potential map shown in Figure 34(d), the Al_8Mn_5 phase with a VPD of ~ 250 mV is also found to be cathodic with respect to the α -Mg matrix. The Al_8Mn_5 phase exhibits the highest cathodic activity, which suggests a more intense micro-galvanic coupling with the α -Mg matrix compared to the coupling between the β -phases (eutectic or lamellar) and the α -Mg matrix. Interestingly, the Volta potential gradient across the $\text{Al}_8\text{Mn}_5/\alpha$ -Mg matrix boundary is not as steep as the ones observed

for the β -phases/ α -Mg matrix interface boundaries (Figure 34(a) and (b)); instead, the Volta potential in the α -Mg matrix surrounding the Al_8Mn_5 particle is similar to the Volta potential of the particle itself, resulting in a peculiar “corona-like” Volta potential gradient around the Al_8Mn_5 particle. This particular corona-like Volta potential gradient surrounding the Al_8Mn_5 intermetallic particle can be associated with the non-uniform distribution of Mg, Al, and Mn content in the α -Mg matrix surrounding the particle as mentioned above and clearly observed in the X-ray maps (Figure 35(b-d)) of the Al_8Mn_5 intermetallic particle shown in Figure 35(a). From these X-rays maps, it is seen that the content of Mg, Al, and Mn gradually change around the Al_8Mn_5 intermetallic particle, especially up to a distance of 6 μm from the Al_8Mn_5 / α -Mg matrix interface boundary. Beyond a distance of 6 μm , the Mg, Al, and Mn contents become more uniform. This behavior can reduce the intensity of micro-galvanic coupling between the Al_8Mn_5 phase and the adjacent α -Mg matrix. In contrast, the gradual distribution of elements surrounding the secondary particle was not observed for the lamellar precipitate (Figure.35(e)) as seen from the X-ray maps in Figure 35(f-h). These X-ray maps showed that near to the lamellar $\alpha + \beta$ phase/ α -Mg matrix boundary, there was a relatively sharp distribution of Al and Mg, which is consistent with the steep-like Volta potential gradient across the boundary shown in Figure 34(a). Nevertheless, it is worth to emphasize that at larger scale, Al content significantly decreased as approaching to the core of α -Mg grains (Figure 33(c)).

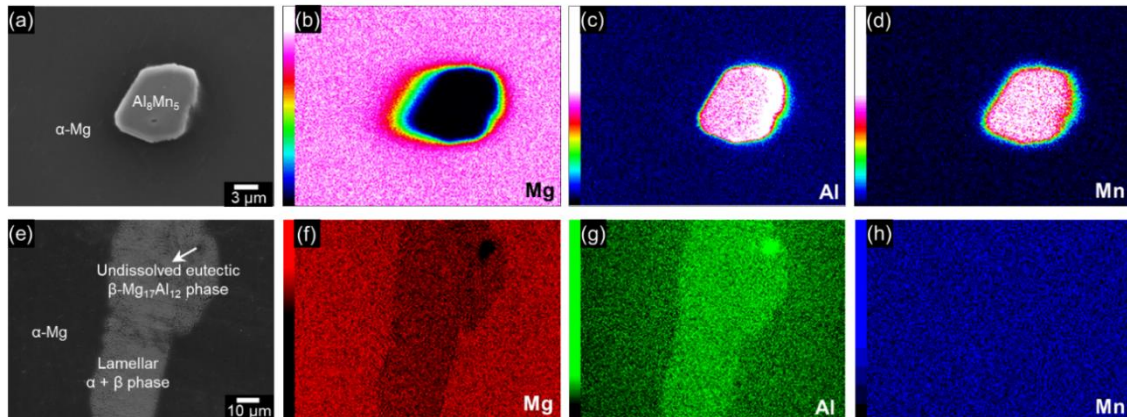


Figure 35. (a) SEM micrograph of an Al_8Mn_5 intermetallic particle and the corresponding (b-d) X-ray elemental maps of Mg, Al, and Mn. (e) SEM micrograph of a lamellar $\alpha + \beta$ precipitate and the corresponding (f-h) X-ray elemental maps of Mg, Al, and Mn.

4.3 Corrosion Initiation in the Peak-Aged AZ91 Alloy Immersed in Chloride-Containing Media

4.3.1 Immersion Testing in 3.5 wt.% NaCl Solution

To investigate the corrosion initiation mechanism of the peak-aged AZ91 alloy, a relatively short immersion test was performed for 6 h in a 3.5 wt.% NaCl solution. Following exposure, surface examination was carried out by using OM and SEM. As predicted from the Volta potential results presented in Figure 34(a), it is expected that micro-galvanic interaction between the lamellar precipitate and the adjacent α -Mg matrix will occur with selective dissolution of the matrix surrounding the precipitate. Indeed, it has been widely proposed that corrosion initiation in Mg-Al alloys is likely to occur at the β -phase/ α -Mg matrix boundary, in which a trenching effect develops at this boundary and is followed by cathodic particle fall-out [5, 49, 62, 106, 117, 118, 132]. However, our findings show that corrosion initiates at the interior of the α -Mg matrix,

which is far from the lamellar precipitates located at the grain boundaries (Figure 36(a-d)) and also occurs inside the lamellar $\alpha + \beta$ phase (Figure 36(e-h)).

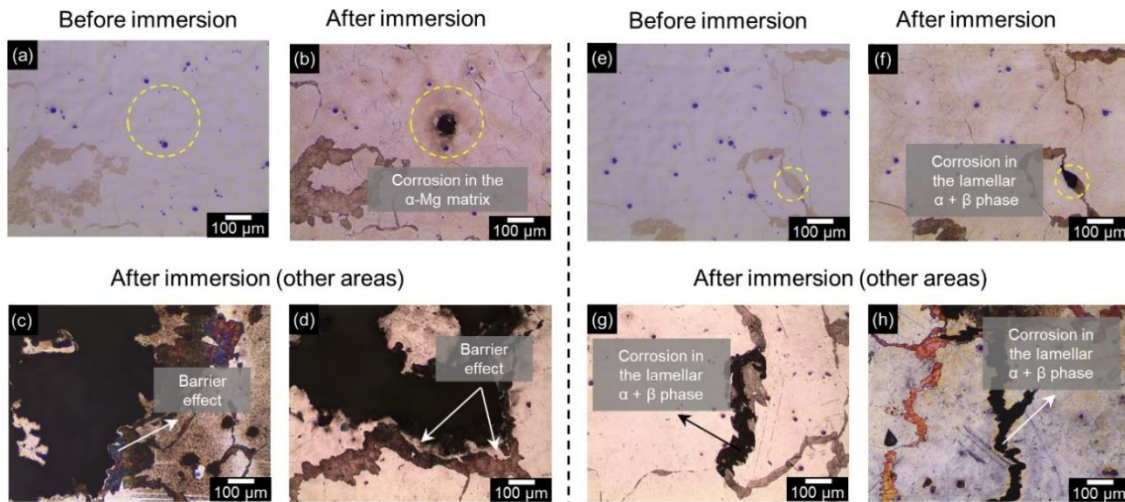


Figure 36. Optical micrographs of the peak-aged AZ91 alloy before and after immersion in 3.5 wt.% NaCl for 6 h showing: (a, b) corrosion initiation at the interior of an α -Mg grain far away from the lamellar precipitate, (c, d) corrosion initiation and propagation inside the α -Mg matrix that is delayed at the lamellar $\alpha + \beta$ phase/ α -Mg matrix boundary, (e, f) corrosion initiation inside the lamellar precipitate, and (g, h) extensive corrosion inside the lamellar precipitate that spreads along the precipitate but is also delayed at the lamellar $\alpha + \beta$ phase/ α -Mg matrix boundary.

Figure 36(b) clearly shows that corrosion did not initiate at the lamellar $\alpha + \beta$ phase/ α -Mg matrix boundary but rather started in the center of the α -Mg grain. Indeed, corrosion seems to propagate towards the grain boundary (Figure 36(c) and (d)). One possible reason for the preferential corrosion initiation in the interior of the α -Mg matrix which is far away from the lamellar precipitate is likely related to the aluminum content gradient from the bulk of the matrix to the vicinity of the lamellar precipitate as shown in Figure 33(c) [133]. The Al solute atom distribution can result in selective anodic

dissolution in the center of the α -Mg matrix that predominates over the micro-galvanic coupling between the lamellar precipitate and the adjacent α -Mg matrix. It is suggested that this anodic dissolution at the interior of the α -Mg matrix is likely accompanied by hydrogen evolution occurring at local cathodic sites, such as in the Al_8Mn_5 intermetallic particles, the lamellar $\alpha + \beta$ precipitates or in the Al-rich zones of the α -Mg matrix. Figure 36(c) and (d) show that during early immersion, corrosion is delayed at the vicinity of the lamellar precipitates, suggesting that they provide a barrier effect due to its high Al content that prevents the propagation of corrosion through the α -Mg grains. Indeed, corrosion tends to propagate along the lamellar $\alpha + \beta$ phase/ α -Mg matrix boundary without any evidence of a trenching effect or particle fall-out, as previously reported elsewhere [5, 62, 106, 117]. This corrosion mechanism involving 1) corrosion initiation in the low Al content regions of the α -Mg matrix that gradually advanced towards the β -phase at the grain boundaries and 2) barrier effect by the β - $\text{Mg}_{17}\text{Al}_{12}$ precipitate that retards corrosion progression through adjacent grains has been reported by previous studies [4, 60, 105, 119, 134]. The barrier protection provided by the lamellar precipitates can be mainly associated with the high volume fraction and the continuous network of these precipitates that can effectively slow the development of corrosion through the α -Mg grains [105, 122, 135]. The continuous net-like structure along the grain boundaries is also less likely to experience undermining due to micro-galvanic corrosion [118]. Furthermore, Pardo et al. [60] proposed that the barrier effect provided by the β -phase in Mg-Al alloys can be attributed to its fine and continuous distribution and to the formation of a semi-protective aluminum-rich oxide layer on the

precipitates that limits corrosion propagation. Finally, Zhang et al. [136] revealed that the absence of corrosion at the α -Mg matrix surrounding the cathodic eutectic β -phase particle, $(\text{Mg}, \text{Zn})_3\text{Gd}$, in as-cast Mg-3Gd-1Zn-0.4Zr alloy was associated with localized alkalinity induced by the eutectic phase (site supporting hydrogen evolution reaction) that promoted passivity of the α -Mg matrix adjacent to the precipitate.

Figure 36(e-h) shows that corrosion also occurs in the lamellar $\alpha + \beta$ phase found in other areas of the peak-aged AZ91 sample. Figure 36(f) shows that corrosion initiates inside the lamellar precipitate instead of occurring at the lamellar $\alpha + \beta$ phase/ α -Mg matrix boundary. These observations are not in agreement with the Volta potential results in Figure 34(a) and the conventional corrosion mechanism that has been widely reported by other researchers involving micro-galvanic coupling between the β -phase and the surrounding α -Mg matrix that results in undermining of the β -phase and further particle fall out due to preferential dissolution of the adjacent α -Mg matrix [5, 62, 106, 117]. The corrosion initiation inside the lamellar $\alpha + \beta$ precipitate seems to occur in the α -Mg phase within this lamellar structure. As shown in Figure 34(c), the Volta potential suggests that the local α -Mg phase inside the lamellar precipitate is anodic with respect to the β -phase. Although this VPD is relatively small compared to the potential difference between the lamellar precipitate and the surrounding α -Mg matrix, it is likely that the selective anodic dissolution inside the precipitate is associated with the cathode-to-anode area ratio and aluminum compositional differences between these phases. The cathode-to-anode area ratio between the β -phase and the α -Mg phase inside the lamellar precipitate is larger than that between the lamellar precipitate and the α -Mg matrix as

shown in Figure 37(a) and (b). Therefore, it is likely that the β -phase and the local α -Mg phase within the lamellar precipitate can establish a stronger micro-galvanic activity, which explains why corrosion preferentially occurs within the lamellar precipitate rather than at the lamellar $\alpha + \beta$ phase/ α -Mg matrix boundary. These observations are in accordance with the results reported by Bland et al. [137] who found that the corrosion rate of Mg-Al alloys in chloride-containing environments increased when the area fraction of Al electrodes embedded in the α -Mg electrodes increased and also when the electrode spacing for a fixed Al electrode area fraction decreased. Similar to the corrosion initiation inside the α -Mg grains, Figure 36(g) and (h) clearly show that corrosion inside the lamellar precipitate spreads along the precipitate but is also delayed at the lamellar $\alpha + \beta$ phase/ α -Mg matrix boundary.

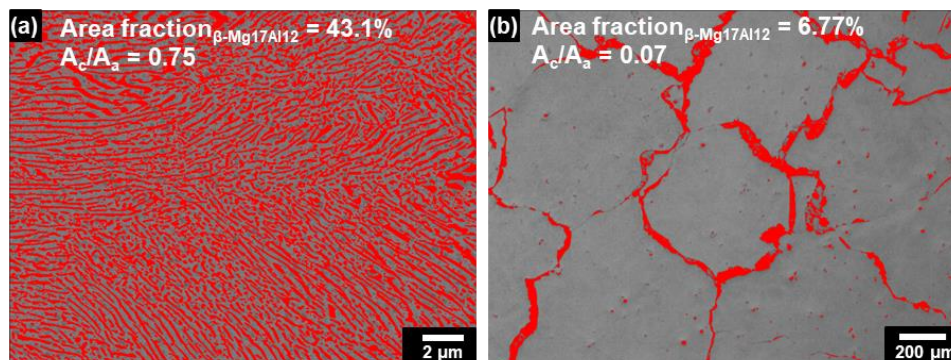


Figure 37. Cathode-to-anode area ratio between (a) the β -Mg₁₇Al₁₂ phase and the local α -Mg phase within the lamellar precipitate and (b) the lamellar precipitate and the α -Mg matrix measured using the ImageJ software.

A more detailed SEM morphology analysis of the corrosion initiation at the interior of the α -Mg matrix is shown in Figure 38. Figure 38(a) shows corroded areas in

the α -Mg matrix far away from the lamellar precipitate. The inset in Figure 38(a) clearly shows corrosion initiation at the interior of the matrix with no signs of corrosion taking place at the $\alpha + \beta$ phase/ α -Mg matrix boundary. Figure 38(b) also shows severe corrosion in the center of an α -Mg grain. X-ray elemental mapping of this region reveals aluminum enrichment in the corroded area, which can be attributed to selective dissolution of magnesium during corrosion of the α -Mg phase matrix (Figure 38(d) and (e)) [60, 103]. Figure 38(f) and (g) shows a mild trenching effect at the Al_8Mn_5 phase/ α -Mg matrix boundary that can be associated with micro-galvanic interactions between these phases. Interestingly, a more aggressive corrosion attack, characterized by large pits, seems to occur in the α -Mg matrix that is located approximately 6 μm from the interface boundary (Figure 38(g)). The preferential attack at these regions, enclosed by a yellow circle in Figure 38(g) can be linked with the corona-like Volta potential gradient and the gradual change in Mg, Al, and Mn content surrounding the Al_8Mn_5 phase, as mentioned above. The corona-like Volta potential gradient can result in a decrease in the driving force for micro-galvanic coupling at the Al_8Mn_5 phase/ α -Mg matrix boundary and instead can induce micro-galvanic coupling between the Al_8Mn_5 phase and the α -Mg matrix located a certain distance away from the precipitate ($\sim 6 \mu\text{m}$). This α -Mg matrix is characterized by a lower Al and Mn content that leads to a significantly large Volta potential difference with the Al_8Mn_5 phase ($\sim 250 \text{ mV}$), thus, making this region more electrochemically active for anodic dissolution than the α -Mg matrix adjacent to the Al_8Mn_5 phase. It is worth mentioning that even though the cathode-to-anode area ratio in this galvanic couple is relatively small, the large VPD between these phases seems to

play a more important role in promoting micro-galvanic interaction between the phases. However, this small area ratio can certainly limit the corrosion propagation by this mechanism. As shown in Figure 38(h), corrosion propagation in α -Mg grains either due to preferential anodic dissolution of low Al-content α -Mg phase or through micro-galvanic corrosion between Al_8Mn_5 intermetallic particles and α -Mg phase is limited when it reaches the lamellar precipitate.

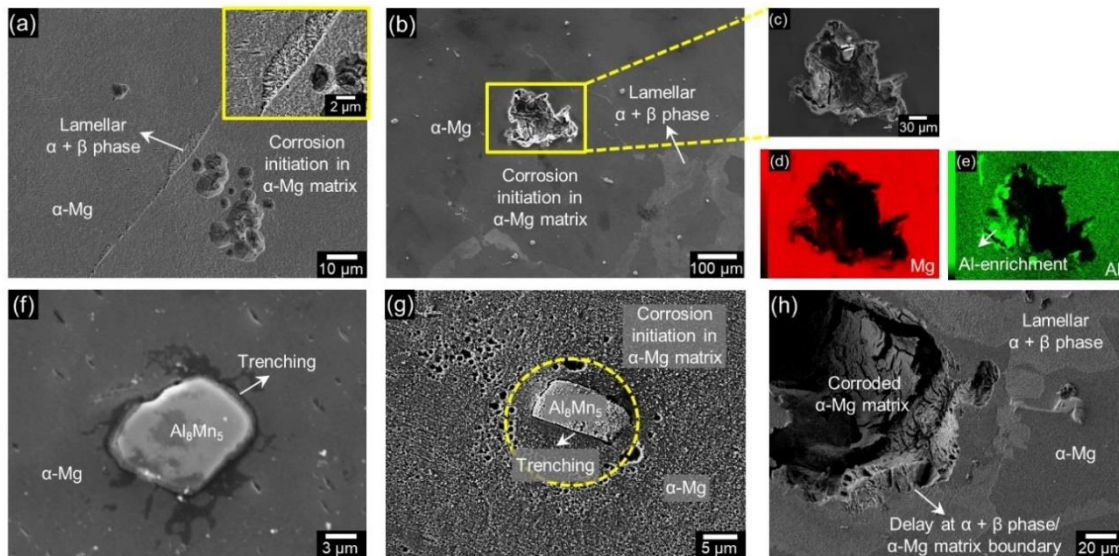


Figure 38. SEM micrographs of the peak-aged AZ91 alloy after immersion in 3.5 wt.% NaCl for 6 h showing: (a-c) corrosion initiation inside the α -Mg matrix, (d-e) X-ray elemental mapping of Al and Mg showing aluminum enrichment in the corroded area shown in c; (f-g) micro-galvanic coupling between Al_8Mn_5 intermetallic particles and the surrounding α -Mg matrix and (h) corrosion propagation in α -Mg grains that is delayed at the lamellar $\alpha + \beta$ phase/ α -Mg matrix boundary.

Figure 39 shows SEM micrographs exhibiting preferential corrosion inside the lamellar precipitate. It is likely that micro-galvanic corrosion between the β -phase and

the local α -Mg phase within the lamellar structure occurs, which is evident by the localized corrosion attack inside the lamellar precipitate. As seen from the inset in Figure 39(a), some regions of the local α -Mg phase preferentially corrode, leading to an unsupported β -phase that eventually detaches from the lamellar precipitate (see the enclosed yellow region). As a result, the morphology of the corroded precipitate follows a lamellar pattern. Figure 39(b) shows a more extended corrosion propagation along the lamellar precipitate. A closer view of the corroded precipitate also shows that corrosion propagates in a lamellar pattern. In addition, this type of lamellar corrosion propagation follows different directions as a result of the anisotropy of growth during the discontinuous precipitation (Figure 33(b)). Similar to the corrosion propagation that is observed inside the α -Mg matrix, the corrosion in the lamellar precipitate did not propagate across the adjacent α -Mg matrix. It seems once again that the interface boundary between the lamellar precipitate and the adjacent α -Mg matrix behaves as a barrier by delaying the corrosion propagation from the lamellar precipitate into the α -Mg matrix and vice versa. As mentioned above, the effectiveness of the barrier effect can be associated with the interconnected network of the lamellar precipitate along the grain boundaries that dominates over the micro-galvanic coupling developed between this precipitate and its surrounding α -Mg matrix. It is interesting to notice from the inset in Figure 39(b) that Al_3Mn_5 intermetallic particles located near the lamellar precipitate did not revealed any sign of trenching or micro-galvanic interaction with neighboring areas, this behavior can be related to the large aluminum content in the β -phase that weakens

the intensity of micro-galvanic coupling between the Al_8Mn_5 particles and the surrounding areas [134].

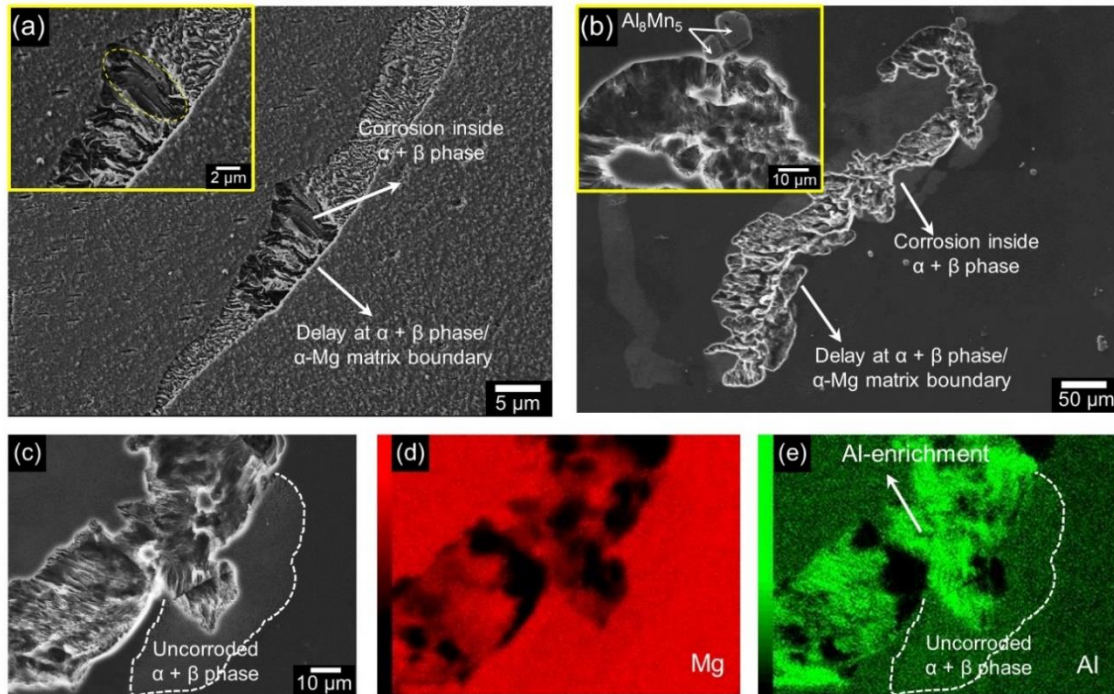


Figure 39. SEM micrographs of the peak-aged AZ91 alloy after immersion in 3.5 wt.% NaCl for 6 h showing: (a-c) corrosion initiation inside the lamellar precipitate due to micro-galvanic coupling between the β -phase and the local α -Mg phase and (d-e) X-ray elemental mapping of Mg and Al showing aluminum enrichment in the corroded area.

Finally, X-ray elemental mapping (Figure 39(d) and (e)) of Figure 39(c) shows that the corroded area of the lamellar precipitate exhibits aluminum enrichment in comparison to that of the uncorroded regions (enclosed by the white lines), which indicates preferential dissolution of magnesium from the local α -Mg phase at the interior of the lamellar precipitate. As reported by Pardo et al. [60], this aluminum enrichment combined with the fine distribution of the β -phase can lead to the formation of an

aluminum-rich oxide layer on the surface of the lamellar precipitate. This aluminum-rich oxide can limit corrosion propagation through α -Mg grains and can slow down the corrosion propagation rate along the lamellar precipitate.

To further explore the corrosion initiation inside the lamellar precipitate, scanning transmission electron microscopy-energy dispersive spectroscopy (STEM-EDS) was performed on the peak-aged AZ91 alloy. As shown in Figure 40, the aluminum and zinc contents in the α -Mg matrix adjacent to the lamellar precipitate (points 1-4 in Figure 40(a)) are approximately 4.7 wt.% and 0.5 wt.%, respectively (Figure 40(f)). These values are much higher than those (\sim 1.5 wt.% Al and 0.05 wt.% Zn) in the local α -Mg phase (points 1-3 in Figure 40(g), also see Figure 40(l)). These results clearly show that the local α -Mg phase at the interior of the lamellar structure is depleted in the less reactive Al and Zn elements when compared to that of the α -Mg matrix adjacent to the precipitate. The observed chemical differences indicate that there is a higher micro-galvanic activity between the local α -Mg phase and the β -phase (\sim 21.2 wt.% Al and 2.3 wt.% Zn; Figure 40(l)), such that micro-galvanic corrosion between these phases outweighs the micro-galvanic coupling between the β -phase and the adjacent α -Mg matrix. The EDS maps (Figure 40(i-k)) at the interior of the lamellar precipitate in Figure 40(h) also show the significant difference in Al and Zn content between the β -phase and the local α -Mg phase, which leads to a strong micro-galvanic coupling. Interestingly, Figure 40(b) shows that the lamellar $\alpha + \beta$ phase/ α -Mg matrix boundary is decorated with fine and closely spaced particles (see the enclosed yellow region) that as confirmed by the EDS maps in Figure 40(c-e), they mainly consist of the

β -phase. The presence of this array of β -Mg₁₇Al₁₂ precipitates at the grain boundary can be responsible for the barrier effect observed at the lamellar $\alpha + \beta$ phase/ α -Mg matrix interface that restricts corrosion propagation across adjacent grains. To the best of our knowledge, this is the first time reporting these findings.

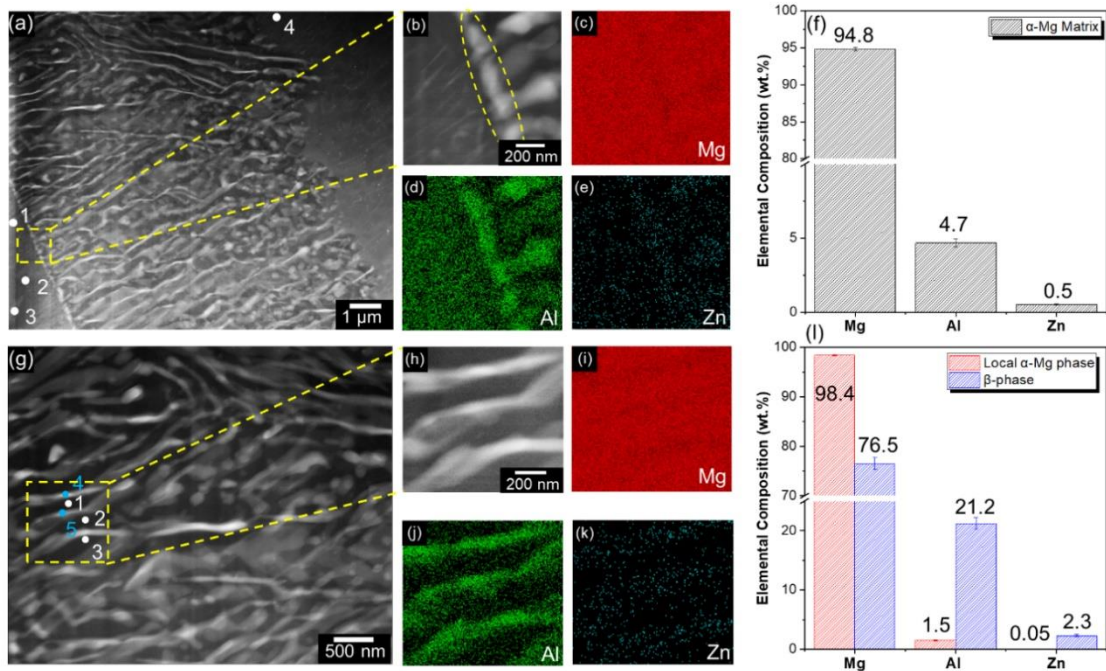


Figure 40. STEM micrographs showing: (a, b) the lamellar $\alpha + \beta$ phase/ α -Mg matrix boundary and (g, h) the interior of the lamellar precipitate. EDX maps of the yellow box regions in a and g indicating the elemental distribution of (c, i) Mg, (d, j) Al and (e, k) Zn. (f, l) Point elemental analysis at the marked regions in a and g showing the lower Al and Zn content in the local α -Mg phase compared to that of the adjacent α -Mg matrix.

Figure 41 shows topography maps and surface roughness profiles of the two distinct corrosion morphologies that are observed in the peak-aged AZ91 alloy sample exposed to 3.5 wt.% NaCl solution for 6 h. Figure 41(a-c) shows the topography and

roughness profile of the corrosion initiation and propagation that occurs inside the α -Mg matrix. As previously shown, corrosion is mainly concentrated in the interior of the α -Mg matrix and did not propagate through the lamellar precipitate. Indeed, it is observed that the deepest corrosion penetration (blue color in Figure 41(b)) is far from the nearest lamellar precipitate, indicating that micro-galvanic coupling between the lamellar precipitate and the adjacent α -Mg matrix is not the corrosion mechanism that describes the anodic dissolution taking place in the α -Mg grains. Furthermore, it is seen that corrosion spread laterally in almost the entire α -Mg matrix with a relatively uniform penetration depth and without any signs of highly localized attack. This corrosion morphology is different from the conventional narrow and deep pits observed in stainless steel and aluminum alloys due to the autocatalytic pitting corrosion mechanism in chloride-containing environments. This different corrosion morphology in the AZ91 alloy can be associated with the production of OH^- ions from the hydrogen evolution reaction ($2\text{H}_2\text{O} + 2\text{e}^- \rightarrow \text{H}_2 + 2\text{OH}^-(\text{aq})$) that decreases the likelihood for development of acidic and highly chloride concentrated environments that can lead to severe localized attack [60]. In addition, the chemical reaction of OH^- ions with Mg^{2+} ions produced from the anodic dissolution process ($\text{Mg}(\text{s}) \rightarrow \text{Mg}^{2+}(\text{aq}) + 2\text{e}^-$) may lead to the formation of a magnesium hydroxide film that can decrease the corrosion penetration rate at local sites ($\text{Mg}^{2+}(\text{aq}) + 2\text{OH}^-(\text{aq}) \rightarrow \text{Mg}(\text{OH})_2$) [132].

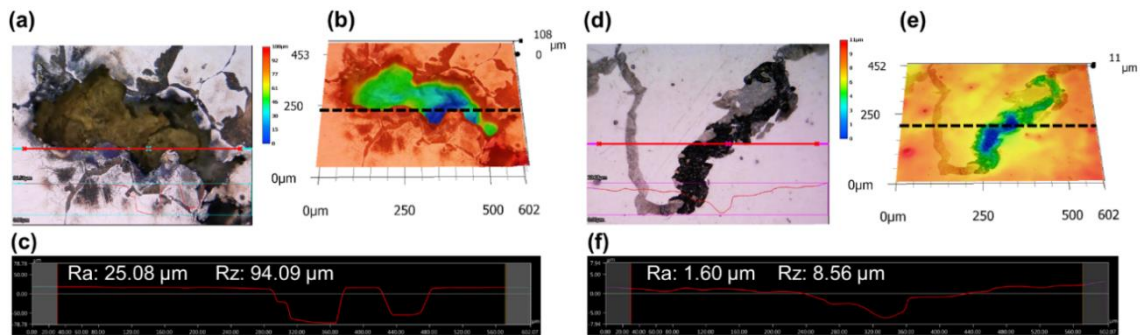


Figure 41. Topography and roughness profiles of the peak-aged AZ91 alloy after immersion in 3.5 wt.% NaCl for 6 h showing: (a-c) corrosion initiation and propagation inside the α -Mg matrix and (d-f) corrosion initiation and propagation along the lamellar precipitate.

Figure 41(d-f) shows the topography and roughness profile of a corroded lamellar precipitate, in which, similar to the corrosion initiation within the α -Mg matrix, the deepest corrosion penetration occurs in the interior of the lamellar precipitate and seems to propagate towards the lamellar $\alpha + \beta$ phase/ α -Mg matrix boundary. These results also confirm that corrosion initiation did not occur due to micro-galvanic coupling between the β -phase and the α -Mg matrix; instead, the lamellar $\alpha + \beta$ phase/ α -Mg matrix boundary represents a barrier against corrosion. From the R_z values in the roughness profiles, a significantly higher penetration depth is observed when corrosion is initiated inside the α -Mg matrix (94.09 μm) compared to that of the corrosion initiation within the lamellar precipitate (8.56 μm). These results suggest that corrosion kinetics inside the α -Mg matrix proceed faster than that inside the lamellar precipitate and therefore, it can dominate during longer immersion times. This observation agrees with the possible formation of an aluminum-rich oxide layer on the lamellar precipitate that can slow down the corrosion propagation inside the precipitate.

4.3.2 In-Situ Corrosion Monitoring in 3.5 wt.% NaCl Solution

A real-time corrosion test was performed and monitored for a longer period of time on specific areas to further investigate the preferential dissolution occurring at the interior of α -Mg grains and inside the lamellar precipitate and to better understand the role of Al_8Mn_5 intermetallic particles and $\beta\text{-Mg}_{17}\text{Al}_{12}$ precipitates on these corrosion initiation processes. Figure 42(a-f) show sequential optical micrographs of in-situ corrosion under observation for up to 30 h in 3.5 wt.% NaCl solution. From Figure 42(b), it can be observed that hydrogen evolution started taking place on an Al_8Mn_5 intermetallic particle after 10 min of immersion. This indicates that the Al_8Mn_5 phase is acting as an effective cathode for hydrogen evolution inducing selective anodic dissolution of the surrounding α -Mg phase. Similar observations were found by Ambat et al. [119] and Lunder et al. [120] who reported vigorous hydrogen evolution at AlFeMn phases and severe corrosion of the adjacent α -Mg matrix. As the immersion time progresses, the hydrogen evolution on the Al_8Mn_5 intermetallic particle becomes more vigorous, and corrosion in the adjacent α -Mg matrix propagates radially around the Al_8Mn_5 intermetallic particle; however, it is slowed at the lamellar $\alpha + \beta$ phase/ α -Mg matrix boundary (Figure 42(c)).

Figure 42(d-f) shows the corrosion initiation occurring in the lamellar precipitate. As shown in Figure 42(d), a large hydrogen bubble forms on the lamellar precipitate after only 20 s of immersion; this bubble grows to a large size for the following 8 min (Figure 42(e)) and then escapes from the sample surface into the electrolyte after 9 min of

immersion. Afterwards, corrosion of the lamellar precipitate underneath the evolved bubble is clearly observed (Figure 42(f)).

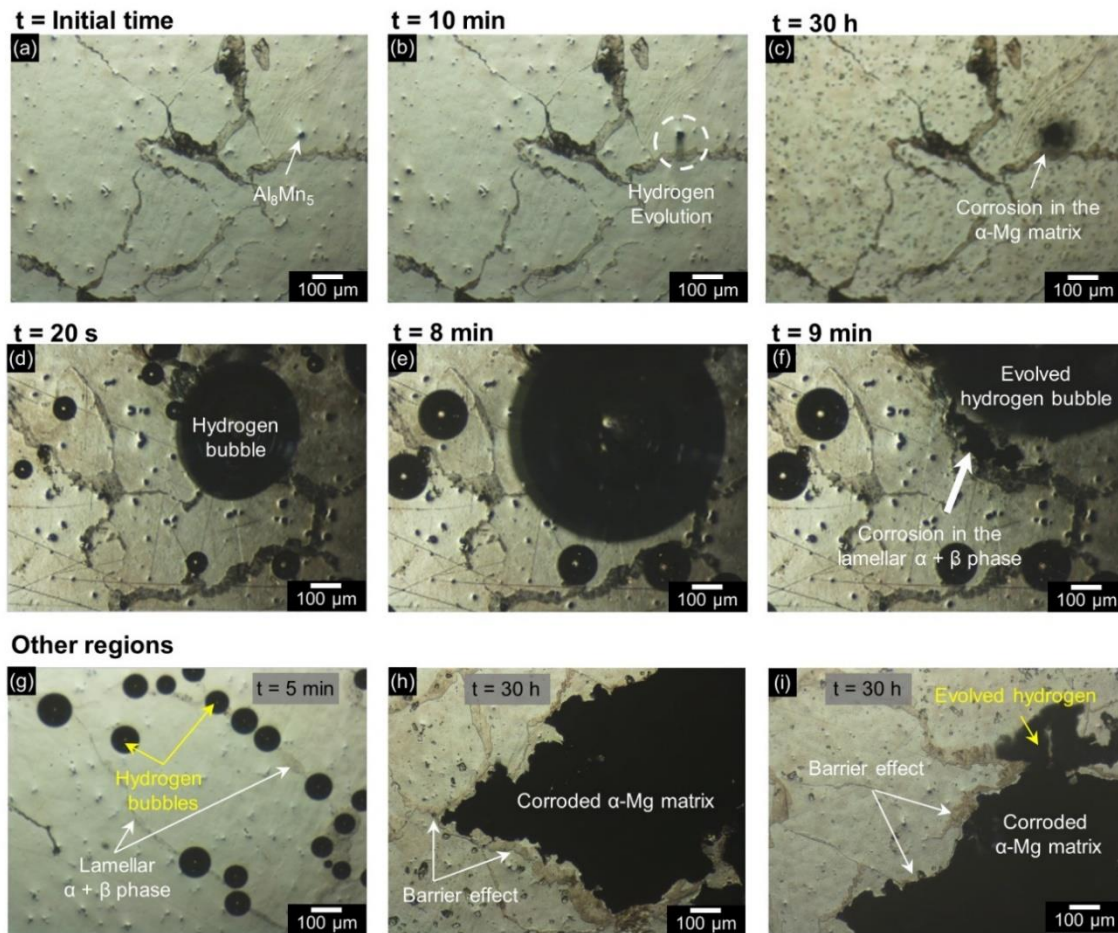


Figure 42. In situ corrosion observations of the peak-aged AZ91 alloy during 30 h in 3.5 wt.% NaCl solution showing: (a-c) micro-galvanic corrosion between the Al_8Mn_5 intermetallic particle and the adjacent α -Mg matrix; (d-f) corrosion initiation in a lamellar $\alpha + \beta$ precipitate that is underneath a hydrogen bubble that evolves after it reaches a relatively large size; (g) formation of hydrogen bubbles mainly at the lamellar precipitates indicating that they can act as effective cathodes; and (h-i) corrosion propagation inside an α -Mg grain that stops at the lamellar precipitate, indicating that the lamellar precipitate acts as a barrier against corrosion propagation.

Figure 42(g-i) shows optical micrographs taken from other regions during the in-situ test. From Figure 42(g), it is seen that after few minutes of immersion (~5 min), there is a large formation of hydrogen bubbles in the lamellar precipitates indicating that they are acting as effective cathodes. This observation suggests that the anodic dissolution at the interior of the α -Mg matrix can be accompanied by hydrogen evolution occurring in the lamellar precipitates. Figure 42(h) and (i) shows that after 30 h of in-situ corrosion observation, there are regions with severe corrosion in the interior of some α -Mg grains; this corrosion spreads laterally to cover almost the entire grain, but is limited at the lamellar $\alpha + \beta$ phase/ α -Mg matrix boundary. Comparing the corrosion attack shown in Figure 42(c) with the corrosion propagation that is observed in Figure 42(h) and (i) taken at relatively similar times, it seems that micro-galvanic corrosion between the Al_8Mn_5 phase and the α -Mg matrix is not truly responsible for the entire corrosion process taking place at the interior of the α -Mg matrix. In that sense, it is suggested that in addition to micro-galvanic coupling between the Al_8Mn_5 phase and the α -Mg matrix, the severe corrosion inside the α -Mg grains can be associated with anodic dissolution of low Al content regions of the α -Mg matrix combined with hydrogen evolution reaction taking place at local cathodic sites (e.g., lamellar α -Mg + β - $\text{Mg}_{17}\text{Al}_{12}$ precipitates or Al-rich zones in the α -Mg matrix) [138]. Further investigation of this phenomenon is needed. As mentioned above, one possible reason for the small contribution of the micro-galvanic coupling between the Al_8Mn_5 phase and the α -Mg matrix to the overall corrosion observed in the α -Mg grains can be related to the small cathode-to-anode area ratio that can limit the corrosion propagation through this mechanism.

4.4 Micro-Electrochemical Behavior of α -Mg Matrix and Lamellar $\alpha + \beta$

Precipitates in Chloride-Containing Media

The local electrochemical behavior of the α -Mg matrix and the lamellar $\alpha + \beta$ precipitates was investigated using the electrochemical microcell technique. In this technique, a glass capillary is sealed with a silicone gasket such that the electrolyte is confined to the area of analysis at the capillary mouth to enclose the electrolyte (Figure 43(a)). The hydrophobic property of silicone prevents the electrolyte from penetrating under the silicone gasket. Therefore, crevice corrosion under the silicone gasket could be avoided. The other benefit of sealing the capillary front end with silicone is that the high deformability of the silicone gasket allows measurements to be performed on rough and even curved surfaces. A glass capillary was obtained by heating borosilicate glass tube with plasma and pulling them when they reached the glass melting temperature. For sealing, the glass capillary was dipped in a silicone lacquer. A stream of air was passed through the glass capillary in order to flush out the silicone inside the capillary and producing a circle opening. Very thin layers of silicone were applied to the capillary tip by repeating this process three times. Figure 43(b) and (c) shows the top and side view of the capillary tip sealed with a silicone gasket, respectively.

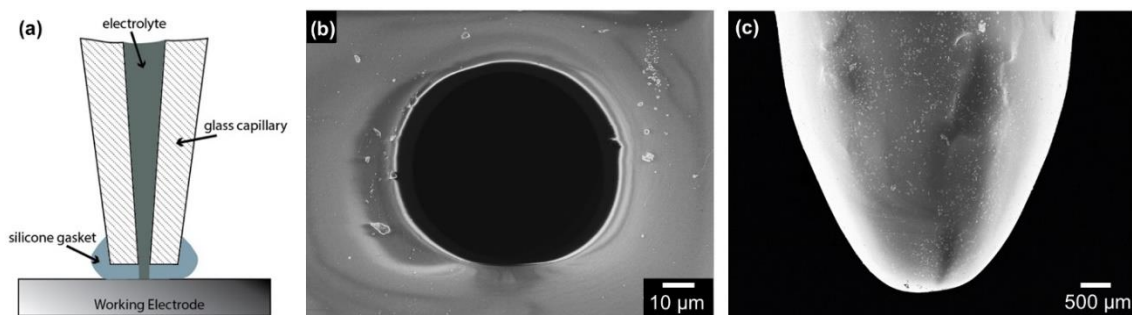


Figure 43. (a) Schematic glass capillary with a silicone gasket and the SEM micrographs of the (b) top view and (c) side view of the silicone sealed capillary.

Figure 44(a) shows the microstructure of the peak-aged AZ91 alloy before the potentiodynamic polarization measurements indicating the different phases (i.e., α -Mg matrix, lamellar $\alpha + \beta$ precipitates, and Al_8Mn_5 intermetallic particles) and the lamellar structure of the $\alpha + \beta$ precipitates. Potentiodynamic polarization measurements were performed in the α -Mg matrix and in a lamellar precipitate as shown in Figure 44(b) and the corresponding results are displayed in Figure 44(c). From the potentiodynamic polarization curves, it is clearly seen that the lamellar precipitate exhibits a more noble corrosion potential (-1.340 V vs. SCE) than that of the α -Mg matrix (-1.644 vs. SCE) as well as a remarkably lower corrosion current density ($5.5 \mu\text{A}/\text{cm}^2$) as compared to that of the α -Mg matrix ($21.5 \mu\text{A}/\text{cm}^2$). Based on the difference in corrosion potential between the lamellar precipitate and matrix, one might expect that corrosion simply initiates at the lamellar precipitate/matrix boundary through micro-galvanic corrosion resulting in preferential dissolution of the matrix, but the fact is not that simple as evidenced by our finding during immersion testing that shows corrosion initiation at points far away from the boundary (Figure 36(b)). The lower corrosion current density

of the lamellar precipitate corroborates that the lamellar precipitates exhibits slower corrosion reaction kinetics than the α -Mg matrix, which might explain why during the immersion testing, the corroded area in the α -Mg matrix is deeper than the one in the precipitate as shown in the topography maps and surface roughness profiles in Figure 41. This indicates that the corrosion occurring at the interior of the α -Mg grains will proceed faster than the corrosion development inside the lamellar precipitate and therefore, it will dominate the corrosion propagation of the peak-aged AZ91 alloy at longer immersion times. A closer observation of the corroded morphologies after the electrochemical microcell measurements are shown in Figure 44(d-g). The morphology of the corroded α -Mg matrix (Figure 44(d) and (e)) shows a typical dissolution of magnesium resulting in a relatively shallow corroded area with the presence of some corrosion products. In contrast, a different morphology was observed in the corroded lamellar precipitate (Figure 44(f) and (g)). As clearly seen in Figure 44(g), the corroded morphology of the lamellar precipitate exhibits a lamellar pattern that follows different directions depending of the orientation of the rod-like β -phase. This morphology is very similar to the one observed in Figure 39(b), which confirms that corrosion inside the lamellar precipitate occurs through micro-galvanic corrosion between the β -phase and the local α -Mg phase leading to preferential dissolution of the α -Mg phase and undermining of the β -phase that results in a “lamellar-type” of corrosion.

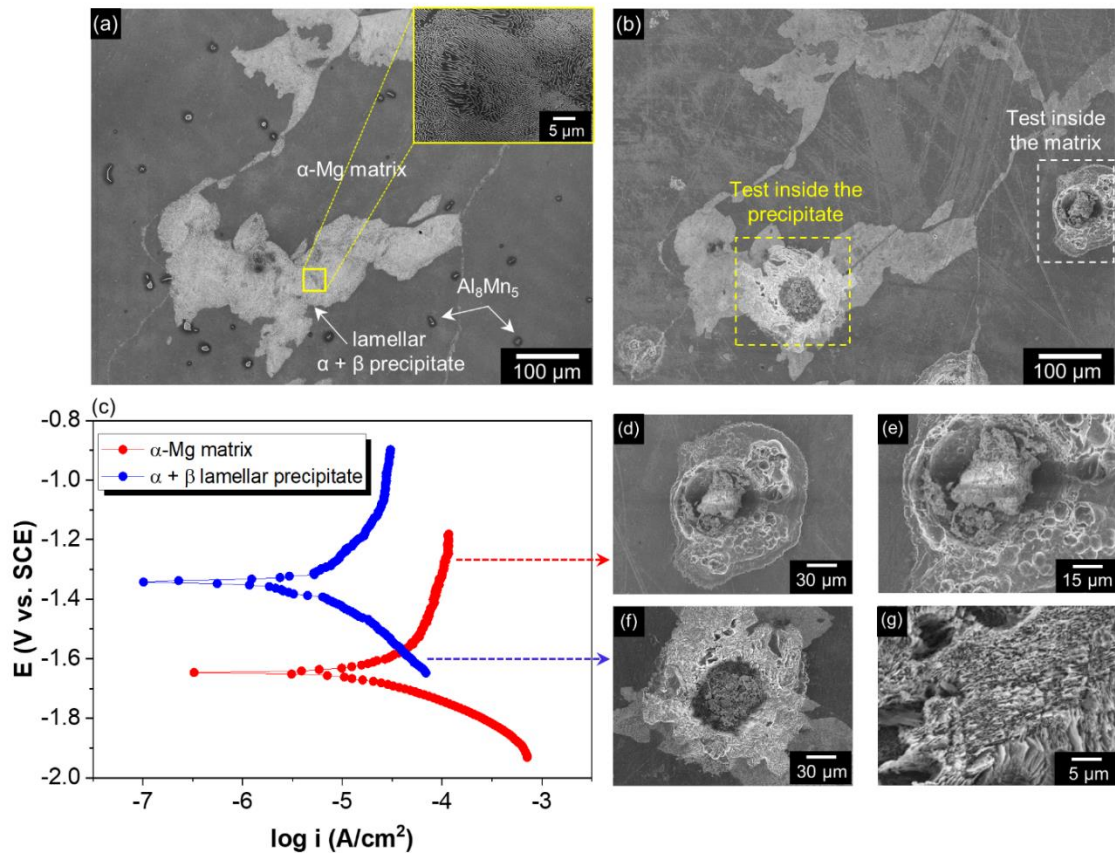


Figure 44. Electrochemical microcell studies showing: morphology of the peak-aged alloy (a) before and (b) after the testing; (c) potentiodynamic polarization measurements of the α -Mg matrix and the lamellar $\alpha + \beta$ precipitate in 3.5 wt.% NaCl solution; closer view of the corroded morphology after the test (d, e) inside the α -Mg matrix and (f, g) inside the lamellar $\alpha + \beta$ precipitate.

4.4 Corrosion Mechanism of Peak-Aged AZ91 Alloy in Chloride-Containing Media

4.4.1 Corrosion Initiation

Figure 45 shows a schematic representation summarizing the mechanisms of corrosion initiation and further propagation of peak-aged AZ91 alloy immersed in a chloride-containing environment. Corrosion in this alloy was initiated in both the interior of the α -Mg grains and inside the lamellar $\alpha + \beta$ phase. Corrosion initiation in the α -Mg

grains was mainly associated with selective anodic dissolution of the low Al-content α -Mg matrix accompanied by the hydrogen evolution reaction occurring at local cathodic sites such as in Al_8Mn_5 intermetallic particles, lamellar precipitates, or in Al-rich zones of the α -Mg matrix. This preferential anodic dissolution was attributed to non-uniform aluminum distribution within the α -Mg grains, which increases as approaching towards the lamellar precipitates located at the grain boundaries, making the interior of the grains more susceptible to corrosion. Furthermore, micro-galvanic corrosion between the Al_8Mn_5 intermetallic particles and the adjacent the α -Mg matrix also contributed to the corrosion initiation inside the α -Mg grains as a result of their large Volta potential difference despite of the small cathode-to-anode area ratio. Conversely, corrosion initiation inside the lamellar precipitates was related to micro-galvanic coupling between the β -phase and the local α -Mg phase within the precipitate. This micro-galvanic coupling predominated over the micro-galvanic coupling between the β -phase and the adjacent α -Mg matrix due to the large cathode-to-anode area ratio regardless of the smaller Volta potential difference between these phases. No signs of trenching or particle fall-out were observed at the lamellar $\alpha + \beta$ phase/ α -Mg matrix boundary, which is attributed to poor or even completely absence of micro-galvanic corrosion between the lamellar precipitate and the adjacent α -Mg matrix. Aluminum enrichment was observed in the corroded areas of the lamellar precipitate due to preferential magnesium dissolution in the local α -Mg phase. This aluminum enrichment combined with the fine distribution of the β - $\text{Mg}_{17}\text{Al}_{12}$ phase in the lamellar precipitate can result in the formation of an aluminum-rich semi-protective oxide layer. The aluminum-rich oxide

layer and the continuous network structure of the lamellar precipitate along the grain boundaries, which are less prone to suffer undermining, provided a barrier for corrosion propagation through α -Mg grains. It was also found the presence of an array of fine and closely-spaced β -Mg₁₇Al₁₂ precipitates at the grain boundaries that can also contribute to the barrier effect observed at the lamellar $\alpha + \beta$ phase/ α -Mg matrix boundary. Finally, Al₈Mn₅ intermetallic particles located at the lamellar precipitates did not induce micro-galvanic corrosion due to the large aluminum content of the β -phase that decreased the intensity of micro-galvanic coupling between these intermetallic particles and their surrounding areas.

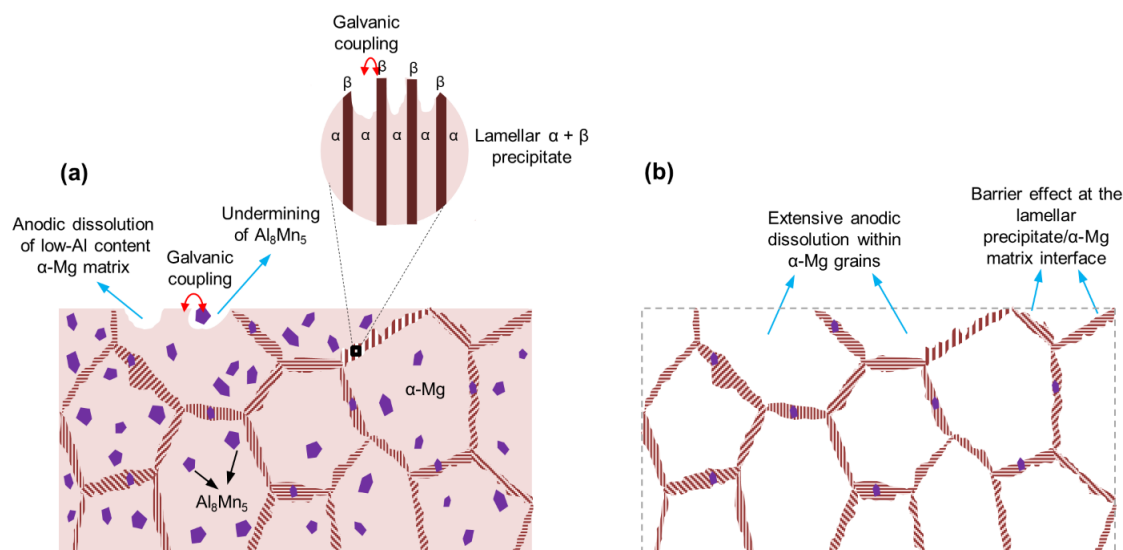


Figure 45. Schematic representation of the mechanism of (a) corrosion initiation and (b) corrosion propagation of peak-aged AZ91 alloy immersed in a NaCl environment.

4.4.2 Corrosion Propagation

In-situ corrosion examination showed that the micro-galvanic corrosion between the Al_8Mn_5 intermetallic particles and the adjacent α -Mg matrix was small, likely, due to the small cathode-to-anode area ratio that can limit the kinetics of this micro-galvanic corrosion process. From the topography measurements, it was found that the penetration depth of the corrosion initiating inside the α -Mg matrix was remarkably higher than the penetration depth observed inside the lamellar precipitate. In addition, the micro-electrochemical analysis of the α -Mg matrix and the β - $\text{Mg}_{17}\text{Al}_{12}$ phase also showed that the corrosion current density of the α -Mg matrix was significantly higher than that of the β - $\text{Mg}_{17}\text{Al}_{12}$ phase, which corroborated that the corrosion reaction kinetics in the α -Mg matrix is considerably faster than in the β - $\text{Mg}_{17}\text{Al}_{12}$ phase. From these results, it seems that selective anodic dissolution of the α -Mg matrix with low aluminum content in the interior of the α -Mg grains dominates over the micro-galvanic corrosion mechanisms (i.e., between the Al_8Mn_5 intermetallic particles and their surrounding α -Mg matrix and between the β - $\text{Mg}_{17}\text{Al}_{12}$ phase and the local α -Mg phase within lamellar precipitate). Indeed, an immersion test over 7 days in a 3.5 wt.% NaCl solution (Figure 46) showed this behavior. Figure 46 shows that during relatively early immersion time (i.e., 1 and 3 days), corrosion in the α -Mg matrix and in the lamellar $\alpha + \beta$ precipitate can be easily identified, however, after longer immersion time (i.e., 5 and 7 days), corrosion in the α -Mg matrix seems to oversee the corrosion occurring in the lamellar precipitates, in which the corrosion morphology was characterized by large corroded areas inside the α -Mg grains confined by the lamellar precipitates, resulting in a “honeycomb-like

structure” with a network of undissolved lamellar precipitates acting as a barrier for corrosion progression. The largely spread corrosion morphology within the grains can be attributed to the production of OH^- ions from the hydrogen evolution reaction that promoted a more uniform corrosion instead of a highly localized attack.

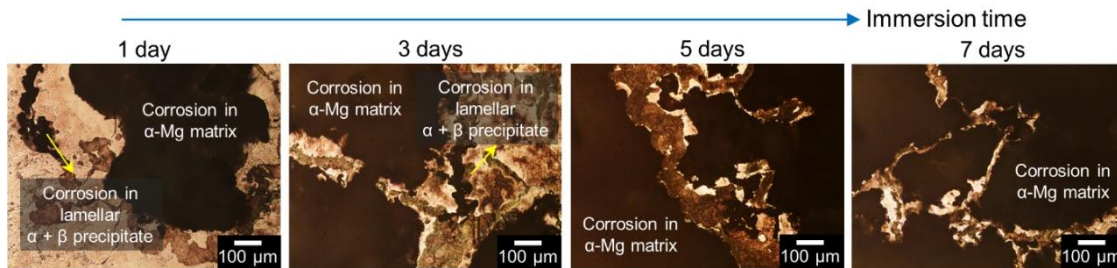


Figure 46. Evolution of the corrosion morphology of the peak-aged AZ91 alloy at different immersion times for up to 7 days in 3.5 wt.% NaCl solution.

4.4 Corrosion Initiation in the As-Cast AZ91 Alloy Immersed in Chloride-Containing Media

Interestingly, this type of competition for corrosion initiation site was not only observed in the peak-aged material but also in the as-cast condition. Figure 47 shows that corrosion in the as-cast AZ91 alloy occurred in the α -Mg matrix but also at the interior of the eutectic and lamellar phases after immersion for 6 h in a 3.5 wt.% NaCl.

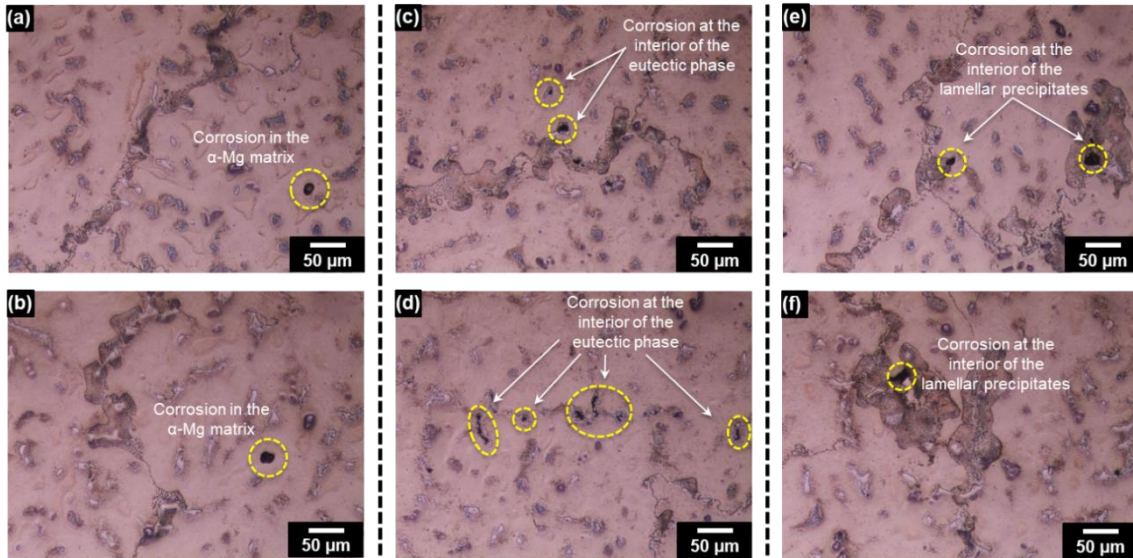


Figure 47. Corrosion initiation in the as-cast AZ91 alloy occurring (a, b) in the α -Mg matrix, (c, d) inside the eutectic phase, and (e, f) inside the lamellar precipitates.

More details of the corrosion initiation inside the eutectic and lamellar phases are shown in Figure 48. Figure 48(a) and (b) show corrosion initiation within the partially divorced eutectic phase, in which the islands of eutectic α -Mg phase at the interior of the eutectic β -phase are preferentially corroded. Furthermore, Figure 48(c) and (d) also shows preferential dissolution of the eutectic α -Mg phase located inside the lamellar β - $\text{Mg}_{17}\text{Al}_{12}$ precipitates. According to these results, it is seen once again that even though the Volta potential measurements indicate micro-galvanic coupling between the β -phases (eutectic and lamellar) and their adjacent α -Mg matrix (Figure 48(e)), no signs of micro-galvanic corrosion are revealed at these regions. Instead, corrosion occurs at the interior of the β -phases due to the discontinuity of these phases with the presence of a high electrochemically active phase (i.e., the eutectic α -Mg phase). In addition, Figure 48(a-d) shows that corrosion is mainly concentrated within the β -phases and did not propagate

into the adjacent α -Mg matrix, similar to the corrosion initiation in the peak-aged condition. This behavior can also be related to a non-uniform aluminum content distribution through these phases that could favor preferential dissolution of the eutectic α -Mg phase located in the interior of the β -phases. It is also likely that the higher cathode-to-anode ratio in the interior of these phases induces a higher micro-galvanic activity compared to the one between the β -phases and the adjacent α -Mg matrix. Figure 48(e) shows that there is indeed a potential difference between the islands of the eutectic α -Mg phase and the eutectic β -phase that can lead to micro-galvanic corrosion once exposed to a corrosive environment. Similar to the peak-aged condition, the Volta potential difference inside these β -phases is smaller compared to the potential difference between the β -phases and the surrounding α -Mg matrix; however, micro-galvanic corrosion within the β -phases in as-cast and peak-aged conditions seem to be predominant. This anomalous behavior can be related to a higher corrosion reaction kinetics in the interior of the β -phases, which is influenced by the cathode-to-anode ratio that oversees the higher thermodynamic tendency based on the potential difference for micro-galvanic coupling between the β -phases and the α -matrix.

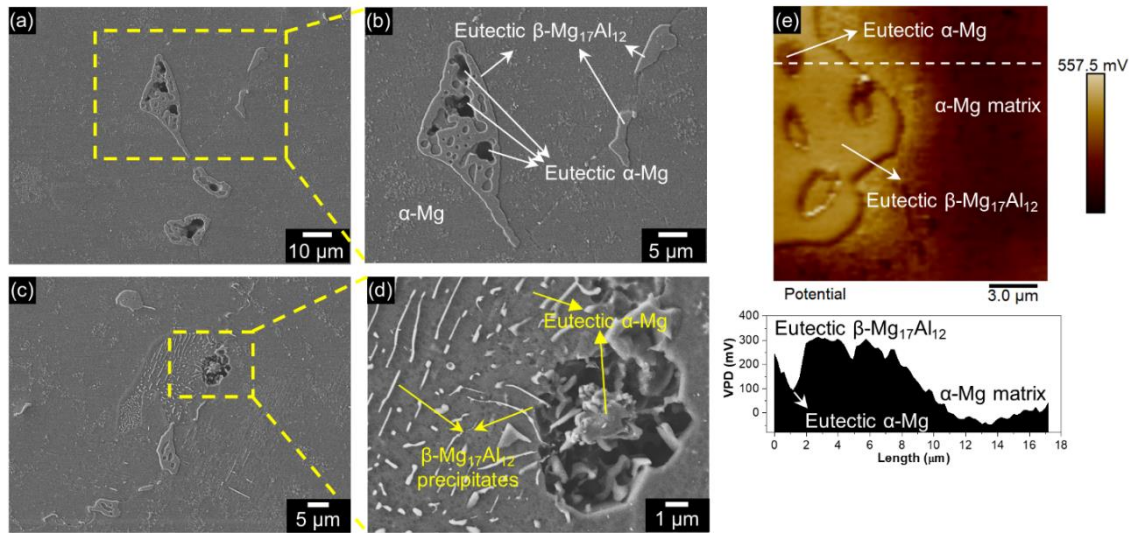


Figure 48. (a-d) SEM micrographs of the as-cast AZ91 alloy after immersion in 3.5 wt.% NaCl for 6 h showing corrosion initiation and propagation inside the eutectic and lamellar precipitates due to micro-galvanic coupling between the β -phases (eutectic and lamellar) and the eutectic α -Mg phase. (e) Volta potential map and profile of the partially divorced eutectic phase.

Figure 49 shows a SEM micrographs of the as-cast AZ91 alloy displaying details of the eutectic and lamellar phases. The X-ray maps in Figure 49(b) and (c) clearly shows a non-uniform distribution of Mg and Al content as approaching to the eutectic β - $Mg_{17}Al_{12}$ phase. Several authors have reported that the non-uniform distribution of Al in the α -Mg solid solution is attributed to Al coring during the dendritic solidification, in which the Al content in the center of the α -Mg grain is significantly less (~ 3 at.%) compared to that in the eutectic α -Mg phase that surrounds the eutectic β - $Mg_{17}Al_{12}$ phase (~ 12 at.%) [103, 119, 122]. It is likely that the gradient in magnesium and aluminum content surrounding the eutectic β - $Mg_{17}Al_{12}$ phase results in a weakening in the micro-galvanic activity at the eutectic β -phase/eutectic α -Mg phase interface that explains why corrosion was not detected at these regions (Figure 48). Furthermore, Figure 49(c) shows

that there is indeed a distinct chemical composition difference in Al content between the eutectic β -phase and the islands of eutectic α -Mg phase at the interior of the eutectic β -phase and between the lamellar precipitate and the surrounding eutectic α -Mg phase. These large differences in microchemistry between these phases combined with their large cathode-to-anode area ratio can explain the preferential corrosion initiation at these regions (Figure 48).

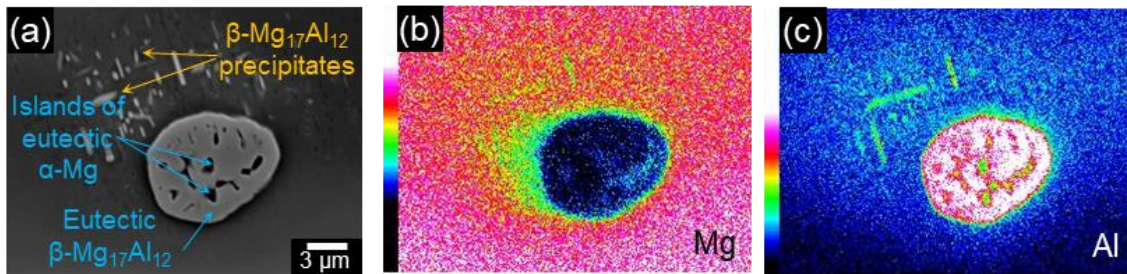


Figure 49. (a) SEM micrograph of the as-cast AZ91 alloy showing the eutectic and lamellar phases and the corresponding X-ray maps of (b) Mg and (c) Al.

4.5 Summary and Conclusions

The mechanisms of corrosion initiation and propagation of a peak-aged alloy AZ91 exposed to a chloride-containing environment were investigated using electrochemical/corrosion techniques coupled with high resolution methods. From the results, the following conclusions can be drawn:

- Corrosion initiation in the peak-aged AZ91 alloy occurred simultaneously in both at the interior of α -Mg grains and inside the lamellar $\alpha + \beta$ phase. The corrosion initiation in the α -Mg grains was mainly attributed to selective anodic dissolution of

low aluminum content α -Mg matrix accompanied by hydrogen evolution taking place at local cathodic sites. Micro-galvanic coupling between Al_8Mn_5 intermetallic particles and the adjacent α -Mg matrix was also observed inside the α -Mg grains, however, this corrosion mechanism was limited presumably due to the small cathode-to-anode area ratio. On the other hand, the corrosion initiation inside the lamellar precipitates was related to micro-galvanic coupling between the β - $\text{Mg}_{17}\text{Al}_{12}$ phase and the local α -Mg phase within the precipitate.

- The selective anodic dissolution at the interior of the α -Mg grains was associated with a non-uniform aluminum distribution inside the grains that gradually increases from the center of the grains towards the lamellar precipitates at the grain boundaries, resulting in preferential corrosion of the aluminum-depleted α -Mg matrix at the interior of the grains. Similarly, the corrosion initiation in the local α -Mg inside the lamellar precipitate was attributed to its lower Al and Zn content compared to that of the adjacent α -Mg matrix, resulting in a stronger micro-galvanic coupling with the β -phase. Furthermore, the cathode-to-anode area ratio inside the lamellar precipitate was higher than the ratio between the β -phase and the adjacent α -Mg matrix leading to a faster micro-galvanic corrosion kinetics between the β -phase and local α -Mg.
- Micro-galvanic corrosion between the lamellar precipitate and the adjacent α -Mg matrix was not identified, but instead, the lamellar $\alpha + \beta$ phase/ α -Mg matrix boundary acted as a barrier against corrosion propagation. The barrier effect at this boundary was mainly attributed to the continuous network of the lamellar

precipitates along the grain boundaries, which is more resistant to undermining and cathodic particle fall-out. The formation of an aluminum-rich semi-protective oxide film in the lamellar precipitate can also be responsible for this barrier. Finally, this barrier effect at the lamellar $\alpha + \beta$ phase/ α -Mg matrix boundary can be attributed to the presence of an array of fine and closely-spaced β -Mg₁₇Al₁₂ precipitates at the grain boundaries.

- The intensity of the micro-galvanic corrosion mechanisms was analyzed from the indirect correlation between Volta potential difference obtained by SKPFM and surface morphology after the immersion testing, it was found that a small Volta potential difference could significantly affect the micro-galvanic corrosion during immersion testing if the cathode-to-anode ratio is large. This was evident by the preferential dissolution of local α -matrix dissolution inside the lamellar precipitate that has a very small surface potential difference (30 mV) with the β -phase but large cathode-to-anode ratio. When the cathode-to-anode area ratio is small but there is a large Volta potential difference, micro-galvanic corrosion can still occur, such as in the case of the Al₈Mn₅ intermetallic particles and the adjacent α -Mg matrix that exhibited a VPD of about 250 mV, however, corrosion propagation will be limited due to the slow micro-galvanic corrosion kinetics.
- The selective anodic dissolution of the aluminum-depleted α -Mg matrix predominated at long-term immersion over the micro-galvanic corrosion mechanisms due to its faster corrosion reaction kinetics. At long immersion time, the corroded morphology of the peak-aged alloy was characterized by a largely spread

corrosion morphology within the α -Mg grains confined by the lamellar precipitates resulting in a “honeycomb-like structure”.

- The as-cast AZ91 alloy also exhibited microgalvanic coupling between a local α -Mg phase (eutectic α -Mg) and the β -phases (eutectic and lamellar). These micro-galvanic corrosion processes between the eutectic α -Mg phase and β -phases were likely driven by the large cathode-to-anode area ratio despite the small Volta potential difference between these phases. No evidence of micro-galvanic corrosion between the β -phases and the external α -Mg phase was identified.

CHAPTER V

EFFECT OF DYNAMIC RECRYSTALLIZATION AND STRAIN-INDUCED DYNAMIC PRECIPITATION ON THE CORROSION BEHAVIOR OF PARTIALLY RECRYSTALLIZED Mg-9Al-1Zn ALLOYS

From chapter III, it was found that corrosion in ECAP-processed alloys seemed to preferentially initiated in the DRXed grains due to micro-galvanic coupling between the β -Mg₁₇Al₁₂ phase precipitated at the grain boundaries and the adjacent α -Mg phase, whereas the heavily-deformed coarse grains appeared to be uncorroded. According to these results, it is of great interest to investigate the reason(s) for this preferential corrosion initiation. High-resolution methods such as SKPFM, TEM, and EBSD will be included in this chapter to elucidate differences in Volta potential, microchemistry, and crystallographic orientation, respectively, between the recrystallized and non-recrystallized regions that allows to identify the predominant factors leading to preferential dissolution in the DRXed grains. Furthermore, the microcell electrochemical technique will be also used to investigated the electrochemically activity of these recrystallized and non-recrystallized regions. In addition, it is also relevant to examine the effect of increasing the strain level during ECAP (i.e., increasing the number of ECAP passes), on the corrosion behavior of the AZ91 alloys. Thus, this chapter will consider ECAPed AZ91 alloys after different ECAP passes, in which variations on grain size of the DRXed grains, DRXed ratio, volume fraction of β -Mg₁₇Al₁₂ phase and size of β -Mg₁₇Al₁₂ precipitates will be correlated with the corrosion response. Electrochemical

measurements such as potentiodynamic polarization and EIS will be included to evaluate the effect of these factors on the corrosion kinetics; a diluted NaCl solution (0.05 M NaCl) will be used to better identify changes in passivation regions and breakdown potentials with increasing the strain level. Immersion testing at short and long immersion time will be also included to further understand the influence of these parameters on the corrosion rate and morphology after corrosion.

5.1 Microstructural Characterization

5.1.1 Initial Microstructure Prior to ECAP

Figure 50 shows the microstructure of the as-received cast alloy (Figure 50(a)), the homogenized alloy at 413 °C for 24 h (Figure 50(b)) and the alloy after pre-heating at 310 °C for 30 min before ECAP processing (Figure 50(c) and (d)). As seen from Figure 50(a), the as-cast alloy exhibits a typical dendritic microstructure with coarse grains of approximately $375 \pm 145 \mu\text{m}$. This dendritic microstructure consists of primary α -Mg matrix, lamellar β -Mg₁₇Al₁₂ precipitates, a partially divorced eutectic $\alpha + \beta$ phase, and Al₈Mn₅ intermetallic particles. After homogenization treatment at 413 °C for 24 h, Figure 50(b) shows that the majority of the lamellar and eutectic phases are dissolved into the α -Mg matrix resulting in a supersaturated solid solution with an average grain size of $515 \pm 99.5 \mu\text{m}$. Figure 50(b) also shows that the Al₈Mn₅ intermetallic particles were still presented after solution heat treatment due to the low solubility of Mn in the Mg matrix as well as their high thermal stability [43, 87]. Typically, some residual eutectic β -Mg₁₇Al₁₂ phase that were not dissolved during homogenization might still be present. During pre-heating to the ECAP temperature of 310 °C for 30 min before the

ECAP processing, large amount of β -Mg₁₇Al₁₂ precipitates were formed at the grain boundaries as well as in the grain interiors (Figure 50(c)). The high magnification SEM image in Figure 50(d) shows the formation of lamellar β -Mg₁₇Al₁₂ precipitates at the grain boundaries (known as discontinuous β -Mg₁₇Al₁₂ precipitates) and lath-shaped β -Mg₁₇Al₁₂ precipitates within the α -Mg grains (known as continuous β -Mg₁₇Al₁₂ precipitates). Similar microstructure with lamellar discontinuous β precipitates at the grain boundaries and lath-shaped continuous β precipitates at the grain interior was reported by Xu et al. [3] during pre-heating of a homogenized AZ91 alloy at 350° C for 5 min before hot compression. The discontinuous precipitation is characterized by the cellular growth of alternating layers of β -Mg₁₇Al₁₂ phase and a less saturated α -Mg phase at high angle grain boundaries resulting in a lamellar structure that grows behind a moving grain boundary into the α -Mg matrix [3, 126]. In contrast, during continuous precipitation, lath-shaped β -Mg₁₇Al₁₂ precipitates nucleate and grow inside the original α -Mg grains, preferentially at defects such as vacancies and dislocations [126].

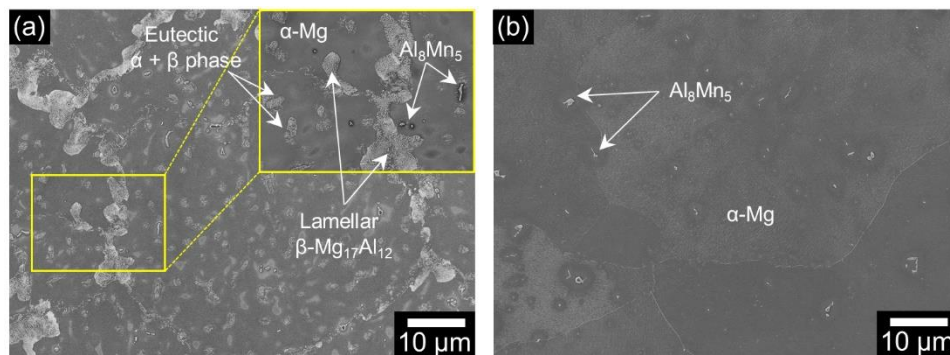


Figure 50. SEM micrographs of the microstructure of (a) as-cast alloy, (b) homogenized alloy and (c and d) alloy after pre-heating at 310 °C for 30 min before ECAP processing.

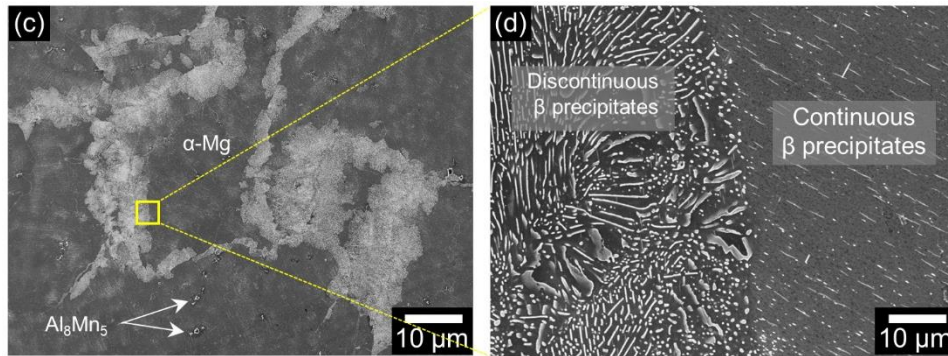


Figure 50. Continued.

5.1.2 Microstructure Evolution During ECAP Processing

Figure 51 shows optical micrographs of the ECAPed alloys after multiple ECAP passes ($N = 1 - 4$). After the first ECAP pass, the ECAPed alloy exhibits a bimodal grain structure consisting of original coarse grains elongated in the shearing direction that are surrounded by new recrystallized fine grains. As seen from Figure 51(a), the coarse grains occupy a significantly larger volume fraction than the fine grains. This bimodal structure and presence of equiaxed fine grains along the original grain boundaries indicates that dynamic recrystallization (DRX) occurred during the ECAP process [3, 11]. It is also seen that increasing the strain level (i.e., number of ECAP passes) results in a gradual increase in the volume fraction of fine grains also known as DRX ratio [139], which increased from 39 % after the first pass up to 77% after the fourth pass. Nevertheless, a fully-recrystallized microstructure was not achieved and coarse grains still exist even after four passes. In this study, the microstructure development of the AZ91 alloy after processing by ECAP is in agreement with the model proposed by Figueiredo and Langdon [9, 140], who suggested that for magnesium alloys with a

coarse-grained initial microstructure, a bimodal grain microstructure with the fine grains forming a necklace-like structure along the original grain boundaries is obtained after the first ECAP pass. They also proposed that this bimodal microstructure becomes more homogeneous as increasing the number of passes until is fully recrystallized. It is worth mentioning that the presence of a bimodal microstructure even after fourth ECAP passes can be associated not only to the initial coarse-grained structure of the homogenized AZ91 alloy but also to the formation of fine β -precipitates during ECAP processing that can retard the grain growth of DRXed grains by providing a pinning effect that limit the grain boundary motion [92]. Considering this fact, the original coarse grains can still occupy a relatively high volume fraction even after several ECAP passes. Therefore, the development of a fully recrystallized microstructure in AZ91 alloys might require more passes than the number predicted by the model proposed by Figueiredo and Langdon.

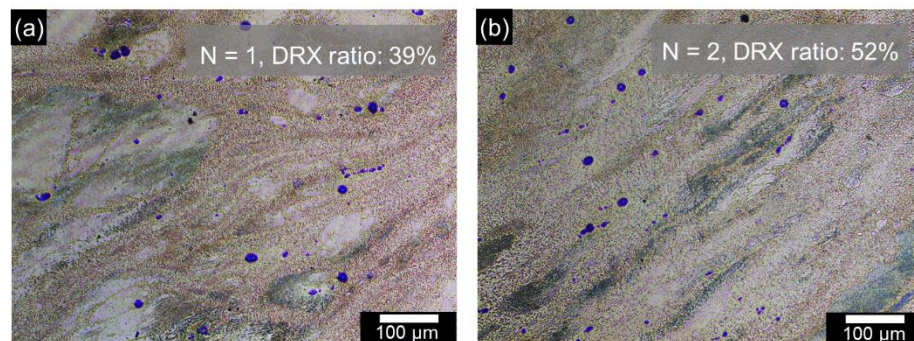


Figure 51. Optical micrographs of the ECAPed specimens with various number of ECAP passes (a) N = 1 (b) N = 2, (c) N = 3 and (d) N = 4.

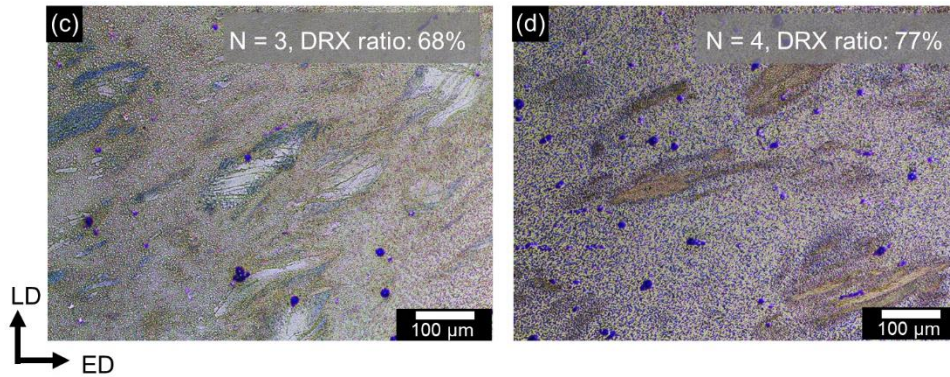


Figure 51. Continued.

SEM micrographs of the ECAPed alloy after the first ECAP pass are shown in Figure 52. From Figure 52(a), it is seen that the microstructure after the first ECAP pass exhibits the aforementioned bimodal grain structure consisting of the original elongated coarse grains and the newly formed equiaxed fine grains denoted in Figure 52(a) as un-DRXed and DRXed regions, respectively. The average grain size of the DRXed grains is $4.08 \pm 0.75 \mu\text{m}$. It has been reported that DRX in AZ91 alloys usually takes place in a discontinuous form (i.e. through discontinuous dynamic recrystallization, DDRX), in which nucleation and subsequent growth of DRXed grains occurs along the original grain boundaries, where the stress concentration is higher and thus both basal and non-basal slip systems are more easily activated, resulting in the formation of a necklace-type structure [11, 93, 141]. Figure 52(b) corresponds to the enlarged view of the micrograph in Figure 52(a) and shows that recrystallization of new fine grains is accompanied by bulging of original grain boundaries with the new grains growing into the primary coarse grains (as indicated by red arrows in Figure 52(b)), which is an indicative of strain-induced grain boundary migration and therefore occurrence of DDRX [42, 43]. Figure

52(b) also shows the presence of a large amount of $\beta\text{-Mg}_{17}\text{Al}_{12}$ precipitates in both, the un-DRXed and DRXed regions. $\beta\text{-Mg}_{17}\text{Al}_{12}$ precipitates with a relatively spherical morphology are seen along the grain boundaries as well as in the grain interior of the DRXed grains. In contrast, lath-shaped continuous precipitates are seen at the grain interior of the original coarse grains. This microstructure also agrees well with the microstructure reported by Xu et al. [3] during hot compression of a homogenized AZ91 alloy. The spherical shape of the precipitates formed in the DRXed regions was found to be more energetically favorable as compared to the lamellar discontinuous precipitates and lath-shaped continuous precipitates formed during traditional heat treatment due to the large density of defects introduced during the ECAP process [7, 11].

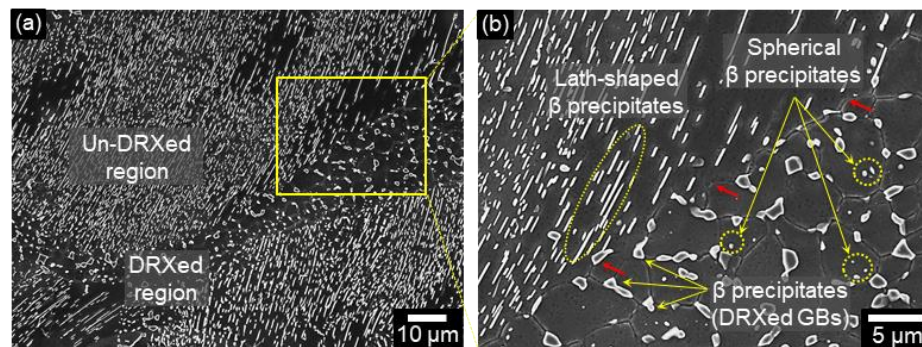


Figure 52. SEM micrographs of the ECAPed alloy after the first pass ($N = 1$) showing (a, b) bimodal grain structure with bulging of the initial grain boundaries and presence of large amount of $\beta\text{-Mg}_{17}\text{Al}_{12}$ precipitates in both the un-DRXed and DRXed regions and (c, d) DRX occurring in neighboring regions of an undissolved eutectic β -phase demonstrating the occurrence of PSN mechanism.

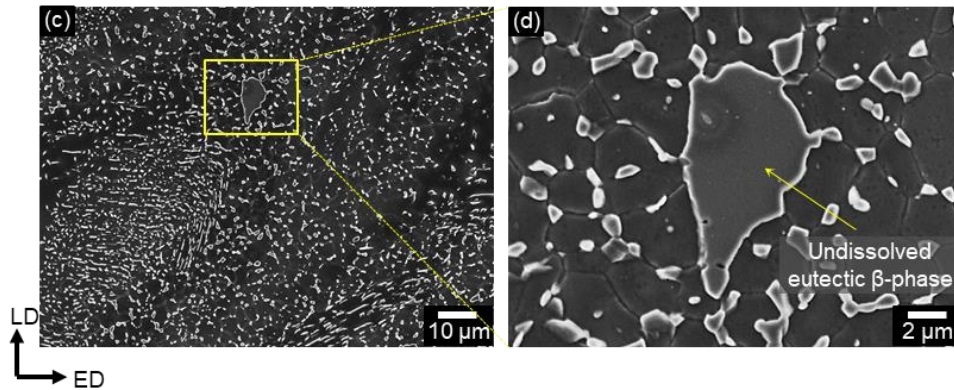


Figure 52. Continued.

The numerous amount of β - $\text{Mg}_{17}\text{Al}_{12}$ precipitates can be attributed to formation of precipitates during the pre-heating process as shown in Figure 51(c) and (d), fracturing of pre-existing precipitates by shearing, and strain-induced dynamic precipitation (SIDP) from the supersaturated α -Mg solid solution taking place during the ECAP process [11, 27, 99]. Dynamic precipitation at the DRXed grain boundaries (DRXed GBs) is promoted as the grain boundaries provide rapid diffusion paths for the solute atoms. In addition, the dynamic precipitation observed at the grain interior of the un-DRXed and DRXed grains can be attributed to the large density of defects such as dislocations and vacancies that can serve as heterogeneous nucleation sites for the β - $\text{Mg}_{17}\text{Al}_{12}$ precipitates. These defects also accelerate the diffusion of solute atoms through the α -Mg matrix [126, 141]. The average size of the β precipitates at the DRXed GBs is $1.46 \pm 0.43 \mu\text{m}$ while the β precipitates at the interior of the DRXed grains are smaller than 100 nm. It has been reported that DRX is greatly influenced by the size of the precipitates, in which coarse β precipitates (diameter $> 1 \mu\text{m}$) can promote dynamic recrystallization through the particle-stimulated nucleation (PSN) mechanism whereas

smaller precipitates (diameter $\leq 1 \mu\text{m}$) can provide a grain boundary pinning effect that restricts grain growth of the recrystallized grains and promotes grain refinement [42, 93, 142, 143]. In the PSN mechanism, the nucleation of DRXed grains is facilitated due to the high stored strain energy at the precipitate/matrix interface that occurs during the severe deformation and leads to accumulation of dislocations at the vicinity of coarse precipitates [99, 144]. These regions with high density of dislocations serve as nucleation sites for new DRXed grains [144]. Figure 52(c) and (d) shows the presence of an un-dissolved eutectic β -phase which is surrounded by DRXed grains. This is an evidence that large β - $\text{Mg}_{17}\text{Al}_{12}$ particles can act as nucleation sites for DRX through the PSN mechanism.

Figure 53 shows the microstructure evolution of the ECAPed specimens as increasing the level of deformation strain. From Figure 53(a-d), it is seen that a bimodal grain structure still exists even after 4 ECAP passes. However, it is noticed that the DRXed ratio increases as increasing the number of ECAP passes resulting in a more uniform recrystallized microstructure. These values are reported in Table 6. The DRXed regions after different ECAP passes are shown in Fig. 53(e-h). From these micrographs, it is seen that the average grain size of the DRXed grains decreased from $4.08 \pm 0.75 \mu\text{m}$ after one pass to $1.58 \pm 0.40 \mu\text{m}$ after four passes. This significant grain refinement can be associated with the combined effect of DRX and SIDP occurring during ECAP processing [141], where the severe imposed strain promotes dynamic recrystallization of new fine grains, and the β precipitates can either accelerate DRX through the PSN mechanism or they can restrict grain growth of the DRXed grains by grain boundary

pinning effect. The concurrent presence of dynamic precipitation and recrystallization during ECAP processing has been denoted as the combined-reaction region, which is characterized by fine grains formed at the original grain boundaries and presence of submicron β precipitates [141]. Although DRX is predominant in alloys with low stacking fault energy (SFE) such as copper, nickel, and austenitic stainless steel whereas dynamic recovery (DRV) should be expected in alloys with high SFE such as aluminum and magnesium ($\gamma \sim 125 \text{ mJ/m}^2$), DRX occurs instead of DRV in magnesium and magnesium alloys such as AZ91 alloy under high temperature deformation due to the limited number of independent slip systems that predominates over the effect of SFE [11, 145]. Figure 53(e-h) also shows that the size and volume fraction of β precipitates in the DRXed regions decrease and increase, respectively, as increasing the strain level. These values are also reported in Table 6 where it is noticed that the volume fraction of precipitates increased from 8.57% after one pass to 20.65% after four passes, whereas the average size decreased from 1.86 ± 0.43 after the first pass to 0.73 ± 0.34 after the fourth pass.

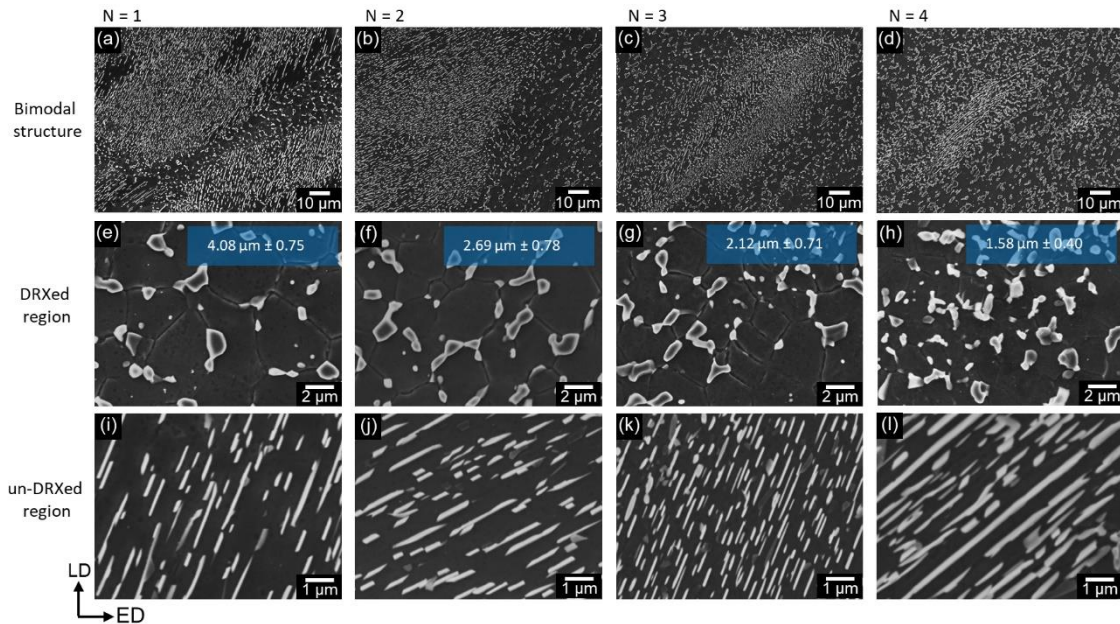


Figure 53. SEM micrographs of the ECAPed specimens with various number of ECAP passes showing (a-d) the bimodal grain structure, (e-h) a DRXed region and (i-l) an un-DRXed region after $N = 1$, $N = 2$, $N = 3$, and $N = 4$, respectively. The values in (e-h) indicate the average grain size of the DRXed grains.

It is worth mentioning that by decreasing the deformation temperature after each ECAP pass, grain growth was prevented not only due to lower mobility of grain boundaries at lower temperatures but also due to the higher amount of precipitates formed at lower temperatures that can facilitate recrystallization and retard grain growth of the DRXed grains [11, 88]. It is well-known that increasing the temperature results in dislocation annihilation by cross-slip, therefore by decreasing the temperature, there is a higher density of dislocations that can serve as nucleation sites for dynamic precipitation [11]. In addition, the presence of finer precipitates as increasing the number of ECAP passes suggests that the pinning effect becomes more predominant as raising the level of deformation strain [75, 92]. Finally, Figure 53(i-l) shows the evolution of the un-DRXed

regions as increasing the number of ECAP passes, where it is noticed that a large volume fraction of lath-shaped continuous β precipitates is formed as increasing the strain level, which increases from 16.32% after the first pass to 32.66% after the fourth pass (Table 6).

Table 6. Microstructural parameters of AZ91 alloys after different ECAP passes

Number of passes	DRXed grain size (μm)	DRX ratio (%)	Volume fraction of β -phase in DRXed grains (%)	Size of β -phase in DRXed GBs (μm)	Volume fraction of β -phase in un-DRXed grains (%)
1	4.08 ± 0.75	39	8.57	1.86 ± 0.43	16.32
2	2.69 ± 0.78	52	11.04	1.27 ± 0.41	18.43
3	2.12 ± 0.71	68	13.24	1.09 ± 0.43	25.99
4	1.58 ± 0.40	77	20.65	0.73 ± 0.34	32.66

Figure 54 shows the XRD patterns of the AZ91 alloy after each ECAP pass. As seen from Figure 54(a), the ECAPed alloys are mainly composed of α -Mg and β -Mg₁₇Al₁₂ phases. In addition, it is also noticed that the intensity of the β -Mg₁₇Al₁₂ phase peaks increases as increasing the number of ECAP passes (as indicated by the vertical dashed lines), implying that the volume fraction of these precipitates increased during multiple passes of ECAP. The gradual increase in the volume fraction of the β -Mg₁₇Al₁₂ phase with the number of ECAP passes confirms that SIDP occurred during ECAP

processing and it was promoted as the deformation strain increased [90]. These results are in agreement with Figure 53 and the values reported in Table 3 showing an increase in the volume fraction of β precipitates in both the DRXed and un-DRXed regions as increasing the level of deformation strain. Figure 54(a) also shows that the intensity of the peaks corresponding to the basal planes (0002) and prismatic planes ($\bar{1}01\bar{0}$) varies as increasing the number of ECAP passes, where it is notorious that the prismatic texture was stronger as increasing the number of passes. This behavior suggests that texture was evolving during the severe deformation [7, 11, 141].

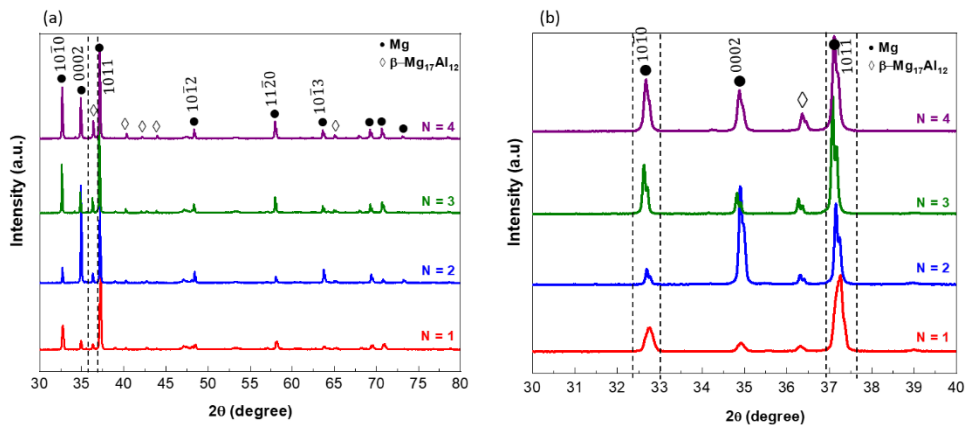


Figure 54. (a) XRD patterns of the ECAPed specimens with various number of ECAP passes. (b) Enlarged patterns for the three major peaks of the Mg matrix showing splitting and shifting of the peaks as increasing the number of ECAP passes.

Figure 54(b) shows an enlarged view of the three major peaks of the Mg matrix, in which it is seen that some of these peaks (highlighted by the vertical dashed lines) split and shift to lower angles as increasing the number of ECAP passes. Ma et al. [141]

attributed this behavior to different content of Al within the original un-DRXed grains and the newly formed DRXed grains.

5.2. Electrochemical and Corrosion Measurements

5.2.1 Corrosion Initiation in ECAPed Alloys with Bimodal Grain Structure

The corrosion initiation of ECAPed AZ91 alloys at different levels of deformation strain was investigated after immersion in 3.5 wt.% NaCl solution for 1 h. Figure 55 shows optical images of the ECAPed alloys with $N = 1$ (a and b) and $N = 4$ (d and e) before and after immersion in the electrolyte solution. The micrographs of the corroded specimens were taken after removal of corrosion products. From these images, it is seen that corrosion initiates in the DRXed regions with no evidence of corrosion occurring in the un-DRXed grains. To gain further insight in the morphology of the corrosion initiation in the DRXed regions, Figure 55(c) and (f) shows SEM micrographs of the ECAPed alloys after the short immersion test. It is clearly evident that corrosion initiates at the DRXed regions, in which it appears that corrosion occurs at the DRXed grain boundaries and it subsequently extends into the interior of the grains. This corrosion initiation at the DRXed grain boundaries occurs as a result of microgalvanic coupling between the β -Mg₁₇Al₁₂ precipitates and the adjacent α -Mg matrix leading to preferential dissolution of the α -Mg matrix and undermining of the β -phase that eventually detaches from the alloy. According to these results, the β -phase formed at the DRXed grain boundaries acts as an effective galvanic cathode that accelerates the anodic dissolution of the α -Mg matrix. This is in agreement with the dual role effect of the β -phase on the corrosion behavior of Mg-Al alloys, in which the presence of discontinuous

β -Mg₁₇Al₁₂ precipitates along the grain boundaries induces galvanic corrosion as these precipitates act as strong galvanic cathodes [121]. Comparing Figure 55(c) and (f), it seems that corrosion in the ECAPed alloy after the first pass is more severe and exhibits a higher penetration depth as compared to the corrosion observed in the ECAPed alloy after the fourth pass. This behavior can be related to the bigger size of the β -Mg₁₇Al₁₂ precipitates formed at the DRXed grain boundaries of the ECAPed alloy after the first pass as shown in Table 6, which can lead to deeper corrosion pits after the precipitates are peeled off from the alloy surface. In contrast, the smaller size of the β -Mg₁₇Al₁₂ precipitates in the ECAPed alloy after the fourth pass results in shallow corrosion pits. In addition to the intergranular corrosion occurring in the DRXed grain boundaries, it is also noticed that corrosion within the DRXed grains also occurs as highlighted by the enclosed yellow regions in Figure 55(f). This behavior is associated with micro-galvanic coupling between the nano-sized spherical β -Mg₁₇Al₁₂ precipitates formed at the interior of the DRXed grains and the adjacent α -Mg matrix. However, it is worth to notice that this intragranular corrosion process is less aggressive compared to the intergranular corrosion occurring at the DRXed grain boundaries. This is mainly attributed to the very small cathode-to-anode area ratio between the nano-sized precipitates at the interior of the grains and the neighboring α -Mg matrix that leads to a slow galvanic corrosion kinetics.

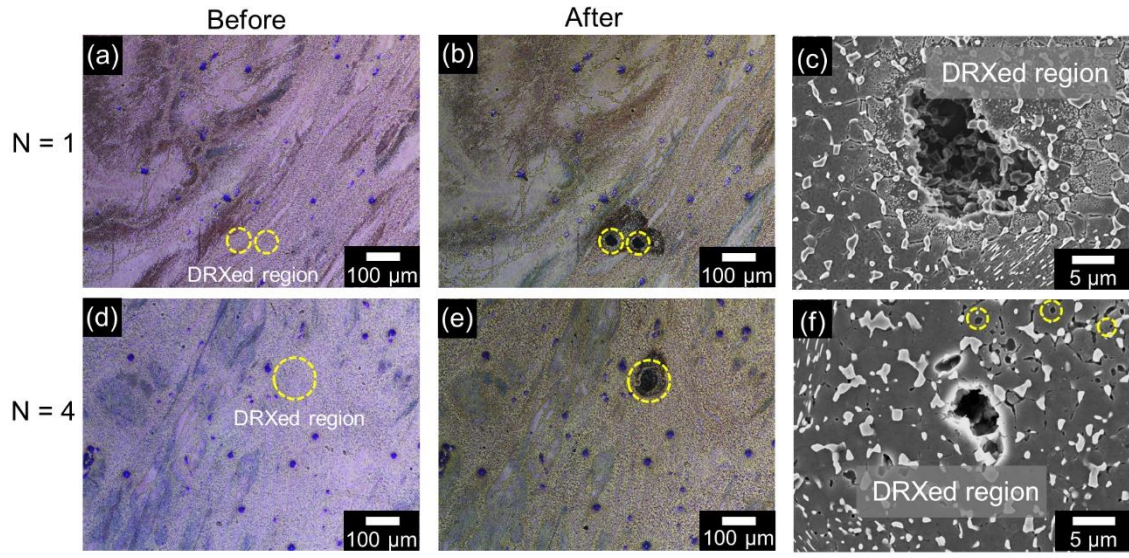


Figure 55. Optical micrographs of the ECAP alloys with (a, b) N = 1 and (c, d) N = 4 before and after immersion for 1 h in 3.5 wt.% NaCl solution. High magnification SEM micrographs of the (c) ECAP alloy with N = 1 and (d) ECAP with N = 4 after immersion for 1 h in 3.5 wt.% NaCl solution showing corrosion initiation in the DRXed regions.

To investigate the cause(s) for preferential corrosion of the DRXed regions, elemental mapping by STEM/EDS was performed on the recrystallized and non-recrystallized regions of an ECAPed alloy with the aim of determining differences in elemental composition between the β -Mg₁₇Al₁₂ phase and the α -Mg phase present in each region. Figure 56 shows STEM micrographs and EDS maps and point scan analysis from an un-DRXed and a DRXed region of an ECAPed alloy after four passes. Micrograph in Figure 56(a) corresponds to un-DRXed region showing the presence of the lath-shaped continuous β -Mg₁₇Al₁₂ precipitates while Figure 56(e) shows the DRXed region with the presence of β -Mg₁₇Al₁₂ precipitates formed at the DRXed grain boundaries and at the grain interior. From the EDS maps of Mg (b and f) and Al (c and g), it appears that there is a higher chemical difference between the matrix and

precipitates in the DRXed region as compared to the one in the un-DRXed region. This is further confirmed by elemental point analysis performed on the β -Mg₁₇Al₁₂ phase and α -Mg matrix in the DRXed and un-DRXed regions. Figure 56(i) shows that the β -Mg₁₇Al₁₂ precipitates formed in the DRXed grains exhibited higher aluminum content (36.2 at.%) than the lath-shaped continuous β -Mg₁₇Al₁₂ precipitates in the un-DRXed grains (33.6 at.%). In contrast, the Al content in the DRXed grains is lower (3.06 at.%) than in the un-DRXed grains (4.05 at.%). The higher microchemistry difference between the β -Mg₁₇Al₁₂ precipitates and matrix in the DRXed regions provides a higher driving force for microgalvanic coupling as compared to the galvanic corrosion activity developed in the un-DRXed region that will lead to preferential corrosion of the DRXed regions upon immersion. Ma et al. [141] reported similar findings when investigated the mechanisms of dynamic precipitation and recrystallization of Mg-9wt%Al alloy processed by ECAP. They found that the recrystallized grains exhibited lower Al solute content as compared to the heavily deformed coarse grains. They attributed these findings to the combined action of dynamic precipitation and recrystallization that promotes the formation of recrystallized grains with a near equilibrium concentration of Al, which is lower compared to the excess Al solute content in the original supersaturated α -Mg matrix. Indeed, they reported that the decrease in chemical potential energy due to the lower Al content in the recrystallized grain represents the dominant thermodynamic driving force for further recrystallization and formation of sub-micron α -Mg grains.

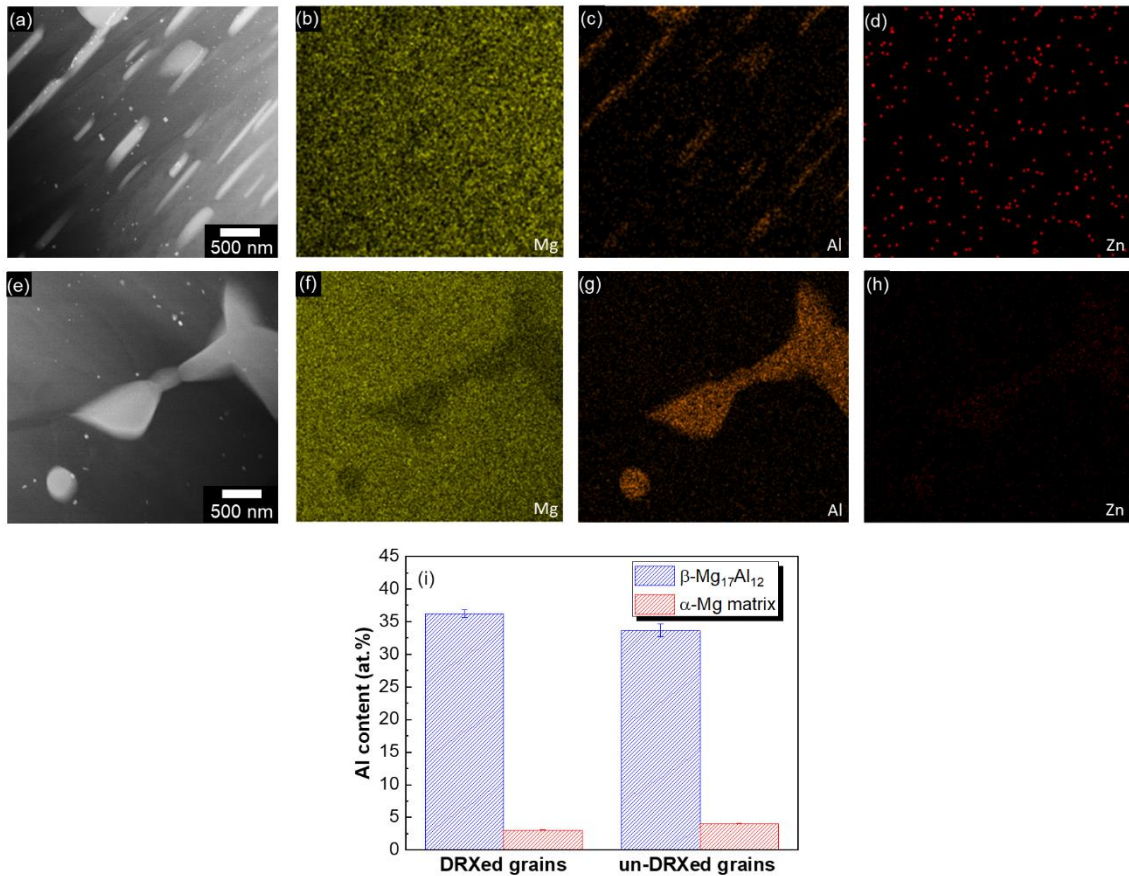


Figure 56. STEM micrographs of the ECAPed alloy with $N = 4$ showing (a) lath-shaped β -Mg₁₇Al₁₂ precipitates formed in the un-DRXed regions and (b) spherical β -Mg₁₇Al₁₂ precipitates formed in the DRXed regions with their corresponding EDS maps of (b, f) Mg, (c, g) Al and (d, h) Zn, respectively. (i) Average aluminum content of the β -Mg₁₇Al₁₂ phase and α -Mg matrix in the DRXed and un-DRXed regions.

It is worth mentioning that dislocation density can also play a role in the corrosion behavior of severely deformed magnesium alloys. Typically, regions with large density of dislocations results in higher anodic dissolution rates owing to the higher distorted energy of the crystallographic defects making these sites more electrochemically active for corrosion processes [24, 66, 135]. In partially recrystallized microstructures, it is well known that the recrystallized grains exhibit relatively lower

dislocation density compared to the heavily deformed unrecrystallized grains that possess a significantly higher dislocation density [7, 11]. In that sense, it would be expected that the unrecrystallized grains are more susceptible to corrosion than the recrystallized grains. However, this study shows that the preferential corrosion initiation and propagation occurs in the recrystallized grains despite they might exhibit a lower dislocation density as compared to the unrecrystallized grains. This behavior indicates that in the ECAPed alloys investigated in this study, the higher difference in microchemistry between the β -Mg₁₇Al₁₂ precipitates and the α -Mg matrix in the DRXed regions plays a more crucial role in the corrosion initiation and propagation than the presumably higher dislocation density in the un-DRXed grains. This corrosion behavior is opposite to the corrosion behavior of partially recrystallized aluminum alloys, in which corrosion preferentially occurred in the unrecrystallized grains due to the high level of stored energy (i.e., high dislocation density) of the subgrain boundaries in these grains that predominated over the intergranular corrosion at the grain boundaries decorated with secondary phases but with less stored energy [146, 147].

The out-of-plane crystal orientation of an ECAPed alloy with four passes have been examined by electron backscatter diffraction (EBSD) to analyze the crystallographic orientation of the DRXed and un-DRXed regions. The inverse pole figure (IPF) map shown in Figure 57(a) has been divided into fine grains and coarse grains IPF maps based on the grain size (6 μ m). As shown in Figure 57(a), dense fine grains occupy most of the region after four ECAP passes indicating a high DRX ratio and the original elongated coarse grains were surrounded and intersected by these

newly-formed fine grains. The pole figure (PF) of the (0002) plane orientation and maximum intensity of the un-DRXed region (Max. intensity = 51.17) indicate a stronger basal texture than the DRXed region (Max. intensity = 5.77). These results are in well agreement with previous studies investigating the crystal orientation of partially recrystallized magnesium alloys [92, 100, 148]. To further examine the DRXed region, Figure 57(b) shows a zoom-in of the black rectangle in Figure 57(a). From Figure 57(b), it is seen that the average grain size of the equiaxed DRXed grains is $1.82 \mu\text{m} \pm 1.96$, which is relatively similar to the values reported in Table 6. The (0002) pole figure in Figure 57(b) exhibits a similar texture as the one of the DRXed grains in Figure 57(a), which confirms the weak basal texture of the DRXed region as compared to basal texture of the un-DRXed region. These results clearly reveal that the un-DRXed grains exhibit a preferential basal texture whereas the DRXed grains are characterized by a more random texture. As mentioned in chapter I, the crystallographic orientation can also play an important role in the corrosion behavior of magnesium alloys. It has been widely and consistently reported that grains with basal crystal orientation are more corrosion resistant than grains with non-basal crystal orientation [14, 70-72, 148]. The higher corrosion resistance of the closely packed basal plane has been associated with its higher atomic density that results in higher binding energy, lower surface energy, and higher activation energy for removal of atoms from the metal lattice [54, 72]. Thus, the basal plane exhibits a higher electrochemical stability and corrosion resistance than the less packed non-basal planes. According to this, it is expected that the DRXed region with a weak basal texture in the ECAPed alloy with four passes is more prone to

corrosion than the highly textured un-DRXed region. Thus, in addition to the higher microchemistry difference between the β -Mg₁₇Al₁₂ phase and α -Mg matrix in the DRXed region, the more random crystal orientation of the DRXed grains can also explain the fact that corrosion preferentially initiates in the DRXed region. These results are in agreement with a previous study reported by Luo et al., who investigated the effect of grain size and crystal orientation on the corrosion behavior of an extruded Mg-6Gd-2Y-0.2Zr alloy. They found that small grains with non-basal orientation were the preferential sites for corrosion initiation in a 5 wt.% NaCl solution. According to the results shown so far, it is believed that the combined effect of lower microchemistry difference between precipitate and matrix and strong basal texture in the un-DRXed grains predominate over the presumably higher dislocation density in these grains, such that they are more corrosion resistant than the DRXed grains.

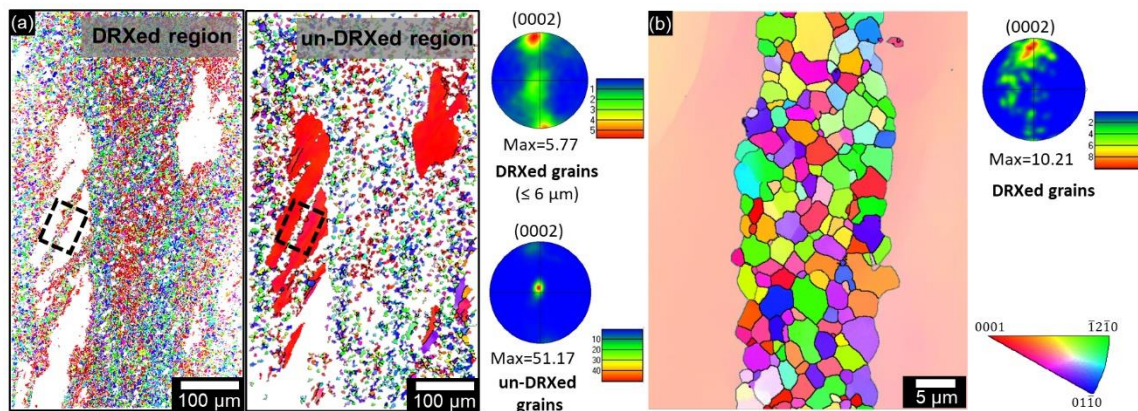


Figure 57. EBSD IPF maps (out-of-plane crystal orientation) of ECAPed alloy with $N = 4$: (a) large region mapping with both DRXed grains and un-DRXed grains with their corresponding (0002) pole figures and (b) zoom-in map from the black rectangle in (a) showing detailed grains information of the DRXed region along with the corresponding (0002) pole figure.

5.2.2 Localized Volta Potential Distribution in the Recrystallized and Non-Recrystallized Regions

SKPFM measurements were performed to further support the results shown above regarding the stronger microgalvanic coupling in the DRXed regions that leads to preferential corrosion initiation in these regions. SKPFM allows to investigate the local nobility of the different constituents in a material such that, it is possible to predict potential cathodes and anodes that will be developed during immersion testing in corrosion environments. Figure 58 shows topography (a) and (d) and Volta potential maps (b) and (e) from the un-DRXed and DRXed regions of an ECAPed alloy after 4 passes. The Volta potential is associated with the electronic activity of a specific phase in the material; typically, the larger the Volta potential with respect to the probe the higher the electrochemical activity under immersion conditions [149]. In that sense, dark and light areas in the Volta potential maps correspond to cathodic and anodic sites, respectively. Figure 58(b) and (e) shows that the β -Mg₁₇Al₁₂ precipitates formed in both the un-DRXed and DRXed regions are cathodic against the α -Mg matrix showing a large potential difference between them. This cathodic behavior is expected since the β -phase is significantly enriched in Al compared to the Al-depleted α -Mg matrix. From these results, it is expected that these precipitates can induce microgalvanic corrosion at the β -phase/ α -Mg matrix interphase when the ECAPed alloy is immersed in an aggressive solution. However, the line profiles shown in Figure 58(c) and (f) shows that the absolute value of the Volta potential difference (VPD) between the β -Mg₁₇Al₁₂ precipitates formed in the DRXed grain boundaries and the α -Mg matrix is higher (86

mV) compared to the VPD between the lath-shaped continuous $\beta\text{-Mg}_{17}\text{Al}_{12}$ precipitates and the $\alpha\text{-Mg}$ matrix in the un-DRXed region (73 mV). This indicates that the β -phase and $\alpha\text{-Mg}$ matrix in the DRXed region forms a stronger galvanic coupling and therefore, the DRXed regions are more susceptible to microgalvanic corrosion. These results support the difference in chemical composition observed from the STEM/EDS analysis shown in Figure 56, in which it was found that there is a higher difference in microchemistry between the β -phase and the $\alpha\text{-Mg}$ matrix in the DRXed region compared to the one in the un-DRXed region that can provide a higher driving force for microgalvanic corrosion.

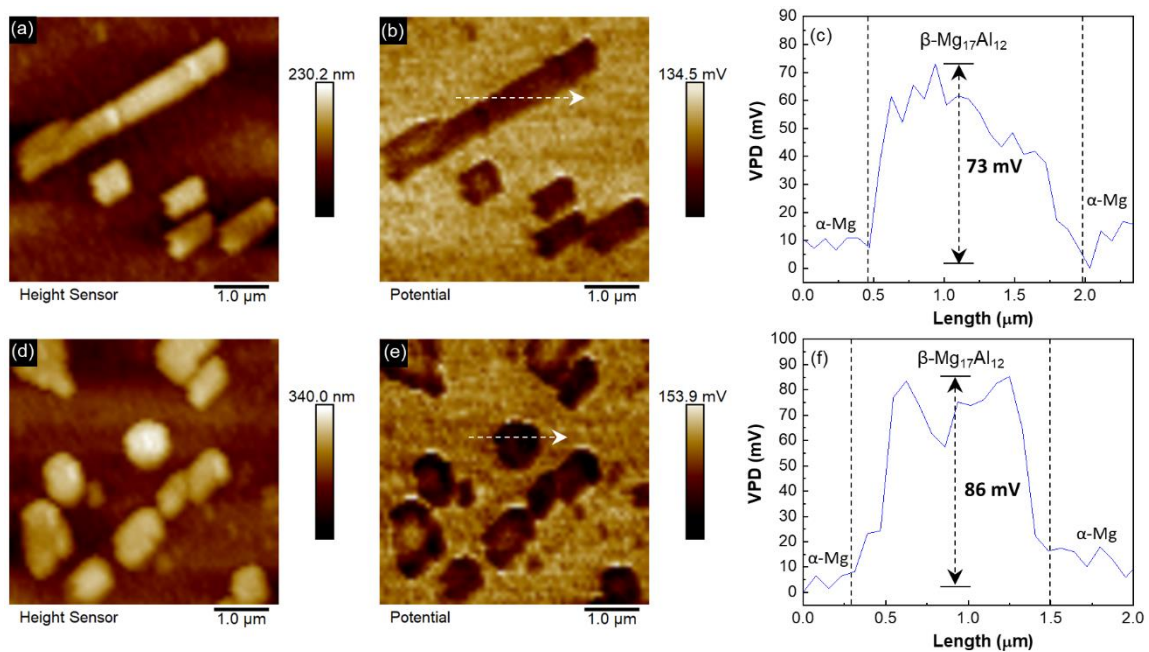


Figure 58. SKPFM measurements of the ECAPed alloy with $N = 4$ showing (a, d) topography, (b, e) Volta potential difference map, and (c, f) the corresponding line profile along the white arrow of a lath-shaped $\beta\text{-Mg}_{17}\text{Al}_{12}$ precipitate in the un-DRXed grains and a spherical $\beta\text{-Mg}_{17}\text{Al}_{12}$ precipitate in the DRXed grains, respectively.

5.2.3 Localized Electrochemical Behavior of Recrystallized and Non-Recrystallized Regions

The local electrochemical behavior of the DRXed and un-DRXed regions of an ECAPed alloy with fourth ECAP passes was investigated by means of the electrochemical microcell technique. Figure 59(a) and (b) show optical images of the ECAPed alloy with fourth passes indicating the DRXed and un-DRXed regions before and after the potentiodynamic polarization (PDP) test in 3.5 wt.% NaCl solution. The local potentiodynamic polarization measurements in the DRXed and un-DRXed regions are shown in Figure 59(c). From these PDP curves, it is clearly noticed that the un-DRXed region exhibits a more noble corrosion potential (-1.495 V vs. SCE) than the corrosion potential in the DRXed region (-1.564 V vs. SCE). Furthermore, it is also seen that the corrosion current density of the un-DRXed region ($4.16 \mu/\text{cm}^2$) is lower than that of the DRXed region ($10.2 \mu/\text{cm}^2$). The lower electrochemical activity of the un-DRXed grains is in agreement with the SKPFM results that show smaller Volta potential difference between the lath-shaped continuous $\beta\text{-Mg}_{17}\text{Al}_{12}$ precipitates and $\alpha\text{-Mg}$ matrix in the un-DRXed grains as compared to the Volta potential difference developed in the DRXed regions between the $\beta\text{-Mg}_{17}\text{Al}_{12}$ precipitates at the DRXed grain boundaries and the neighboring $\alpha\text{-Mg}$ matrix. These local electrochemical results confirmed that the DRXed region exhibits a faster corrosion reaction kinetics than the un-DRXed region, which is in agreement with the preferential corrosion initiation in the DRXed grains observed after the short-term immersion testing shown in Figure 55. In addition, the faster corrosion kinetics of the DRXed region suggests that corrosion propagation at

longer immersion time will tend to proceed along the DRXed grains and less corrosion attack should be expected in the un-DRXed grains.

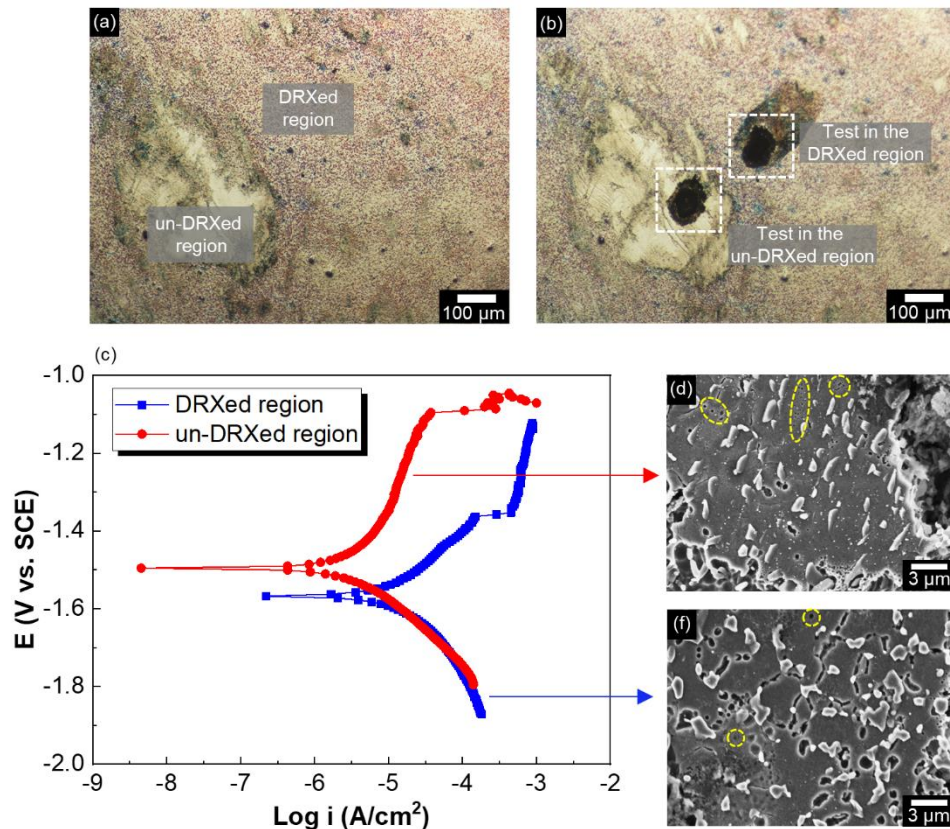


Figure 59. Optical micrographs of the ECAPed alloy with fourth passes (a) before and (b) after the local potentiodynamic polarization test in 3.5 wt.% NaCl using the electrochemical microcell technique. (c) local potentiodynamic polarization curves of the DRXed and un-DRXed regions in the ECAPed alloy with fourth passes. SEM micrographs of the (d) un-DRXed region and (f) the DRXed region after the local electrochemical test and after removal of corrosion products.

As explained above, the higher electrochemical activity of the DRXed regions can be associated with the higher microchemistry difference between the β -Mg₁₇Al₁₂

precipitates formed at the DRXed grain boundaries and the adjacent α -Mg matrix that will induce a stronger microgalvanic coupling. It is also likely that the higher corrosion susceptibility of the DRXed grains is related to the weaker basal texture of these grains as compared to the highly textured un-DRXed grains, which makes the DRXed grains more vulnerable to electrochemical reactions. Figure 59(d) and (f) show SEM micrographs of the un-DRXed and DRXed regions, respectively, after the local potentiodynamic polarization test and after removal of the corrosion products. From comparison of Figure 59(d) and (f), it is seen that corrosion in the DRXed region seems more aggressive than in the un-DRXed region, which is in accordance with the higher corrosion current density obtained for the DRXed region. Furthermore, it is clearly seen in Figure 59(f) that corrosion in the DRXed region occurs mainly at the DRXed grain boundaries due to microgalvanic coupling between the β -Mg₁₇Al₁₂ precipitates formed at the grain boundaries and the adjacent α -Mg matrix that leads to preferential corrosion of the matrix. A minor corrosion was also observed at the interior of the DRXed grains (highlighted by the yellow circles in Figure 59(f)) that as mentioned above can be related to micro-galvanic coupling between the nano-sized β -Mg₁₇Al₁₂ precipitates within the DRXed grains and the adjacent α -Mg matrix. It is likely that this micro-galvanic coupling will not play a significant role in the corrosion propagation of the DRXed region due to the significantly small cathode-to-anode area ratio that drastically limits the reaction kinetics of this galvanic process. Similar to the DRXed region, micro-galvanic corrosion is also observed in the un-DRXed region (Figure 59(d)) occurring at the interface between the lath-shaped continuous β -Mg₁₇Al₁₂ precipitates and the

surrounding α -Mg matrix. However, it is worth to notice that corrosion also occurs in the bulk of the α -Mg matrix as highlighted by the yellow circles in Figure 59(d). These results indicate that the microgalvanic coupling between precipitate and matrix in the un-DRXed region is relatively weak, such that, microgalvanic corrosion is not the only corrosion mechanism taking place in the un-DRXed region and instead localized corrosion in the bulk matrix can also occur by means of preferential anodic dissolution.

5.2.4 Corrosion Propagation in ECAPed Alloys with Bimodal Grain Structure

Immersion testing for longer time was also performed to investigate the corrosion propagation in ECAPed alloys at different levels of deformation strain. Figure 60 shows SEM micrographs of the ECAPed alloys with $N = 1$ and $N = 4$ after immersion in a 3.5 wt.% NaCl solution for 24 h and after removal of corrosion products. Figure 60(a-c) show the corroded morphology of the ECAPed alloy after the first pass while Figure 60(d-f) corresponds to the morphology of the ECAPed alloy after the fourth pass. Comparing the low magnification SEM micrographs in Figure 60(a) and (d), it is clearly evident that the ECAPed alloy after the first pass exhibits a more severe and localized corrosion compared to the ECAPed alloy after the fourth pass that shows a more uniform corrosion morphology with a relatively shallow penetration depth. As mentioned above, the deeper penetration observed for the ECAPed alloy after the first pass can be related to the bigger size of the β -Mg₁₇Al₁₂ precipitates along the DRXed grain boundaries that after peeling-off from the alloy due to micro-galvanic corrosion, a wider and deeper corrosion pit will be developed on the attacked region. The bigger corrosion pits formed on the ECAPed alloy after the first pass exposes a bigger active area that further

accelerates the corrosion rate at these regions. In addition, it was also shown above that corrosion preferentially initiates in the DRXed regions due to the stronger micro-galvanic coupling between the β -Mg₁₇Al₁₂ precipitates along the DRXed grain boundaries and the adjacent α -Mg matrix. According to this and owing to the fact that the ECAPed alloy after the first pass exhibits a low DRXed ratio (i.e., lower volume fraction of DRXed grains; 39% for N = 1), it is expected that corrosion in this alloy will appear more localized and it will penetrate deeper into the DRXed regions of the material. In contrast, the lower size of the β -Mg₁₇Al₁₂ precipitates along the DRXed grain boundaries of the ECAPed alloy after the fourth pass combined with a higher DRXed ratio results in a less severe and uniform corrosion that spreads through the high volume fraction of DRXed grains. It is also likely that the higher volume fraction of well-dispersed fine β -Mg₁₇Al₁₂ precipitates formed in the ECAPed alloy after the fourth pass can further promote a more uniform corrosion morphology. This is because numerous micro-galvanic cells will be formed over almost the entire alloy surface preventing the development of a highly localized attack.

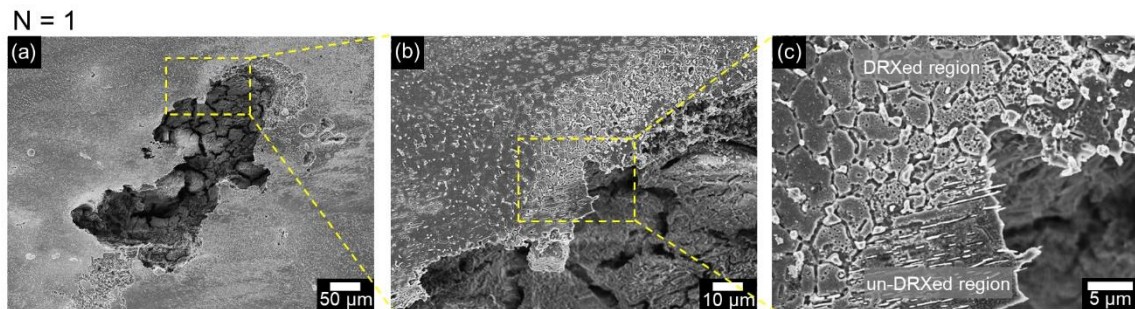


Figure 60. SEM micrographs of the ECAP alloys with (a, b, c) N = 1 and (d, e, f) N = 4 after immersion for 24 h in 3.5 wt.% NaCl solution.

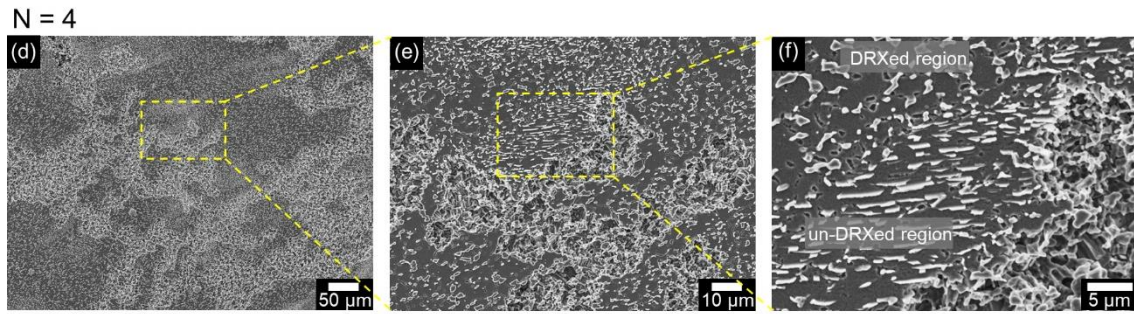


Figure 60. Continued.

From high magnification SEM images, it is seen that corrosion in both ECAPed alloys is mainly concentrated in the DRXed regions. For the ECAPed alloy after the first pass, severe corrosion is observed in the DRXed regions as shown in Figure 60(c), in which corrosion initiates along the grain boundaries due to microgalvanic corrosion and then it propagates into the grain interiors. Figure 60(c) also reveals that in addition to the microgalvanic corrosion occurring at the DRXed grain boundaries, corrosion in the un-DRXed regions is also evident, in which it appears that corrosion initiated at the interphase between the lath-shaped precipitates and the adjacent α -Mg matrix due to microgalvanic corrosion between these phases. However, it is worth to notice that the corrosion in the un-DRXed region is significantly less severe in comparison to the corrosion developed in the DRXed region. Figure 60(f) shows that the corrosion in the ECAPed alloy after the fourth pass is remarkably less aggressive than in the ECAPed alloy after the first pass. Furthermore, it is noticed that corrosion mainly takes place in the DRXed region and almost no corrosion attack was identified in the un-DRXed region. This behavior can be related to microstructural changes in the recrystallized and non-recrystallized regions as increasing the level of deformation strain that will induce a

more distinct difference in the electrochemical activity of the DRXed and un-DRXed regions, such that corrosion will preferentially initiate and propagate through the DRXed regions. These observations are in agreement with the local PDP results obtained from the electrochemical microcell technique, in which the DRXed region exhibits a higher corrosion current density as compared to the one in the un-DRXed region, indicating that the DRXed regions has indeed a faster corrosion kinetics that will promote the corrosion development along these regions.

To evaluate the penetration depth of the ECAP alloys at different levels of deformation strain, 3D profilometry analysis were performed after immersion for 24 h. Figure 61 shows topography and roughness profiles of the ECAPed alloys with $N = 1$ and $N = 4$ after immersion for 24 h and after removal of corrosion products. In accordance with Figure 60, the topography maps show that corrosion in the ECAPed alloy after the first pass is more localized and exhibits a higher penetration depth as compared to the ECAPed after the fourth pass, which is characterized by a more uniform corrosion with a shallow penetration depth. Figure 61 also includes linear roughness profiles along the regions with the highest penetration (i.e., blue regions) to analyze the changes in penetration depth as increasing the level of strain. The roughness parameters, R_a (arithmetical mean height) and R_z (maximum height profile) were extracted from the depth profile; these parameters represent the average roughness and the maximum roughness along the line profile, respectively. The uncorroded areas served as the baseline for calculating the maximum roughness such that, these values correspond to the maximum pit depth. In that sense, it is seen that the maximum pit depth in the

ECAPed alloy after the first pass is drastically higher (113.64 μm) than the maximum pit depth in the ECAPed alloy after the fourth pass (7.71 μm). These results confirm that smaller DRX ratio combine with bigger precipitates formed along DRXed grain boundaries promote the development of a localized corrosion morphology with high penetration depth. In contrast, the higher DRXed ratio and the smaller precipitates along the DRXed grain boundaries of the ECAPed alloy after the fourth pass will facilitate the formation of a more uniform corrosion morphology with a shallow penetration depth.

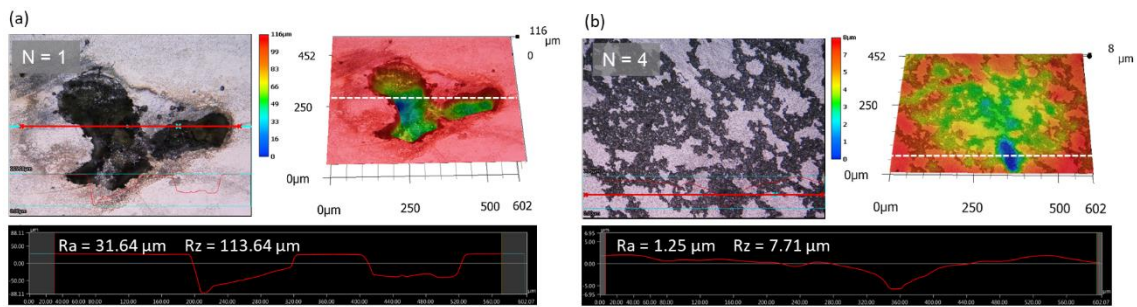


Figure 61. Topography and roughness profiles of the ECAPed alloys with (a) $N = 1$ and (b) $N = 4$ after immersion in 3.5 wt.% NaCl for 24 h.

Figure 62 shows the variation of the maximum penetration depth as function of the size of the $\beta\text{-Mg}_{17}\text{Al}_{12}$ precipitates formed at the DRXed grain boundaries for the different ECAPed alloys. Figure 62 shows that there is linear correlation between the maximum penetration depth and the size of the $\beta\text{-Mg}_{17}\text{Al}_{12}$ precipitates formed at the DRXed grain boundaries, in which it is evident that as increasing the level of deformation strain, the size of the precipitates becomes smaller, and these finer precipitates will consequently result in lower penetration depths. As explained above,

corrosion in the DRXed regions occurs through microgalvanic coupling between the β -phase along the grain boundaries and the adjacent α -Mg matrix with the preferential dissolution of the matrix. This microgalvanic corrosion process results in undermining and subsequent detachment of the β -phase from the alloy leaving behind corrosion pits in the attacked regions. As a result, the bigger the precipitates the wider and deeper the corrosion pits. These observations therefore confirm that increasing the level of deformation strain during ECAP processing of AZ91 alloy will be beneficial for promoting the formation of shallow corrosion pits upon immersion of the alloy in chloride containing media.

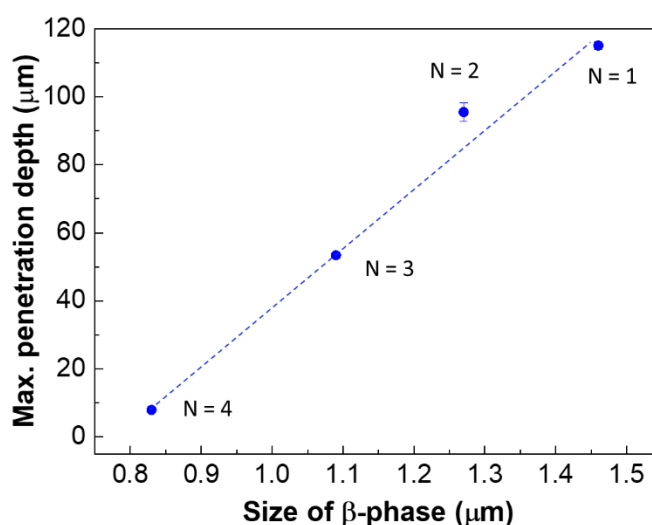


Figure 62. Maximum penetration depth of the ECAPed alloys after 24 h of immersion in 3.5 wt.% NaCl solution against size of the β -Mg₁₇Al₁₂ precipitates formed at the grain boundaries of the DRXed grains.

5.2.5 Influence of Dynamic Recrystallization and Refined Precipitates on the Corrosion Rate

Corrosion rate was obtained from weight loss measurements of the ECAPed alloys after different ECAP passes immersed in 3.5 wt.% NaCl solution for seven days. Figure 63(a) shows that the corrosion rate appears to exhibit a linear relationship with the number of ECAP passes, in which the corrosion rate decreases as increasing the number of passes. The inserted corroded morphologies shown in Figure 63(a) shows that there is substantial loss of material after the first and second ECAP passes, particularly from the periphery of the material, however the loss of material is significantly reduced after the third and fourth ECAP passes. These results further confirm that increasing the level of deformation strain improves the corrosion resistance of the ECAPed alloys. The corrosion rate decreases from 4.43 mmpy after the first ECAP pass to 1.68 mmpy after the fourth pass. The decrease in corrosion rate as increasing the strain level is mainly attributed to the presence of fine β -Mg₁₇Al₁₂ precipitates along the DRXed grain boundaries that promote shallow pitting during the micro-galvanic corrosion process that leads to less material loss. The lower corrosion rate as increasing the number of ECAP passes can also be related to an increase in the DRX ratio and volume fraction of well-distributed fine β -Mg₁₇Al₁₂ precipitates that can prevent the development of severe and accelerated localized corrosion attack. Instead, these microstructural features can promote a more uniform corrosion. Furthermore, it has been also reported that the corrosion resistance of AZ91 alloys after severe plastic deformation is enhanced due to the formation of uniformly distributed fine β -Mg₁₇Al₁₂ precipitates, which can induce

the formation of an Al-rich oxide layer at the alloy surface that exhibits a more protective ability against chloride species as compared to the traditional MgO/Mg(OH)₂ layer [150]. It is speculated that the Al-rich oxide layer is formed due to redeposition of β -Mg₁₇Al₁₂ precipitates on the alloy surface during the micro-galvanic corrosion process [150].

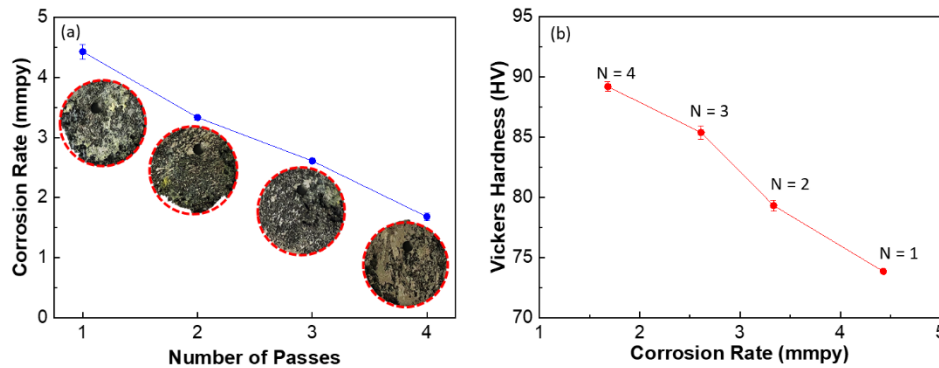


Figure 63. (a) Corrosion rate obtained from weight loss measurements of the ECAPed alloys immersed in 3.5 wt.% NaCl solution for seven days. (b) Vickers hardness against corrosion rate for the different ECAPed samples showing the simultaneous improvement in hardness and corrosion resistance as increasing the number of ECAP passes.

Figure 63(b) shows the variation of Vickers hardness against corrosion rate obtained from the weight loss measurements of the ECAPed alloys after immersion in 3.5 wt.% NaCl solution for seven days. This plot shows that increasing the level of strain during ECAP processing results in a simultaneous improvement of hardness and corrosion resistance. The hardness increases from 73.8 HV after the first ECAP pass to 89.1 HV after the fourth pass. The improvement in hardness as increasing the level of deformation strain can be mainly attributed to grain boundary strengthening and

precipitation hardening [3, 7, 11, 100]. The grain boundary strengthening is associated with the significant grain refinement during ECAP processing, which is promoted by DRX and pinning effect of the β -Mg₁₇Al₁₂ precipitates at the DRXed grain boundaries that can restrict grain growth. In addition, the precipitation hardening is related to the formation of a high volume fraction of fine β -Mg₁₇Al₁₂ precipitates due to SIDP during ECAP processing. It is well known that smaller grain size enhances the grain boundary strengthening according to the Hall-Petch relationship while finer precipitates promote a more effective strengthening via the Orowan mechanism [3, 141, 151]. Thus, the combination of smaller DRXed grain size, higher DRX ratio and higher volume fraction of uniformly distributed fine β -Mg₁₇Al₁₂ precipitates that results as increasing the number of ECAP passes contributes to the improvement of hardness (and strength) of the ECAPed alloys. The simultaneous improvement of hardness and corrosion resistance of the ECAPed AZ91 alloys at high levels of severe plastic strain provides a potential opportunity for the use of magnesium alloys in a wide variety of engineering applications.

5.2.6 Influence of Dynamic Recrystallization and Dynamic Precipitation on the Passive Behavior

It has been widely reported that grain refinement can be beneficial to improve the corrosion resistance of magnesium alloys [14, 24, 152]. Most of these studies agree that the improvement of corrosion resistance with decreasing the grain size is mainly attributed to the formation of a more coherent, uniform, and protective oxide film, which is more resistance to localized breakdown by aggressive species. In order to analyze the

influence of DRXed grain size on the corrosion behavior of ECAPed AZ91 alloys, electrochemical measurements including OCP, potentiodynamic polarization and EIS were conducted on the ECAPed alloys after different number of ECAP passes in a diluted 0.05 M NaCl solution. The diluted NaCl solution allows to identify passivation regions as well as differences in the breakdown potential as increasing the number of ECAP passes (i.e., decreasing the DRXed grain size). Figure 64(a) shows the OCP evolution of the ECAPed alloys during one hour of immersion in the 0.05 M NaCl solution prior to EIS and potentiodynamic polarization test. A similar OCP trend is observed for the different ECAPed alloys, in which the OCP values rapidly increase after the first few minutes of immersion (~ 10 min) and then these values tend to stabilize at longer immersion time. The initial increase in OCP has been related to the formation of an oxide film on the alloy surface while the plateau at longer immersion time suggests that the oxide film is protective and stable with no evidence of localized breakdown under the immersion conditions [16]. After 1 h of immersion, it is seen that the OCP values are more positive as increasing the number of ECAP passes; Table 7 shows that the OCP value of the ECAPed alloy after the first pass is -1.540 V vs. SCE while the OCP value of the ECAPed alloy after the fourth pass is -1.492 V vs. SCE corresponding to an increase of about 50 mV. Previous studies have reported that more positive OCP values are associated with more protective oxide films [16, 18]. In that sense, the results shown herein indicate that increasing the level of strain promotes the formation of a more protective oxide film.

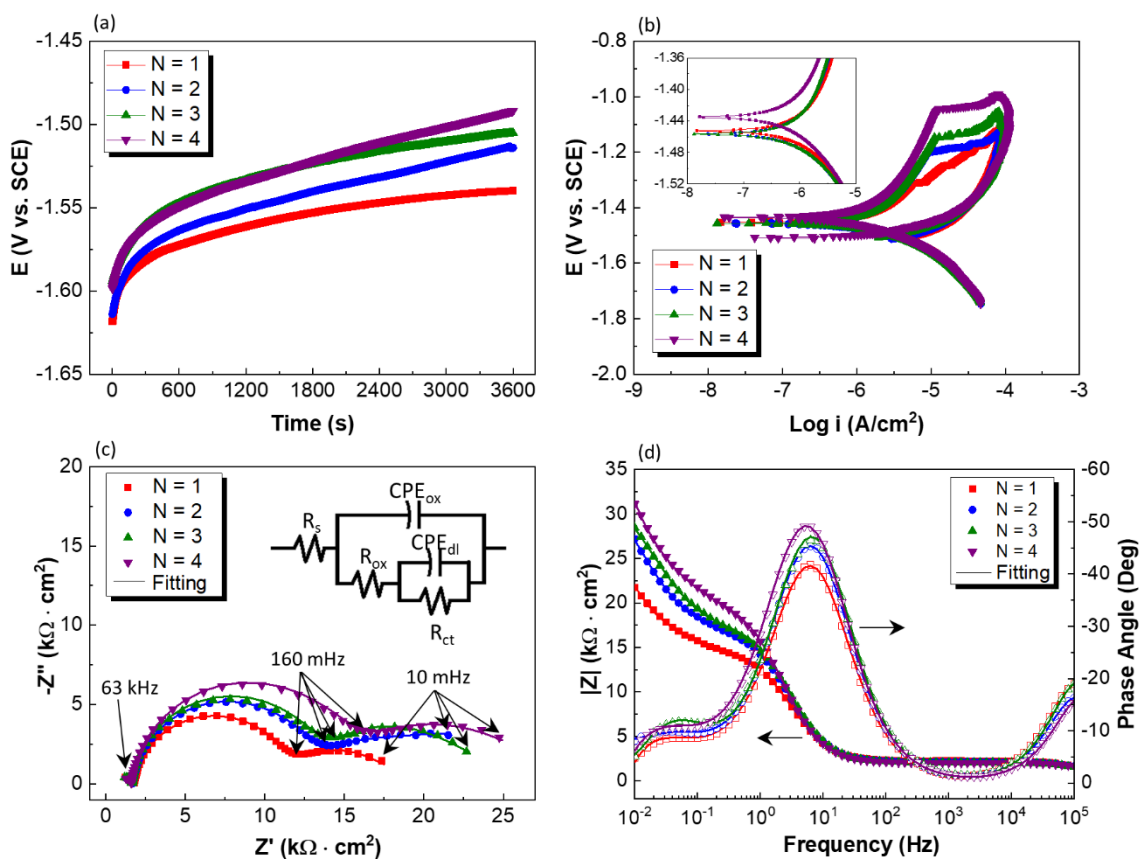


Figure 64. (a) Open circuit potential (OCP), (b) potentiodynamic polarization and EIS measurements showing the (c) Nyquist representation and the (d) the Bode plot of ECAPed alloys with various number of passes immersed in 0.05 M NaCl solution.

Table 7. Electrochemical parameters obtained from OCP and polarization measurements of ECAPed AZ91 alloys after different ECAP passes immersed in 0.05 M NaCl solution

Passes	OCP	E_{corr}	i_{corr}	E_b	$E_b - E_{corr}$
	(V vs. SCE)	(V vs. SCE)	($\mu\text{A}/\text{cm}^2$)	(V vs. SCE)	(V)
1	-1.540	-1.452	1.530	-1.308	0.144
2	-1.514	-1.457	1.306	-1.201	0.256
3	-1.505	-1.457	1.214	-1.143	0.314
4	-1.492	-1.434	1.021	-1.042	0.392

To further investigate the protective properties of the oxide films formed on the ECAPed alloys, potentiodynamic polarization measurements were performed in the diluted 0.05 M NaCl solution. Figure 64(b) shows the potentiodynamic polarization curves of the ECAPed alloys immersed in 0.05 M NaCl solution. In addition, Table 7 summarizes the values of corrosion potential (E_{corr}), corrosion current density (i_{corr}), breakdown potential of the oxide film (E_b), and the magnitude of the passive region ($E_b - E_{\text{corr}}$) that were derived from Tafel extrapolation. From Table 7, it is seen that E_{corr} values are slightly more positive and i_{corr} values are smaller as increasing the strain level. The i_{corr} values decrease from $1.530 \mu\text{A}/\text{cm}^2$ for the ECAPed alloy after the first pass to $1.021 \mu\text{A}/\text{cm}^2$ for the ECAPed alloy after the fourth pass. According to Faraday's law, the lower i_{corr} values indicate that the corrosion rate of the ECAPed alloys decreases as increasing the strain level, which is in agreement with the weight loss measurements reported in Figure 63. The cathodic and anodic branches of the polarization curves in Figure 64(b) represent the hydrogen evolution and the dissolution of Mg, respectively. Figure 64(b) clearly shows that the ECAPed alloys exhibit a passive behavior in the anodic branch, which corroborates the formation of an oxide film on the alloy surface. Furthermore, Figure 64(b) shows that the breakdown potential of the oxide film increases as increasing the level of strain. From Table 7, it is seen that E_b of the ECAPed alloy after the first pass is -1.308 V vs. SCE whereas the E_b of the ECAPed alloy after the fourth pass is -1.042 V vs. SCE . According to these results, there is an increase in the magnitude of the passive region ($E_b - E_{\text{corr}}$) as increasing the strain level, where the passive region of the ECAPed alloy after the first pass has a magnitude of 144 mV ,

while this magnitude increases to 392 mV after the alloy is extruded for four passes. The inset in Figure 64(b) also shows that the anodic current density decreases as increasing the strain level. These results further confirmed that the protective properties of the oxide film are enhanced as increasing the strain level. Consequently, it is believed that the significant grain refinement of the DRXed grains and the higher volume fraction of DRXed grains that result as increasing the strain level promote the formation of a more protective oxide film with a higher resistance to localized breakdown by aggressive species.

A similar cathodic response is observed for the ECAPed alloys indicating that the cathodic reaction rate (i.e., hydrogen evolution rate) is not significantly influenced by the level of strain. From the inset in Figure 64(b), it is seen that there is a slightly increase in the cathodic current density as increasing the strain level; this behavior has been associated with the increase in the volume fraction of β -Mg₁₇Al₁₂ precipitates as increasing the strain level that serves as sites for cathodic reactions resulting in a faster cathodic reaction kinetics [14]. However, Table 7 shows that there is an overall decrease in the i_{corr} values as increasing the strain level, these results suggest that the decrease in the anodic current density as increasing the strain level predominates over the slightly increase in cathodic current density. Thus, the corrosion process of the ECAPed alloys in the diluted NaCl solution is controlled by the anodic reaction kinetics (i.e., protective properties of the oxide film).

Ralston et al. [153] provided a linear correlation between corrosion current density and the reciprocal square root of grain size ($d^{-1/2}$), analogous to the Hall-Petch

relation; $i_{\text{corr}} = A + Bd^{-1/2}$, where the constant A was related to the nature of the environment while constant B was associated with material properties. According to this relationship and for negative values of B, it is evident that i_{corr} decreases as decreasing grain size. They attributed the enhanced corrosion resistance with decreasing grain size to the formation of a more protective oxide film. In this study, a similar correlation was found, however, instead of correlating i_{corr} with the grain size, a relationship between the magnitude of the passive region ($E_b - E_{\text{corr}}$) and grain size was analyzed. It is believed that the magnitude of the passive region ($E_b - E_{\text{corr}}$) obtained from the anodic branch of the polarization curve represents a better parameter to analyze the protective properties of the oxide film as function of grain size. Figure 65(a) shows the variation of $E_b - E_{\text{corr}}$ as function of grain size. It is clearly seen that there is an excellent linear correlation between $E_b - E_{\text{corr}}$ and $d^{-1/2}$, in which decreasing the grain size (i.e., increasing the number of ECAP passes) results in a higher passivation region, and therefore in a more protective oxide film with a higher resistance to localized breakdown by aggressive species. It has been reported that the high volume fraction of grain boundaries (i.e., smaller grains size) in ultra-fine grained magnesium alloys serve as nucleation sites for the oxide film formation resulting in a more compact and adherent surface protective layer [18, 65, 154]. Other authors have proposed that ultra-fine grained microstructures can relieve stresses induced at the substrate/oxide interface due to the volume mismatching between the Mg substrate and the MgO layer, resulting in a MgO layer that is less susceptible to cracking, and therefore more resistant against migration of aggressive species [14, 24]. Furthermore, for Mg-Al alloys with high aluminum content

such as the AZ91 alloy, the grain size is not the only determining factor that can influence the properties of the oxide film [14]. It is believed that the high volume fraction of β -Mg₁₇Al₁₂ precipitates at the DRXed grain boundaries can also play an important role on enhancing the protective ability of the oxide film as they can promote the formation of an aluminum-enriched oxide (Mg, Al)_xO_y film with better protective properties than the semi-protective MgO/Mg(OH)₂ oxide film and with a higher stability over a wide range of pH values [102, 150]. Figure 65(b) shows the variation of $E_b - E_{corr}$ as function of the volume fraction of β -Mg₁₇Al₁₂ precipitates at the DRXed grain boundaries for the different ECAPed alloys. It is seen that the magnitude of the passive region increases as increasing the volume fraction of precipitates (i.e., increasing the strain level). Although the relationship between these parameters seem to be more complex than the one between $E_b - E_{corr}$ and $d^{-1/2}$, it is clearly evident that increasing the volume fraction of precipitates can contribute in the formation of a more protective and stable passive film with a higher resistance to localized breakdown. According to this, it is likely that the significant grain refinement coupled with a high volume fraction of well-distributed β -Mg₁₇Al₁₂ precipitates can provide a synergistic effect on promoting the formation of a more protective oxide film, and this synergistic effect can overcome the negative effect of the β -Mg₁₇Al₁₂ precipitates in accelerating the cathodic reaction kinetics.

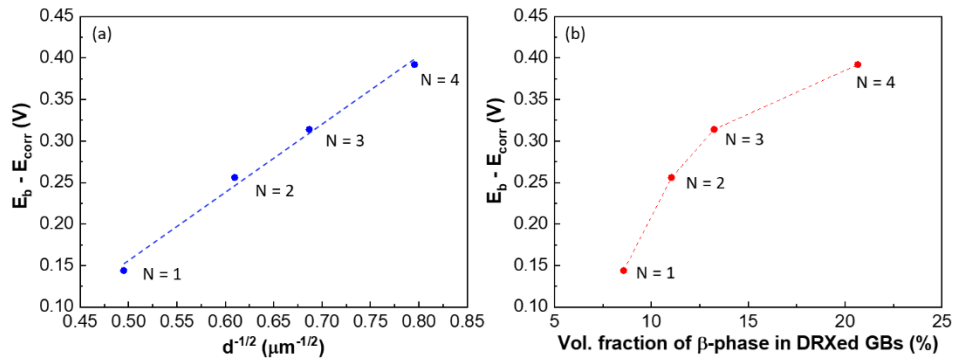


Figure 65. Variation of $E_b - E_{\text{corr}}$ of the ECAPed alloys with different number of ECAP passes against (a) reciprocal square root of grain size and (b) volume fraction of β - $\text{Mg}_{17}\text{Al}_{12}$ precipitates at the DRXed grain boundaries.

Figure 64(c) and (d) shows Nyquist and Bode representations, respectively of the ECAPed alloys immersed in 0.05 M NaCl solution. EIS measurements were performed to support the potentiodynamic polarization results regarding the improvement in the protective ability of the oxide film with increasing the strain level. From Figure 64(c), it is seen that the EIS spectra of the ECAPed alloys exhibited two capacitive loops; one capacitive loop from high to intermediate frequencies (60 kHz – 160 mHz) and a capacitive loop at low frequencies (160 mHz – 10 mHz). Furthermore, it is also noticed that the radius of these capacitive loops increases with increasing the strain level. According to previous studies, the high-frequency capacitive loop has been associated with the protective properties of the oxide film whereas the low-frequency capacitive loop is attributed to the charge transfer during electrochemical reactions at the metal/electrolyte interface [102, 108]. The higher the radius of the high-frequency loop, the higher the protective ability of the oxide film. Similarly, the higher the radius of the low-frequency loop the higher the resistance of the Mg alloy to charge transfer

processes. Therefore, Figure 64(c) shows that increasing the level of strain results in the formation of a more protective oxide film. The enhanced oxide film as increasing the strain level can subsequently improve the corrosion resistance of the Mg alloy by blocking active anodic and cathodic sites such that, charge transfer processes are delayed at the alloy surface. The Bode plots in Figure 64(d) showing the impedance magnitude ($|Z|$) and the phase angle against frequency, further support these observations. Typically, the impedance magnitude at the lowest frequency ($|Z|_{0.01 \text{ Hz}}$) is associated with the total impedance of the system and the higher the $|Z|_{0.01 \text{ Hz}}$ value, the higher the corrosion resistance of a material. In this sense, Figure 64(d) shows that the $|Z|_{0.01 \text{ Hz}}$ values of the ECAPed alloys increase with increasing the strain level, indicating that ECAP processing at higher strain levels improved the corrosion resistance of the ECAPed alloys. The phase angle curve confirms the presence of the two time constants observed from the Nyquist representation. Furthermore, it is also seen that the phase angle of the high-frequency time constant decreases with increasing the strain level, these results also indicate that the protective properties of the oxide film are enhanced as increasing the strain level.

The EIS spectra of the different ECAPed alloys was fitted using the equivalent electrical circuit shown in Figure 64(c) to further explore the electrochemical response of these ECAPed alloys. In this circuit, R_s corresponds to the resistance of the electrolyte, CPE_{ox} and R_{ox} describe the capacitance and the resistance of the oxide film, respectively, and CPE_{dl} and R_{ct} represent the double layer capacitance and the charge transfer resistance, respectively, of the charge transfer process taking place at the Mg

alloy/electrolyte interface. Constant phase elements (CPEs) were used instead of capacitances to account for nonideal capacitive behavior due to heterogeneities in the system (e., surface roughness, electrode porosity, non-uniform potential and current distribution, etc.) [155]. The CPE element is defined in terms of the parameters T and n; in which T corresponds to the CPE magnitude and n is an empirical exponent that varies between 0 and 1. For $n = 0$, the CPE element becomes a pure resistor and for $n = 1$, the CPE element is identical to a pure capacitor. As seen in Figure 64(c) and (d), there is a good agreement between the EIS experimental data and the fitted results obtained from the equivalent circuit. The different electrical parameters obtained after the EIS fitting process are reported in Table 8. From these results, it is clearly evident that the resistance of the oxide film (R_{ox}) increases as increasing the strain level, from $12.36 \text{ k}\Omega \cdot \text{cm}^2$ for the ECAPed alloy after the first pass to $17.56 \text{ k}\Omega \cdot \text{cm}^2$ for the ECAPed alloy after the fourth pass, which corroborates that increasing the strain level during ECAP processing results in ECAPed alloys that form more protective oxide films with a higher resistance against aggressive species. Accordingly, Table 8 shows that the capacitance of the oxide film (CPE-T_{ox}) decreases as increasing the strain level. This parameter has been related to the thickness of the oxide film where lower values of CPE-T_{ox} are associated with relatively thick and compact films [16, 18, 148]. Therefore, the lower CPE-T_{ox} values as increasing the strain level indicates the formation of a more compact oxide film that hinder the migration of aggressive species towards the Mg surface. It is expected that the improvement in the protective properties of the oxide film can subsequently improve the corrosion resistance of the Mg alloy by preventive aggressive

species to reach the metallic surface and to initiate electrochemical reactions at the alloy surface/electrolyte interface. This is indeed the case here where it can be seen from Table 3 that there is an increase in the charge transfer resistance (R_{ct}) and a decrease in the double layer capacitance ($CPE-T_{dl}$) as increasing the strain level. The increase in the R_{ct} values as increasing the strain level indicates that the ECAPed alloys with severe plastic strain exhibits a higher resistance for electrochemical reactions induced by the corrosive environment. Furthermore, the decrease in the $CPE-T_{dl}$ values as increasing the strain level implies that the active area available for charge transfer processes decreases as increasing the strain level.

Table 8. Electrical parameters obtained from fitting the EIS data of the ECAPed alloys immersed in 0.05 M NaCl solution

ECAP passes	R_s ($k\Omega \cdot cm^2$)	R_{ox} ($k\Omega \cdot cm^2$)	$CPE-T_{ox}$ ($\mu F \cdot s^{n-1} \cdot cm^2$)	$CPE-n_{ox}$	R_{ct} ($k\Omega \cdot cm^2$)	$CPE-T_{dl}$ ($\mu F \cdot s^{n-1} \cdot cm^2$)	$CPE-n_{dl}$
1	1.06	12.36	7.47	0.910	7.87	632.9	0.735
2	1.18	14.43	6.44	0.924	11.47	428.2	0.691
3	1.02	15.28	5.92	0.930	14.79	360.1	0.796
4	1.10	17.56	5.11	0.924	15.42	329.2	0.662

These EIS results and equivalent circuit analysis correspond well with the potentiodynamic polarization results confirming that increasing the number of ECAP passes leads to formation of more protective oxide films that are more effective in blocking active sites for the development of electrochemical processes at the alloy

surface. Consequently, the enhanced protective ability of these oxide films can further improve the corrosion resistance of the ECAPed alloys. As mentioned above, the superior protective ability of the oxide film on the ECAPed alloys with higher strain levels can be associated with a potential synergistic effect between the significant grain refinement coupled and a high volume fraction of well-distributed β -Mg₁₇Al₁₂ precipitates.

5.3 Summary and Conclusions

The corrosion susceptibility of recrystallized and non-recrystallized regions and the combined effect of dynamic recrystallization and dynamic precipitation on the electrochemical behavior of partially recrystallized ECAPed AZ91 alloys at different strain levels was investigated. The main conclusions from this study are summarized as follows:

- The immersion testing of the ECAPed alloys during short and long immersion time in 3.5 wt.% NaCl solution showed that corrosion primarily initiated and propagated in the DRXed grains through microgalvanic coupling between the β -Mg₁₇Al₁₂ precipitates formed at the DRXed grain boundaries and the adjacent α -Mg matrix. These results were confirmed by SKPFM and local PDP measurements where it was found that the DRXed region exhibited a higher Volta potential difference and higher corrosion current density than the un-DRXed region. The higher corrosion susceptibility of the DRXed region was mainly attributed to higher microchemistry difference between the precipitates and the matrix and a weaker basal texture of DRXed grains.

- The corrosion morphology of the ECAPed alloys changed as increasing the level of deformation strain from highly localized and deep at low strain levels to more uniform and shallower at higher strain levels. The increase in strain level also led to lower corrosion rates of the ECAPed alloys. The more uniform corrosion with shallow penetration depth at high strain levels was attributed to the higher DRXed ratio and the high volume fraction of well-dispersed fine β -Mg₁₇Al₁₂ precipitates formed at the DRXed grain boundaries. A linear correlation was found between maximum penetration depth and size of β -Mg₁₇Al₁₂ precipitates.
- Increasing the level of deformation strain promotes of the formation of a more protective oxide film on the ECAPed alloys with higher resistance to localized breakdown by aggressive species. The higher properties protective of the oxide film as increasing the strain level was associated with the significant grain refinement that promote the formation of a more compact and adherent surface protective layer. Furthermore, the high volume fraction of well-dispersed β -Mg₁₇Al₁₂ precipitates at the DRXed grain boundaries can also induce the formation of an aluminum-enriched oxide layer with a more protective ability as compared to the MgO/Mg(OH)₂ layer. Correlations between $E_b - E_{\text{corr}}$ and $d^{-1/2}$ and $E_b - E_{\text{corr}}$ and volume fraction of precipitates were established.
- A simultaneous improvement in corrosion resistance and hardness was achieved as increasing the level of deformation strain, these results serve as a platform for future alloy design.

CHAPTER VI

CONCLUSIONS AND FUTURE DIRECTIONS

This study provided a comprehensive understanding of the influence of microstructural features on the corrosion behavior of AZ91 alloys processed by different methods with a focus on the role of grain size, grain structure, size and distribution of secondary phases, dislocation density, and crystallographic texture. The main findings of this study can be summarized as follows:

- An AZ91 alloy processed by equal channel angular pressing for four passes exhibited a good combination of strength, ductility, and corrosion resistance in chloride-containing environments with superior properties than the traditional as-cast and heat-treated AZ91 alloys. The improvement in strength was mainly associated with significant grain refinement during ECAP processing that provided grain boundary strengthening as well as formation of large amount of well-dispersed fine β -Mg₁₇Al₁₂ precipitates that further promoted grain boundary strengthening and precipitation hardening. The refined grain structure combined with the presence of uniformly distributed β -Mg₁₇Al₁₂ precipitates also induced a more uniform plastic deformation resulting in higher ductility. Lastly, the superior corrosion resistance properties of the ECAPed alloy was mainly attributed to the presence of a more protective oxide film, formation of more protective layer of corrosion products upon long-term immersion, and presence of well-distributed fine precipitates that induced the development of a more uniform corrosion with shallow penetration depth.

- Corrosion initiation in a peak-aged AZ91 alloy simultaneously occurred at the interior of the α -Mg matrix and in the local α -Mg inside the $\alpha + \beta$ lamellar precipitate. The corrosion initiation inside the α -Mg matrix occurred due to the lower aluminum content at these regions that induced preferential anodic dissolution of the aluminum-depleted α -Mg matrix; this process occurred in the presence of hydrogen evolution taking place in local cathodic sites. Micro-galvanic coupling between the Al_3Mn_5 intermetallic particles and the adjacent α -Mg matrix also occurred inside the α -Mg matrix, however this process was limited due to the small cathode-to-anode area ratio that led to slow galvanic corrosion kinetics. Corrosion inside the $\alpha + \beta$ lamellar precipitate occurred through microgalvanic coupling between the β -phase and the local α -Mg phase; this microgalvanic corrosion process prevailed over the microgalvanic coupling between the lamellar precipitate and the adjacent α -Mg matrix due to the higher microchemistry difference between the β -phase and the local α -Mg phase and the higher cathode-to-anode area ratio. It was also found that the β - $\text{Mg}_{17}\text{Al}_{12}$ phase/ α -Mg matrix interface acted as a barrier against corrosion propagation through adjacent Mg grains. This barrier effect was attributed to the continuous network of the lamellar precipitate along grain boundaries that made these precipitates more resistant to undermining. Furthermore, this barrier effect can be also related to the formation of an aluminum-enriched oxide film on the lamellar precipitate and the presence of an array of closely-spaced β - $\text{Mg}_{17}\text{Al}_{12}$ precipitates at the grain boundary. At long-immersion time, the anodic dissolution at the interior of the Mg grains dominated the corrosion propagation process due to the faster kinetics

of this process compared to the kinetics of the micro-galvanic corrosion processes. Thus, the corrosion morphology at long immersion time is characterized by a honeycomb structure of dissolved matrix surrounded by undissolved β -Mg₁₇Al₁₂ precipitates along the grain boundaries.

- Corrosion in ECAPed AZ91 alloys preferentially occurred in the recrystallized grains due to the higher microchemistry difference between the β -Mg₁₇Al₁₂ precipitates and the α -Mg matrix in this region compared to the one the in non-recrystallized region. In addition, the weakened basal texture of the recrystallized grains could also be responsible for the corrosion initiation and propagation in these regions. These factors resulted in a larger Volta potential difference and higher corrosion current density than those of the non-recrystallized regions. The preferential corrosion inside the DRXed grains occurred mainly through microgalvanic coupling between the β -Mg₁₇Al₁₂ precipitates formed along the DRXed grain boundaries and the adjacent α -Mg matrix leading to corrosion initiation at the grain boundaries that subsequently propagated into the grain interior. The corrosion morphology of the ECAPed alloys changed from highly localized and deep to more uniform and shallower as increasing the level of deformation strain. From corrosion and electrochemical measurements, it was found that the corrosion rate decreased, the breakdown potential of the oxide film increased, and the resistance of the oxide increased as increasing the strain level. In addition, the hardness of the material was also increased as increasing the level of deformation. It was concluded that the simultaneous improvement in corrosion resistance and

hardness (strength) as increasing the level of strain was related to the combination of smaller grain size of the DRXed grains, higher volume fraction of DRXed grains and higher volume fraction of uniformly distributed fine β -Mg₁₇Al₁₂ precipitates.

This study showed the superiority of ECAPed AZ91 alloys in strength, ductility, and corrosion resistance. Therefore, it would be of great interest to further explore the mechanical behavior and corrosion resistance of this alloy using this type of severe plastic deformation methods. For the particular case of ECAP processing, there are several processing conditions that can be investigated to develop ECAPed AZ91 alloys with even better mechanical and corrosion resistance performance as the one reported in this study. Parameters such as temperature, route, and number of ECAP passes are highly attractive since they can be easily controlled and they do not require any changes in the design. Furthermore, it is well known that these factors drastically influence the grain structure, texture and characteristics of β -Mg₁₇Al₁₂ precipitates (i.e., size, volume fraction, distribution, shape, etc.).

This study also showed that a refined grain structure with the presence of well-distributed fine β -Mg₁₇Al₁₂ precipitates led to better mechanical properties and corrosion resistance of the ECAPed alloy with four passes compared to the as-cast alloy, traditional heat-treated alloys, and ECAPed alloys with fewer number of passes. However, it would be interesting to investigate the corrosion behavior in a fully recrystallized microstructure and to find if there is a critical limit at which more grain refinement or more formation of fine precipitates is detrimental for the corrosion resistance of these heavily deformed AZ91 alloys.

REFERENCES

- [1] M. Gzyl, A. Rosochowski, S. Boczkal, L. Olejnik, The role of microstructure and texture in controlling mechanical properties of AZ31B magnesium alloy processed by I-ECAP, *Materials Science and Engineering: A*, 638 (2015) 20-29.
- [2] M. Esmaily, J.E. Svensson, S. Fajardo, N. Birbilis, G.S. Frankel, S. Virtanen, R. Arrabal, S. Thomas, L.G. Johansson, Fundamentals and advances in magnesium alloy corrosion, *Progress in Materials Science*, 89 (2017) 92-193.
- [3] S.W. Xu, N. Matsumoto, S. Kamado, T. Honma, Y. Kojima, Effect of $Mg_{17}Al_{12}$ precipitates on the microstructural changes and mechanical properties of hot compressed AZ91 magnesium alloy, *Materials Science and Engineering: A*, 523 (2009) 47-52.
- [4] R. Arrabal, B. Mingo, A. Pardo, E. Matykina, M. Mohedano, M. Merino, A. Rivas, A. Maroto, Role of alloyed Nd in the microstructure and atmospheric corrosion of as-cast magnesium alloy AZ91, *Corrosion Science*, 97 (2015) 38-48.
- [5] R. Ambat, N.N. Aung, W. Zhou, Studies on the influence of chloride ion and pH on the corrosion and electrochemical behaviour of AZ91D magnesium alloy, *Journal of Applied Electrochemistry*, 30 (2000) 865-874.
- [6] K.A. Unocic, H.H. Elsentriecy, M.P. Brady, H. Meyer, G. Song, M. Fayek, R.A. Meisner, B. Davis, Transmission electron microscopy study of aqueous film formation and evolution on magnesium alloys, *Journal of the Electrochemical Society*, 161 (2014) C302-C311.
- [7] Y.C. Yuan, A.B. Ma, J.H. Jiang, Y. Sun, F.M. Lu, L.Y. Zhang, D. Song, Mechanical properties and precipitate behavior of Mg–9Al–1Zn alloy processed by equal-channel angular pressing and aging, *Journal of Alloys and Compounds*, 594 (2014) 182-188.
- [8] N. Birbilis, A.D. King, S. Thomas, G.S. Frankel, J.R. Scully, Evidence for enhanced catalytic activity of magnesium arising from anodic dissolution, *Electrochimica Acta*, 132 (2014) 277-283.

[9] R.B. Figueiredo, T.G. Langdon, Grain refinement and mechanical behavior of a magnesium alloy processed by ECAP, *Journal of Materials Science*, 45 (2010) 4827-4836.

[10] T.G. Langdon, The principles of grain refinement in equal-channel angular pressing, *Materials Science and Engineering: A*, 462 (2007) 3-11.

[11] S. Khani, M. Aboutalebi, M. Salehi, H. Samim, H. Palkowski, Microstructural development during equal channel angular pressing of as-cast AZ91 alloy, *Materials Science and Engineering: A*, 678 (2016) 44-56.

[12] ASTM B661-12, Standard Practice for Heat Treatment of Magnesium Alloys, ASTM International, West Conshohocken, PA, 2012.

[13] W.J. Kim, H.G. Jeong, H.T. Jeong, Achieving high strength and high ductility in magnesium alloys using severe plastic deformation combined with low-temperature aging, *Scripta Materialia*, 61 (2009) 1040-1043.

[14] D. Orlov, K.D. Ralston, N. Birbilis, Y. Estrin, Enhanced corrosion resistance of Mg alloy ZK60 after processing by integrated extrusion and equal channel angular pressing, *Acta Materialia*, 59 (2011) 6176-6186.

[15] G.B. Hamu, D. Eliezer, L. Wagner, The relation between severe plastic deformation microstructure and corrosion behavior of AZ31 magnesium alloy, *Journal of Alloys and Compounds*, 468 (2009) 222-229.

[16] H. Miao, H. Huang, Y. Shi, H. Zhang, J. Pei, G. Yuan, Effects of solution treatment before extrusion on the microstructure, mechanical properties and corrosion of Mg-Zn-Gd alloy in vitro, *Corrosion Science*, 122 (2017) 90-99.

[17] L. Zhang, K.-k. Deng, K.-b. Nie, F.-j. Xu, K. Su, W. Liang, Microstructures and mechanical properties of Mg–Al–Ca alloys affected by Ca/Al ratio, *Materials Science and Engineering: A*, 636 (2015) 279-288.

[18] P.-p. Wu, F.-j. Xu, K.-k. Deng, F.-y. Han, Z.-z. Zhang, R. Gao, Effect of extrusion on corrosion properties of Mg-2Ca- χ Al ($\chi= 0, 2, 3, 5$) alloys, *Corrosion Science*, 127 (2017) 280-290.

[19] N. Birbilis, K. Ralston, S. Virtanen, H. Fraser, C. Davies, Grain character influences on corrosion of ECAPed pure magnesium, *Corrosion Engineering, Science and Technology*, 45 (2010) 224-230.

[20] D. Song, A. Ma, J. Jiang, P. Lin, D. Yang, J. Fan, Corrosion behavior of equal-channel-angular-pressed pure magnesium in NaCl aqueous solution, *Corrosion Science*, 52 (2010) 481-490.

[21] M.P. Brady, W.J. Joost, C. David Warren, Insights from a recent meeting: Current status and future directions in magnesium corrosion research, *Corrosion*, 73 (2016) 452-462.

[22] Magnesium: uses, Metalpedia, Asian Metal, Available from: <http://metalpedia.asianmetal.com/metal/magnesium/application.shtml>. Accessed 10 May 2019.

[23] USCAR materials partnership maps path to increased use of magnesium in vehicles, United States Council for Automotive Research LCC, April 16, 2007. Available from: https://uscar.org/guest/article_view.php?articles_id=104. Accessed 10 May 2019.

[24] H.S. Kim, W.J. Kim, Enhanced corrosion resistance of ultrafine-grained AZ61 alloy containing very fine particles of Mg₁₇Al₁₂ phase, *Corrosion Science*, 75 (2013) 228-238.

[25] F. Cao, G.-L. Song, A. Atrens, Corrosion and passivation of magnesium alloys, *Corrosion Science*, 111 (2016) 835-845.

[26] B. Jiang, Q. Xiang, A. Atrens, J. Song, F. Pan, Influence of crystallographic texture and grain size on the corrosion behaviour of as-extruded Mg alloy AZ31 sheets, *Corrosion Science*, 126 (2017) 374-380.

[27] E. Dogan, S. Wang, M.W. Vaughan, I. Karaman, Dynamic precipitation in Mg-3Al-1Zn alloy during different plastic deformation modes, *Acta Materialia*, 116 (2016) 1-13.

[28] C. Bettles, M. Barnett, *Advances in wrought magnesium alloys: fundamentals of processing, properties and applications*, Elsevier Science and Technology, Cambridge, United Kingdom, 2012.

[29] R.W. Hertzberg, *Deformation and fracture mechanics of engineering materials*, Wiley, New York, 1989.

[30] T.G. Langdon, Twenty-five years of ultrafine-grained materials: Achieving exceptional properties through grain refinement, *Acta Materialia*, 61 (2013) 7035-7059.

[31] R.Z. Valiev, T.G. Langdon, Principles of equal-channel angular pressing as a processing tool for grain refinement, *Progress in Materials Science*, 51 (2006) 881-981.

[32] Q. Wei, S. Cheng, K.T. Ramesh, E. Ma, Effect of nanocrystalline and ultrafine grain sizes on the strain rate sensitivity and activation volume: fcc versus bcc metals, *Materials Science and Engineering: A*, 381 (2004) 71-79.

[33] E. Dogan, Role of crystallographic texture and grain size on low temperature deformation and formability of a Mg alloy, PhD Dissertation, Mechanical Engineering, Texas A&M University, 2014. Available from: <http://oaktrust.library.tamu.edu/>.

[34] C.W. Su, L. Lu, M.O. Lai, A model for the grain refinement mechanism in equal channel angular pressing of Mg alloy from microstructural studies, *Materials Science and Engineering: A*, 434 (2006) 227-236.

[35] H.K. Kim, W.J. Kim, Microstructural instability and strength of an AZ31 Mg alloy after severe plastic deformation, *Materials Science and Engineering: A*, 385 (2004) 300-308.

[36] S.H. Kang, Y.S. Lee, J.H. Lee, Effect of grain refinement of magnesium alloy AZ31 by severe plastic deformation on material characteristics, *Journal of Materials Processing Technology*, 201 (2008) 436-440.

[37] Y. Miyahara, Z. Horita, T.G. Langdon, Exceptional superplasticity in an AZ61 magnesium alloy processed by extrusion and ECAP, *Materials Science and Engineering: A*, 420 (2006) 240-244.

[38] C. Chung, R. Ding, Y. Chiu, W. Gao, Effect of ECAP on microstructure and mechanical properties of cast AZ91 magnesium alloy, *Journal of Physics: Conference Series*, IOP Publishing, 2010, pp. 012101.

[39] J. Jiang, Y. Wang, Z. Du, J. Qu, Y. Sun, S. Luo, Enhancing room temperature mechanical properties of Mg–9Al–Zn alloy by multi-pass equal channel angular extrusion, *Journal of Materials Processing Technology*, 210 (2010) 751-758.

[40] B. Chen, D.-L. Lin, L. Jin, X.-Q. Zeng, C. Lu, Equal-channel angular pressing of magnesium alloy AZ91 and its effects on microstructure and mechanical properties, *Materials Science and Engineering: A*, 483–484 (2008) 113-116.

[41] K. Máthis, J. Gubicza, N.H. Nam, Microstructure and mechanical behavior of AZ91 Mg alloy processed by equal channel angular pressing, *Journal of Alloys and Compounds*, 394 (2005) 194-199.

[42] K. Huang, R.E. Logé, A review of dynamic recrystallization phenomena in metallic materials, *Materials & Design*, 111 (2016) 548-574.

[43] M.R. Ghandehari Ferdowsi, M. Mazinani, G.R. Ebrahimi, Effects of hot rolling and inter-stage annealing on the microstructure and texture evolution in a partially homogenized AZ91 magnesium alloy, *Materials Science and Engineering: A*, 606 (2014) 214-227.

[44] A. Atrens, G.L. Song, M. Liu, Z. Shi, F. Cao, M.S. Dargusch, Review of recent developments in the field of magnesium corrosion, *Advanced Engineering Materials*, 17 (2015) 400-453.

[45] Z.P. Cano, Filiform-like corrosion mechanism on magnesium-aluminum and magnesium-aluminum-zinc alloys, MS Thesis, *Materials Science and Engineering*, McMaster University, 2015. Available from: <http://hdl.handle.net/11375/16758>.

- [46] R. Lindström, L.G. Johansson, J.E. Svensson, The influence of NaCl and CO₂ on the atmospheric corrosion of magnesium alloy AZ91, *Materials and Corrosion*, 54 (2003) 587-594.
- [47] A. Pardo, M.C. Merino, A.E. Coy, R. Arrabal, F. Viejo, E. Matykina, Corrosion behaviour of magnesium/aluminium alloys in 3.5wt.% NaCl, *Corrosion Science*, 50 (2008) 823-834.
- [48] M. Taheri, R.C. Phillips, J.R. Kish, G.A. Botton, Analysis of the surface film formed on Mg by exposure to water using a FIB cross-section and STEM-EDS, *Corrosion Science*, 59 (2012) 222-228.
- [49] G. Song, A. Atrens, Understanding magnesium corrosion—a framework for improved alloy performance, *Advanced Engineering Materials*, 5 (2003) 837-858.
- [50] S. Salleh, S. Thomas, J. Yuwono, K. Venkatesan, N. Birbilis, Enhanced hydrogen evolution on Mg(OH)₂ covered Mg surfaces, *Electrochimica Acta*, 161 (2015) 144-152.
- [51] M. Curioni, The behaviour of magnesium during free corrosion and potentiodynamic polarization investigated by real-time hydrogen measurement and optical imaging, *Electrochimica Acta*, 120 (2014) 284-292.
- [52] N. Birbilis, A. King, S. Thomas, G. Frankel, J. Scully, Evidence for enhanced catalytic activity of magnesium arising from anodic dissolution, *Electrochimica Acta*, 132 (2014) 277-283.
- [53] G. Williams, N. Birbilis, H.N. McMurray, Controlling factors in localised corrosion morphologies observed for magnesium immersed in chloride containing electrolyte, *Faraday Discussions*, 180 (2015) 313-330.
- [54] K. Ralston, N. Birbilis, Effect of grain size on corrosion: a review, *Corrosion*, 66 (2010) 075005-075005-075013.
- [55] D. Ahmadkhaniha, M. Fedel, M. Heydarzadeh Sohi, F. Deflorian, Effect of friction stir processing on the corrosion behavior of pure Mg, *Protection of Metals and Physical Chemistry of Surfaces*, 53 (2017) 895-901.

- [56] G.-L. Song, The effect of texture on the corrosion behavior of AZ31 Mg alloy, *JOM*, 64 (2012) 671-679.
- [57] G.R. Argade, S.K. Panigrahi, R.S. Mishra, Effects of grain size on the corrosion resistance of wrought magnesium alloys containing neodymium, *Corrosion Science*, 58 (2012) 145-151.
- [58] K.D. Ralston, N. Birbilis, C.H.J. Davies, Revealing the relationship between grain size and corrosion rate of metals, *Scripta Materialia*, 63 (2010) 1201-1204.
- [59] J. Liao, M. Hotta, N. Yamamoto, Corrosion behavior of fine-grained AZ31B magnesium alloy, *Corrosion Science*, 61 (2012) 208-214.
- [60] A. Pardo, M.C. Merino, A.E. Coy, F. Viejo, R. Arrabal, S. Feliú, Influence of microstructure and composition on the corrosion behaviour of Mg/Al alloys in chloride media, *Electrochimica Acta*, 53 (2008) 7890-7902.
- [61] M.F. Hurley, C.M. Efav, P.H. Davis, J.R. Croteau, E. Graugnard, N. Birbilis, Volta potentials measured by scanning Kelvin probe force microscopy as relevant to corrosion of magnesium alloys, *Corrosion*, 71 (2014) 160-170.
- [62] M.-C. Zhao, M. Liu, G. Song, A. Atrens, Influence of the β -phase morphology on the corrosion of the Mg alloy AZ91, *Corrosion Science*, 50 (2008) 1939-1953.
- [63] G. Song, A. Atrens, M. Dargusch, Influence of microstructure on the corrosion of diecast AZ91D, *Corrosion Science*, 41 (1998) 249-273.
- [64] S.W. Xu, S. Kamado, N. Matsumoto, T. Honma, Y. Kojima, Recrystallization mechanism of as-cast AZ91 magnesium alloy during hot compressive deformation, *Materials Science and Engineering: A*, 527 (2009) 52-60.
- [65] Y.S. Jeong, W.J. Kim, Enhancement of mechanical properties and corrosion resistance of Mg–Ca alloys through microstructural refinement by indirect extrusion, *Corrosion Science*, 82 (2014) 392-403.

- [66] T. Zhang, Y. Shao, G. Meng, Z. Cui, F. Wang, Corrosion of hot extrusion AZ91 magnesium alloy: I-relation between the microstructure and corrosion behavior, *Corrosion Science*, 53 (2011) 1960-1968.
- [67] M. Ben-Haroush, G. Ben-Hamu, D. Eliezer, L. Wagner, The relation between microstructure and corrosion behavior of AZ80 Mg alloy following different extrusion temperatures, *Corrosion Science*, 50 (2008) 1766-1778.
- [68] N.N. Aung, W. Zhou, Effect of grain size and twins on corrosion behaviour of AZ31B magnesium alloy, *Corrosion Science*, 52 (2010) 589-594.
- [69] C. op't Hoog, N. Birbilis, Y. Estrin, Corrosion of pure Mg as a function of grain size and processing route, *Advanced Engineering Materials*, 10 (2008) 579-582.
- [70] K. Hagihara, M. Okubo, M. Yamasaki, T. Nakano, Crystal-orientation-dependent corrosion behaviour of single crystals of a pure Mg and Mg-Al and Mg-Cu solid solutions, *Corrosion Science*, 109 (2016) 68-85.
- [71] S. Pawar, T.J.A. Slater, T.L. Burnett, X. Zhou, G.M. Scamans, Z. Fan, G.E. Thompson, P.J. Withers, Crystallographic effects on the corrosion of twin roll cast AZ31 Mg alloy sheet, *Acta Materialia*, 133 (2017) 90-99.
- [72] G.-L. Song, Z. Xu, Crystal orientation and electrochemical corrosion of polycrystalline Mg, *Corrosion Science*, 63 (2012) 100-112.
- [73] G.-L. Song, R. Mishra, Z. Xu, Crystallographic orientation and electrochemical activity of AZ31 Mg alloy, *Electrochemistry Communications*, 12 (2010) 1009-1012.
- [74] G.-L. Song, Z. Xu, Effect of microstructure evolution on corrosion of different crystal surfaces of AZ31 Mg alloy in a chloride containing solution, *Corrosion Science*, 54 (2012) 97-105.

- [75] L. Zhang, Q. Wang, W. Liao, W. Guo, B. Ye, H. Jiang, W. Ding, Effect of homogenization on the microstructure and mechanical properties of the repetitive-upsetting processed AZ91D alloy, *Journal of Materials Science & Technology*, 33 (2017) 935-940.
- [76] R.G. Kelly, J.R. Scully, D. Shoesmith, R.G. Buchheit, *Electrochemical techniques in corrosion science and engineering*, CRC Press, 2002.
- [77] F. Cao, Z. Shi, G.-L. Song, M. Liu, M.S. Dargusch, A. Atrens, Influence of hot rolling on the corrosion behavior of several Mg–X alloys, *Corrosion Science*, 90 (2015) 176-191.
- [78] Z. Shi, A. Atrens, An innovative specimen configuration for the study of Mg corrosion, *Corrosion Science*, 53 (2011) 226-246.
- [79] G. Song, A. Atrens, D. StJohn, An hydrogen evolution method for the estimation of the corrosion rate of magnesium alloys, *Essential Readings in Magnesium Technology*, Springer International Publishing, Cham, 2016, pp. 565-572.
- [80] A.K. Dahle, Y.C. Lee, M.D. Nave, P.L. Schaffer, D.H. StJohn, Development of the as-cast microstructure in magnesium–aluminium alloys, *Journal of Light Metals*, 1 (2001) 61-72.
- [81] Y. Wang, G. Liu, Z. Fan, Microstructural evolution of rheo-diecast AZ91D magnesium alloy during heat treatment, *Acta Materialia*, 54 (2006) 689-699.
- [82] K.N. Braszczynska-Malik, Discontinuous and continuous precipitation in magnesium–aluminium type alloys, *Journal of Alloys and Compounds*, 477 (2009) 870-876.
- [83] M. Danaie, R.M. Asmussen, P. Jakupi, D.W. Shoesmith, G.A. Botton, The role of aluminum distribution on the local corrosion resistance of the microstructure in a sand-cast AM50 alloy, *Corrosion Science*, 77 (2013) 151-163.

- [84] R. Zeng, Precipitation hardening in AZ91 magnesium alloy, PhD Dissertation, School of Metallurgy and Materials, University of Birmingham, 2013. Available from: etheses.bham.ac.uk.
- [85] S. Liu, Y. Zhang, H. Han, Role of manganese on the grain refining efficiency of AZ91D magnesium alloy refined by Al_4C_3 , *Journal of Alloys and Compounds*, 491 (2010) 325-329.
- [86] S. Lun Sin, D. Dubé, R. Tremblay, Characterization of Al–Mn particles in AZ91D investment castings, *Materials Characterization*, 58 (2007) 989-996.
- [87] V. Jain, R.S. Mishra, A.K. Gupta, Gouthama, Study of β -precipitates and their effect on the directional yield asymmetry of friction stir processed and aged AZ91C alloy, *Materials Science and Engineering: A*, 560 (2013) 500-509.
- [88] S.W. Xu, N. Matsumoto, S. Kamado, T. Honma, Y. Kojima, Dynamic microstructural changes in Mg–9Al–1Zn alloy during hot compression, *Scripta Materialia*, 61 (2009) 249-252.
- [89] J.-G. Jung, S.H. Park, H. Yu, Y.M. Kim, Y.-K. Lee, B.S. You, Improved mechanical properties of Mg–7.6Al–0.4Zn alloy through aging prior to extrusion, *Scripta Materialia*, 93 (2014) 8-11.
- [90] F. Guo, D. Zhang, X. Yang, L. Jiang, F. Pan, Strain-induced dynamic precipitation of $Mg_{17}Al_{12}$ phases in Mg–8Al alloys sheets rolled at 748K, *Materials Science and Engineering: A*, 636 (2015) 516-521.
- [91] Y. Yuan, A. Ma, J. Jiang, F. Lu, W. Jian, D. Song, Y.T. Zhu, Optimizing the strength and ductility of AZ91 Mg alloy by ECAP and subsequent aging, *Materials Science and Engineering: A*, 588 (2013) 329-334.
- [92] S.H. Park, B.S. You, Effect of homogenization temperature on the microstructure and mechanical properties of extruded Mg–7Sn–1Al–1Zn alloy, *Journal of Alloys and Compounds*, 637 (2015) 332-338.

- [93] Z. Li, J. Dong, X.Q. Zeng, C. Lu, W.J. Ding, Influence of $Mg_{17}Al_{12}$ intermetallic compounds on the hot extruded microstructures and mechanical properties of Mg–9Al–1Zn alloy, *Materials Science and Engineering: A*, 466 (2007) 134-139.
- [94] G. Purcek, H. Yanar, M. Demirtas, Y. Alemdag, D.V. Shangina, S.V. Dobatkin, Optimization of strength, ductility and electrical conductivity of Cu–Cr–Zr alloy by combining multi-route ECAP and aging, *Materials Science and Engineering: A*, 649 (2016) 114-122.
- [95] M. Maghsoudi, A. Zarei-Hanzaki, H. Abedi, A. Shamsolhodaei, The evolution of γ - $Mg_{17}Al_{12}$ intermetallic compound during accumulative back extrusion and subsequent ageing treatment, *Philosophical Magazine*, 95 (2015) 3497-3523.
- [96] M.X. Zhang, P.M. Kelly, Crystallography of $Mg_{17}Al_{12}$ precipitates in AZ91D alloy, *Scripta Materialia*, 48 (2003) 647-652.
- [97] S.H. Park, J.H. Bae, S.-H. Kim, J. Yoon, B.S. You, Effect of initial grain size on microstructure and mechanical properties of extruded Mg–9Al–0.6Zn alloy, *Metallurgical and Materials Transactions A*, 46 (2015) 5482-5488.
- [98] S. Xu, S. Kamado, T. Honma, Effect of homogenization on microstructures and mechanical properties of hot compressed Mg–9Al–1Zn alloy, *Materials Science and Engineering: A*, 528 (2011) 2385-2393.
- [99] C.-j. Wang, K.-k. Deng, K.-b. Nie, S.-j. Shang, W. Liang, Competition behavior of the strengthening effects in as-extruded AZ91 matrix: Influence of pre-existed $Mg_{17}Al_{12}$ phase, *Materials Science and Engineering: A*, 656 (2016) 102-110.
- [100] H.Y. Wang, Z.P. Yu, L. Zhang, C.G. Liu, M. Zha, C. Wang, Q.C. Jiang, Achieving high strength and high ductility in magnesium alloy using hard-plate rolling (HPR) process, *Scientific Reports*, 5 (2015) 17100.
- [101] L. Wang, B.-P. Zhang, T. Shinohara, Corrosion behavior of AZ91 magnesium alloy in dilute NaCl solutions, *Materials & Design*, 31 (2010) 857-863.

- [102] J. Li, Q. Jiang, H. Sun, Y. Li, Effect of heat treatment on corrosion behavior of AZ63 magnesium alloy in 3.5 wt.% sodium chloride solution, *Corrosion Science*, 111 (2016) 288-301.
- [103] O. Lunder, J. Lein, S. Hesjevik, T.K. Aune, K. Nişancioğlu, Corrosion morphologies on magnesium alloy AZ91, *Materials and Corrosion*, 45 (1994) 331-340.
- [104] T. Beldjoudi, C. Fiaud, L. Robbiola, Influence of homogenization and artificial aging heat treatments on corrosion behavior of Mg-Al alloys, *Corrosion*, 49 (1993) 738-745.
- [105] G. Song, A.L. Bowles, D.H. StJohn, Corrosion resistance of aged die cast magnesium alloy AZ91D, *Materials Science and Engineering: A*, 366 (2004) 74-86.
- [106] G. Baril, C. Blanc, N. Pébère, AC impedance spectroscopy in characterizing time-dependent corrosion of AZ91 and AM50 magnesium alloys characterization with respect to their microstructures, *Journal of the Electrochemical Society*, 148 (2001) B489-B496.
- [107] H. Feng, S. Liu, Y. Du, T. Lei, R. Zeng, T. Yuan, Effect of the second phases on corrosion behavior of the Mg-Al-Zn alloys, *Journal of Alloys and Compounds*, 695 (2017) 2330-2338.
- [108] L.G. Bland, K. Gusieva, J.R. Scully, Effect of crystallographic orientation on the corrosion of magnesium: Comparison of film forming and bare crystal facets using electrochemical impedance and raman spectroscopy, *Electrochimica Acta*, 227 (2017) 136-151.
- [109] R.D. Davidson, Y. Cubides, C. Fincher, P. Stein, C. McLain, B.-X. Xu, M. Pharr, H. Castaneda, S. Banerjee, Tortuosity but not percolation: Design of exfoliated graphite nanocomposite coatings for extended corrosion protection of aluminum alloys, *ACS Applied Nano Materials*, 2 (2019) 3100-3116.
- [110] E.M. Salleh, H. Zuhailawati, S.N.F.M. Noor, N.K. Othman, In vitro biodegradation and mechanical properties of Mg-Zn Alloy and Mg-Zn-hydroxyapatite composite produced by mechanical alloying for potential application in bone repair, *Metallurgical and Materials Transactions A*, 49 (2018) 5888-5903.

- [111] S. Feliu, I. Llorente, Corrosion product layers on magnesium alloys AZ31 and AZ61: Surface chemistry and protective ability, *Applied Surface Science*, 347 (2015) 736-746.
- [112] Z. Cui, X. Li, K. Xiao, C. Dong, Atmospheric corrosion of field-exposed AZ31 magnesium in a tropical marine environment, *Corrosion Science*, 76 (2013) 243-256.
- [113] L. Wang, T. Shinohara, B.-P. Zhang, Corrosion behavior of Mg, AZ31, and AZ91 alloys in dilute NaCl solutions, *Journal of Solid State Electrochemistry*, 14 (2010) 1897-1907.
- [114] J. Liao, M. Hotta, Corrosion products of field-exposed Mg-Al series magnesium alloys, *Corrosion Science*, 112 (2016) 276-288.
- [115] M. Jönsson, D. Persson, The influence of the microstructure on the atmospheric corrosion behaviour of magnesium alloys AZ91D and AM50, *Corrosion Science*, 52 (2010) 1077-1085.
- [116] M. Jönsson, D. Persson, C. Leygraf, Atmospheric corrosion of field-exposed magnesium alloy AZ91D, *Corrosion Science*, 50 (2008) 1406-1413.
- [117] M.C.L. de Oliveira, V.S.M. Pereira, O.V. Correa, N.B. de Lima, R.A. Antunes, Correlation between the corrosion resistance and the semiconducting properties of the oxide film formed on AZ91D alloy after solution treatment, *Corrosion Science*, 69 (2013) 311-321.
- [118] W. Zhou, T. Shen, N.N. Aung, Effect of heat treatment on corrosion behaviour of magnesium alloy AZ91D in simulated body fluid, *Corrosion Science*, 52 (2010) 1035-1041.
- [119] R. Ambat, N.N. Aung, W. Zhou, Evaluation of microstructural effects on corrosion behaviour of AZ91D magnesium alloy, *Corrosion Science*, 42 (2000) 1433-1455.

[120] O. Lunder, J. Lein, T.K. Aune, K. Nisancioglu, The role of $Mg_{17}Al_{12}$ phase in the corrosion of Mg alloy AZ91, *Corrosion*, 45 (1989) 741-748.

[121] G.-L. Song, A. Atrens, X. Wu, B. Zhang, Corrosion behaviour of AZ21, AZ501 and AZ91 in sodium chloride, *Corrosion Science*, 40 (1998) 1769-1791.

[122] B. Mingo, R. Arrabal, M. Mohedano, A. Pardo, E. Matykina, A. Rivas, Enhanced corrosion resistance of AZ91 alloy produced by semisolid metal processing, *Journal of the Electrochemical Society*, 162 (2015) C180-C188.

[123] A.J. López, C. Taltavull, B. Torres, E. Otero, J. Rams, Characterization of the corrosion behavior of a Mg alloy in chloride solution, *Corrosion*, 69 (2013) 497-508.

[124] S. Mathieu, C. Rapin, J. Hazan, P. Steinmetz, Corrosion behaviour of high pressure die-cast and semi-solid cast AZ91D alloys, *Corrosion Science*, 44 (2002) 2737-2756.

[125] M. Jönsson, D. Persson, R. Gubner, The initial steps of atmospheric corrosion on magnesium alloy AZ91D, *Journal of the Electrochemical Society*, 154 (2007) C684-C691.

[126] K. Braszczyńska-Malik, Precipitates of γ - $Mg_{17}Al_{12}$ phase in Mg-Al alloys, *Magnesium Alloys - Design, Processing and Properties*, IntechOpen, 2011. Available from: <https://www.intechopen.com/books/magnesium-alloys-design-processing-and-properties/precipitates-of-gamma-mg17al12-phase-in-mg-al-alloys>.

[127] K. Braszczyńska-Malik, Thermal analytical investigations of the magnesium alloy AZ91, *Archives of Foundry Engineering*, 7 (2007) 177-180.

[128] J.-F. Nie, Precipitation and hardening in magnesium alloys, *Metallurgical and Materials Transactions A*, 43 (2012) 3891-3939.

[129] M. Jönsson, D. Thierry, N. LeBozec, The influence of microstructure on the corrosion behaviour of AZ91D studied by scanning Kelvin probe force microscopy and scanning Kelvin probe, *Corrosion Science*, 48 (2006) 1193-1208.

- [130] C. Örnek, D.L. Engelberg, Correlative EBSD and SKPFM characterisation of microstructure development to assist determination of corrosion propensity in grade 2205 duplex stainless steel, *Journal of Materials Science*, 51 (2016) 1931-1948.
- [131] C. Örnek, D. Engelberg, SKPFM measured Volta potential correlated with strain localisation in microstructure to understand corrosion susceptibility of cold-rolled grade 2205 duplex stainless steel, *Corrosion Science*, 99 (2015) 164-171.
- [132] Z. Hu, R.L. Liu, S.K. Kairy, X. Li, H. Yan, N. Birbilis, Effect of Sm additions on the microstructure and corrosion behavior of magnesium alloy AZ91, *Corrosion Science*, 149 (2019) 144-152.
- [133] R.S. Raman, The role of microstructure in localized corrosion of magnesium alloys, *Metallurgical and Materials Transactions A*, 35 (2004) 2525-2531.
- [134] R. Arrabal, A. Pardo, M. Merino, S. Merino, M. Mohedano, P. Casajús, Corrosion behaviour of Mg/Al alloys in high humidity atmospheres, *Materials and Corrosion*, 62 (2011) 326-334.
- [135] D. Song, A.B. Ma, J.H. Jiang, P.H. Lin, D.H. Yang, J.F. Fan, Corrosion behaviour of bulk ultra-fine grained AZ91D magnesium alloy fabricated by equal-channel angular pressing, *Corrosion Science*, 53 (2011) 362-373.
- [136] X. Zhang, S.K. Kairy, J. Dai, N. Birbilis, A closer look at the role of nanometer scale solute-rich stacking faults in the localized corrosion of a magnesium alloy GZ31K, *Journal of the Electrochemical Society*, 165 (2018) C310-C316.
- [137] L.G. Bland, N. Birbilis, J.R. Scully, Exploring the effects of intermetallic particle size and spacing on the corrosion of Mg-Al alloys using model electrodes, *Journal of the Electrochemical Society*, 163 (2016) C895-C906.
- [138] A.D. Südholz, N.T. Kirkland, R.G. Buchheit, N. Birbilis, Electrochemical properties of intermetallic phases and common impurity elements in magnesium alloys, *Electrochemical and Solid-State Letters*, 14 (2011) C5-C7.

- [139] S.W. Xu, N. Matsumoto, S. Kamado, T. Honma, Y. Kojima, Effect of pre-aging treatment on microstructure and mechanical properties of hot compressed Mg–9Al–1Zn alloy, *Materials Science and Engineering: A*, 517 (2009) 354-360.
- [140] R.B. Figueiredo, T.G. Langdon, Principles of grain refinement and superplastic flow in magnesium alloys processed by ECAP, *Materials Science and Engineering: A*, 501 (2009) 105-114.
- [141] X. Ma, S.E. Prameela, P. Yi, M. Fernandez, N.M. Krywopusk, L.J. Kecskes, T. Sano, M.L. Falk, T.P. Weihs, Dynamic precipitation and recrystallization in Mg-9wt.% Al during equal-channel angular extrusion: A comparative study to conventional aging, *Acta Materialia*, 172 (2019) 185-199.
- [142] J.D. Robson, D.T. Henry, B. Davis, Particle effects on recrystallization in magnesium–manganese alloys: Particle-stimulated nucleation, *Acta Materialia*, 57 (2009) 2739-2747.
- [143] J.D. Robson, D.T. Henry, B. Davis, Particle effects on recrystallization in magnesium–manganese alloys: Particle pinning, *Materials Science and Engineering: A*, 528 (2011) 4239-4247.
- [144] A. Chalay-Amoly, A. Zarei-Hanzaki, P. Changizian, S.M. Fatemi-Varzaneh, M.H. Maghsoudi, An investigation into the microstructure/strain pattern relationship in backward extruded AZ91 magnesium alloy, *Materials & Design*, 47 (2013) 820-827.
- [145] S.E. Ion, F.J. Humphreys, S.H. White, Dynamic recrystallisation and the development of microstructure during the high temperature deformation of magnesium, *Acta Metallurgica*, 30 (1982) 1909-1919.
- [146] X. Zhang, X. Zhou, J.-O. Nilsson, Z. Dong, C. Cai, Corrosion behaviour of AA6082 Al-Mg-Si alloy extrusion: Recrystallized and non-recrystallized structures, *Corrosion Science*, 144 (2018) 163-171.
- [147] X. Zhang, X. Zhou, T. Hashimoto, J. Lindsay, O. Ciuca, C. Luo, Z. Sun, Z. Tang, The influence of grain structure on the corrosion behaviour of 2A97-T3 Al-Cu-Li alloy, *Corrosion Science*, 116 (2017) 14-21.

- [148] Y. Luo, Y. Deng, L. Guan, L. Ye, X. Guo, A. Luo, Effect of grain size and crystal orientation on the corrosion behavior of as-extruded Mg-6Gd-2Y-0.2Zr alloy, *Corrosion Science*, (2019) 108338.
- [149] C. Oernek, D.L. Engelberg, Correlative EBSD and SKPFM characterisation of microstructure development to assist determination of corrosion propensity in grade 2205 duplex stainless steel, *Journal of Materials Science*, 51 (2016) 1931-1948.
- [150] Q. Liu, Q.-x. Ma, G.-q. Chen, X. Cao, S. Zhang, J.-l. Pan, G. Zhang, Q.-y. Shi, Enhanced corrosion resistance of AZ91 magnesium alloy through refinement and homogenization of surface microstructure by friction stir processing, *Corrosion Science*, 138 (2018) 284-296.
- [151] D. Song, C. Li, N. Liang, F. Yang, J. Jiang, J. Sun, G. Wu, A. Ma, X. Ma, Simultaneously improving corrosion resistance and mechanical properties of a magnesium alloy via equal-channel angular pressing and post water annealing, *Materials & Design*, 166 (2019) 107621.
- [152] H. Torbati-Sarraf, S.A. Torbati-Sarraf, A. Poursaee, T.G. Langdon, Electrochemical behavior of a magnesium ZK60 alloy processed by high-pressure torsion, *Corrosion Science*, 154 (2019) 90-100.
- [153] K. Ralston, N. Birbilis, C. Davies, Revealing the relationship between grain size and corrosion rate of metals, *Scripta Materialia*, 63 (2010) 1201-1204.
- [154] S. Yin, W. Duan, W. Liu, L. Wu, J. Yu, Z. Zhao, M. Liu, P. Wang, J. Cui, Z. Zhang, Influence of specific second phases on corrosion behaviors of Mg-Zn-Gd-Zr alloys, *Corrosion Science*, (2019) 108419.
- [155] J.-B. Jorcin, M.E. Orazem, N. Pébère, B. Tribollet, CPE analysis by local electrochemical impedance spectroscopy, *Electrochimica Acta*, 51 (2006) 1473-1479.